Development and Parameterization of a DFT/MRCI Hamiltonian based on Different Density Functionals

---

Inaugural-Dissertation

zur

Erlangung des Doktorgrades der

Mathematisch-Naturwissenschaftlichen Fakultät

der Heinrich-Heine-Universität Düsseldorf

vorgelegt von

Dennis Ralph Dombrowski

aus Willich

Düsseldorf, August 2023

aus dem Institut für Theoretische Chemie und Computerchemie
der Heinrich-Heine-Universität Düsseldorf

Gedruckt mit der Genehmigung der
Mathematisch-Naturwissenschaftlichen Fakultät der
Heinrich-Heine-Universität Düsseldorf

Berichterstatter:

1. Univ.-Prof. Dr. Christel M. Marian
2. PD Dr. Oliver Weingart

Tag der mündlichen Prüfung: 25.10.2023

Eidesstattliche Erklärung

Ich versichere an Eides Statt, dass die Dissertation von mir selbständig und ohne unzulässige fremde Hilfe unter Beachtung der „Grundsätze zur Sicherung guter wissenschaftlicher Praxis" an der Heinrich-Heine-Universität Düsseldorf erstellt worden ist. Die aus fremden Quellen direkt oder indirekt übernommenen Gedanken sind als solche gekennzeichnet. Die Dissertation wurde in der vorliegenden oder in ähnlicher Form noch bei keiner anderen Prüfungsbehörde eingereicht. Es wurden keine früheren erfolglosen Promotionsversuche unternommen.

Düsseldorf, den

The road goes ever on and on

J. R. R. Tolkien

Abstract

This thesis deals with an extension to the semi-empirical combined density functional theory and multireference configuration interaction (DFT/MRCI) method to improve on the description of doubly excited states. The method was originally developed by Grimme and Waletzke [J. Chem. Phys. 111, 5645 (1999)] and combines the information of dynamic correlation in the Kohn-Sham orbitals with static correlation contributions in the multireference configuration interaction (MRCI) expansion in an efficient and elegant way to calculate excited state properties. In this way, medium to large molecules can be studied, which would otherwise be computationally too demanding to be accurately computed with other high-level computational methods. Since its beginnings, the method was constantly improved on and further developed to a wide range of different applications, including bichromophores, doublet states of radicals and transition metal complexes. One of the remaining problems was the description of doubly excited states, which were in all DFT/MRCI Hamiltonians until now vastly underestimated and could deteriorate the accuracy of calculated properties of energetically close lying singly excited states. The above mentioned extension of this method to enable an accurate description for doubly excited states is obtained through a detailed study of former critical cases. This study led to various modifications to the DFT/MRCI Hamiltonian and a splitting of the parameters for intra- and interorbital interactions, and resulted in the use of five global spin-invariant parameters in the new DFT/MRCI Hamiltonian, named R2022. In this way the root mean square deviation in these critical cases is reduced to 0.32 eV compared to the 1.65 eV to 1.84 eV of the former Hamiltonians. Particular attention was paid to ensure that the new Hamiltonian maintains the excellent accuracy and performance of the former Hamiltonians. To verify this, the R2022 Hamiltonian was tested on the assessment sets of the older Hamiltonians. Furthermore, results of the new Hamiltonian are compared to experimental excitations energies obtained by highly resolved anion photodetachment-photoelectron gas phase spectra of *para*-oligophenylenes and substituted anthracene derivatives to get the best possible validation.

Zusammenfassung

Diese Arbeit befasst sich mit einer Erweiterung der semiempirischen DFT/MRCI Methode, um die Beschreibung von doppelt angeregten Zuständen zu verbessern. Die Methode wurde ursprünglich von Grimme und Waletzke [J. Chem. Phys. 111, 5645 (1999)] entwickelt und kombiniert die Informationen über dynamische Korrelationseffekte in den Kohn-Sham-Orbitalen mit statischen Korrelationsbeiträgen in der MRCI-Entwicklung auf effiziente und elegante Weise, um die Eigenschaften angeregter Zustände in mittleren bis großen Molekülen zu berechnen, die mit anderen hochgenauen Methoden zu rechenintensiv wären. Seit ihren Anfängen wurde die Methode ständig verbessert und weiterentwickelt, um ein breites Spektrum unterschiedlicher Anwendungen, darunter Bichromophore, Dublettzustände von Radikalen und Übergangsmetalle, abzudecken. Eines der verbleibenden Probleme ist die zuverlässige Beschreibung doppelt angeregter Zustände, die bisher in allen DFT/MRCI-Hamiltonoperatoren stark unterschätzt wurden und die im schlimmsten Fall die Genauigkeit der berechneten Eigenschaften energetisch nahe beieinander liegender einfach angeregter Zustände beeinträchtigen können. Die oben erwähnte Erweiterung dieser Methode wird durch gründliche Untersuchung früherer kritischer Fälle erreicht, die zu verschiedenen Modifikationen und einer Aufteilung der Parameter für intra- und interorbitale Wechselwirkungen im DFT/MRCI-Hamiltonoperator führten. Insgesamt verwendet der neue DFT/MRCI-Hamiltonoperator, der den Namen R2022 trägt, fünf globale spinunabhängige Parameter. Auf diese Weise wird die mittlere quadratische Abweichung in diesen kritischen Fällen von 1,65 eV bis 1,84 eV in den früheren Hamiltonoperatoren auf 0,32 eV reduziert. Besonderes Augenmerk wurde darauf gelegt, sicherzustellen, dass der neue R2022 Hamiltonoperator die hervorragende Genauigkeit und Leistung der früheren Hamiltonianoperatoren beibehält. Um dies zu überprüfen, wurde die Genauigkeit des R2022-Hamiltonoperators anhand der Testsätze der älteren DFT/MRCI-Hamiltonoperatoren bestätigt. Darüber hinaus werden die Ergebnisse des neuen Hamiltonoperators mit experimentellen Anregungsenergien verglichen, die durch hochaufgelöste Photodetachment-Photoelektronenspektren von *para*-Oligophenylenen und substituierten Anthracenderivaten erhalten wurden, um diesen bestmöglich zu validieren.

Danksagung

In diesem Abschnitt möchte ich allen Personen danken, die mich während der Promotion unterstützt haben.

Als Erstes möchte ich mich besonders bei meiner Doktormutter Prof. Dr. Christel M. Marian für die Möglichkeit und Betreuung meiner Promotion bedanken. Die zahlreichen Ratschläge und hilfreichen Diskussionen haben mir während meiner Promotionszeit sehr weitergeholfen.

Darüber hinaus möchte ich mich bei PD Dr. Oliver Weingart für die Übernahme des Zweitgutachtens bedanken.

Außerdem möchte ich meinem Mentor Prof. Michael Schmitt danken.

Und natürlich möchte ich mich auch bei dem gesamten Arbeitskreis der TC für die angenehme und freundliche Atmosphäre bedanken. Besonders Timo Schulz für die hilfreichen und angenehmen Gespräche und die Unterstützung während der Promotionszeit. Auch möchte ich mich bei Dr. Martin Kleinschmidt für die technische und fachliche Unterstützung besonders im Zusammenhang mit dem DFT/MRCI Programm bedanken.

Für die finanzielle Unterstützung dieser Promotion möchte ich mich außerdem noch bei der Deutschen Forschungsgemeinschaft (DFG) bedanken.
(Projektnummer MA 1051/14-2 und MA 1051/20-1)

Und natürlich möchte ich mich auch ganz besonders bei meiner Familie und meinen Freunden bedanken, die mich während meiner Promotion unterstützt haben.

Contents

List Of Publications

Included in this thesis

1. **R2022: A DFT/MRCI Ansatz with Improved Performance for Double Excitations**
   J. Phys. Chem. A, **2023**, 127, 2011-2025
   Dennis R. Dombrowski, Timo Schulz, Martin Kleinschmidt and Christel M. Marian

   Own Contributions: Development and implementation of the R2022 Hamiltonian; collection of reference energies for double excited states; quantum chemical calculations and statistical evaluation; creation of figures and tables; first draft of the manuscript; contribution to corrections of the manuscript; creation of the electronic supporting information

2. **Electron affinities and lowest triplet and singlet state properties of *para*-oligophenylenes (n=3-5): Theory and experiment**
   Phys. Chem. Chem. Phys., **2023**, submitted
   Timo Schulz, Paul Konieczny, Dennis R. Dombrowski, Simon Metz, Christel M. Marian and Rainer Weinkauf

   Own Contributions: Analysis of electronical and geometrical data; creation of figures and tables; creation of the electronic supporting information

Not included in this thesis

3. **Electron-Rich Dipyrrolonaphthyridinediones: Synthesis and Optical Properties**
   J. Org. Chem., **2018**, 83, 11645-11653
   Bartlomiej Sadowski, Marcel Loebnitz, Dennis R. Dombrowski, Daniel H. Friese and Daniel T. Gryko

   Contributions: Quantum chemical calculations

List of Abbreviations

CASSCF complete active space self-consistent field.

CASPT2 second-order perturbation theory corrected CASSCF.

CC coupled cluster.

CI configuration interaction.

CIS configuration interaction singles.

CISD configuration interaction singles and doubles.

CSFs configuration state functions.

DFT Kohn-Sham density functional theory.

DFT/MRCI combined density functional theory and multireference configuration interaction method.

HF Hartree-Fock method.

HOMO highest occupied molecular orbital.

LSDA local spin density approximation.

LUMO lowest unoccupied molecular orbital.

MRCI multireference configuration interaction.

NEVPT2 second-order n-electron valence state perturbation theory.

PD-PE photodetachment-photoelectron.

RMSD root mean square deviation.

SIE self-interaction error.

TBEs theoretical best estimates.

TDDFT time-dependent density functional theory.

List of Figures

List of Tables

Chapter 1

Introduction

Nowadays photoactive organic molecular systems are getting more attention in the context of increasing environmental problems and rising criticism on fossil energy sources. These systems are used in optoelectronic applications like solar cells, organic light-emitting diodes (OLEDs) and sensors because they can be modified easily and are less expensive compared to their inorganic counterparts.[3] On a molecular level radiative and non-radiative processes compete for being the dominating one and optoelectronic devices require careful tuning of these processes. In the race for ever more efficient solar cells, singlet fission and triplet-triplet upconversion are two processes which are getting more and more attention. Singlet fission originates from a molecule which is excited into a higher singlet state and eventually transforms into two coupled triplet states. Afterwards in the optimal case separate charge carriers would be build, which can then be used to produce energy.[4] The idea behind the use of triplet-triplet upconversion in solar cells is to faciliate the absorption of low energy photons. In most solar cells, only photons above a certain energy threshold can be used to produce energy. The triplet-triplet upconversion process can circumvent this problem by enabling the absorption of two low energy photons which are then converted into one high energy photon.[5, 6]

To understand these processes and design potential materials which utilize them, thorough quantum chemical investigations are helpful. One of the key elements in these processes are doubly excited states. In a many-electron picture a doubly excited state refers to a state which has significant contributions from doubly excited Slater determinants or configuration state functions (CSFs).[2] Its definition is often ambiguous, because it depends on the used reference determinant as well as the investigator's classification when a contribution is significant.[2] In this context it was argued that some states, which are commonly seen as doubly excited states, are singly excited states when relaxed orbitals in the excited states are used.[7, 8] Nevertheless, in the context of this thesis, the commonly used definition for a doubly excited state is used, which is a state with a significant contribution of doubly excited

CSFs in the configuration interaction expansion.

The importance of these states limits the choice of quantum chemical methods. The time-dependent density functional theory (TDDFT) in its adiabatic form [9–11] is nowadays commonly used for excited states, because of its ability to achieve reliable results with low computational demands. The disadvantage is that TDDFT is not able to describe doubly excited states explicitly, and must rely on implicit consideration in the exchange-correlation functional for these states which decreases the accuracy.[12] Furthermore TDDFT is facing other problems like the self-interaction error [13–15], the delocalization error [13–15] and the erroneous description of charge-transfer [16–18] and Rydberg states [19, 20], albeit range-seperated hybrids can reduce some of these problems.[19, 20] One possible solution to introduce double excitations explicitly is to use spin-flip TDDFT [12, 21–23], although not all configurations needed for higher states can be obtained.[12, 23]

Another possible solution to calculate doubly excited states are coupled cluster (CC) methods like CC3[24, 25], CCSDT [26] and CCSDTQ [27]. [28] These methods achieve highly accurate results, albeit their computational scaling is at least N^7 and therefore only applicable for small molecules. [2]

Alternatively methods based on complete active space self-consistent field (CASSCF) [29] like the second-order perturbation theory corrected CASSCF (CASPT2) [30] or the second-order n-electron valence state perturbation theory (NEVPT2) [31–33] can be used. Since both methods scale exponentially with the number of electrons and orbitals, their active space is still limited. [2]

The combined density functional theory and multireference configuration interaction method (DFT/MRCI) [34–38] is a promising semi-empirical method to calculate this type of excitations. The original idea was to utilize information from the Kohn-Sham density functional theory (DFT) orbitals in a configuration interaction (CI) expansion to enable a significant reduction of the computational demands through an extensive selection of the most important configurations while maintaining a good accuracy. [34, 38] A double counting of electron correlation is prevented by using a set of optimized parameters to scale the integral contribution in the effective Hamiltonian. It was later extended to utilize multiplicity-independent parameters [35] to accurately describe excitations in dimer systems, enable the calculation of doublet states [36] to investigate radicals and improve the accuracy for transition metal complexes. [37] Since its development this method has been extensively used for a wide range of applications, including excited state calculations of organic molecules[39–54], organometallic complexes[55–61], metal organic frameworks [62, 63] and thermally activated delayed fluorescence emitters.[64–70] Furthermore it was used in QM/MM calculations of biomolecules [71–73] and in benchmarks with other methods. [74–78] In 2016 Vladimir Jovanović et al. [76] discovered that for

doubly excited states with $n^2 \rightarrow \pi^{*2}$ or $n, n' \rightarrow \pi^*, \pi^{*\prime}$ characters the vertical excitation energies calculated with the DFT/MRCI method are vastly underestimated. Igor Lyskov concluded in his Ph.D. thesis [79] that the problems with doubly excited states cannot be ignored, because they are energetically close to singly excited states and can therefore interact and mix with them, which can cause a deterioration of the accuracy for these states. Especially important in his opinion is the dependence on the number of open-shells and the orbital type.[79] He guessed that the error has its origin in a missing scaling of the dynamic correlation, because the error is largest, when strongly localized orbitals like non-bonding orbitals are involved.[79] Another hint of a possible solution was given by Adrian Heil in his Ph.D. thesis. [80] He investigated radicals and found, that the calculated spectra could be improved when instead of BH-LYP orbitals modified PBE0 orbitals were used. [80]

Therefore the main goal of this work is the thorough investigation of the origin of these errors, starting with an assessment of possible alternative density functionals. Afterwards, the main integral contributions to doubly excited states are worked out and in the end a new DFT/MRCI Hamiltonian with improved performance for double excitations is proposed. For this purpose, the first chapter presents the essential theoretical principles on which the DFT/MRCI method is based. Furthermore additional key aspects of the underlying density functional theory are explained, which will be important in the analysis of the suitability of different density functionals for the DFT/MRCI method. In the second chapter the training and assessment sets as well as the key aspects of the parameterization will be introduced. The investigations of the suitability of alternative density functionals will be presented in the third chapter. Afterwards, the fourth chapter describes the analysis of the integral contributions to the doubly excited states and the different prototype Hamiltonians, which were designed to alter these contributions. At the end of this chapter, the new R2022 Hamiltonian is obtained. The last chapter is about an assessment of the performance of the new Hamiltonian based on highly resolved experimental spectra.

Chapter 2

Theory

2.1 Configuration Interaction

One of the conceptually simplest methods to go beyond the mean-field approach of the Hartree-Fock method (HF) is the configuration interaction (CI) method. The wavefunction is described as a linear combination built from Slater determinants or configuration state functions (CSFs), which are built by exciting electrons to unoccupied orbitals in the reference configuration. For single reference CI the reference configuration is usually the HF configuration and the trial wavefunction is written as [81]

$$\Psi_{CI} = a_0\Phi_{HF} + \sum_S a_S\Phi_i^a + \sum_D a_D\Phi_{ij}^{ab} + \sum_T a_T\Phi_{ijk}^{abc} + ... \tag{2.1}$$

where i, j, and k are occupied and a, b, and c are virtual orbitals in the HF configuration Φ_{HF}, a are the expansion coefficients, which are determined variationally, and S, D, and T stands for sums over singly, doubly, triply, etc excited configurations relative to the HF configuration. If all possible configurations are used in Eq. 2.1, the exact non-relativistic solution in the given basis is obtained. The difference between the HF energy E^{HF} and the exact non-relativistic energy E^{exact} of a CI calculation is called correlation energy and given by: [82]

$$E_{corr} = E^{exact} - E^{HF} \tag{2.2}$$

The correlation energy can be separated into dynamic and non-dynamic correlation. The former is caused by the spontaneous short-ranged interactions between electrons due to Coulomb repulsion and can be described by excitations into high-lying virtual orbitals, while the latter is caused by the interaction of nearly degenerate configurations and often associated with the physically right behavior in dissociation processes. Since the number of Slater determinants and CSFs steeply increases

with the number of basis functions and electrons, in all but the smallest molecules a truncation is necessary. The excitation level is often used to truncate the expansion, which results in methods like configuration interaction singles (CIS) and configuration interaction singles and doubles (CISD). The resulting wavefunctions can be written as:

$$\Psi_{CIS} = a_0\Phi_{HF} + \sum_S a_S\Phi_i^a \tag{2.3}$$

$$\Psi_{CISD} = a_0\Phi_{HF} + \sum_S a_S\Phi_i^a + \sum_D a_D\Phi_{ij}^{ab} \tag{2.4}$$

To further improve on these wavefunctions, more than one reference configuration can be used, which leads to multireference configuration interaction (MRCI). For example, all configurations which are singly or doubly excited relative to at least one reference configuration can be used in the expansion. The increased amount of CSFs can make further truncations necessary. Perturbation theory might be used to find the most important configuration by approximating their interaction with the reference configuration. [83]

Wetmore and Segal [84, 85] expressed the spin-independent CI Hamiltonian in second quantization as

$$\hat{\mathcal{H}} = \sum_{\rangle|} \langle_{\rangle|} \sum_\sigma \dashv^\dagger_{\rangle\sigma} \dashv_{|\sigma} + \frac{\infty}{\in} \sum_{\rangle|||\updownarrow} \mathcal{V}_{\rangle|||\updownarrow} \sum_{\sigma\tau} \dashv^\dagger_{\rangle\sigma} \dashv^\dagger_{\|\tau} \dashv_{\updownarrow\tau} \dashv_{|\sigma} \tag{2.5}$$

where i, j, k, and l are arbitrary spatial orbitals, σ and τ are spin coordinates, h_{ij} are one-electron integrals, $V_{ikjl} = \langle i(1)k(2)| \frac{1}{r_{12}} |j(1)l(2)\rangle$ are two-electron integrals in Dirac notation and $\hat{a}^\dagger_{i\sigma}$ and $\hat{a}_{i\sigma}$ are the creator and annihilator operators, respectively, which create or annihilate an electron of spin σ in the i-th orbital and obey the anti-commutator relation:

$$[\hat{a}^\dagger_{i\sigma}, \hat{a}_{j\sigma}]_+ = \delta_{ij}\delta_{\sigma\tau} \tag{2.6}$$

$$[\hat{a}^\dagger_{i\sigma}, \hat{a}^\dagger_{j\sigma}]_+ = [\hat{a}_{i\sigma}, \hat{a}_{j\sigma}]_+ = 0 \tag{2.7}$$

The one-electron excitation operator acting on the space coordinates can then be written as

$$\hat{E}_i^j = \hat{a}^\dagger_{i\alpha}\hat{a}_{j\alpha} + \hat{a}^\dagger_{i\beta}\hat{a}_{j\beta} \tag{2.8}$$

and the one acting on the spin coordinates as

$$\hat{\epsilon}_\sigma^\tau = \hat{a}^\dagger_{i\sigma}\hat{a}_{i\tau} \tag{2.9}$$

The spin-independent Hamiltonian (Eq. 2.5) can then be rewritten in terms of these

excitation operators as

$$\hat{\mathcal{H}} = \sum_{\rangle|} \langle_{\rangle|} \hat{\mathcal{E}}^{|}_{\rangle} + \frac{\infty}{\in} \sum_{\rangle|||\updownarrow} \mathcal{V}_{\rangle|||\updownarrow} \left(\hat{\mathcal{E}}^{|}_{\rangle} \hat{\mathcal{E}}^{\updownarrow}_{\|} - \delta_{|||} \hat{\mathcal{E}}^{\updownarrow}_{\rangle} \right) \tag{2.10}$$

and finally expressed through its difference from the closed-shell anchor configuration

$$\begin{aligned} \hat{\mathcal{H}} - \mathcal{E}^{\mathcal{HF}} = & - \sum_{i} F_{ii} \bar{w}_i + \frac{1}{2} \sum_{ij} \left(V_{ijij} - \frac{1}{2} V_{ijji} \right) \bar{w}_i \bar{w}_j \\ & + \sum_{ij} F_{ij} \hat{E}^{j}_{i} - \sum_{ijk} \left(V_{ikjk} - \frac{1}{2} V_{ikkj} \right) \bar{w}_k \hat{E}^{j}_{i} \\ & + \frac{1}{2} \sum_{ijkl} V_{ikjl} \left(\hat{E}^{j}_{i} \hat{E}^{l}_{k} - \delta_{jk} \hat{E}^{l}_{i} \right) \end{aligned} \tag{2.11}$$

where the Fock matrix elements F_{ij} and SCF energy E^{HF} are given by

$$F_{ij} = h_{ij} + \sum_{k} \bar{w}_k \left(V_{ikjk} - \frac{1}{2} V_{ikkj} \right) \tag{2.12}$$

$$E^{HF} = \sum_{i} \bar{w}_i F_{ii} - \frac{1}{2} \sum_{ik} \bar{w}_i \bar{w}_k \left(V_{ikik} - \frac{1}{2} V_{ikki} \right) \tag{2.13}$$

In the CI Hamiltonian, only configurations which differ by at most a two-electron difference can interact with each other. Hence, equation 2.12 can be further divided into three categories: Diagonal elements $\hat{\mathcal{H}}_{nn}$ with the same spatial occupation, and off-diagonal elements with one- and two-electron differences, $\hat{\mathcal{H}}_{nn'}$ and $\hat{\mathcal{H}}_{nn''}$, respectively:

- Diagonal element $\hat{\mathcal{H}}_{nn}$:

$$\begin{aligned} \hat{\mathcal{H}}^{CI}_{nn} - E^{HF} = & \sum_{i} F_{ii} \Delta w_i + \frac{1}{2} \sum_{i \neq j} V_{ijij} \Delta w_i \Delta w_j \\ & + \frac{1}{2} \sum_{i \neq j} V_{ijji} \left(-\frac{1}{2} \Delta w_i \Delta w_j + \frac{1}{2} w_i w_j - w_i + \eta^{ji}_{ij} \right) \\ & + \frac{1}{2} \sum_{i} V_{iiii} \left(\frac{1}{2} \Delta w_i \Delta w_i + \frac{1}{2} w_i w_i - w_i \right) \end{aligned} \tag{2.14}$$

- One-electron difference $\hat{\mathcal{H}}_{nn'}$:

$$\begin{aligned}\hat{\mathcal{H}}^{CI}_{nn'} =& F_{ij}\eta^j_i + \sum_{k\neq i,j} V_{ikjk}\Delta w'_k \eta^j_i \\ &+ \sum_{k\neq i,j} V_{ikkj}\left(-\frac{1}{2}\Delta w'_k\eta^j_i + \frac{1}{2}w'_k\eta^j_i - \eta^j_i + \eta^{kj}_{ik}\right) \\ &+ V_{iiij}\left(\frac{1}{2}\Delta w'_i + \frac{1}{2}w'_i\right)\eta^j_i - V_{ijjj}\left(\frac{1}{2}\Delta w'_j + \frac{1}{2}w'_j - 1\right)\eta^j_i\end{aligned} \tag{2.15}$$

- Two-electron difference $\hat{\mathcal{H}}_{nn''}$:

$$\hat{\mathcal{H}}^{CI}_{nn''} = \left(V_{ikjl}\eta^{jl}_{ik} + V_{iklj}\eta^{lj}_{ik}\right)\left[\left(1+\delta_{ik}\right)\left(1+\delta_{jl}\right)\right]^{-1} \tag{2.16}$$

where n, n' and n'' are configurations, which can be further separated into their spatial w and spin ω arrangements, $\Delta w_i = w_i - \bar{w}_i$ is the difference in occupation of the orbital i between the configuration under consideration w_i and the anchor configuration $\bar{w}_i$, and η^j_i and η^{ji}_{ij} are the one- and two-electron spin coupling coefficients:

$$\eta^j_i = \langle\omega w|E^j_i|\omega' w'\rangle \tag{2.17}$$

$$\eta^{jl}_{ik} = \langle\omega w|E^j_i E^l_k|\omega'' w''\rangle \tag{2.18}$$

The diagonal elements $\hat{\mathcal{H}}_{nn}$ also include the interaction between CSFs with the same spatial- but different spin-arrangement:

$$\langle\omega w|\hat{\mathcal{H}}^{CI}|\omega' w\rangle = \frac{1}{2}\sum_{i\neq j} V_{ijji}\eta^{ji}_{ij} \tag{2.19}$$

2.2 Density Functional Theory

Kohn-Sham density functional theory (DFT) is nowadays a popular method to obtain improved results compared to Hartree-Fock theory with similar computational costs. The first fundamental aspects of density functional theory were discovered in 1927 by Thomas and Fermi. [86, 87] They developed a model in which the energy could be calculated as a functional of the one-electron density ρ. This functional has the form:

$$E_{TF}[\rho] = T_{TF}[\rho] + E_{ne}[\rho] + J[\rho] \tag{2.20}$$

where $E_{ne}[\rho]$ is the electron-nuclei attraction, $J[\rho]$ the Coulomb part of the electron-electron repulsion and $T_{TF}[\rho]$ the kinetic energy derived from the electron distribu-

tion of a uniform electron gas in the Thomas-Fermi model. [81] This model was later extended by Dirac [88] to include the exchange energy functional $K[\rho]$:

$$E_{TF}[\rho] = T_{TF}[\rho] + E_{ne}[\rho] + J[\rho] + K[\rho] \tag{2.21}$$

The breakthrough for this theory came in 1964 when Hohenberg and Kohn published two theorems, which allowed one to use the one-electron density $\rho(r)$ instead of the ground state wavefunction Ψ of a n-electron system. [89]

1. The external potential $v(r)$ is uniquely defined by the electron density $\rho(r)$. [89] To proof that, they considered two external potentials $v(r)$ and $v'(r)$ that differ by more than a constant and result in the same ground state density $\rho(r)$. As a result two different Hamiltonians $\hat{H}$ and $\hat{H}^{'}$ with two different wave functions Ψ and Ψ' are obtained. If the minimum-energy principle is employed for H with Ψ' as the trial function, the obtained energy for the ground state has to be higher for Ψ' than the ground state energy obtained with the exact wavefunction Ψ [90] for the Hamiltonian $\hat{H}$:

$$E_0 < \langle \Psi' | \hat{H} | \Psi' \rangle = \langle \Psi' | \hat{H}^{'} | \Psi' \rangle \langle \Psi' | \hat{H}^{'} - \hat{H} | \Psi' \rangle \tag{2.22}$$

$$= E_0' + \int \rho(r)[v(r) - v'(r)]dr \tag{2.23}$$

where E_0 and E_0' are the energies of the ground state of H and H', respectively. An analogous result is obtained for H' in combination with Ψ:

$$E_0' < \langle \Psi | \hat{H}^{'} | \Psi \rangle = \langle \Psi | \hat{H} | \Psi \rangle \langle \Psi | \hat{H}^{'} - \hat{H} | \Psi \rangle \tag{2.24}$$

$$= E_0 + \int \rho(r)[v(r) - v'(r)]dr \tag{2.25}$$

Adding those terms results in the contradiction:

$$E_0 + E_0' < E_0 + E_0' \tag{2.26}$$

Therefore two different external potentials $v(r)$ and $v'(r)$ cannot share the same ground state electron density $\rho(r)$.

2. The energy functional $E_v[\rho]$ (Eq. 2.28) has a minimum at the exact ground-state electron density if the functional is restricted by the condition

$$\int \rho(r)dr = n \tag{2.27}$$

which states that the integration of the electron density over the whole space yields the number of electrons. [89] The form of the functional $E_v[\rho]$ is equiv-

alent to Eq. 2.21 and given by

$$E_v[\rho] = T[\rho] + V_{ne}[\rho] + V_{ee}[\rho] \tag{2.28}$$

$$= \int \rho(r)v(r)dr + F_{HK}[\rho] \tag{2.29}$$

where $T[\rho]$, $V_{ne}[\rho]$ and $V_{ee}[\rho]$ are the kinetic energy, the electron-nuclei attraction and the electron-electron repulsion, respectively. The kinetic energy $T[\rho]$ and the electron-electron repulsion V_{ee} are collected in a universal functional $F_{HK}[\rho]$, which is independent of the number of particles and the external potential [89]:

$$F_{HK}[\rho] = T[\rho] + V_{ee}[\rho] \tag{2.30}$$

For an energy functional $\epsilon_v[\Psi']$ of a trial wavefunction Ψ', which has the form

$$\epsilon_v[\Psi'] = \langle \Psi' | V_{ne} | \Psi' \rangle + \langle \Psi' | T + V_{ee} | \Psi' \rangle \tag{2.31}$$

the energy has the minimal value if the exact wavefunction Ψ is used and the number of particles is unchanged. Since $E_v[\rho]$ (Eq. 2.28) has the form of $\epsilon_v[\Psi']$ (Eq. 2.31), this statement is also true for $E_v[\rho]$.

The significance of these two theorems is the gained simplicity and practicability in DFT. The first theorem allows the replacement of the $3n$ coordinates of the wavefunction by the three coordinates of the electron density, which reduces the complexity of the minimization procedure, while the second theorem is the working equation of DFT, because it presents a way to systematically obtain a good approximation for the ground state electron density. Unfortunately the kinetic energy $T[\rho]$ is poorly represented in orbital-free models, and therefore the accuracy of the results are rather poor. [81] In 1965, Kohn and Sham [91] reintroduced orbitals to separate the kinetic energy $T[\rho]$ into a part $T_s[\rho]$, that can be exactly calculated and a small correction, which was included in the exchange-correlation functional $E_{xc}[\rho]$. The energy functional is then given by

$$E[\rho] = T_s[\rho] + J[\rho] + E_{xc}[\rho] \tag{2.32}$$

where the exchange-correlation functional $E_{xc}[\rho]$ has the form

$$E_{xc}[\rho] = T[\rho] - T_s[\rho] + V_{ee}[\rho] - J[\rho] \tag{2.33}$$

Here, $T[\rho]$ is the exact kinetic energy of the real system and $T_s[\rho]$ is the exact kinetic energy of a system with non-interacting electrons, which share the same density as the real system. [81, 90] Since most of the kinetic energy is contained in $T_s[\rho]$,

Kohn-Sham DFT is more robust to inaccuracies in the kinetic energy approximation compared to the orbital-free DFT. [81]

2.3 Self-Interaction and Static Correlation Error

The self-interaction error (SIE) is one of the problems of DFT and common in local and hybrid density functionals. [14, 92] The simplest case is a one-electron system. Here, the electron-electron interaction V_{ee} is zero and the Coulomb- and exchange energy, J and E_x, exactly cancel each other.

$$V_{ee} = J + E_x = 0 \tag{2.34}$$

Hartree-Fock theory fulfills Equation 2.34, since the self-interaction Coulomb energy J_{11} is exactly canceled by the self-exchange energy K_{11} as can be seen in equations 2.35 to 2.37 on the example of only one spatial orbital.

$$E^{HF}(N) = \sum_{i}^{N} (h_{ii}) + \frac{1}{2} \sum_{i}^{N} \sum_{j}^{N} (J_{ij} - K_{ij}) \tag{2.35}$$

$$E^{HF}(1) = h_{11} + \frac{1}{2} (J_{11} - K_{11}) \tag{2.36}$$

$$= h_{11} \tag{2.37}$$

where h_{ii} are the one-electron integrals. Therefore, Hartree-Fock theory is by construction self-interaction free. Similarly, for DFT to be self-interaction free, the Coulomb interaction energy $J[\rho_1^\alpha]$ of the alpha spin density ρ_1^α needs to be canceled by the exchange functional $E_x[\rho_1^\alpha]$ (Equation 2.38), and the correlation functional $E_c[\rho_1^\alpha]$ has to be zero (Equation 2.39). [93]

$$J[\rho_1^\alpha] + E_x[\rho_1^\alpha] = 0 \tag{2.38}$$

$$E_c[\rho_1^\alpha] = 0 \tag{2.39}$$

While the exact exchange-correlation functional fulfills both equations, approximate exchange-correlation functionals do not. Correlation functionals derived from wave-function theory like LYP[94] can fulfill Equation 2.39, but exchange functionals do not obey Equation 2.38. SIE contributes to the so called delocalization error of commonly used density functionals, which cause an artificial stabilization of delocalized states. To remedy this error, hybrid functionals use an admixture of non-local exchange. The optimal amount of non-local exchange is system dependent. While for the uniform electron gas, the local spin density approximation is exact and self-interaction free, one-electron systems need full non-local exchange. [14]

There are schemes that remove the SIE, but SIE-corrected DFT is orbital dependent and often worsens the results for molecules with small SIE.[14] While description of the SIE as an error implies that it causes only drawbacks, some advantages are also introduced with the SIE. It was shown that the SIE mimics non-dynamic correlation. [93, 95] Cremer et al. [93] investigated potential energy curves of the bond dissociation of the H_2 molecule and found, that the hole due to the SIE drastically increases the probability of the second electron to be at the opposite H atom when using restricted DFT, thereby introducing left-right correlation implicitly. Additionally they compared densities calculated with various density functionals with wavefunction methods like MP2, MP4 and CCSD(T) to identify correlation effects at different levels. [95] They conclude that non-dynamic correlation effects are covered implicitly by the SIE in density functionals, which in wavefunction methods requires mixing of low-lying, quasi-degenerate CSFs and propose, that for methods combining DFT and wavefunction theory, functionals with small SIE should be used to avoid double counting of correlation effects. [93]

2.4 DFT Functionals

This section contains a short overview of the approximate density functionals, which played a key role in this thesis, especially in the investigation of alternative suitable functionals for the DFT/MRCI method.

2.4.1 BH-LYP

The BH-LYP [94, 96] functional is the most important functional for the DFT/MRCI method, since all published Hamiltonians until now utilize a one-particle basis calculated with this density functional. It is a hybrid density functional that consists of an equal mix of Hartree-Fock (HF) exchange and local spin density approximation (LSDA) [97, 98] with B88 [99] correction. The correlation energy is calculated with the LYP correlation functional [94]. The total form of the BH-LYP functional is then given by:

$$E_{XC}^{BHLYP} = 0.5E_X^{HF} + 0.5E_X^{LSDA} + 0.5\Delta E_X^{B88} + E_C^{LYP} \tag{2.40}$$

2.4.2 PBE0

The PBE0 functional [100, 101] is a hybrid functional that combines the PBE functional [102] with 25% HF exchange and the PW correlation functional [103]. It has

the form:

$$E_{XC}^{PBE0} = 0.75E_X^{LSDA} + 0.75E_X^{PBE} + 0.25E_X^{HF} + E_C^{PW} + E_C^{PBE} \tag{2.41}$$

2.4.3 B3LYP

The B3LYP functional [96, 104, 105] is another popular functional. It has with 20% a similiar HF exchange as the PBE0 functional and uses the LSDA and B88 exchange functionals in combination with the LYP and VWN [106] correlation functionals:

$$E_{XC}^{B3LYP} = 0.80E_X^{LSDA} + 0.72E_X^{B88} + 0.20E_X^{HF} + 0.19E_C^{VWN} + 0.81E_C^{VWN} \tag{2.42}$$

2.4.4 M06, M06-2X and M06-HF

In searching for a suitable functional for the DFT/MRCI method in section 4, the M06 series of density functionals was used to cover density functionals with a larger range of non-local exchange. The M06-HF functional [107, 108] uses 100% non-local exchange and therefore is the most non-local functional in this thesis. Its form is given by:

$$E_{XC}^{M06-HF} = E_{XC}^{M06-HF} + E_X^{HF} \tag{2.43}$$

Note that this functional contains local exchange in additional to the 100% non-local exchange to enforce the uniform electron gas limit.

The M06 functional has an admixture of 27% non-local exchange and therefore is comparable to the PBE0 and B3LYP functional. The exchange-correlation energy is given by:

$$E_{XC}^{M06} = 0.73E_{XC}^{M06} + 0.27E_X^{HF} \tag{2.44}$$

In the M06-2X functional, the admixture of non-local exchange is doubled to 54% compared to the M06 functional and therefore comparable to the BH-LYP functional. The exchange-correlation energy is given by:

$$E_{XC}^{M06-2X} = 0.46E_{XC}^{M06} + 0.54E_X^{HF} \tag{2.45}$$

2.4.5 The XCFUN library

In addition to the above mentioned density functionals, modified functionals with a custom admixture of non-local exchange were also utilized to allow a detailed study of the dependence of DFT/MRCI Hamiltonians on the underlying density functional.

For this purpose the XCFUN library [109] was used to modify the B3LYP and the PBE0 density functionals. This library allows the user to chose an exchange and correlation functional as well as the admixture of non-local exchange and combine them in an arbitrary way.

2.4.6 B75LYP

The B75LYP functional [110] is a modified BH-LYP functional with 75% non-local exchange, which was used in this thesis because of its small self-interaction error. [110] The exchange-correlation energy of this functional is given by:

$$E_{XC}^{B75LYP} = 0.75E_X^{HF} + 0.25E_X^{LSDA} + 0.25\Delta E_X^{B88} + E_C^{LYP} \tag{2.46}$$

2.4.7 PBE50 and PBE75

The PBE50 [111] and PBE75 functionals are similar to the PBE0 functional. The only differences is the amount of non-local exchange. Therefore, their exchange-correlation energy is given by:

$$E_{XC}^{PBEX} = (1-X)E_{XC}^{LSDA} + (1-X)E_{XC}^{PBE} + XE_XHF + E_C^{PW} + E_C^{PBE} \tag{2.47}$$

where X is the amount of non-local exchange (0.50 for PBE50, 0.75 for PBE75). The PBE50 functional was used because of its small self-interaction error [110], while the PBE75 was used to compare it with the B75LYP functional.

2.5 The DFT/MRCI Method

The combined density functional theory and multireference configuration interaction method (DFT/MRCI) [34–38] is a well tested method for calculating multi-configurational states which are difficult to describe by DFT alone. It is suitable for medium to large sized molecules which are too costly for other high level methods. The DFT/MRCI method takes advantage of the electron correlation included in a DFT calculation, while adding static electron correlation through the CI treatment. Therefore, significantly less configurations which describe excitations in high-lying orbitals are needed to account for dynamic electron correlation and the CI wave-function expansion can be effectively truncated to shorten the calculation time. The information of a DFT calculation is utilized by replacing the SCF energy E^{HF} and the diagonal of the Fock matrix F_{ii}^{HF} by the KS energy of the anchor configuration E^{KS} and the KS orbital energies F_{ii}^{HF} in the diagonal CI matrix elements. The

modified diagonal elements $\hat{\mathcal{H}}_{nn}^{KS}$ can then be expressed as:

$$\hat{\mathcal{H}}_{nn}^{KS} - E^{KS} = \hat{\mathcal{H}}_{nn}^{CI} - E^{HF} - \sum_i \Delta w_i F_{ii}^{HF} + \sum_i \Delta w_i F_{ii}^{KS} + \Delta E_{DFT/MRCI} \quad (2.48)$$

where the sums are over all orbitals i and the $\Delta E_{DFT/MRCI}$ term collects all semiempirical corrections to the diagonal element. In addition also the off-diagonal elements, $\hat{\mathcal{H}}_{nn'}^{DFT}$ and $\hat{\mathcal{H}}_{nn''}^{DFT}$ are scaled by p_1 and damped by the damping function f_{damp}:

$$\hat{\mathcal{H}}_{nn'}^{DFT} = p_1 \cdot f_{damp} \cdot \hat{\mathcal{H}}_{nn'}^{CI} \quad (2.49)$$

$$\hat{\mathcal{H}}_{nn''}^{DFT} = p_1 \cdot f_{damp} \cdot \hat{\mathcal{H}}_{nn''}^{CI} \quad (2.50)$$

While the scaling parameter p_1 mainly avoids double counting of non-dynamic electron correlation as further discussed in section 4, the damping function avoids double counting of dynamic electron correlation. To achieve this, the damping function reduces the interaction of CSFs based on their energy gap δe,

$$\delta e = \sum_i \Delta w_i F_{ii}^{KS} \quad (2.51)$$

CSFs which are separated by a large energy gap mainly contribute to dynamic electron correlation and therefore must be scaled to zero. This aspect of the DFT/MRCI method permits a truncation of the CI expansion based on these estimations. Since contributions from CSFs, which are too high in energy, are damped to zero by the damping function, the MRCI space is built by only including CSFs which are smaller than the sum of the energy of the highest desired root in the reference space E_{max}^{ref} and a selection threshold E_{sel}, i.e.,

$$\delta e < E_{max}^{ref} + E_{sel} \quad (2.52)$$

$$\iff \sum_i \Delta w_i F_{ii}^{KS} < E_{max}^{ref} + E_{sel} \quad (2.53)$$

Note that E_{max}^{ref} varies for each case and, as a result, the selection criterion differs for each case, too. For the user-defined selection threshold E_{sel} mainly two values are used:

- The standard selection threshold of 1.0 E_h which is used for small and medium sized molecules.
- The tight selection threshold of 0.8 E_h which is used for larger molecules where the standard selection threshold is too costly, as well as in first runs of a DFT/MRCI calculation to speed up the generation of the reference space

for subsequent calculations, which is further explained hereafter.

To improve the results further in an economic way, the reference space is created iteratively, starting from a user-defined restricted active space. The most important configurations of this calculation are identified by their weights and included in the reference space of subsequent calculations, while unimportant configurations which are originally in the restricted active space, are removed from the reference space. Therefore, the amount of CSFs is significantly and effectively reduced in a DFT/MRCI calculation.

Since the development of the DFT/MRCI method in 1999 by Stefan Grimme and Mirko Waletzke [34], multiple Hamiltonians were developed. In contrast to various DFT functionals, the DFT/MRCI Hamiltonians are built up on each other and aim to generally improve on the deficits of the predecessor to maintain an as balanced as possible description of different excitation types and molecular systems. In the following subsections a brief overview of the different DFT/MRCI Hamiltonians with focus on their solution to preceding deficits is given.

2.5.1 The Original Hamiltonian

The first DFT/MRCI Hamiltonian was developed by Stefan Grimme and Mirko Waletzke in 1999. [34] Their approach to the correction term $\Delta E_{DFT/MRCI}$ was to use three parameters to correct multiple excitations as an averaged sum over single excitation contributions, i.e.,

$$\Delta E^{orig}_{DFT/MRCI} = \frac{1}{n_{exc}} \sum_{i\in a}^{n_{exc}} \sum_{j\in c}^{n_{exc}} (p_J V_{ijij} - {}^m p[N_o] V_{ijji}) \tag{2.54}$$

where n_{exc} is the excitation class, a and c denote annihilated and created electrons, respectively, and the p_J parameter scales the Coulomb integrals. The exchange scaling term ${}^m p[N_o]$ has different forms depending on the multiplicity m and the number of open shells N_o:

$${}^1 p[N_o] = {}^1 p[0] + N_o^1 \alpha \tag{2.55}$$

$${}^3 p[N_o] = N_o^3 \alpha \tag{2.56}$$

where α and ${}^1 p[0]$ are the remaining two parameters. The parameters were separately fitted for singlet and triplet multiplicity to experimental vertical excitation energies. Note that the representation of the correction term (Eq. 2.54) as an averaged sum over single excitation contributions means that neither any integrals between two created or two annihilated electrons nor self-repulsion Coulomb integrals V_{iiii} are involved in the correction term. In contrast, the diagonal CI matrix elements $\hat{\mathcal{H}}^{CI}_{nn}$

(Eq. 2.15), which are modified by DFT/MRCI, include these integrals.

Furthermore, the diagonal elements with different spin-arrangement $\langle \omega w | \hat{\mathcal{H}}^{CI} | \omega' w \rangle$ (Eq. 2.19) are not corrected and therefore the unmodified CI matrix element is used:

$$\langle \omega w | \hat{\mathcal{H}}^{KS} | \omega' w \rangle = \langle \omega w | \hat{\mathcal{H}}^{CI} | \omega' w \rangle \tag{2.57}$$

An exponential term was used for the damping function in the correction of the off-diagonal elements (see Eq. 2.49 and Eq. 2.50):

$$f_{damp} = e^{-p_2 \cdot \Delta E^4} \tag{2.58}$$

where p_2 is a parameter which determines the steepness of the wavefunction's decline and ΔE is the energy difference between the interacting configurations. In case of multiple CSFs belonging to a configuration, the energy of the CSFs were averaged to determine the energy difference ΔE.

2.5.2 The R2016 Hamiltonian

The original Hamiltonian has two major drawbacks, which were investigated by Lyskov et al. [35] and eventually led to a new Hamiltonian in 2016. They investigated dimers which are separated by a long distance. In these dimers, the excited states which describe a simultaneous excitation on both monomers follow approximately a symmetry of degenerate states with different spin multiplicity. The original Hamiltonian breaks this symmetry, because of the dependency of the diagonal element correction (see Eq. 2.54) on the excitation class n_{exc} and the separate parameter set for singlet and triplet multiplicities. As an example, consider a simultaneous excitation at monomer a from orbital 1 to orbital 3 and monomer b from orbital 2 to orbital 4. The Coulomb term for this configuration is then given by:

$$V_{1212} + V_{3434} - V_{1313} - V_{1414} - V_{2323} - V_{2424} \tag{2.59}$$

Since the considered monomers do not interact with each other because of the spatial separation, all Coulomb integrals between these two monomers are close to zero:

$$V_{1212} = V_{3434} = V_{1414} = V_{2323} = 0 \tag{2.60}$$

Only the two integrals describing a one-electron transition on each monomer (V_{1313} and V_{2424}) are surviving. This means that the Coulomb part of the dimer in this case is simply the sum of the Coulomb parts on each individual monomer, which is

the expected behavior since the two monomers do not interact with each other:

$$E^{a+b}_{Coulomb} = E^{a}_{Coulomb} + E^{b}_{Coulomb} \tag{2.61}$$

In the original Hamiltonian the dependency on the excitation class n_{exc} in Eq. 2.54 means, that the two surviving integrals are erroneously divided by 2 in the case of the dimer, and therefore Eq. 2.61 can not be satisfied in the Coulomb part of the Hamiltonian independent of the multiplicity under consideration:

$$E^{a+b,orig}_{Coulomb} \neq E^{a,orig}_{Coulomb} + E^{b,orig}_{Coulomb} \tag{2.62}$$

$$\iff \frac{1}{2} p^{m}_{J} \left(-V_{1313} - V_{2424}\right) \neq p^{m\prime}_{J} \left(-V_{1313} - V_{2424}\right) \tag{2.63}$$

Considering for example two independent triplet excitations on the monomers, which are then coupled to a singlet state in the dimer. In this case, the problem is enhanced by the separate parameter sets for singlet and triplet multiplicities, which cause the parameters p^{m}_{J} and $p^{m\prime}_{J}$ to be different on both sides of Eq. 2.63.

Not only the Coulomb part is affected by the separate parameter sets. The exchange part of the correction describes singlet and triplet states differently, too. Considering for example the above mentioned case of two independent triplet excitations, but this time coupled to a singlet and a triplet state in the dimer. These two states should be degenerate. In the original Hamiltonian, the exchange part of the correction in Eq. 2.54 is given by:

$$\Delta E^{orig,ex}_{DFT/MRCI} = \frac{1}{n_{exc}} \sum_{i\in a}^{n_{exc}} \sum_{j\in c}^{n_{exc}} \left(-{}^{m}p[N_o] V_{ijji}\right) \tag{2.64}$$

$$= -{}^{m}p[N_o] \cdot \frac{1}{n_{exc}} \sum_{i\in a}^{n_{exc}} \sum_{j\in c}^{n_{exc}} V_{ijji} \tag{2.65}$$

Here, the only part which is different for singlet and triplet multiplicities and can therefore break the degeneracy in the exchange part is the ${}^{m}p[N_o]$ term. For this example, the number of open shells for both multiplicities is four. Therefore the respective ${}^{m}p[N_o]$ terms for singlet and triplet multiplicity become:

$${}^{1}p[4] = {}^{1}p[0] + 4 \cdot \alpha = 0.595 + 4 \cdot 0.106 = 1.019 \tag{2.66}$$

$${}^{3}p[4] = 4 \cdot \alpha = 4 \cdot 0.056 = 0.224 \tag{2.67}$$

where the standard parameter set for the original Hamiltonian was used. By comparing the effective values for each multiplicity in Eq. 2.66 and Eq. 2.67, it

becomes obvious that this way of parameterization breaks the degeneracy of the states in the exchange part of the original Hamiltonian, which can be avoided by treating states of different multiplicity with the same parameter set in the same way. Furthermore a correction factor of 1.019 for singlet states means, that about 102% of the exchange integral is removed, which will result in a vast underestimation of their energies.

With these problems in mind, Lyskov et al. [35] concluded that a new Hamiltonian should use the same parameterization for each spin multiplicity and that a dependency of the Hamiltonian on the number of open shells or excitation class is unsuitable if open-shell doubly excited states on dimers are to be calculated. The diagonal correction of their R2016 Hamiltonian is given by:

$$\begin{aligned}\Delta E^{R2016}_{DFT/MRCI} = p_J &\left(-\sum_{\substack{i,j\in c\\ i>j}}^{n_{exc}} V_{ijij} - \sum_{\substack{i,j\in a\\ i>j}}^{n_{exc}} V_{ijij} + \sum_{i\in c}^{n_{exc}}\sum_{j\in a}^{n_{exc}} V_{ijij} \right) \\ - p_x &\left(\frac{1}{2}\sum_{i\in c}^{n_{exc}}\sum_{j\in a}^{n_{exc}} V_{ijji} + \sum_{\substack{i,j\in o\\ i>j}}^{N_o} V_{ijji}\eta^{ji}_{ij} \right)\end{aligned} \tag{2.68}$$

where o denotes an open shell, and the first three sums are the correction to the electron-electron and hole-hole repulsions and the electron-hole attraction and the last two sums are the spin-independent and spin-dependent exchange corrections, respectively. Furthermore they recognized that the coupling of different CSFs of the same configuration and multiplicity contains only exchange interactions (see Eq. 2.19) and therefore should also be scaled by p_x to achieve a consistent splitting between these CSFs. Their coupling element is then given by:

$$\langle \omega w|\hat{\mathcal{H}}^{DFT/MRCI}|\omega' w\rangle = (1-p_x)\,\langle \omega w|\hat{\mathcal{H}}^{CI}|\omega' w\rangle \tag{2.69}$$

In addition to these changes to the diagonal corrections, the damping function for the off-diagonal elements was also changed to an inverse arctangent function:

$$f_{damp} = \frac{1}{1+(p_2\Delta E)^5 \cdot arctan\,(p_2\Delta E)^5} \tag{2.70}$$

In this way, the above mentioned problems for the original Hamiltonian were solved, because only one multiplicity-independent parameter set is used and the splitting between different multiplicities is treated by the spin coupling coefficients η^{ji}_{ij} like in the ab-initio CI diagonal matrix elements (see Eq. 2.15).

2.5.3 The R2017 Hamiltonian

The R2017 Hamiltonian was developed by Heil and Marian [36] to extend and generalize the formula of the R2016 Hamiltonian to open-shell systems. The diagonal correction is given by:

$$\Delta E^{R2017}_{DFT/MRCI} = p_J \left(-\sum_{\substack{i,j\in c \\ i>j}}^{n_{exc}} V_{ijij} - \sum_{\substack{i,j\in a \\ i>j}}^{n_{exc}} V_{ijij} + \sum_{i\in c}^{n_{exc}} \sum_{j\in a}^{n_{exc}} V_{ijij} + \sum_{i\in s}^{n_{single}} \frac{1}{2} V_{iiii} |\Delta w_i| \right) \tag{2.71}$$

$$- p_x \left(\frac{1}{2} \sum_{i\in c}^{n_{exc}} \sum_{j\in a}^{n_{exc}} V_{ijji} - \sum_{\substack{i,j\in c \\ j\in s}}^{n_{exc}} V_{ijji} - \sum_{\substack{i,j\in a \\ j\in s}}^{n_{exc}} V_{ijji} + \sum_{\substack{i,j\in o \\ i>j}}^{N_o} V_{ijji} \eta^{ji}_{ij} \right)$$

where the sums involving single occupied orbitals in the anchor configuration s are added in comparison to the R2016 Hamiltonian. Additionally, all elements are shifted by $\frac{1}{4}V_{ssss}$. This counteracts an unphysical shift in the diagonal CI element (see Eq. 2.15). If the anchor configuration has open shells, the energy is already shifted by $-\frac{1}{4}V_{ssss}$ without any involved excitations according to the last sum in Eq. 2.15:

$$\frac{1}{2} \sum_i V_{iiii} \left(\frac{1}{2} \Delta w_i \Delta w_i + \frac{1}{2} w_i w_i - w_i \right) = \frac{1}{2} \sum_i V_{iiii} \left(\frac{1}{2} \cdot 0 \cdot 0 + \frac{1}{2} \cdot 1 \cdot 1 - 1 \right) \tag{2.72}$$

$$= -\frac{1}{4} \sum_i V_{iiii} \tag{2.73}$$

This applies to every orbital which is singly occupied in the anchor configuration. The excitation energies are not affected by this, because all states are shifted by the same value as long as the number of electrons is not changed. Only the calculation of ionization potentials and electron affinities are affected by this shift. The treatment of the off-diagonal elements are not changed in comparison to the R2016. Due to technical limitations of the DFT/MRCI program, this Hamiltonian was only implemented for systems with one open shell in the anchor configuration.

2.5.4 The R2018 Hamiltonian

The next advancement was the change of the damping function in the R2018 Hamiltonian by Heil et al. [37], which leads to an improved description of excitation energies in transition metal complexes. The new damping function has an exponential form similar to the original Hamiltonian:

$$f_{damp} = e^{-p_2 \cdot \Delta E^6} \tag{2.74}$$

This function delays the damping effect until the energy difference is about 0.6 E_h and then declines less steep compared to the R2016 damping function. The power of 6 compared to the power of 4 in the original Hamiltonian leads to a much smaller decline at the beginning of the function and a more pronounced steepness in the end. Therefore allowing configurations with higher energy gap to interact with each other.

After the introduction of the parameterization procedure and the training and asses sment sets in the next chapter, different modifications to the DFT/MRCI method will be made, including the change of the underlying density functional to try to improve on doubly excited states.

Chapter 3

Training and Testing

3.1 Parameterization Procedure

A schematic representation of the parameterization procedure is given in Figure 3.1. In the parameterization procedure, the Nelder-Mead simplex algorithm [112] was used to find a set of parameters that minimize the root mean square deviation (RMSD). In the beginning, the algorithm starts a Python script, which executes the DFT/MRCI runs of the molecules in the training set described in Section 3.2 and afterwards gathers the excitation energies, which are needed for the calculation of the RMSD. The Python script was already used in the parameterization of the previous redesigned Hamiltonians [113–115], but was rewritten by the author of this thesis to allow the utilization of multiple cores to calculate the excitation energies in parallel. In this way, the molecules used for parameterization are distributed over the defined number of cores, so that each core calculates a single molecule. The calculated states are compared to a reference state to identify the state that should have the experimental energy. The reference states were calculated with the same functional and basis set as the ones used in the training set. A calculated state is matched to the reference state if the inner product between them is larger than 0.7. In this way, the state of interest will be identified while at the same time allowing a moderate change in state character. After the calculations are done, the RMSD for this parameter set is calculated and returned to the Nelder-Mead simplex algorithm. Then, the algorithm evaluates the RMSD, calculates a new set of parameters, and restarts the Python script until a convergence criterion of 10^{-7} eV is fulfilled.

After a converged parameter set is found, the Hamiltonian is tested on the assessment set described in Section 3.3, starting with the critical cases subset. To assess the performance of the Hamiltonian the RMSD as well as the mean deviation is analyzed to identify possible errors in the formulation and parameterization of the Hamiltonian. If the results of this subset are satisfying, the other subsets are used

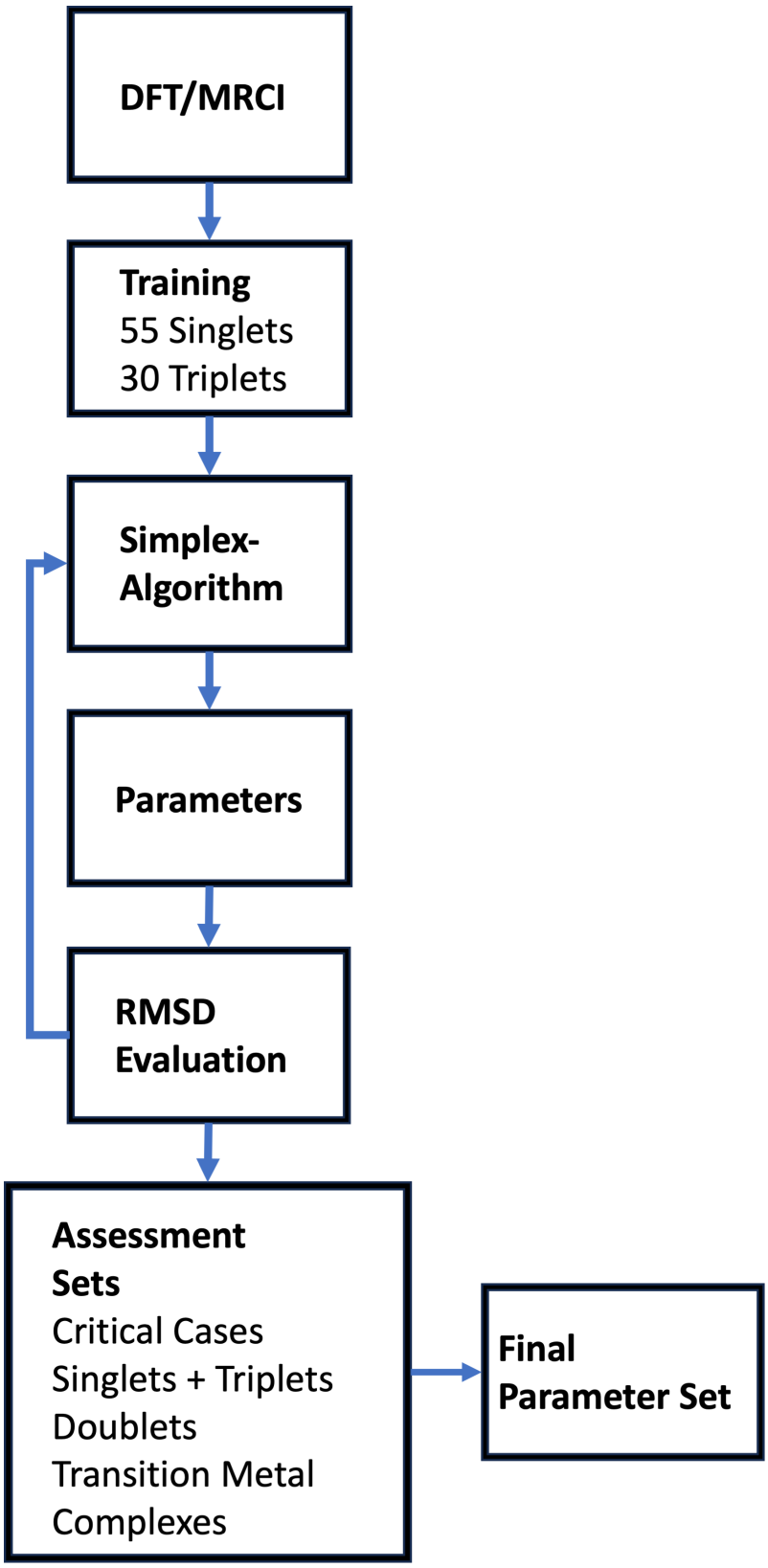

Figure 3.1: Schematic representation of parameterization and assessment procedure.

to verify that the Hamiltonian is also suited for the same molecules as the previous Hamiltonians.

3.2 The Training Set

The training set for the investigated Hamiltonians consists of 85 excited state energies. 42 singlet and 29 triplet states were used from the R2018 training set, which consists mainly of $n \rightarrow \pi^*$ and $\pi \rightarrow \pi^*$ excited state energies in small organic compounds, as well as two long range separated dimers and the copper cation. [115] The open-shell molecules were not used, because their use in the training set does not significantly influence the parameters of the Hamiltonian as can be seen from the difference of the R2016 and R2017 parameters. Additionally 11 theoretical best estimates and 3 experimental energies for doubly excited states were included to fit the parameters of the Hamiltonian for this kind of excitations. The theoretical best estimates were derived by Loos et al. [2]. An overview of all molecules of the training set can be found in Figure 3.2.

3.3 The Assessment Set

The assessment set consists of four subsets, each evaluating the performance for a different kind of excitations. The first and most important subset for this thesis includes the critical doubly excited states discovered by Jovanović et al. [76]. It is the main benchmark to assess whether the problems of former Hamiltonians with doubly excited states are resolved. Only if this subset result in satisfactory deviations, the next three subsets are evaluated to guarantee that the performance for singly excited states is the same as for the former Hamiltonians. The second subset includes 97 singlet and 63 triplet excitations in small metal-free compounds from the R2016 assessment set. [113] The third one includes 150 doublet states from the R2017 testing set to guarantee, that the new Hamiltonian is also usable for open-shell molecules. [114] The last subset incorporates excitations in metal compounds from the R2018 assessment set.[115] An overview of every subset can be found in Fig. 3.3 to Fig. 3.9.

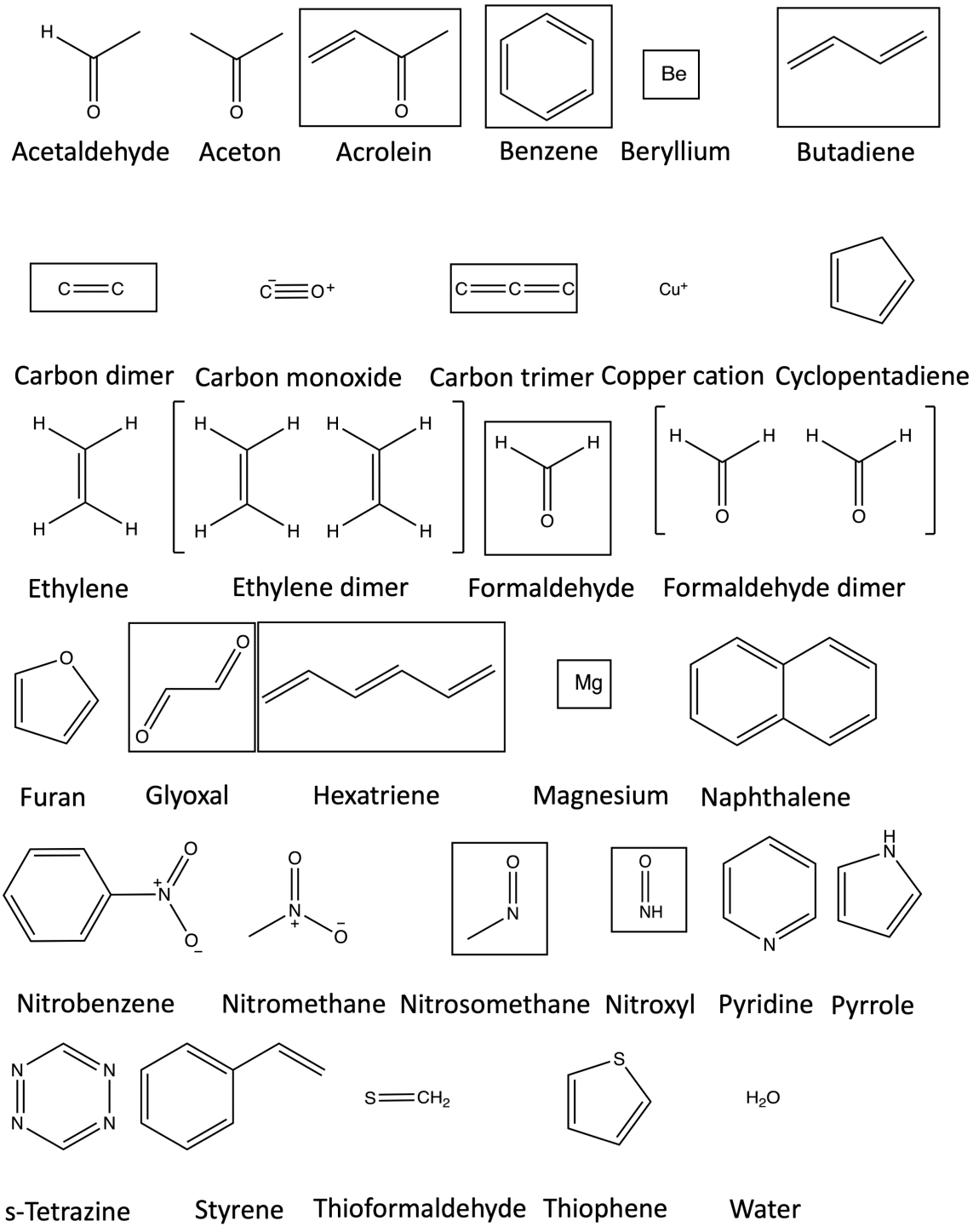

Figure 3.2: Overview of the molecules in the training set. Bordered structures indicate, that doubly excited states of this molecule were used in the training set.

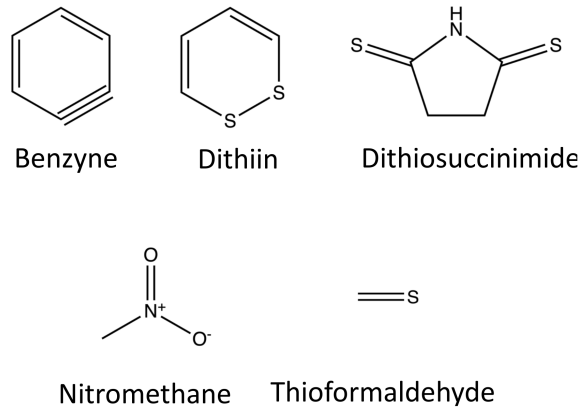

Figure 3.3: Overview of the molecules in the critical cases subset.

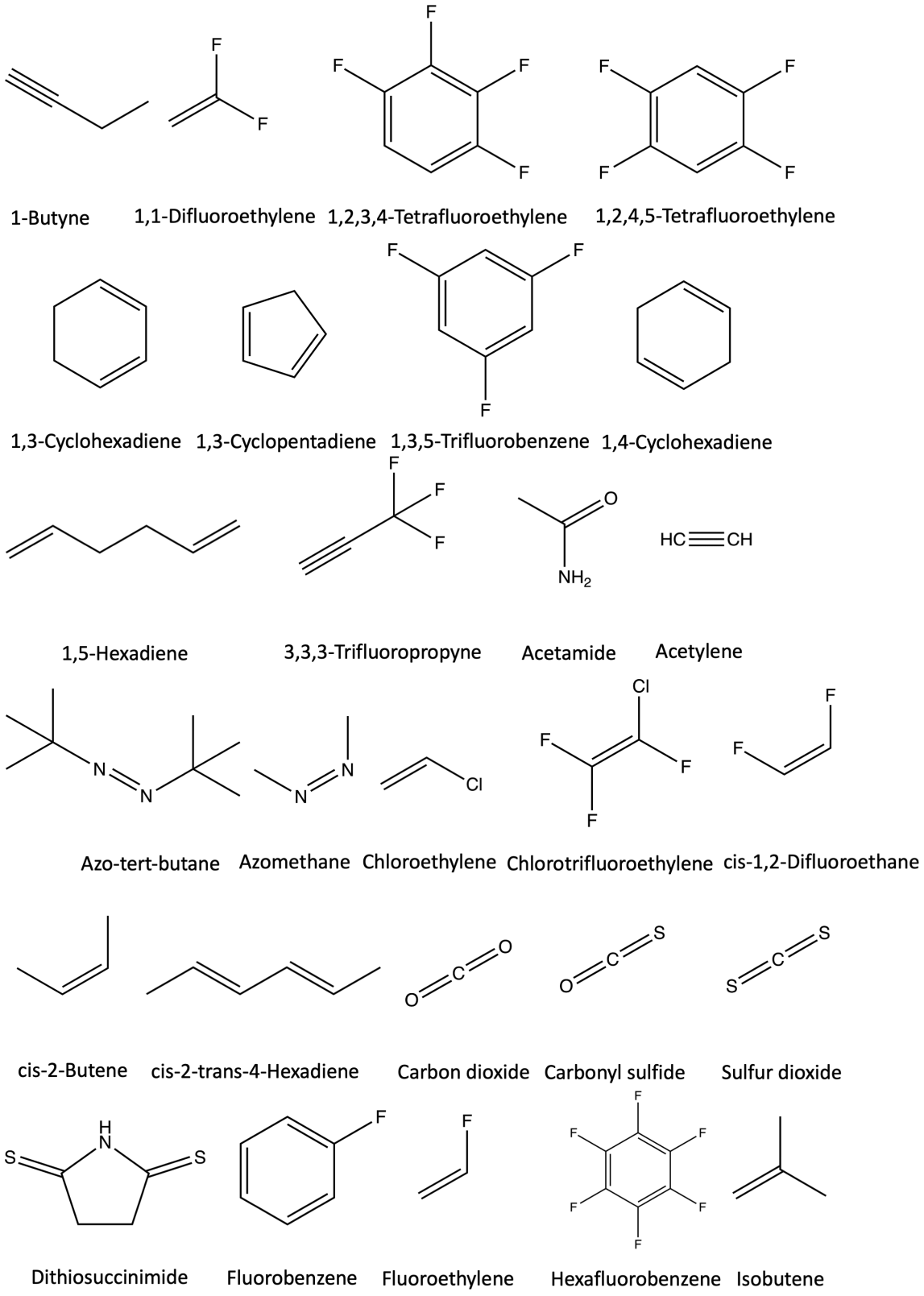

Figure 3.4: Overview of the molecules in the singlet-triplet subset.

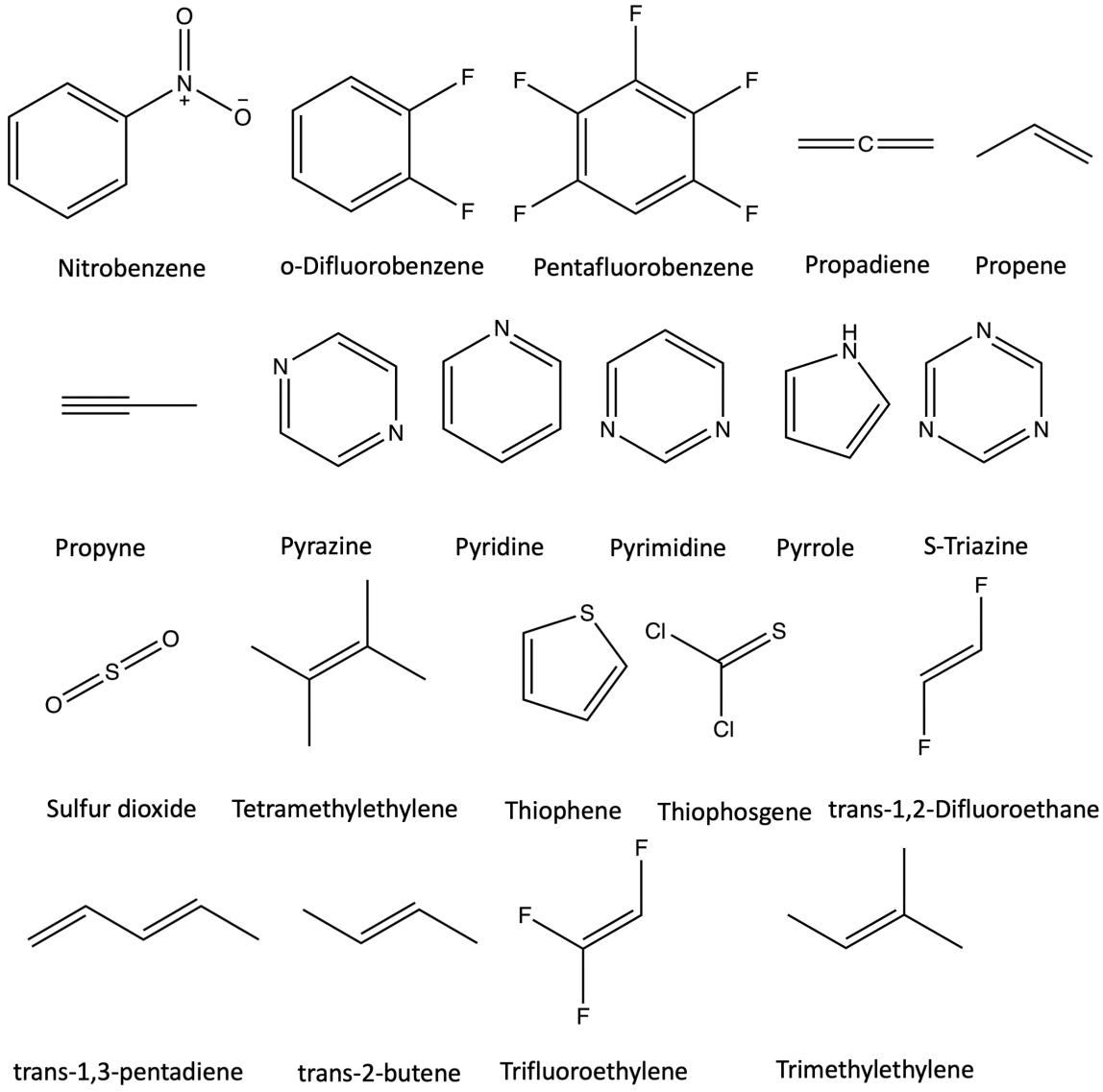

Figure 3.5: Continued overview of the molecules in the singlet-triplet subset.

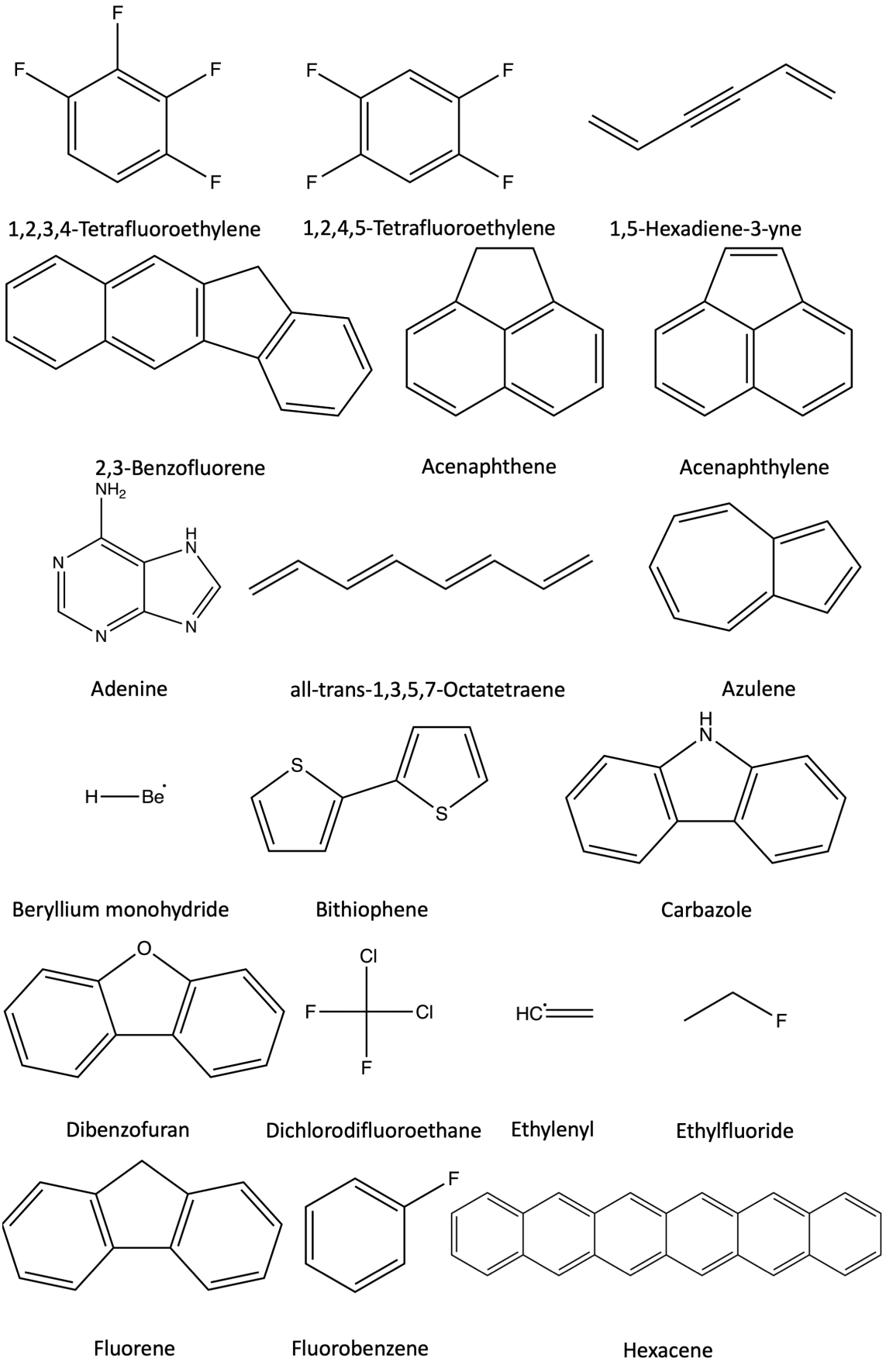

Figure 3.6: Overview of the molecules in the open-shell subset.

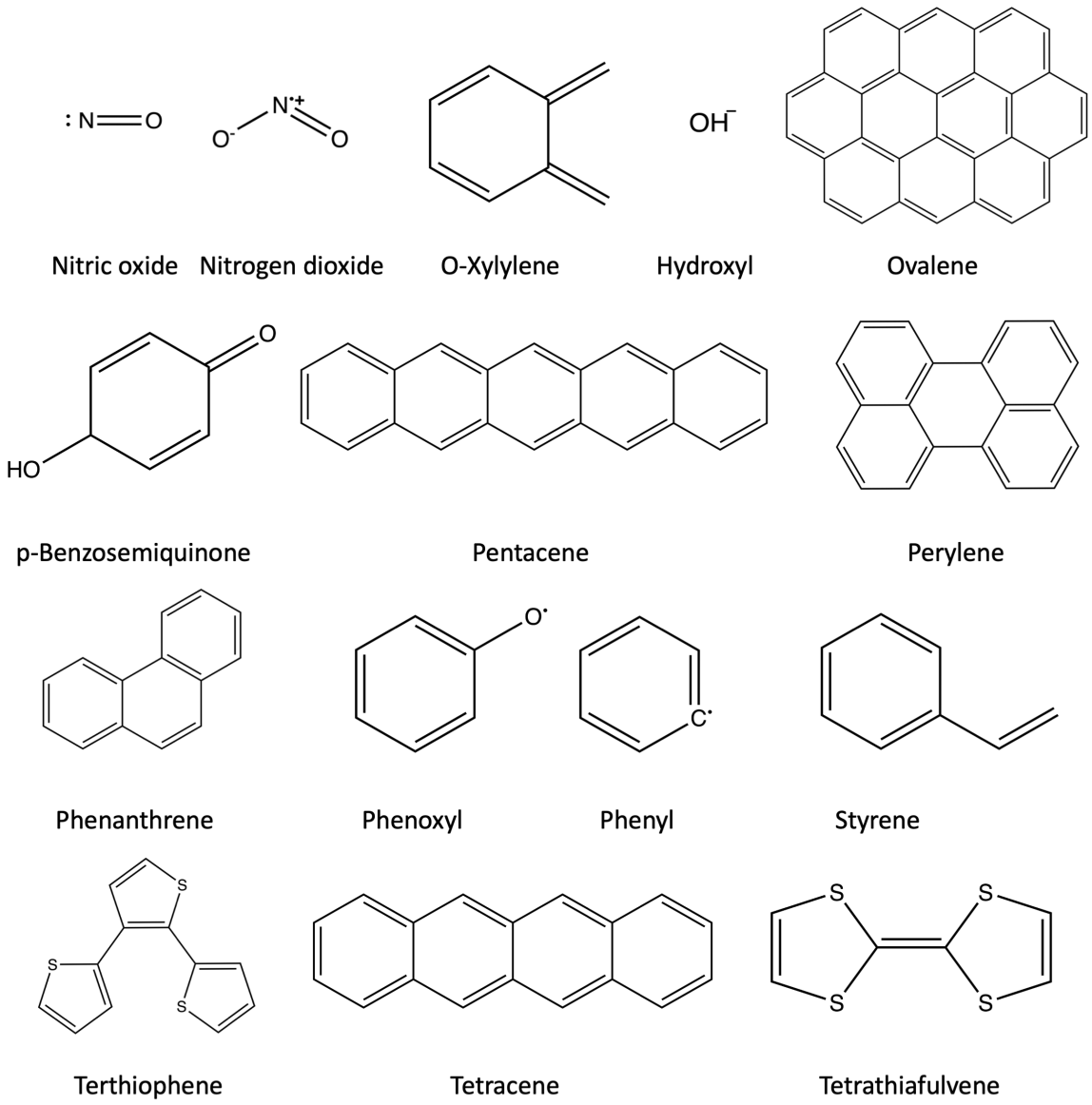

Figure 3.7: Continued overview of the molecules in the open-shell subset.

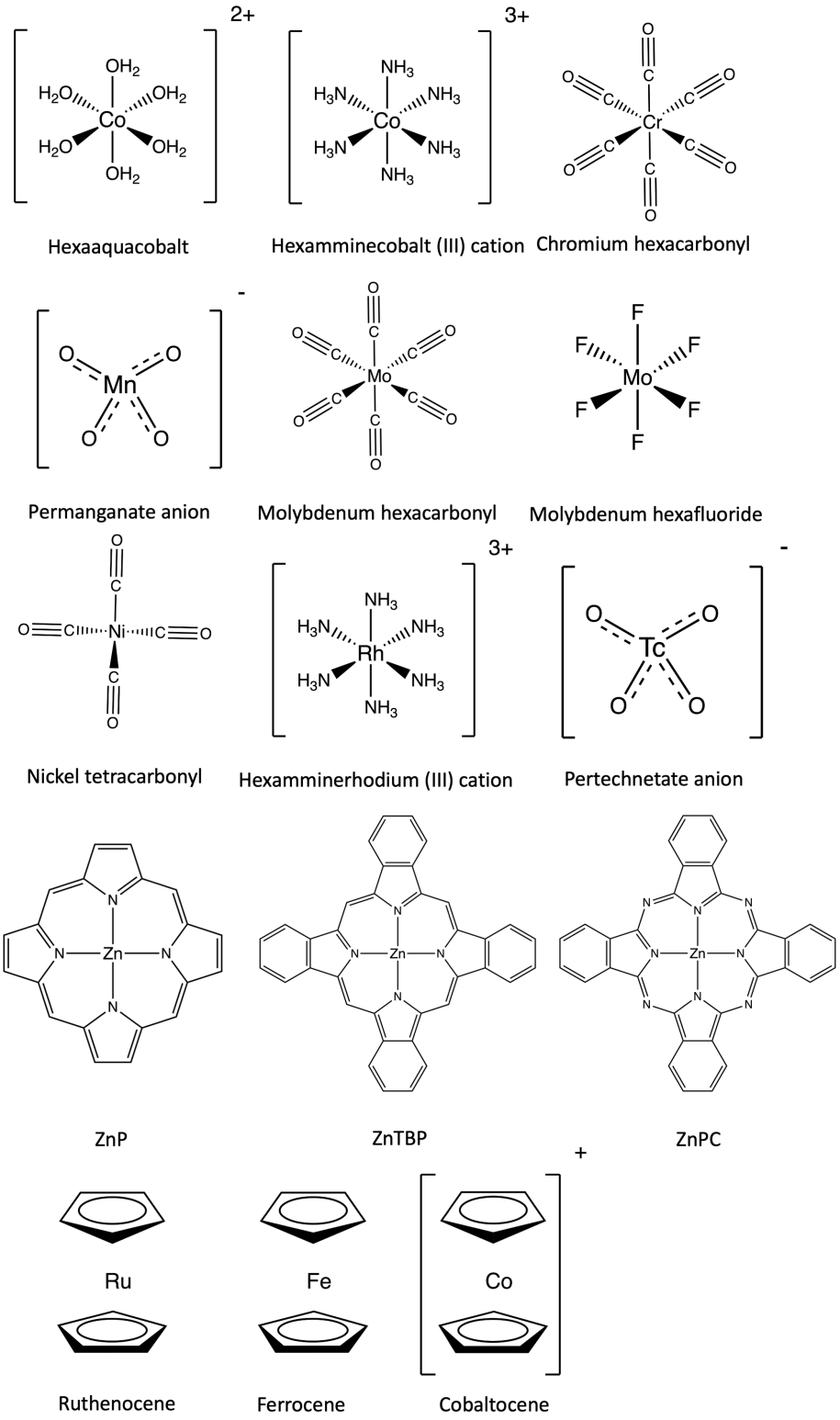

Figure 3.8: Overview of the molecules in the transition metal subset. P stands for porphine, TBP for tetrabenzoporphyrin and PC for phthalocyanine.

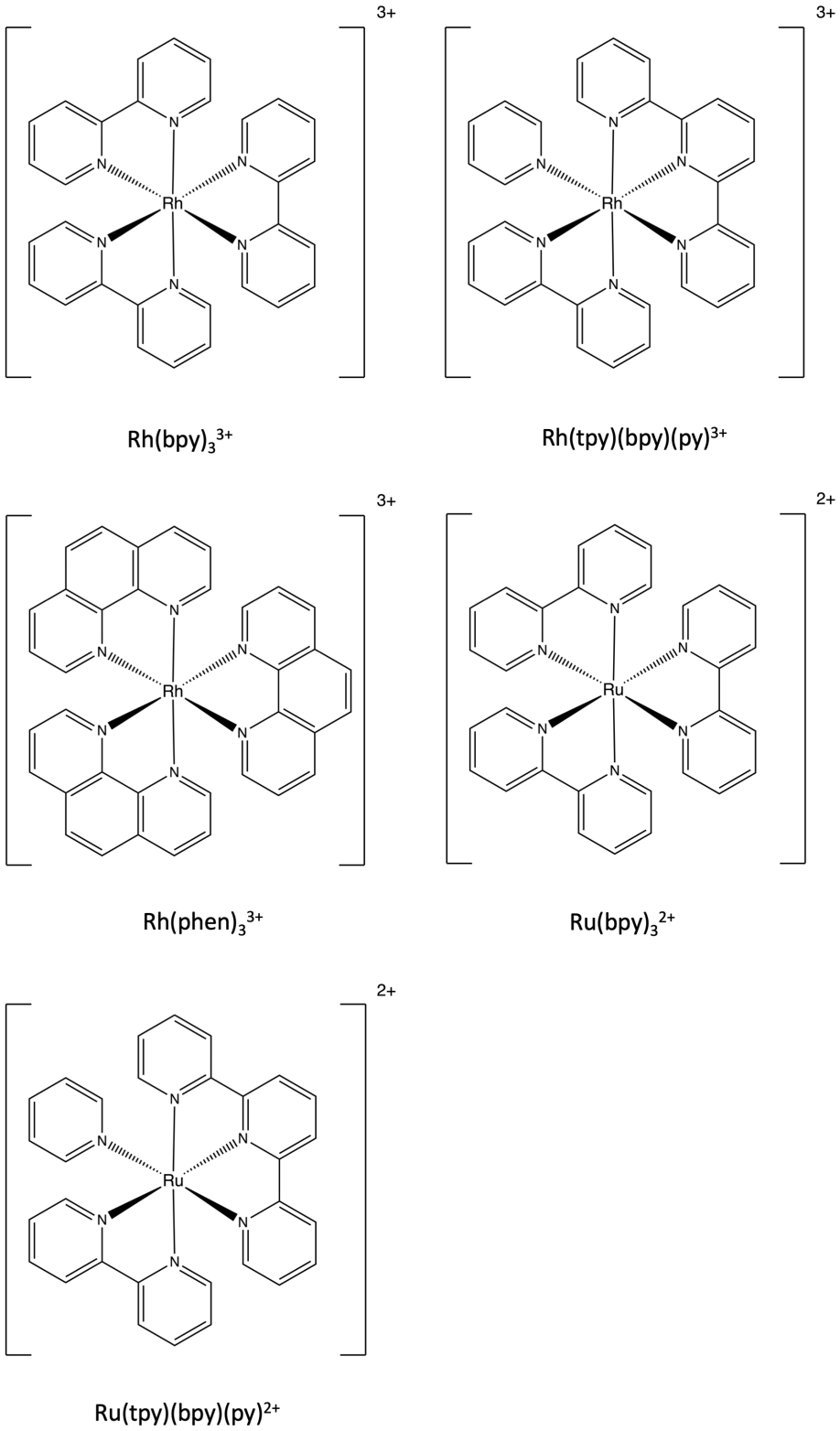

Figure 3.9: Continued overview of the molecules in the transition metal subset. py denotes pyridine ligands and phen denotes phenanthroline ligands.

Chapter 4

DFT/MRCI based on other Functionals

In this chapter, an investigation of the suitability of various density functionals as a basis for the DFT/MRCI method is presented. More detailed investigations were performed in conjunction with the PBE0 functional, which was assumed to give a better orbital basis for DFT/MRCI to resolve problems in doubly excited states or radicals. For simplicity, the functional of which the DFT/MRCI calculation is based is indicated in front of DFT/MRCI in these chapters, e.g., BH-LYP DFT/MRCI for DFT/MRCI based on BH-LYP orbitals. Furthermore the sums over singly occupied orbitals in the R2017 Hamiltonian (see Eq. 2.72) are used in every Hamiltonian in this and the next chapters but are for simplicity not written in the formula of the Hamiltonians, because the investigations mainly focus on singlet and triplet states and these sums only affect doublet states.

In their original DFT/MRCI method formulation, Grimme and Waletzke tested several density functionals. [34] They discovered that different functionals gave qualitatively similar results compared to the BH-LYP functional but that the results were best if the optimal portion of 40% to 50% non-local exchange was included. They argued that most of the functionals are not able to correctly describe the potential in the outer region of molecules, which becomes essential if excited states are involved. A similar observation has been made by Horbatenko et al. [12] for mixed-reference spin-flip TDDFT as they investigated whether the inclusion of doubly-excited configurations is beneficial for linear response theory. While for linear response TDDFT the optimal amount of non-local exchange is around 20%, an inclusion of doubly excited configurations via the mixed-reference spin-flip TDDFT needs around 40% to 50%. They argued that the linear response formalism benefits from the implicit account of non-dynamic correlation, which can, to some degree, compensate for the missing doubly excited configurations, while the mixed-reference spin-flip TDDFT explicitly accounts for doubly excited configurations and therefore

needs a more self-interaction error-free functional. In contrast, Heil [80] suggested that PBE0 orbitals could be superior based on an investigation of the absorption spectra of radicals, which could be improved if modified PBE0 orbital energies were used. To this end, he used a linear regression equation between PBE0 and BH-LYP orbital energies to modify the PBE0 orbital energies, which are close to the singly occupied molecular orbital, while keeping the parameters unaltered. While the spectra with unchanged BH-LYP orbitals are significantly blue shifted by around 0.6 eV with respect to the experimental spectrum, the modified PBE0 orbital energies reduce this blue shift to 0.4 eV. Therefore, modified PBE0 orbital energies reduced the error by around one-third in these cases.

4.1 The Influence of non-local Exchange

With this in mind, multiple reparameterizations of the R2018 DFT/MRCI Hamiltonian for several density functionals were done in this thesis with the training set explained in Section 3.2 without the added doubly excited states to assess the suitability of different functionals on cases, which were unproblematic for previous Hamiltonians. Since parameterizations with the PBE0 functional using the R2018 training set resulted in unsatisfyingly high RMSDs of about 0.40 eV, the training set was reduced to only contain vertical excitation energies from states with singlet or triplet multiplicity. This sped up the search for a new functional and simplified the DFT/MRCI Hamiltonian expression by removing the sums over all singly occupied molecular orbitals in the diagonal element correction of the R2017 and R2018 Hamiltonian (see Eq. 2.72). Additionally, the selection threshold has to be altered for each density functional to prevent a massive increase in computational cost, which would arise due to the small orbital energy gap and the associated selection of more configurations. The variation in the selection threshold impedes a strict comparison between the different functionals, but since the difference between the 'standard' and 'tight' selection threshold in BH-LYP DFT/MRCI has a rather small influence on the RMSD of a parameterization as can be seen, for example, in Igor Lyskov's or Adrian Heil's Ph.D. theses [79, 80] for the R2016 and R2017 Hamiltonians, where the difference was only 0.030 eV and 0.004 eV, a qualitative comparison is possible. The results of these reparameterizations for different density functionals are given in Figure 4.1 and Table 4.1. These results agree with Grimme's and Waletzke's observation that the optimal amount of non-local exchange is around 40% to 50%. To further verify and generalize this observation, parameters were fitted for a custom BxLYP functional, where x represents the amount of non-local exchange used in the functional. Setting $x = 50$ results in the BH-LYP, which is generally applied in the DFT/MRCI method. For this purpose, the XCFUN [109] library was used in the

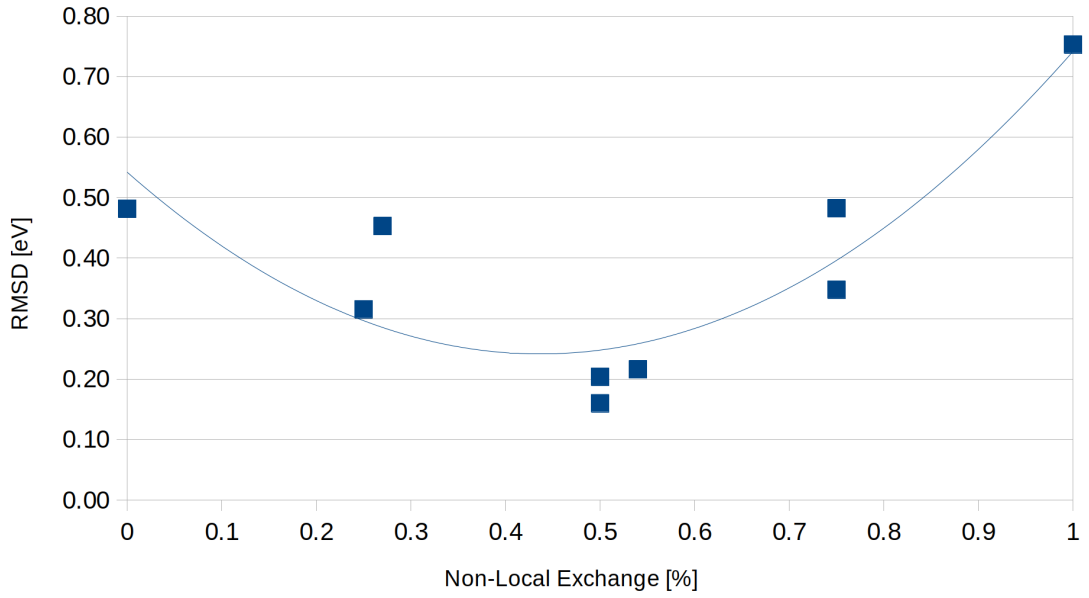

Figure 4.1: Dependency of the RMSD on the admixture of non-local exchange in different density functionals given in Table 4.1. The training set without the newly added doubly excited states and the R2018 Hamiltonian were used for reparameterization.

Table 4.1: Resulting parameters and RMSDs of parameterizations with different functionals. The training set without the added doubly excited states was used. Parameters and RMSD for the R2018 Hamiltonian are given for comparison.

Functional	% Non-local Exchange	E_{sel}	p_1	p_2	p_c	p_x	RMSD
M06-HF	100	1.0	0.65	1.78	-0.01	0.26	0.75
PBE75	75	1.0	0.88	2.69	0.26	0.29	0.48
B75LYP	75	1.0	0.73	3.52	0.21	0.36	0.35
M06-2X	54	1.0	0.55	4.00	0.51	0.39	0.22
PBE50	50	1.0	0.57	1.91	0.50	0.36	0.20
M06	27	0.8	0.36	10.73	0.79	0.50	0.45
PBE0	25	0.8	0.49	44.43	0.79	0.50	0.36
BH-LYP (R2018)	50	1.0	0.57	3.96	0.51	0.36	0.18

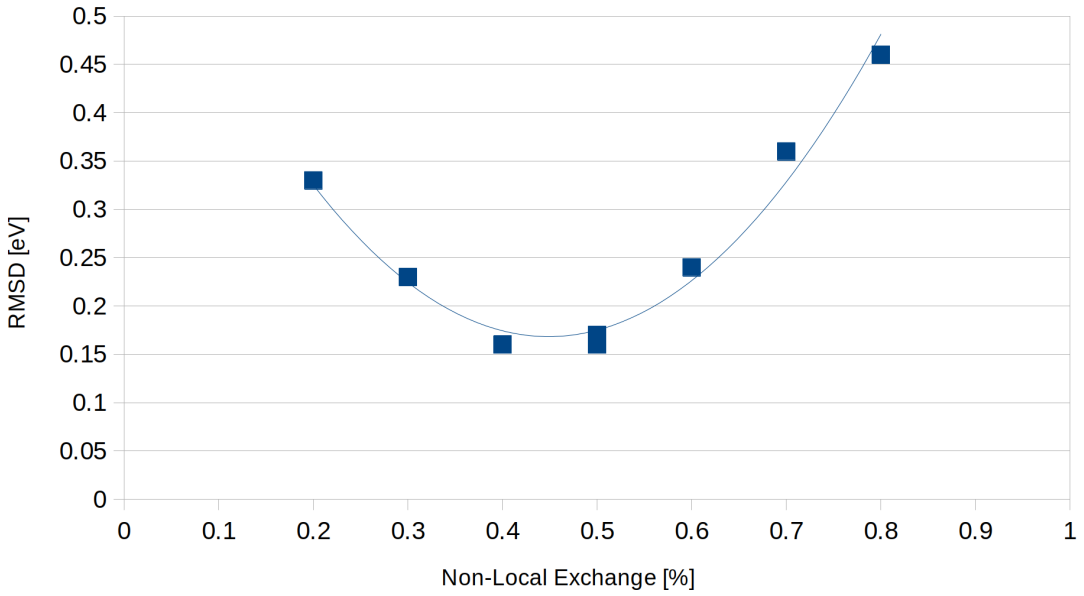

Figure 4.2: Dependency of the RMSD on the admixture of non-local exchange in BxLYP. The training set without the newly added doubly excited states and the R2018 Hamiltonian were used for reparameterization.

TURBOMOLE program. [116, 117] The resulting RMSDs for every admixture of non-local exchange are depicted in Figure 4.2, and the corresponding parameters are given in Table 4.2. Interesting trends can be observed from this results. As already mentioned in the original publication by Grimme and Waletzke [34], the Coulomb scaling parameter p_c roughly takes the value of the amount of DFT exchange in the underlying functional with deviations of usually around 0.01 to 0.04 for the DFT functionals in Table 4.1, while for BxLYP the values deviate further to up to 0.12 in the case of B20LYP. Furthermore, the off-diagonal correction parameter p_1 correlates strongly with the admixture of non-local exchange. Increasing the admixture of non-local exchange leads to a larger p_1 parameter and, therefore, less downscaling to the DFT/MRCI off-diagonal matrix elements. Since this parameter scales quasi-degenerate configurations, which are essential for non-dynamic correlation, it can be assumed that DFT/MRCI benefits from a self-interaction free functional to prevent further double counting of non-dynamic correlation. This assumption is affirmed by the SIE4x4 benchmark results of Lonsdale and Goerigk.[110] Here, BH-LYP is already the third most self-interaction free global-hybrid density functional. In contrast, most functionals with a small admixture of non-local exchange, like PBE0, have a significantly more pronounced self-interaction error and, as a result, more implicit non-dynamic correlation. Since the MRCI part should mainly introduce this kind of correlation, additional corrections must be made to prevent double counting. Moreover, the implicit inclusion of non-dynamic correlation complicates the

Table 4.2: Resulting parameters and RMSDs of parameterizations with a different admixture of non-local exchange in the BxLYP functional. The training set without the newly added doubly excited states was used. For 50% non-local exchange, R2016 and R2018 parameters are given for comparison.

$\%DFT$	E_{sel}	p_1	p_2	p_c	p_x	RMSD
20	1.0	0.70	1.71	0.08	0.10	0.33
30	1.0	0.66	2.00	0.24	0.20	0.23
40	1.0	0.62	2.88	0.38	0.28	0.16
R2016	1.0	0.57	18.3	0.51	0.36	0.16
R2018	1.0	0.56	4.47	0.51	0.36	0.17
60	0.8	0.54	12.34	0.63	0.40	0.24
70	0.8	0.47	16.3	0.74	0.46	0.36
80	0.7	0.50	13.24	0.89	0.53	0.46

situation because the introduced amount of correlation effects are unquantifiable. On the positive side, a stricter truncation could be possible since more correlation is already accounted for by the underlying functional. Another possible drawback of functionals with a high amount of DFT exchange is the breakdown of excitation spectra above the positive energy of the HOMO $-\epsilon_H$ as has already been discovered by Casida et al. in 1998. [118] As one approaches this limit, more spurious Rydberg states will appear and disturb the excitation spectrum by mixing with other states. [119] Therefore, pure DFT or hybrid functionals with a small admixture of non-local exchange may suffer from this problem due to higher HOMO energies. The following sections focus on possible modifications to the DFT/MRCI Hamiltonian to facilitate PBE0 orbitals as the one-particle basis. To this end, the differences between the usually used BH-LYP and the PBE0 orbital basis are presented in the next section.

4.2 Difference between BH-LYP and PBE0 Orbitals

The differences between the used density functionals are essential to investigate because the resulting orbital energies and two-electron repulsion integrals of the underlying one-particle basis are the main contributions to the energy of a configuration. Therefore insight into their behavior enables the prediction of the required modifications and the possible influence and performance of DFT/MRCI Hamiltonians. Since it was assumed that PBE0 orbital energies could be an improvement over BH-LYP orbital energies in the case of radicals, the PBE0 functional was used. [80] The occupied orbital energies in PBE0 have smaller negative values, while the unoccupied orbital energies are smaller, and therefore leading to smaller occupied-virtual

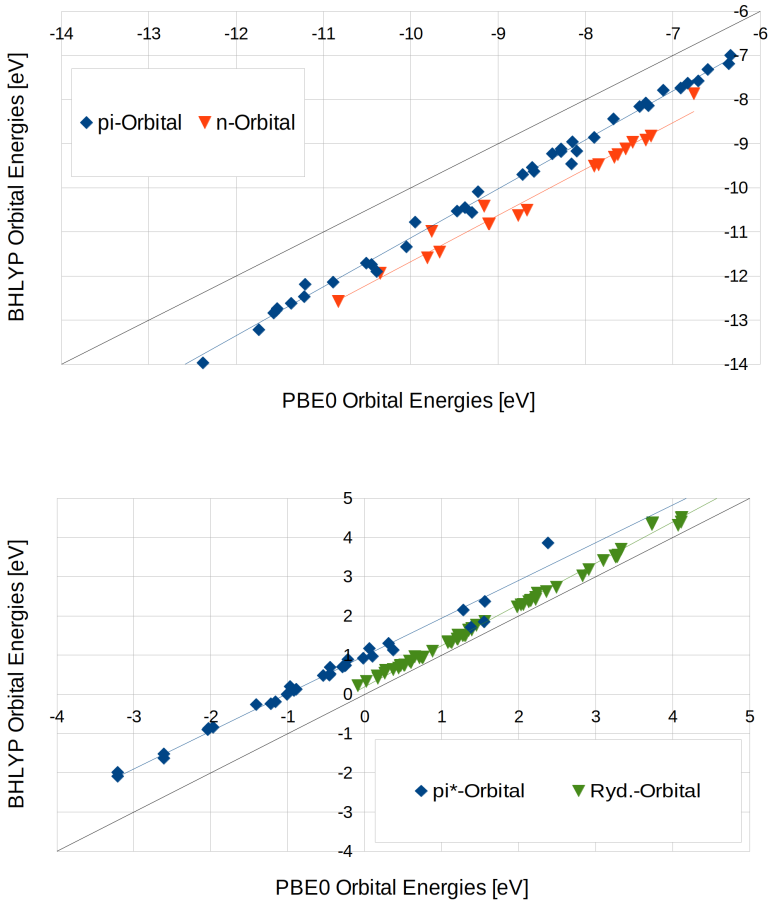

Figure 4.3: Comparison of PBE0 and BH-LYP orbital energies of 487 occupied (top) and virtual (bottom) orbitals of the molecules in the singlet and triplet training set.

orbital energy gaps as can be seen in Figure 4.3. Since the DFT/MRCI Hamiltonian has to compensate for smaller energy gaps, the corrections are predicted to be larger with PBE0 orbitals. Additionally, the selection criterion is based on the orbital energy differences. It must be reduced accordingly to match the same configurations and computational costs as the previous Hamiltonians. More problems become apparent if the orbital energies are sorted according to their orbital character into π, n, π^*, and Rydberg orbitals, which was, in this case, done by visual inspection. The results can be seen in Figure 4.3. Every group of orbitals behaves differently compared to the BH-LYP orbital energies, with n and π^* orbital energies affected the most. In contrast, the small change in Rydberg orbital energies is rooted in the exchange-correlation potential in the DFT functional. This potential differs between different density functionals, and in general, neither has the correct behavior close to the atoms of the molecule nor the correct asymptotic $-1/r$ behavior. As a result, orbital energies are, in general, too high. [119] This shortcoming of the potential significantly increases the orbital energy for valence orbitals, which are located mainly in the molecular region. However, since this is the case for all valence orbitals, their differences are unaffected. In contrast, a Rydberg electron is in the potential's outer region. Therefore the orbital energy is less influenced by the wrong shape of the potential, which then leads to fewer differences in these orbital energies between density functionals. Since the Rydberg orbital energies are less affected, they will need a higher selection threshold to be included in the calculation, which will affect to some extent the calculation of those states.

Similar observations can be made for the two-electron repulsion integrals. In Figure 4.4, Coulomb and exchange integrals involved in the singlet state excited energies of the training set are presented. Coulomb integrals resulting from a transition to a Rydberg orbital are less affected by a change of the density functional than $\pi \rightarrow \pi^*$ or $n \rightarrow \pi^*$ transitions. Especially the $n \rightarrow \pi^*$ Coulomb integrals have many outliers and differ significantly between the two functionals. The deviations are less pronounced for the exchange integrals than for Coulomb integrals, mainly because transitions with participating non-bonding or Rydberg orbitals usually have small exchange interactions. Since the performance of all previous BH-LYP based DFT/MRCI Hamiltonians is satisfactory for these different types of orbitals and transitions, as can be seen in the publications of previous DFT/MRCI Hamiltonians [113–115], worsening of the accuracy due to different behaviors for each excitation type is expected. In the following section, this influence and possible solutions will be investigated.

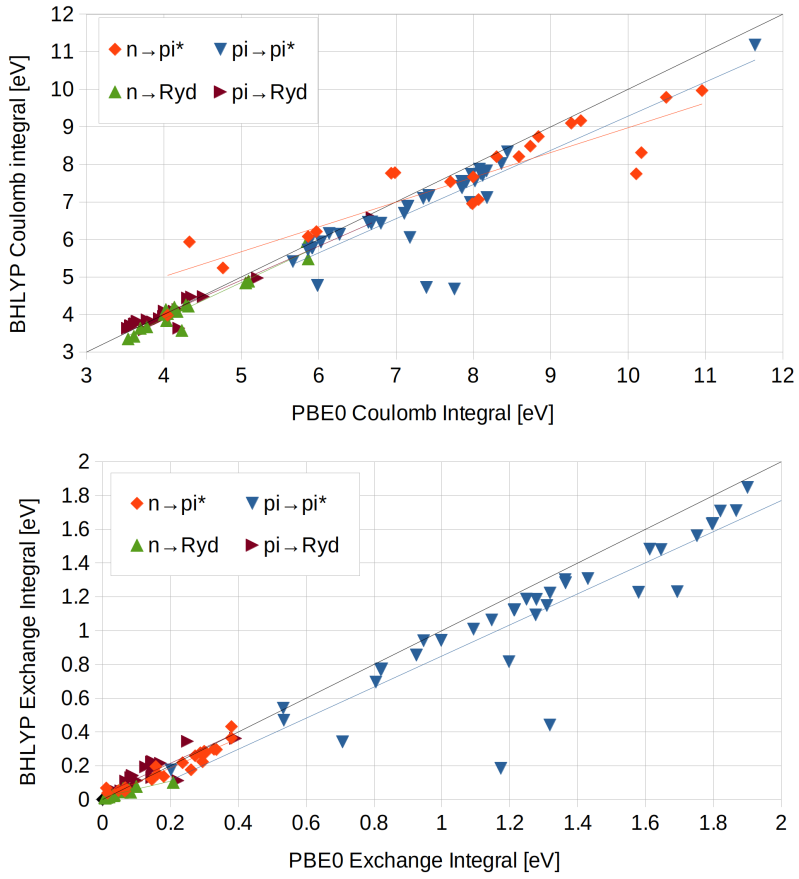

Figure 4.4: Coulomb- (top) and exchange (bottom) integrals involved in the singly excited singlet state energies in the training set divided by transition character. All values are in eV.

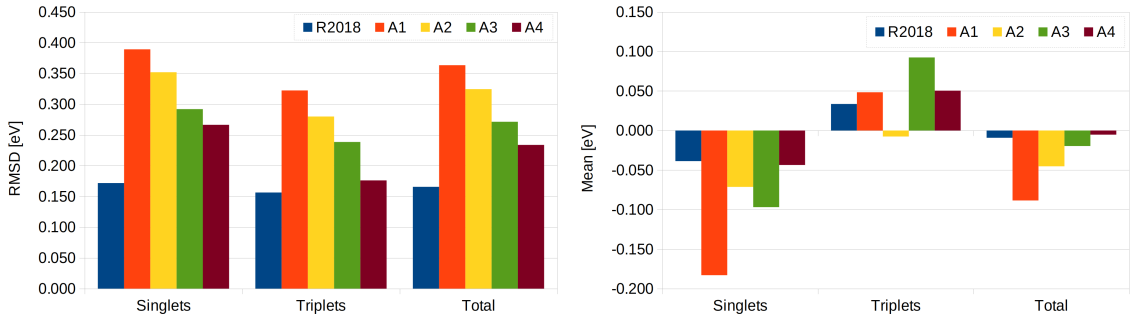

Figure 4.5: RMSD and mean deviation of different approaches to DFT/MRCI with PBE0 orbitals. For comparison the results of the R2018 Hamiltonian with BH-LYP orbitals are given.

Table 4.3: Reoptimized parameters for the training set with PBE0 orbitals for the R2018 parameterization scheme and a selection threshold of 0.8 E_h. The unmodified R2018 standard parameters, RMSD, and mean deviation for a selection threshold of 1.0 E_h are also given for comparison.

Hamiltonian	p_1	p_2	p_c	p_x	p_5	RMSD [eV]	Mean [eV]
R2018	0.5584	4.4717	0.5089	0.3624		0.17	0.00
A1 (Eq. 4.1)	0.4870	44.4304	0.7901	0.4970		0.36	-0.09
A2 (Eq. 4.2)	0.3967	8.3884	0.7905	0.3806	0.9440	0.32	-0.05
A3 (Eq. 4.3)	0.4655	10.9044	0.7029	0.5061	0.0930	0.27	-0.02
A4 (Eq. 4.4)	0.4867	8.0248	0.7394	0.4178	0.8424	0.23	-0.01

4.3 DFT/MRCI based on PBE0 Orbitals

Based on the insights of the previous section, different Hamiltonians based on PBE0 orbitals were designed, and their performance in comparison to BH-LYP DFT/MRCI were assessed. For the parameterization of the standard selection threshold, a value of 0.8 E_h was found to give about the same computational time and number of configurations as the standard selection threshold in BH-LYP DFT/MRCI. The RMSD and mean values for these reparameterizations are shown in Figure 4.5 and Table 4.3. While PBE0 DFT/MRCI can reach the accuracy of BH-LYP DFT/MRCI for specific kinds of excitations, the overall performance remains poor. In the following, the modifications to the DFT/MRCI Hamiltonian starting from the R2018 formulation and the most important differences and insights are explained. The A1 Hamiltonian is a reparameterization of the R2018 Hamiltonian without any modifications to the Hamiltonian itself, hence its diagonal elements are

the same as for the R2017 and the R2018 Hamiltonians:

$$\Delta E^{A1}_{DFT/MRCI} = p_J \left(-\sum_{\substack{i,j\in c \\ i>j}}^{n_{exc}} V_{ijij} - \sum_{\substack{i,j\in a \\ i>j}}^{n_{exc}} V_{ijij} + \sum_{i\in c}^{n_{exc}} \sum_{j\in a}^{n_{exc}} V_{ijij} + \sum_{i\in s}^{n_{single}} \frac{1}{2} V_{iiii} |\Delta w_i| \right) \tag{4.1}$$

$$- p_x \left(\frac{1}{2} \sum_{i\in c}^{n_{exc}} \sum_{j\in a}^{n_{exc}} V_{ijji} - \sum_{\substack{i,j\in c \\ j\in s}}^{n_{exc}} V_{ijji} - \sum_{\substack{i,j\in a \\ j\in s}}^{n_{exc}} V_{ijji} + \sum_{\substack{i,j\in o \\ i>j}}^{N_o} V_{ijji} \eta^{ji}_{ij} \right)$$

The differences between the two parameter sets in Table 4.3 illustrate the problems arising using PBE0 as the underlying functional. Since the orbital gaps are smaller for PBE0 orbitals than the BH-LYP ones, and the integrals are significantly less affected, the corrections must be larger for the PBE0 cases to result in the same excitation energies. Figure 4.6 illustrates this on the example of the highest occupied molecular orbital (HOMO) to lowest unoccupied molecular orbital (LUMO) excitation in butadiene. Here, the red arrows are the unscaled contributions, while the green ones are scaled by the DFT/MRCI parameters. The experimental reference excitation energy is shown as a dashed line. The PBE0 orbital energy difference is already close to the experimental value. As a result, the corrections must modify the integral contributions of the Coulomb- and exchange interactions such that they almost cancel each other to reach the experimental reference. This cancellation provides less influence from the integrals than from the orbital energies. Therefore, additional corrections to the orbital energies are likely to be required. In contrast, the BH-LYP orbital energy is higher, and Coulomb- and exchange interactions have different magnitudes. Therefore information from the integrals can be better used to reach the experimental reference, and corrections mainly focus on altering the integral contributions. The A1 Hamiltonian results in doubled RMSD and MAE compared to R2018 from 0.17 eV to 0.36 eV. Only triplet states with $n \rightarrow \pi^*$ character are improved by this Hamiltonian. The agreement for the other states is significantly deteriorated. Especially the $\pi \rightarrow \pi^*$ excitations deviate strongly from the experimental excitations. A first improvement is brought about by the splitting of the η-independent from the η-dependent exchange correction terms as can be seen in Equation 4.2, where the η-independent term is scaled by p_5, and the η-dependent term is scaled by p_x. Lyskov et al. [113] found for the R2016 Hamiltonian that the parameter for the former is roughly one-half of the latter and therefore decided to unite these into one parameter. Therefore, for $p_x = p_5$ the unmodified R2016 Hamiltonian is obtained. Since in the case of the A1 Hamiltonian, the p_x parameter differs from the one used in R2016 to R2018 by about 0.14, the above statement has to be reevaluated for the use with PBE0 orbitals. To this end, the A2 Hamiltonian

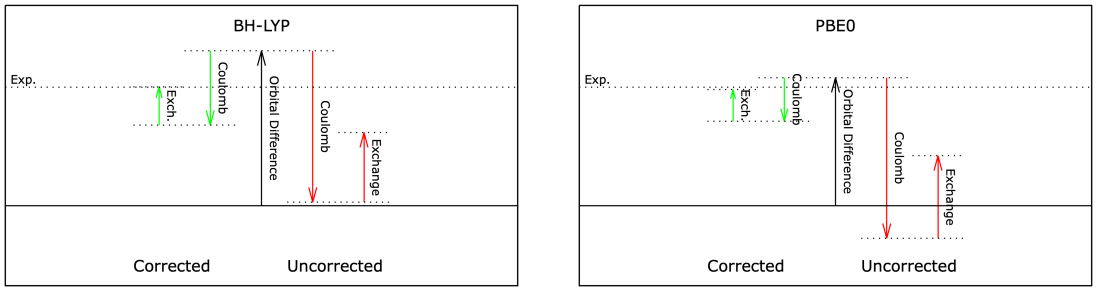

Figure 4.6: Representation of the contributions to the DFT/MRCI energy of the HOMO to LUMO transition in butadiene. Red arrows represent unscaled and green arrows scaled integral contributions. For BH-LYP, the R2018 Hamiltonian was used, while for PBE0, the A1 Hamiltonian was utilized.

with an extra parameter for the η-independent exchange correction was introduced.

$$\Delta E^{A2}_{DFT/MRCI} = p_c\Big(- \sum_{\substack{i,j\in c\\ i>j}}^{n_{exc}} V_{ijij} - \sum_{\substack{i,j\in a\\ i>j}}^{n_{exc}} V_{ijij} + \sum_{i\in c}^{n_{exc}}\sum_{j\in a}^{n_{exc}} V_{ijij}\Big) \\ - \frac{p_5}{2}\sum_{i\in c}^{n_{exc}}\sum_{j\in a}^{n_{exc}} V_{ijji} - p_x \sum_{\substack{i,j\in c\\ i>j}}^{n_{exc}} V_{ijji}\eta^{ji}_{ij} \tag{4.2}$$

The formula for singlet and triplet multiplicity is given by Equation 4.2, where the factor of one-half was retained to emphasize the difference between the p_x and p_5 parameters. As seen in Table 4.3, p_5 is doubled compared to p_x, and therefore the observation of Igor Lyskov et al. is not valid in the case of PBE0 orbitals. A parameterization in this way improves the RMSD and MAE, especially for the states with $\pi \rightarrow \pi^*$ character. In contrast, $n \rightarrow \pi^*$ states have a slightly larger RMSD in comparison to A1. However, this Hamiltonian still performs significantly less satisfactory than the former BH-LYP DFT/MRCI Hamiltonians.

Since a correction of the Coulomb- and exchange integrals is not able to achieve acceptable performance in this context, the other possible starting point involves the orbital energies. Motivated by the difference in orbital energies in Figure 4.3 and early work of Grimme [120], who used a correction for the occupied orbitals in his DFT/SCI method, the A3 Hamiltonian introduces an additional parameter p_5 to scale the occupied orbital energies. A diagonal element of the A3 Hamiltonian

has the form:

$$\begin{aligned}\Delta E^{A3}_{DFT/MRCI} = p_J &\left(-\sum_{\substack{i,j\in c\\ i>j}}^{n_{exc}} V_{ijij} - \sum_{\substack{i,j\in a\\ i>j}}^{n_{exc}} V_{ijij} + \sum_{i\in c}^{n_{exc}}\sum_{j\in a}^{n_{exc}} V_{ijij} \right) \\ &- p_x \left(\frac{1}{2}\sum_{i\in c}^{n_{exc}}\sum_{j\in a}^{n_{exc}} V_{ijji} + \sum_{\substack{i,j\in o\\ i>j}}^{N_o} V_{ijji}\eta^{ji}_{ij} \right) \\ &+ p_5 \sum_{i\in occ} \Delta w_i F^{KS}_{ii}\end{aligned} \tag{4.3}$$

The optimal value for p_5 was found to be 0.09 which means that every occupied orbital energy is increased by 9% of their original value. Parameterized in this way a RMSD of 0.27 eV was achieved. Scaling of the virtual or all orbitals resulted in less satisfactory results with an RMSD of 0.33 eV and 0.34 eV, respectively. Parameterized in this way, the Hamiltonian improves $\pi \rightarrow \pi^*$ excitations with a high amount of Coulomb interaction, for example, in nitromethane.

The A4 ansatz was the last attempt to reach sufficient accuracy with PBE0 orbitals as the basis of DFT/MRCI. It combines corrections in the A2 and A3 Hamiltonians so that the occupied orbitals are scaled by 0.09 and the p_5 parameter handles the η-independent exchange correction. The diagonal elements then have the form:

$$\begin{aligned}\Delta E^{A4}_{DFT/MRCI} = p_c\big(&-\sum_{\substack{i,j\in c\\ i>j}}^{n_{exc}} V_{ijij} - \sum_{\substack{i,j\in a\\ i>j}}^{n_{exc}} V_{ijij} + \sum_{i\in c}^{n_{exc}}\sum_{j\in a}^{n_{exc}} V_{ijij}\big) \\ &- \frac{p_5}{2}\sum_{i\in c}^{n_{exc}}\sum_{j\in a}^{n_{exc}} V_{ijji} - p_x \sum_{\substack{i,j\in c\\ i>j}}^{n_{exc}} V_{ijji}\eta^{ji}_{ij} \\ &+ 0.09 \sum_{i\in occ} \Delta w_i F^{KS}_{ii}\end{aligned} \tag{4.4}$$

It improved the RMSD to 0.23 eV, just 0.05 eV higher than the R2018. This deviation is mainly caused by singlet states of $n \rightarrow \pi^*$ character, which are still significantly underestimated.

In conclusion, all tested modifications did not achieve acceptable performance compared to the former DFT/MRCI Hamiltonians. As already assumed in the former section, the different behaviors of the orbital energies involved in $n \rightarrow \pi^*$, $\pi \rightarrow \pi^*$, $n \rightarrow Ryd$, $\pi \rightarrow Ryd$ transitions are also visible in the above tried Hamiltonians.

Nonetheless, an assessment of their performance on the critical cases identified by Jovanović et al. [76] was done. They comprised open- and closed-shell double

Table 4.4: Vertical excitation energies in comparison to the TBE of the critical double excitations. For formaldehyde, the TBE was taken from Ref.[2], while for the other cases, the TBEs of Ref. [1] were used. All values in eV. For comparison, the R2018 results with the BH-LYP functional are given.

Molecule	State	Character	TBE	R2018	A1	A2	A3	A4
Formaldehyde	$^1A_1$	$n^2 \rightarrow \pi^{*2}$	10.35	9.37	8.63	8.64	8.80	8.72
Thioformaldehyde	$^1A_1$	$n^2 \rightarrow \pi^{*2}$	7.37	5.92	5.18	5.17	5.50	5.38
Dithiin	^1A	$\pi^2 \rightarrow \pi^{*2}$	4.91	4.71	4.66	4.39	4.86	4.64
Dithiosuccinimide	$^1A_1$	$n_1, n_2 \rightarrow \pi_1^*, \pi_2^*$	7.13	5.14	4.72	4.43	4.83	4.82

excitations in small organic molecules. As seen from the results in Table 4.4, PBE0 orbitals, at least with the modifications tried in this work, are unsuitable for improving these cases. Almost every attempt worsened the results, with the attempts with scaled occupied orbital energies performing better than the other two. This points towards a problem with the orbital energies, which the DFT/MRCI corrections can not sufficiently alter. Furthermore, since the deviations in the excitation energies of doubly excited states got more severe compared to the redesigned Hamiltonians, it is apparent that the original deficiencies are not resolved, and the problems mentioned earlier added up. Overall, PBE0, and probably other functionals with similar amounts of non-local exchange, significantly increase the deviations with reference to the experimental results. Significant corrections to all input quantities must be made to reach comparable RMSD for the training set as the redesigned Hamiltonians. Therefore, implicit effects in the underlying density functional cannot be corrected by simply scaling the input. The SIE as one of these implicit effects was already discussed in Section 2.3.

Chapter 5

Towards an Improved Description of Doubly Excited States

In the last chapter, the suitability of other density functionals concerning their performance for the training set and the known critical doubly excited states were investigated. The results suggest that none of the investigated functionals is better suited to be used in conjunction with the DFT/MRCI method than the BH-LYP functional. In this chapter, interactions are investigated with regard to their contribution to doubly excited state energies, and how they are influenced by the DFT/MRCI parameterization of the Hamiltonian. To this end, doubly excited states have been classified into different types, each characterized by its orbital character and number of open shells that cause the original and redesigned Hamiltonians to perform differently, as seen in Table 5.1 for a few examples. The first type comprises closed-shell excitations with spatially strongly localized orbitals like the non-bonding, and to a lesser degree also the π^*, orbitals in dithiosuccinimide shown in Figure 5.1. Here, the interelectronic distance between the created holes or electrons in the same orbital is, on average, smaller than the distance between particles in different orbitals. Therefore short-range dynamic correlation is expected to be more critical in these cases, and the parameters have to be adjusted accordingly. In the DFT/MRCI method, these cases can usually be identified by a minor to moderate

Table 5.1: Representative types of doubly excited states used to evaluate different type-specific characteristics. All values in eV.

Molecule	State	Character	NEVPT2	Original	R2018
Dithiin	$^1A_1$	$\pi^2 \rightarrow \pi^{*2}$	4.91	4.80	4.71
Dithiosuccinimide	$^1A_1$	$n^2 \rightarrow \pi^{*2}$	5.85	6.07	5.14
	$^3B_2$	$n, n' \rightarrow \pi^{*2}$	5.86	4.60	3.52
o-Benzyne	$^1A_1$	$\pi, \pi' \rightarrow \pi^*, \pi'^*$	7.23	4.24	6.56

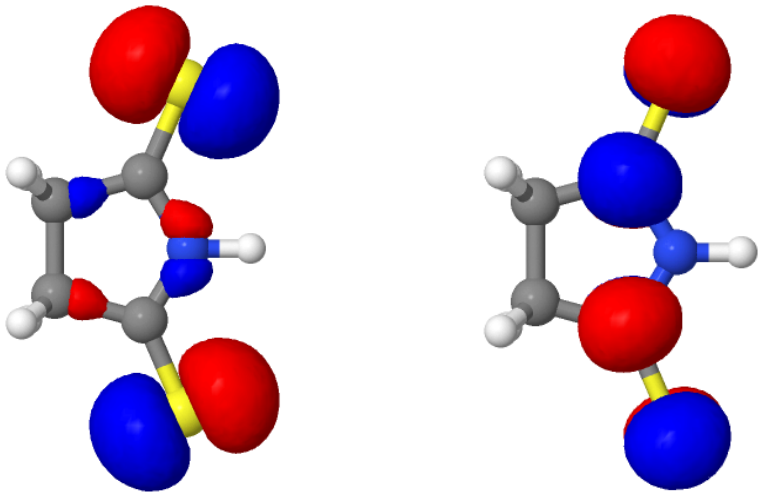

(a) n (b) π^*

Figure 5.1: Orbitals involved in the closed-shell doubly excited state of dithiosuccinimide.

overestimation for the original Hamiltonian and vast underestimations for the redesigned Hamiltonians, as can be seen, for example, in formaldehyde, where values of 11.19 eV and 9.37 eV are calculated with the original and R2018 Hamiltonian for the doubly excited $n^2 \rightarrow \pi^2$ excitation, respectively, while the theoretical best estimate is at 10.35 eV. The energy of such a closed-shell doubly excited configuration in the DFT/MRCI method is given by

$$\begin{aligned} \langle \Psi_{ii}^{aa} | \hat{\mathcal{H}}^{\mathcal{DFT}/\mathcal{MRCI}} | \ominus_{\rangle\rangle}^{\dashv\dashv} \rangle &= E^{scf} - 2F_{ii} + 2F_{aa} - 4J_{ia} + J_{ii} + J_{aa} + 2K_{ia} \\ &\quad + \Delta E_{coul} - \Delta E_{exch} \end{aligned} \tag{5.1}$$

$$\Delta E_{coul}^{orig} - \Delta E_{exch}^{orig} = 2\big(p_j J_{ia} - {}^{m}\, p[0] K_{ia}\big) \tag{5.2}$$

$$\Delta E_{coul}^{red} - \Delta E_{exch}^{red} = p_j\big(4J_{ia} - J_{ii} - J_{aa}\big) - 2.5 p_x K_{ia} \tag{5.3}$$

where electrons are promoted from orbitals i to a, and F_{ii} is an element of the effective one-electron matrix constructed from the given KS orbitals, J_{ia} is the Coulomb integral V_{iaia}, and K_{ia} is the exchange integral V_{iaai}. The reason for the above-mentioned deviations becomes apparent when the corrections of the original Hamiltonian (Equation 5.2) and the redesigned Hamiltonians (Equation 5.3) are compared. The exchange interaction between the n and π^* orbitals is compared to the involved Coulomb integrals small and therefore negligible in a first approximation when analyzing the cause of the error. Hence, only the Coulomb integrals J_{aa}, J_{ii}, and J_{ia} contribute to the DFT/MRCI energy. The above-mentioned small interelectronic distance manifests itself as large contributions from the diagonal two-electron repulsion integrals J_{ii} and J_{aa}, which are usually 20% to 50% larger than the J_{ia} integrals in the observed critical cases. In the R2016 to R2018 Hamiltonian correction terms,

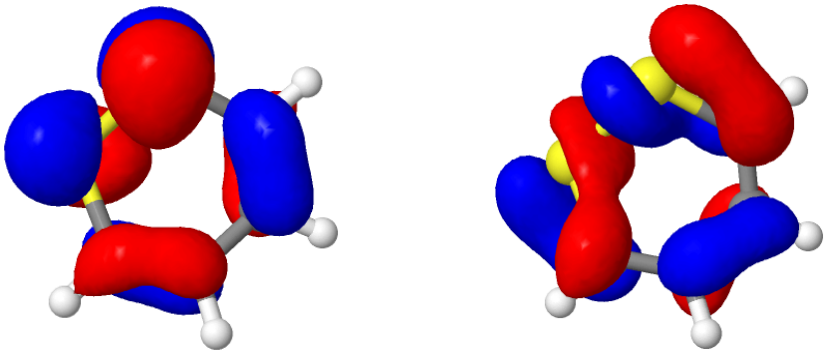

(a) π (b) π^*

Figure 5.2: Orbitals involved in the doubly excited state of dithiin.

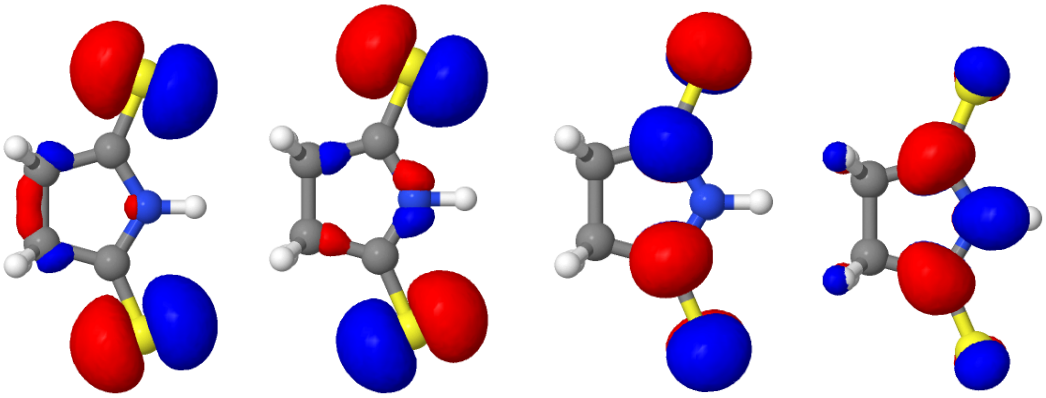

(a) n (b) n' (c) π^* (d) π'^*

Figure 5.3: Orbitals involved in the four open shell doubly excited state of dithiosuccinimide.

the diagonal Coulomb integrals are scaled the same as the other Coulomb integrals, resulting in an overestimated correction of these diagonal integrals and a significant reduction in energy. In contrast, the original formulation does not suffer from this error because J_{aa} and J_{ii} are not used for the correction. The less problematic limiting cases are related to spatially delocalized orbitals. In these orbitals, the electrons are farther apart from each other and therefore, the short-range dynamic correlation is less important, resulting in the involved diagonal integrals being less dominant. An example for this are the π and π^* orbitals in dithiin depicted in Figure 5.2. The second problematic case is caused by missing exchange corrections in the parameterization of the DFT/MRCI Hamiltonian. These corrections are important when two holes or electrons are created in different orbitals that share the same spatial region. The error can easily be identified when a diagonal matrix element of a model configuration with four electrons in four orbitals is investigated. For the $n, n' \rightarrow \pi^*, \pi'^*$ excitation involving the orbitals depicted in Figure 5.3, the

DFT/MRCI Hamiltonians are given by

$$\begin{aligned}
\langle \Psi_{ij}^{ab} | \, \hat{\mathcal{H}}^{\mathcal{DFT}/\mathcal{MRCI}} \, | \ominus_{\rangle|}^{\dashv\llcorner} \rangle &= E^{scf} - F_{ii} - F_{jj} + F_{aa} + F_{bb} \\
&\quad - J_{ia} - J_{ib} - J_{ja} - J_{jb} + J_{ij} + J_{ab} \\
&\quad + \eta_{ia}^{ai} K_{ia} + \eta_{ib}^{bi} K_{ib} + \eta_{ja}^{aj} K_{ja} + \eta_{jb}^{bj} K_{jb} \\
&\quad + (\eta_{ij}^{ji} - 1) K_{ij} + (\eta_{ab}^{ba} - 1) K_{ab} \\
&\quad + \Delta E_{coul} - \Delta E_{exch} \qquad (5.4) \\
\Delta E_{coul}^{orig} - \Delta E_{exch}^{orig} &= 0.5\big(p_j\big(J_{ia} + J_{ib} + J_{ja} + J_{jb}\big) \\
&\quad - {}^{m}p[4]\big(K_{ia} + K_{ib} + K_{ja} + K_{jb}\big)\big) \qquad (5.5) \\
\Delta E_{coul}^{red} - \Delta E_{exch}^{red} &= p_j\big(J_{ia} + J_{ib} + J_{ja} + J_{jb} - J_{ij} - J_{ab}\big) \\
&\quad - p_x\big(\big(0.5 + \eta_{ia}^{ai}\big) K_{ia} + \big(0.5 + \eta_{ib}^{bi}\big) K_{ib} \\
&\quad + \big(0.5 + \eta_{ja}^{aj}\big) K_{ja} + \big(0.5 + \eta_{jb}^{bj}\big) K_{jb} \\
&\quad + \eta_{ij}^{ji} K_{ij} + \eta_{ab}^{ba} K_{ab}\big) \qquad (5.6)
\end{aligned}$$

where the electrons are promoted from orbitals i and j to a and b. While Equations 5.4 to 5.6 seem cumbersome initially, only the exchange terms are essential for the error analysis. For the sake of clarity, all Coulomb terms are collected in a variable R:

$$\begin{aligned}
\langle \Psi_{ij}^{ab} | \, \hat{\mathcal{H}}_{\lceil\S\rfloor\langle}^{\mathcal{DFT}/\mathcal{MRCI}} \, | \ominus_{\rangle|}^{\dashv\llcorner} \rangle &= R + \eta_{ia}^{ai} K_{ia} + \eta_{ib}^{bi} K_{ib} + \eta_{ja}^{aj} K_{ja} + \eta_{jb}^{bj} K_{jb} \\
&\quad + (\eta_{ij}^{ji} - 1) K_{ij} + (\eta_{ab}^{ba} - 1) K_{ab} \\
&\quad - \Delta E_{exch} \qquad (5.7) \\
-\Delta E_{exch}^{orig} &= 0.5\big(- {}^{m}p[4]\big(K_{ia} + K_{ib} + K_{ja} + K_{jb}\big)\big) \qquad (5.8) \\
-\Delta E_{exch}^{red} &= -p_x\big(\big(0.5 + \eta_{ia}^{ai}\big) K_{ia} + \big(0.5 + \eta_{ib}^{bi}\big) K_{ib} \\
&\quad + \big(0.5 + \eta_{ja}^{aj}\big) K_{ja} + \big(0.5 + \eta_{jb}^{bj}\big) K_{jb} \\
&\quad + \eta_{ij}^{ji} K_{ij} + \eta_{ab}^{ba} K_{ab}\big) \qquad (5.9)
\end{aligned}$$

When comparing Eq. 5.7 with 5.9, two irregularities become apparent. First, for the electron-hole exchange integrals K_{ia}, K_{ib}, K_{ja} and K_{jb}, the additional factor of one-half is missing in Eq. 5.7 compared to Eq. 5.9, and therefore an η-independent shift is introduced in the redesigned Hamiltonians. This shift was introduced by Igor Lyskov et al. [113] in the R2016 Hamiltonian to improve triplet excited state energies, which are described poorly by corrections to the Coulomb integrals alone. Table 5.2 lists all occurrences of exchange integrals in singly and doubly excited configurations of singlet multiplicity in the unscaled CI element and the redesigned DFT/MRCI correction terms. In the case of the critical open-shell doubly excited configuration, the above-mentioned η-independent shift can easily be identified in the

Table 5.2: Occurrence of exchange integrals in the unscaled CI matrix element and the DFT/MRCI correction terms, for example cases of singlet multiplicity. Note that all occupations are built from a closed-shell anchor configuration. The difference in the occurrence of the exchange integrals between the unscaled matrix elements and DFT/MRCI correction terms is shown in the last column.

Occupation	CSF	Integral	η_{ij}^{ji}	$\hat{\mathcal{H}}_{\rceil\S\rfloor\langle}^{\mathcal{CI}}$	$-\Delta E_{exch}^{red}$	$\Delta(\hat{\mathcal{H}}_{\rceil\S\rfloor\langle}^{\mathcal{CI}} + \cdot\mathcal{E}_{\rceil\S\rfloor\langle}^{\nabla\rceil\lceil})$
$222000 \rightarrow 221100$	1	K_{34}	2	2	-2.5	-0.5
$222000 \rightarrow 220200$	1	K_{34}	0	2	-2	0
$222000 \rightarrow 220110$	1	K_{34}	0	1	-1	0
		K_{35}	0	1	-1	0
		K_{45}	2	1	-2	-1
$222000 \rightarrow 211200$	1	K_{24}	0	1	-1	0
		K_{34}	0	1	-1	0
		K_{23}	2	1	-2	-1
$222000 \rightarrow 211110$	1	K_{24}	1.5	1.5	-2	-0.5
		K_{25}	1.5	1.5	-2	-0.5
		K_{34}	1.5	1.5	-2	-0.5
		K_{35}	1.5	1.5	-2	-0.5
		K_{23}	0	-1	0	-1
		K_{45}	0	-1	0	-1
	2	K_{24}	0.5	0.5	-1	-0.5
		K_{25}	0.5	0.5	-1	-0.5
		K_{34}	0.5	0.5	-1	-0.5
		K_{35}	0.5	0.5	-1	-0.5
		K_{23}	2	1	-2	-1
		K_{45}	2	1	-2	-1

last column of the excitation 222000 ← 211110 for electron-hole exchange integrals. Here for all electron-hole exchange terms, the difference between the unscaled matrix element $\hat{\mathcal{H}}^{\mathcal{CI}}_{\rceil\S\rfloor\langle}$ and the DFT/MRCI correction term $-\Delta E^{red}_{exch}$ is -0.5. Note that the η-independent shift only appears in electron-hole pairs, which are located in an open shell. For example the exchange integral K_{24} in the occupation 222000 → 211200 does not have this shift, because orbital 4 is doubly occupied. If one or both particles are in a closed shell, the η-independent shift does not take effect. To illustrate this, one can compare the occurrence of the electron-hole exchange integrals of the 222000 → 220200 and the 222000 → 211110 occupations. Secondly, for hole-hole or electron-electron exchange interactions, the correction is missing a term with a constant factor of 1, which can result in significant underestimation. For example in the above case of the $n, n' \rightarrow \pi^*, \pi'^*$ excitation of dithiosuccinimide, $K_{n,n'}$ (K_{23} in Table 5.2) is approximately 4.3 eV. The spin coefficient η^{ji}_{ij} is zero for the first CSF. Therefore, no correction is made for this integral, and the configuration is lowered by the unscaled 4.3 eV. In comparison, would the integral be scaled by p_x, which is approximately 0.36 for the redesigned Hamiltonians, the configuration would only be lowered by 2.75 eV, a difference of 1.5 eV to the unscaled element. The case is reversed for the second CSF. Here, the integral contributes +4.3 eV to the unscaled configuration, but the correction reduces this contribution, due to the prefactor of -2, to 1.2 eV. In total, the exchange integral in the first CSF is unscaled. In contrast, the same integral in the second CSF is reduced by 72% and therefore significantly overcorrected in comparison to the 36% of K_{34} in the 222000 → 220200 and 45% of K_{34} in the 222000 → 221100 cases. Therefore two problems arise that have to be investigated to modify the DFT/MRCI Hamiltonian to be suitable for doubly excited configurations: First, the diagonal Coulomb integrals J_{ii} have to be scaled to account for more short-range correlation. Second, the correction to the exchange integrals has to be revised to guarantee that the correct number of integrals is scaled. To this end, different attempts to resolve these problems will be assessed and discussed in the following section.

5.1 Developments Leading to the R2022 Hamiltonian

Through analysis of the critical cases found by Jovanović et al. [76] two characteristic problems were detected, which led to various attempts to improve doubly excited state energies. The RMSD and mean deviation of the most important attempts, B1 to B4, as well as for two Hamiltonians with modifications to the η-independent shift, S1 and S2, for the training set and critical cases are depicted in Figure 5.4. A

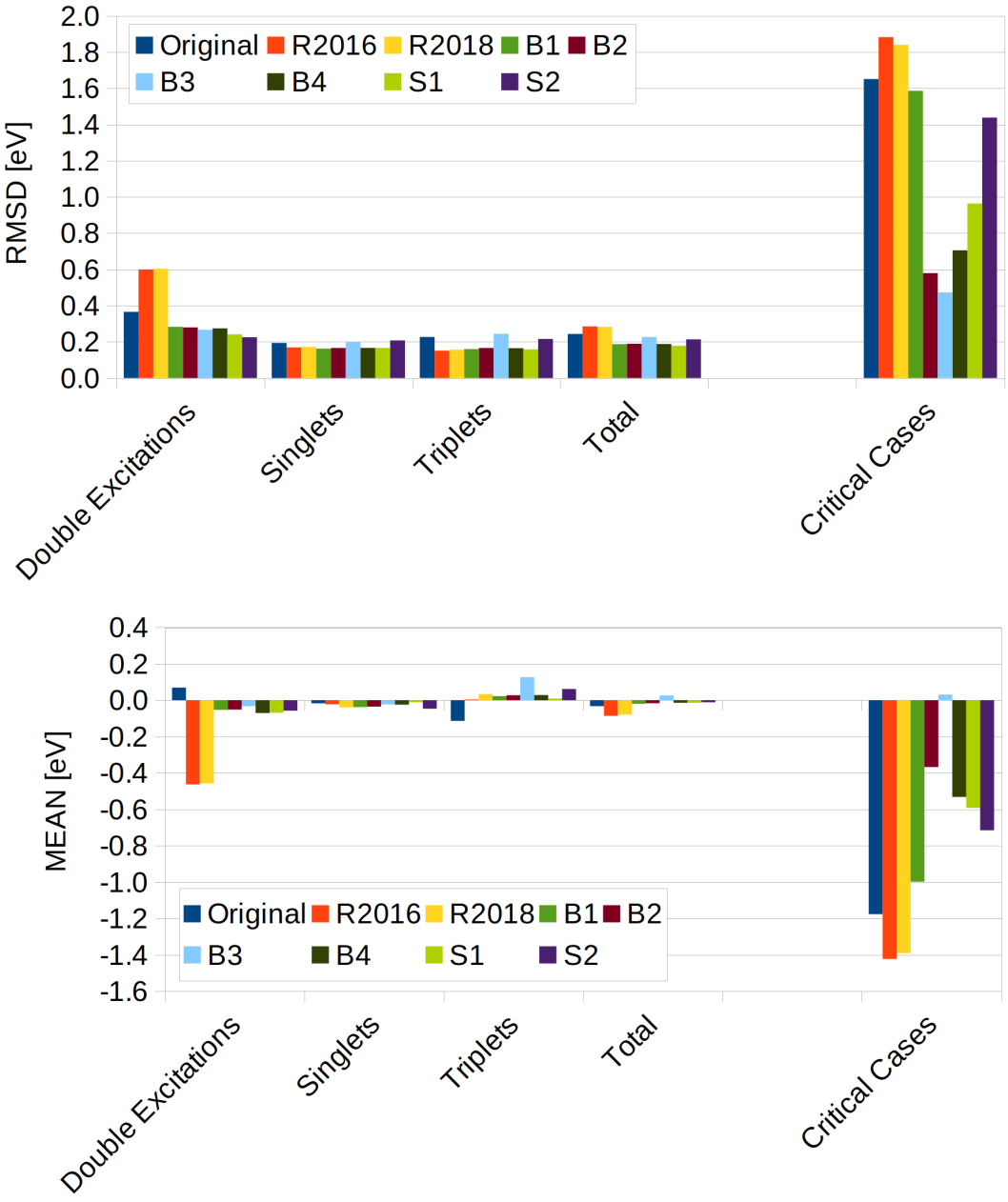

Figure 5.4: RMSD (left) and mean deviation(right) for the training set with a standard selection threshold for different attempts to correct doubly excited states. Numbers in brackets indicate the amount of states without dimers for the original Hamiltonian.

decrease in the deviation from the theoretical best estimates (TBEs) for the added doubly excited state energies in the training set and the critical cases is evident.

The first significant attempt was the B1 Hamiltonian. The B1 Hamiltonian improves the closed-shell doubly excited state energies by addressing the first type of problems mentioned in the previous section. To this end, the Hamiltonian introduced a fifth parameter p_5, which scaled the Coulomb integrals between two created holes or electrons:

$$\begin{aligned} B1 = p_5 \cdot \left(-\sum_{\substack{i,j \in c \\ i>j}}^{n_{exc}} V_{ijij} - \sum_{\substack{i,j \in a \\ i>j}}^{n_{exc}} V_{ijij} \right) + p_j \cdot \left(\sum_{i \in c}^{n_{exc}} \sum_{j \in a}^{n_{exc}} V_{ijij} \right) \\ - p_x \cdot \left(0.5 \cdot \sum_{i \in c}^{n_{exc}} \sum_{j \in a}^{n_{exc}} V_{ijji} + \sum_{\substack{i,j \in o \\ i>j}}^{N_o} V_{ijji} \eta_{ij}^{ji} \right) \end{aligned} \tag{5.10}$$

In the training set, the results are promising. The RMSD is with 0.16 eV for the singlet and triplet subsets of the training set on the same level as the redesigned Hamiltonians with around 0.17 eV and 0.15 eV for singlets and triplets, respectively. Therefore, the excellent results of its predecessors are retained. Additionally, the RMSD of the added doubly excited states is significantly improved from around 0.60 eV in the redesigned Hamiltonians to 0.28 eV in B1. At first, this is unexpected since the difference between the p_j and p_5 parameter is 0.03 and, therefore, relatively small. However, if critical cases are considered, the Coulomb interaction between holes or electrons in the same orbital V_{iiii} can reach enormous values. In the case of the HOMO and LUMO of formaldehyde, these interactions reach 14.68 eV and 9.51 eV, respectively. With only a difference of 3%, the change in energy of the involved configurations is 0.44 eV for two holes in the HOMO and 0.29 eV for two electrons in the LUMO, adding up to a total of 0.73 eV increase in energy. In contrast to the training set, the effect on the critical cases is smaller. Here, the RMSD is with 1.59 eV only marginally better than the original Hamiltonian with 1.65 eV and therefore unsatisfying. The deviation from the TBE is shown in Figure 5.5, where it can be seen that, on average, the B1 Hamiltonian underestimates the TBEs by 1.0 eV in these cases, which is an expected behavior since the critical cases contain mostly open-shell doubly excited states, where the missing modifications to the exchange correction will dominate the error. In the $^1A_1$ state of dithiosuccinimide, for example, the energy compared to the R2018 Hamiltonian is improved by 0.32 eV but still 3.32 eV below the NEVPT2 result.

Therefore the next step is a correction for the second kind of problem, which is connected to the exchange interactions between two created holes or electrons as

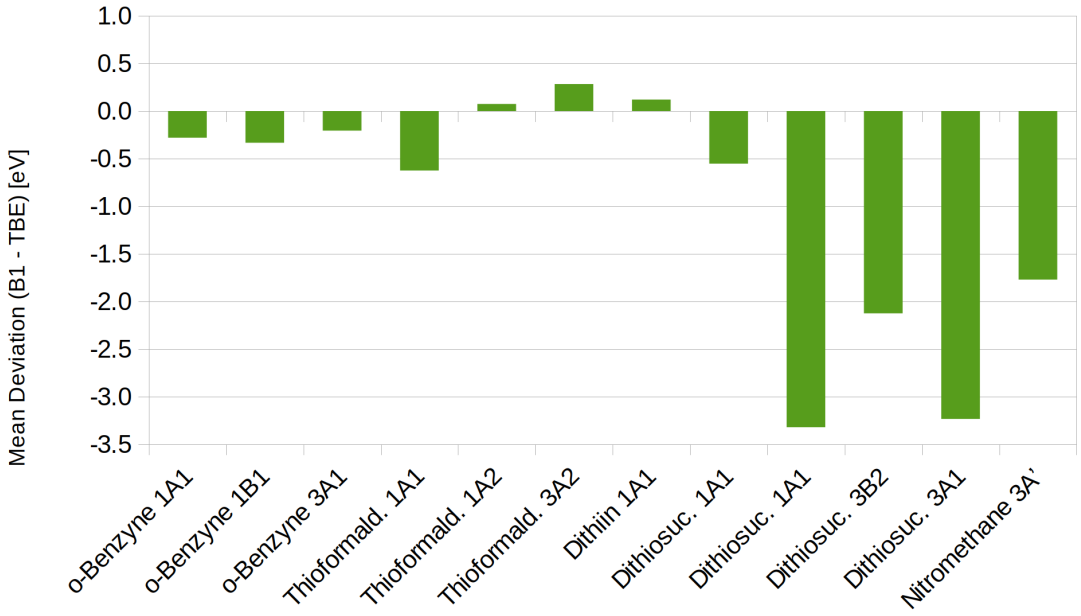

Figure 5.5: Mean deviation of the B1 Hamiltonian to the TBEs of the critical cases.

occurring in open-shell double excitations. The B2 Hamiltonian add the missing term with a factor of 1 in these cases:

$$
\begin{aligned}
B2 = p_5 \cdot \left(-\sum_{\substack{i,j\in c \\ i>j}}^{n_{exc}} V_{ijij} - \sum_{\substack{i,j\in a \\ i>j}}^{n_{exc}} V_{ijij} \right) + pj \cdot \left(\sum_{i\in c}^{n_{exc}} \sum_{j\in a}^{n_{exc}} V_{ijij} \right) \\
- p_x \cdot \left(0.5 \cdot \sum_{i\in c}^{n_{exc}} \sum_{j\in a}^{n_{exc}} V_{ijji} + \sum_{\substack{i,j\in o \\ i>j}}^{N_o} V_{ijji} \eta_{ij}^{ji} \right) \\
- 0.5 p_x \sum_{\substack{i\neq j \\ \Delta w_i \Delta w_j > 0}} \left(-0.5 \Delta w_i \Delta w_j + 0.5 w_i w_j - w_i \right) V_{ijji}
\end{aligned}
\tag{5.11}
$$

The last term introduces the correction mentioned above. Here, the summation is over orbitals instead of particles because in this way it is guaranteed that every exchange integral has the same prefactor as in the ab-initio matrix element. For the training set, the additional terms hardly change any statistics compared to B1, but the difference is clearly visible for the critical cases. The RMSD and mean deviation are reduced by 64% to 0.58 eV and -0.37 eV, respectively. Each state's deviation to the TBE is shown in Figure 5.6. Notably, the former worst-case scenarios of the four open-shell excitations are significantly improved from -3.3 eV deviation in B1 to only -1.1 eV in B2. For $\pi_1, \pi_2 \rightarrow \pi_1^*, \pi_2^*$ excitations, which had only slight deviations before, the B2 correction is notably smaller and, therefore, preventing an overcorrection. For example, the $^1A_1$ state in *o*-benzyne is only raised by 0.15 eV from

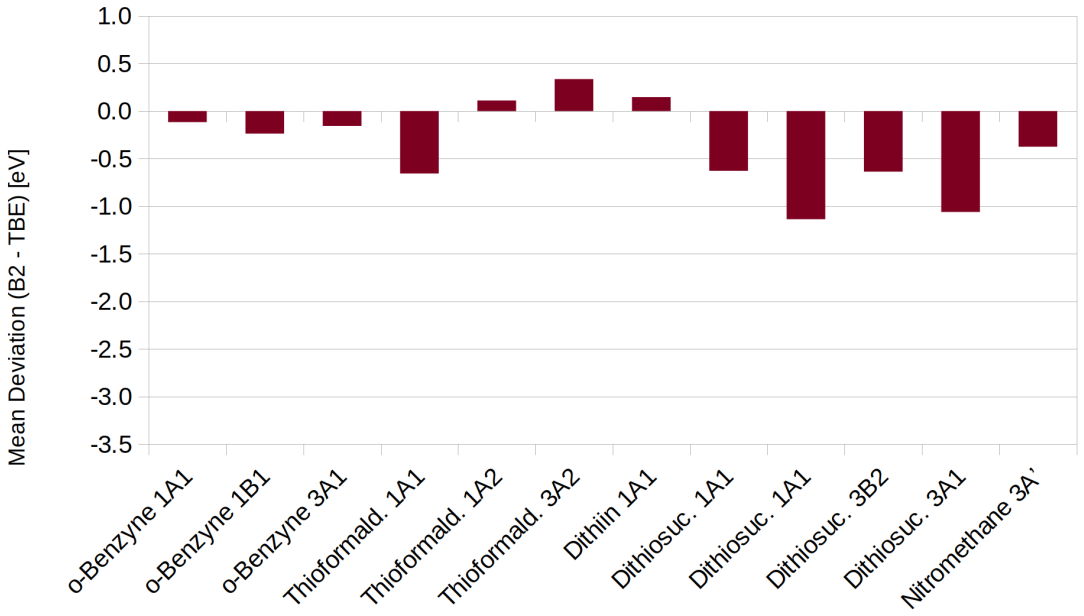

Figure 5.6: Mean deviation of the B2 Hamiltonian to the TBEs of the critical cases.

6.95 eV in B1 to 7.11 eV in B2. These results indicate that the exchange correction being the dominant error in doubly excited states. Therefore, it is reasonable to investigate the influence of the η-independent exchange shift in the next step. The B3 Hamiltonian was designed to remove this shift:

$$
\begin{aligned}
B3 = p_5 \cdot \left(- \sum_{\substack{i,j \in c \\ i>j}}^{n_{exc}} V_{ijij} - \sum_{\substack{i,j \in a \\ i>j}}^{n_{exc}} V_{ijij} \right) + pj \cdot \left(\sum_{i \in c}^{n_{exc}} \sum_{j \in a}^{n_{exc}} V_{ijij} \right) \\
- p_x \cdot \left(\sum_{\substack{i,j \in o \\ i>j}}^{N_o} V_{ijji} \eta_{ij}^{ji} \right) \\
- 0.5 p_x \sum_{i \neq j} \left(- 0.5 \Delta w_i \Delta w_j + 0.5 w_i w_j - w_i \right) V_{ijji}
\end{aligned}
\tag{5.12}
$$

In contrast to B2, the first term in the fourth sum is removed, and the last sum includes all orbital combinations and not just the ones between created particles. As a result, the exchange correction in the last term closely resembles the first three sums in the exchange part of the diagonal ab-initio matrix element (Eq. 2.15). To illustrate the effect on the matrix elements, one can calculate the exchange integral corrections for singly excited configurations. The last term in Eq. 5.12 is zero for singlet multiplicity and only the part with the spin coupling coefficient η_{ij}^{ji} can contribute. Therefore the new exchange correction would result in $-2p_x V_{ijji}$, which is the proper prefactor, as can be seen from a comparison with the first line of Table 5.2.

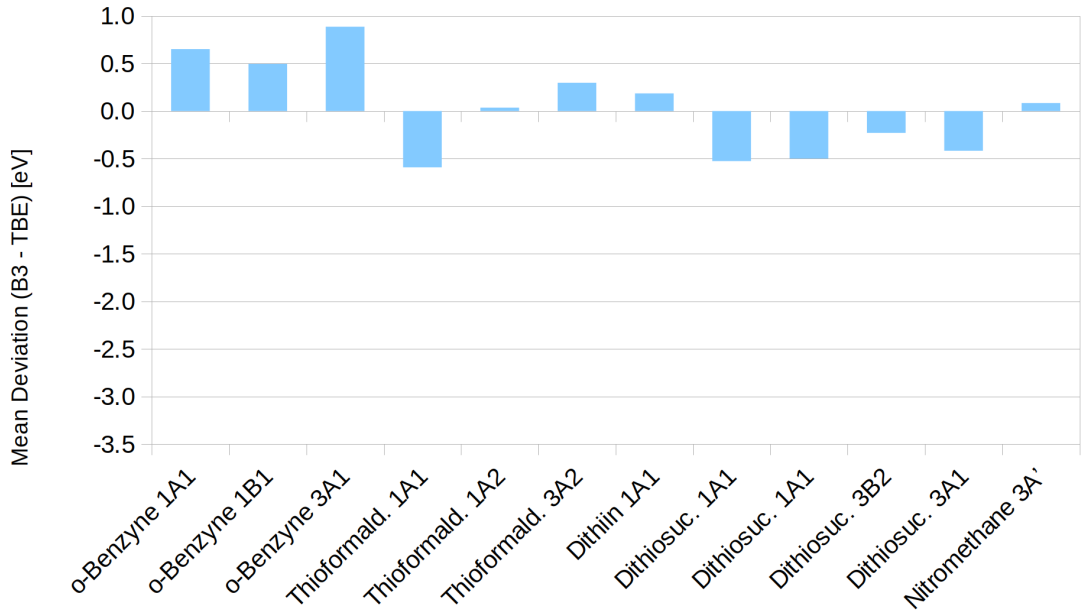

Figure 5.7: Mean deviation of the B3 Hamiltonian to the TBEs of the critical cases.

This attempt increases the RMSD by around 0.07 eV compared to the former two modifications. Especially the triplet states are overestimated and described less satisfactory, as can be seen from the mean deviation of 0.07 eV and RMSD of 0.22 eV. This observation is in agreement with the initial one from Igor Lyskov et al. [113], who included this shift to lower the energy of excited triplet states. Unexpectedly, the double excitations in the training set and the critical cases are slightly better described with an RMSD of 0.27 eV and 0.51 eV. Especially for the critical cases, the RMSD decreases by around 13% from 0.58 eV in B2 to 0.51 eV in B3, and the mean deviation is with 0.03 eV significantly better than the B2 with -0.37 eV, which further supports the need to improve the exchange corrections for doubly excited configurations without sacrificing accuracy of triplet states. Another option would be a consistent η-independent shift for all excitations. To this end, prefactors of the involved exchange integrals in different excitations for the ab-initio and redesigned DFT/MRCI Hamiltonians in Table 5.2 can be reinvestigated with a focus on a modification towards a consistent shift for all excitations. Note that the missing exchange term was already corrected in B2, and the values in the Table 5.2 have to be altered accordingly, which means the factor of the exchange correction terms $-\Delta E^{red}_{exch}$ is increased by 1 for every interaction between two created holes or electrons. The η-independent shift only affects cases where the electron and hole are in open shells after excitations. In every other case, the prefactor of the correction is in accordance with the occurrence of the integral in the unscaled diagonal element. The problem is the form of the shift for the different types of double excitations. In the case of the first CSF in a four open-shell double excitation, the correction term

changes to a positive sign. There are two options for how to handle this situation:

1. A uniform shift could be used that is sign independent and therefore reduces the $p_x V_{ijji}$ to a $0.5 p_x V_{ijji}$ in the situation mentioned above.

2. The shift could have the same sign as the prefactor of the correction, which would lead to $1.5 p_x V_{ijji}$ in the above case.

For the first case, a possible Hamiltonian (from here on dubbed S1) is given by:

$$
\begin{aligned}
S1 = p_5 \cdot \Bigg(- \sum_{\substack{i,j \in c \\ i>j}}^{n_{exc}} V_{ijij} - \sum_{\substack{i,j \in a \\ i>j}}^{n_{exc}} V_{ijij} \Bigg) + pj \cdot \Bigg(\sum_{i \in c}^{n_{exc}} \sum_{j \in a}^{n_{exc}} V_{ijij} \Bigg) \\
- p_x \cdot \Bigg(0.5 \cdot \sum_{i \in c}^{n_{exc}} \sum_{j \in a}^{n_{exc}} V_{ijji} + 0.5 \cdot \sum_{\substack{i,j \in c \\ i>j}}^{n_{exc}} V_{ijji} + 0.5 \cdot \sum_{\substack{i,j \in a \\ i>j}}^{n_{exc}} V_{ijji} \\
+ \frac{1}{2} \cdot \sum_{i \in c}^{n_{exc}} \sum_{\substack{j \in a \\ \Delta|w_i|=2 \\ or \\ \Delta|w_j|=2}}^{n_{exc}} V_{ijji} + \sum_{\substack{i,j \in o \\ i>j}}^{N_o} V_{ijji} \eta_{ij}^{ji} \Bigg) \\
- 0.5 p_x \sum_{\substack{i \neq j \\ \Delta w_i \Delta w_j > 0}} \Bigg(- 0.5 \Delta w_i \Delta w_j + 0.5 w_i w_j - w_i \Bigg) V_{ijji}
\end{aligned}
\tag{5.13}
$$

Here the second and third sums in the second row will add 0.5 times the exchange integrals between created holes or electrons, and the first sum in the third row will do the same if at least w_i or w_j are a vacant or closed shell. In this way, every involved exchange integral will contribute a shift of -0.5 times its value towards the diagonal element of the DFT/MRCI matrix. This modification yields the best results for the training set of all investigated Hamiltonians with an RMSD of 0.18 eV. With the doubly excited states in the training set excluded, it is on the same level as the R2016 with an RMSD of 0.16 eV. Unfortunately, the results for the critical cases are significantly worse, with an RMSD of 0.96 eV. The open-shell doubly excited states are vastly underestimated, as can be seen in Figure 5.8, since a shift for the immense exchange interactions in these cases will significantly reduce the energy of these already underestimated states, resulting in a mean deviation for this subset of -0.59 eV.

A possible improvement is given by option 2), where in comparison to the option mentioned above, the sign of the shift can be positive if the exchange integral in the unscaled matrix element has an overall negative sign, which is given if $1 - \eta_{ij}^{ji} > 0$. Therefore exchange integrals in Table 5.2 are shifted by $-0.5 V_{ijji}$ if $1 - \eta_{ij}^{ji} < 0$ and $0.5 V_{ijji}$ if $1 - \eta_{ij}^{ji} > 0$.

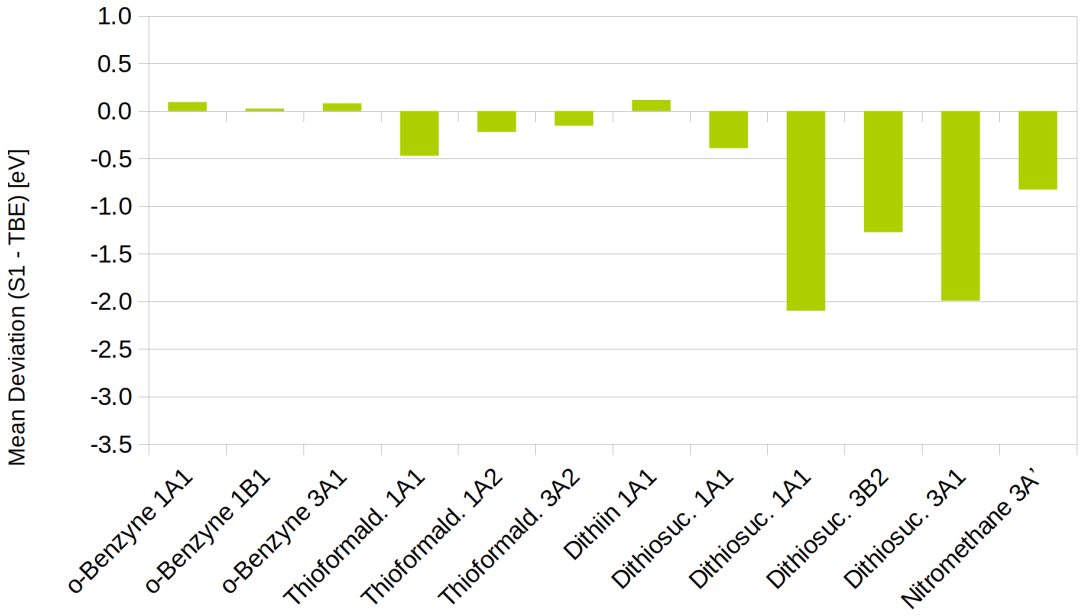

Figure 5.8: Mean deviation of the S1 Hamiltonian to the TBEs of the critical cases.

The S2 Hamiltonian has the form:

$$
\begin{aligned}
S2 = p_5 \cdot \Bigg(&- \sum_{\substack{i,j\in c \\ i>j}}^{n_{exc}} V_{ijij} - \sum_{\substack{i,j\in a \\ i>j}}^{n_{exc}} V_{ijij} \Bigg) + pj \cdot \Bigg(\sum_{i\in c}^{n_{exc}} \sum_{j\in a}^{n_{exc}} V_{ijij} \Bigg) \\
&- p_x \cdot \Bigg(0.5 \cdot \sum_{i\in c}^{n_{exc}} \sum_{j\in a}^{n_{exc}} V_{ijji} + 0.5 \cdot \sum_{\substack{i,j\in c \\ i>j \\ \eta_{ij}^{ji}\geq 1}}^{n_{exc}} V_{ijji} + 0.5 \cdot \sum_{\substack{i,j\in a \\ i>j \\ \eta_{ij}^{ji}\geq 1}}^{n_{exc}} V_{ijji} \\
&- 0.5 \cdot \sum_{\substack{i,j\in c \\ i>j \\ \eta_{ij}^{ji}<1}}^{n_{exc}} V_{ijji} - 0.5 \cdot \sum_{\substack{i,j\in a \\ i>j \\ \eta_{ij}^{ji}<1}}^{n_{exc}} V_{ijji} \\
&+ \frac{1}{2} \cdot \sum_{i\in c}^{n_{exc}} \sum_{\substack{j\in a \\ \Delta|w_i|=2 \\ or \\ \Delta|w_j|=2}}^{n_{exc}} V_{ijji} + \sum_{\substack{i,j\in o \\ i>j}}^{N_o} V_{ijji}\eta_{ij}^{ji} \Bigg) \\
&- 0.5p_x \sum_{\substack{i\neq j \\ \Delta w_i \Delta w_j > 0}} \Big(- 0.5\Delta w_i \Delta w_j + 0.5 w_i w_j - w_i \Big) V_{ijji}
\end{aligned}
\tag{5.14}
$$

In contrast to the expectation, the Hamiltonian increases the RMSD of the critical cases subset compared to S1 by 0.47 eV to 1.43 eV. As seen in Figure 5.9, the deviation from the TBE significantly worsens for almost all states. The shift with variable sign cause the $\pi, \pi' \rightarrow \pi^*, \pi'^*$ excitations in *o*-benzyne to be overestimated, while the $n, n' \rightarrow \pi^*, \pi'^*$ excitation in dithiosuccinimide is underestimated, resulting

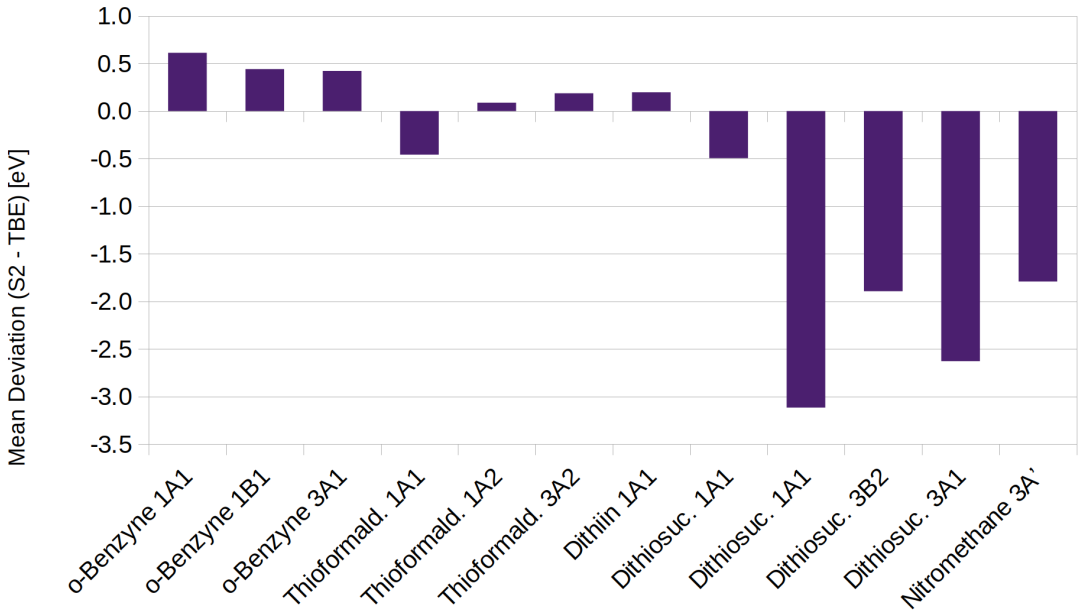

Figure 5.9: Mean deviation of the S2 Hamiltonian to the TBEs of the critical cases.

in an overall decrease of accuracy.

Another idea for a correction was inspired by the fact that the original Hamiltonian performed far better for closed-shell doubly excited states than the redesigned Hamiltonians, as can be seen from the doubly excited states in the training set. Here the original Hamiltonian has an RMSD of 0.37 eV with the tendency to overestimate, on average, excitation energies by 0.07 eV. In contrast to this, the redesigned Hamiltonians have an RMSD of 0.60 eV and vastly underestimate, on average, the excitation energies by -0.46 eV. Therefore the B4 Hamiltonian tries to incorporate some of the ideas of the original Hamiltonian by utilizing information from the diagonal Coulomb integrals like the R2018 Hamiltonian but modifying them with their differences to their averaged Coulomb contribution over single excitations:

$$
\begin{aligned}
B4 = pj \cdot & \left(- \sum_{\substack{i,j \in c \\ i>j}}^{n_{exc}} V_{ijij} - \sum_{\substack{i,j \in a \\ i>j}}^{n_{exc}} V_{ijij} + \sum_{i \in c}^{n_{exc}} \sum_{j \in a}^{n_{exc}} V_{ijij} \right) \\
& + p_5 \cdot \left(0.5 \cdot \sum_{i \in c}^{n_D} \left(V_{iiii} - \frac{1}{n_{exc}} \cdot \sum_{k \in a}^{n_{exc}} V_{ikik} \right) + 0.5 \cdot \sum_{i \in a}^{n_D} \left(V_{iiii} - \frac{1}{n_{exc}} \cdot \sum_{k \in c}^{n_{exc}} V_{ikik} \right) \right) \\
& - p_x \cdot \left(0.5 \cdot \sum_{i \in c}^{n_{exc}} \sum_{j \in a}^{n_{exc}} V_{ijji} + \sum_{\substack{i,j \in o \\ i>j}}^{N_o} V_{ijji} \eta_{ij}^{ji} \right) \\
& - 0.5 p_x \sum_{\substack{i \neq j \\ \Delta w_i \Delta w_j > 0}} \left(- 0.5 \Delta w_i \Delta w_j + 0.5 w_i w_j - w_i \right) V_{ijji}
\end{aligned}
\tag{5.15}
$$

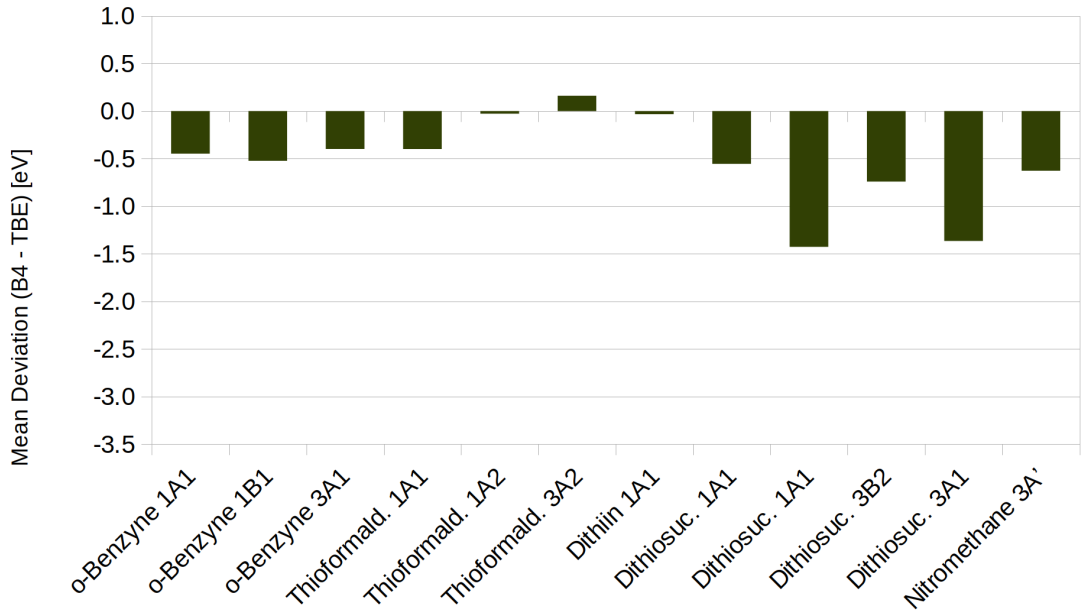

Figure 5.10: Mean deviation of the B4 Hamiltonian to the TBEs of the critical cases.

Here, every integral V_{iiii} that is related to an orbital with two created holes or electrons is scaled by an additional term, which is built by the difference of the integral with the averaged sum over all involved single excitations. This Hamiltonian achieves an RMSD of 0.19 eV for the training set with 0.27 eV for the subset with double excitations and is therefore comparable to B2. For the critical excitations, the performance is inferior, with an RMSD of 0.71 eV compared to 0.58 eV for B2. While the closed-shell excitations in this subset are slightly better described by about 0.1 to 0.2 eV, for open shells it performs worse by 0.3-0.4 eV, as can be seen in Figure 5.10. Additionally, the drawback of this kind of parameterization is that generalization to every combination of two created holes or electrons is not possible without breaking the symmetry of states in separated dimers. For example, the two components of the doubly degenerate state $^1\Delta_g$ in carbon dimer are splitting by 0.4 eV for the original, 0.1 eV for the R2016, R2018 and B1 to B3, and 0.2 eV for the B4 Hamiltonian. The B4 Hamiltonian increases the splitting between these states, because it scales the inter- and intraorbital hole-hole and electron-electron interactions differently compared to the other Hamiltonians B1 to B3. Therefore, correcting the interorbital hole-hole and electron-electron Coulomb interaction the same way as the intraorbital one is required to achieve good results. Additionally, the usage of averaging over one-electron excitations should be avoided to prevent further splitting of degenerate states.

For these series of Hamiltonians, some similarities in the parameters can be observed in Table 5.3. First, the p_1 parameter, which scales the off-diagonal elements, is around 0.61 in all cases and, therefore, significantly closer to the parameter of the

Table 5.3: Fitted parameters for the modified Hamiltonians preceding the R2022 Hamiltonian and RMSD and mean deviation in the training set. Parameters for the original and R2018 Hamiltonian are given for comparison. The $p[0]$ and α parameters refer only to the original Hamiltonian.

Hamiltonian	p_1	p_2	p_c	$p_x, p[0]$	p_5, α	RMSD [eV]	Mean [eV]
Original	0.6195	3.2719	0.5102	0.5945	0.1058	0.24	-0.03
R2018	0.5584	4.4717	0.5089	0.3624		0.28	-0.08
B1 (Eq. 5.10)	0.6007	4.9782	0.5162	0.3512	0.4908	0.19	-0.02
B2 (Eq. 5.11)	0.6096	4.8683	0.5187	0.3614	0.4976	0.19	-0.02
B3 (Eq. 5.12)	0.6222	4.8976	0.5124	0.4099	0.4812	0.22	0.00
B4 (Eq. 5.15)	0.6179	7.6248	0.5230	0.3621	0.1868	0.19	-0.01
S1 (Eq. 5.13)	0.6013	5.0933	0.5133	0.3350	0.4712	0.18	-0.01
S2 (Eq. 5.14)	0.6323	10.6220	0.5121	0.4309	0.4806	0.21	-0.01

Table 5.4: Dependency of the $n^2 \rightarrow \pi^{*2}$ excitation energy in formaldehyde on the p_1 parameter in the redesigned Hamiltonians.

Hamiltonian	p_1	Excitation energy [eV]
R2016	0.5000	9.7020
	0.5682	9.3599
	0.6200	8.7924
R2018	0.5000	9.6712
	0.5584	9.3694
	0.6200	9.0398

original Hamiltonian with 0.62 than for the redesigned Hamiltonians with around 0.56. This points towards an implicit correction effect to double excitations of the p_1 parameter in the redesigned Hamiltonians since reduced values for the p_1 parameter leads to higher energies in these states. This assumption is supported by the dependency of the excitation energy of the $n^2 \rightarrow \pi^{*2}$ doubly excited state in formaldehyde on the p_1 parameter in the redesigned Hamiltonians as can be seen in Table 5.4. Here, the state energy is significantly more underestimated with -0.57 eV and -0.33 eV for the R2016 and R2018 Hamiltonians, respectively, if the original p_1 value is applied. Since the above series of Hamiltonians explicitly corrects for doubly excited states, this implicit effect of the p_1 is no longer necessary, and parameter values similar to the original Hamiltonian are needed. The Coulomb scaling parameter p_c for electron-hole interactions is roughly the same across all Hamiltonians and, therefore, almost independent of the choice of the added modifications. p_x, which handles the exchange corrections, is independent of the modification, too, if the exchange shift is not altered. Removing the exchange shift for electron-hole exchange interactions or adding a unified shift to all exchange integrals alters this parameter.

Removing the shift results in an expected increase of the parameter from 0.36 to 0.43 to compensate for the reduced exchange correction. Surprisingly, the exchange shift for double excitations with adaptive sign change also leads to 0.43, while a uniform exchange shift with a negative sign slightly reduces this parameter to 0.34. The newly introduced p_5 parameter, which scales the hole-hole and electron-electron Coulomb interaction is around 0.49 to 0.47, with the latter value reached when an exchange shift for hole-hole and electron-electron pairs is introduced in the S1 and S2 Hamiltonians.

To this point, three key elements are identified to be important for a new Hamiltonian:

1. Exchange energy is not properly scaled by the current Hamiltonians. A missing term in the formula causes the prefactor of the corrections to be off by one for open-shell double excitations, where the error can cause underestimations of up to several eV. This error is easily corrected by introducing an exchange interaction correction that is in line with the correct ab-initio CI expressions.

2. The intraorbital Coulomb interaction between two created holes or electrons includes an amount of short-range dynamic correlation that is different in comparison to the electron-hole Coulomb interactions. Therefore the correction for this type of interaction needs another parameter adjusted for the different nature of these excitations. This error is most notable on purely closed-shell doubly excited states with spatially dense orbitals, where it can lead to underestimations of 1 to 2 eV.

3. To prevent a splitting of degenerate doubly excited states, for example, in the carbon dimer, the interorbital interactions between two created holes or electrons must be scaled in the same way as the intraorbital interactions. Otherwise, the splitting can reach values of around 0.3 eV.

While modifications to 1. and 2. were discussed in this section, the next section focuses on ways to solve 3., too.

5.2 The Degeneracy Problem in Doubly Excited States

The splitting of formally degenerate doubly excited states was briefly introduced in the explanation of the B4 Hamiltonian. In this section, the reason for this artificial splitting is elaborated, and possible modifications are investigated. One of the smallest accessible model systems is the carbon dimer. In its $^1\Sigma_g^+$ ground state

the valence configuration is given by $\pi_{u_x}^2 \pi_{u_y}^2 \sigma_g^0$. The doubly degenerate $^1\Delta_g$ state consists of two components Θ_1 and Θ_2. In a first approximation, Θ_1 is a linear combination of two CSFs $|xx\rangle$ and $|yy\rangle$, whose spatial configurations are given by $\pi_{u_x}^2 \pi_{u_y}^0 \sigma_g^2$ and $\pi_{u_x}^0 \pi_{u_y}^2 \sigma_g^2$. The second state Θ_2 comprises only one CSF $|xy\rangle$, whose spatial configuration is $\pi_{u_x}^1 \pi_{u_y}^1 \sigma_g^2$. In total, their energy can be expressed as a sum over involved matrix elements:

$$E(\Theta_1) = \frac{1}{2} \langle xx| \hat{\mathcal{H}}^{\mathcal{DFT}} |\S\S\rangle + \frac{\infty}{\in} \langle \dagger\dagger| \hat{\mathcal{H}}^{\mathcal{DFT}} |\dagger\dagger\rangle - \langle \S\S| \hat{\mathcal{H}}^{\mathcal{DFT}} |\dagger\dagger\rangle \tag{5.16}$$

$$E(\Theta_2) = \langle xy| \hat{\mathcal{H}}^{\mathcal{DFT}} |\S\dagger\rangle \tag{5.17}$$

To be energetically degenerate, the involved matrix elements must be equal:

$$E(\Theta_2) = E(\Theta_1) \tag{5.18}$$

$$\langle xy| \hat{\mathcal{H}}^{\mathcal{DFT}} |\S\dagger\rangle = \langle xx| \hat{\mathcal{H}}^{\mathcal{DFT}} |\S\S\rangle - \langle \S\S| \hat{\mathcal{H}}^{\mathcal{DFT}} |\dagger\dagger\rangle \tag{5.19}$$

where the right-hand side of the equation has been simplified by using $\langle xx| \hat{\mathcal{H}}^{\mathcal{DFT}} |\S\S\rangle = \langle \dagger\dagger| \hat{\mathcal{H}}^{\mathcal{DFT}} |\dagger\dagger\rangle$. By inserting the matrix elements for the ab-initio CI-Hamiltonian the involved integrals become apparent:

$$V_{xyxy} + V_{xyyx} = V_{xxxx} - V_{xyyx} \tag{5.20}$$

$$\Leftrightarrow V_{xxxx} = V_{xyxy} + 2V_{xyyx} \tag{5.21}$$

where the equation was simplified by using the equality of terms $F_{xx} = F_{yy}$, $V_{x\sigma x\sigma} = V_{y\sigma y\sigma}$ and $V_{x\sigma\sigma x} = V_{y\sigma\sigma y}$. To be useful for a parameterized DFT/MRCI Hamiltonian, equation 5.20 has to be dressed with arbitrary parameters:

$$(1 - q_J^{hhee})V_{xyxy} + (1 - q_X^{hhee})V_{xyyx} = (1 - q_J^{eeee})V_{xxxx} - q_1 V_{xyyx} \tag{5.22}$$

where q_J^{eeee} and q_J^{hhee} scale the Coulomb integrals between two created holes or electrons in the same and different orbitals, respectively, q_X^{hhee} scale the exchange integrals between two created holes and electrons in different orbitals, and q_1 is the prefactor of the off-diagonal matrix elements. While this equation looks cumbersome initially, it can be simplified by inserting the relation between integrals in equation 5.21 and separating Coulomb and exchange integrals.

$$(1 - q_J^{hhee})V_{xyxy} + (1 - q_x^{hhee})V_{xyyx} = (1 - q_j^{eeee})(V_{xyxy} + 2V_{xyyx}) - q_1 V_{xyyx} \tag{5.23}$$

$$\Leftrightarrow (-q_J^{hhee} + q_J^{eeee})V_{xyxy} = (2(1 - q_J^{eeee}) - (1 - q_x^{hhee}) - q_1)V_{xyyx} \tag{5.24}$$

The expressions in parentheses have to vanish to fulfill the degeneracy condition. As a result, the following relations have to be obeyed:

$$q_J^{hhee} = q_J^{eeee} \tag{5.25}$$

$$q_1 = 1 - 2q_J^{eeee} + q_x^{hhee} = 1 - 2q_J^{hhee} + q_x^{hhee} \tag{5.26}$$

The first relation requires the interorbital Coulomb interactions between two holes or two electrons to be scaled in the same way as the intraorbital terms. Additionally, the second relation states that the off-diagonal correction must depend on the parameters of the diagonal elements. In the redesigned Hamiltonians, relation 5.25 is fulfilled because only one global parameter p_J is used to scale every Coulomb integral. In contrast, relation 5.26 is unfulfilled because the prefactor of off-diagonal elements p_1 is not related to the diagonal correction and, as a result, splits the energy of degenerate states. To improve this behavior, a new Hamiltonian needs to fulfill these criteria:

- The different natures of inter- and intraorbital interactions have to be accounted for while fulfilling relation 5.25 at the same time. Since the above-discussed degeneracy is independent of correction parameters affecting only electron-hole interactions, the best solution is to split the Coulomb correction parameters into a parameter, which takes care of the interaction between created holes or electrons and a parameter for the electron-hole interactions.

- The η-independent exchange shift has to be included for electron-hole exchange interactions since otherwise triplet state energies are vastly overestimated. At the same time, an analogous shift can not be introduced to the hole-hole or electron-electron exchange integrals because no suited and systematic way was found that improves the performance. As a result, just like in the case of Coulomb interactions, also the exchange correction parameters should be split into the two categories mentioned above because the parameter for electron-hole interactions has to take into account the involved η-independent shift, while the parameter for exchange interactions between two holes or electrons do not have this additional term.

- The prefactor of the off-diagonal elements needs to be dependent on the diagonal correction parameters as given by relation 5.26 to keep degeneracy between states in these cases.

5.3 The R2022: A Hamiltonian for improved Doubly Excited States (Paper 1)

In this section, a brief summary of the key elements of the published R2022 Hamiltonian is given.

The R2022 Hamiltonian is the newest all-multiplicity Hamiltonian and is meant to be a direct upgrade to its predecessors. The above considerations led to new corrections, which were included in the Hamiltonian and resulted in the following expression for the diagonal matrix elements:

$$
\begin{aligned}
\langle \omega w | \, \hat{\mathcal{H}}^{\mathcal{DFT}} \, | \omega \sqsupseteq \rangle = E^{KS} &+ \sum_i F_{ii}^{KS} \Delta w_i + \frac{1}{2}\left(1 - p_J^{he}\right) \sum_{\substack{i \neq j \\ \Delta w_i \Delta w_j \leq 0}} V_{ijij} \Delta w_i \Delta w_j \\
&+ \frac{1}{2}\left(1 - p_j^{hhee}\right) \sum_{\substack{i \neq j \\ \Delta w_i \Delta w_j > 0}} V_{ijij} \Delta w_i \Delta w_j \\
&+ \frac{1}{2}\left(1 - p_x^{he}\right) \sum_{\substack{i \neq j \\ \Delta w_i \Delta w_j \leq 0}} V_{ijji} \left(-\frac{1}{2} \Delta w_i \Delta w_j + \frac{1}{2} w_i w_j - w_i + \eta_{ij}^{ji} \right) \\
&+ \frac{1}{2}\left(1 - p_x^{hhee}\right) \sum_{\substack{i \neq j \\ \Delta w_i \Delta w_j > 0}} V_{ijji} \left(-\frac{1}{2} \Delta w_i \Delta w_j + \frac{1}{2} w_i w_j - w_i + \eta_{ij}^{ji} \right) \\
&+ \frac{1}{2}\left(1 - p_j^{eeee}\right) \sum_{i \notin s} V_{iiii} \left(\frac{1}{2} \Delta w_i \Delta w_i + \frac{1}{2} w_i w_i - w_i \right) \\
&\frac{1}{4}\left(1 - p_j^{he}\right) \sum_{i \in s} V_{iiii} |\Delta w_i| + \frac{1}{4} p_x^{he} \sum_{\substack{i \neq j \\ \Delta w_i \Delta w_j < 0 \\ i,j \notin s}} V_{ijji} \Delta w_i \Delta w_j
\end{aligned}
\tag{5.27}
$$

Eq. 5.27 looks unfamiliar initially because the sums are over orbitals instead of particles like in the previous Hamiltonians. Summing over orbitals instead of particles in a similar manner as the ab-initio matrix elements guarantees that every integral is properly scaled even for higher excitations. In this way, all the interactions between two created holes or electrons are scaled by p_j^{hhee} and p_x^{hhee}, while the hole-electron interactions are scaled by p_j^{he} and p_x^{he}.

Parameterized in this way, the R2022 Hamiltonian reaches a high accuracy for doubly excited states, as can be seen in a comparison of the RMSD and mean deviation with other DFT/MRCI Hamiltonians in Figure 5.11. Here, the R2022 reaches significantly lower deviations from NEVPT2 with a RMSD of only 0.32 eV compared to 1.65 eV for the original Hamiltonian and 1.84 eV for the redesigned Hamiltonians. Especially the open-shell excitations are vastly improved by including

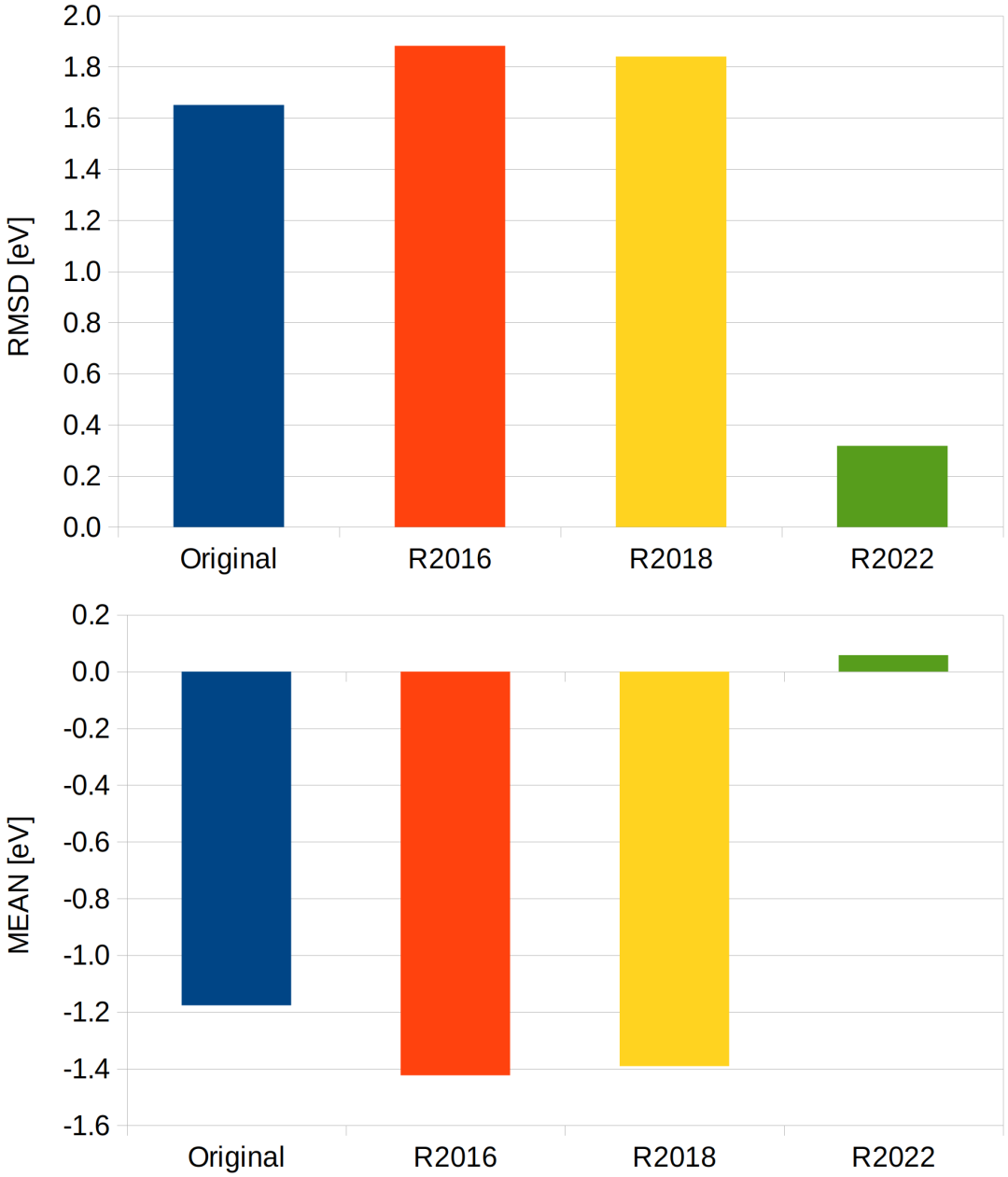

Figure 5.11: RMSD (top) and mean deviation (bottom) with respect to the NEVPT2 TBEs for the critical cases with a standard selection threshold for different Hamiltonians.

Table 5.5: Vertical excitation energies of the critical cases in eV. For the DFT/MRCI Hamiltonians, the difference to the TBE is given.

Molecule	State	Character	NEVPT2	Original	R2018	R2022
o-Benzyne	$^1A_1$	$\pi, \pi' \rightarrow \pi^*, \pi^{*\prime}$	7.23	-2.99	-0.67	0.04
	$^1B_1$	$\pi, \pi' \rightarrow \pi^*, \pi^{*\prime}$	8.15	-2.41	-0.75	-0.04
	$^3A_1$	$\pi, \pi' \rightarrow \pi^*, \pi^{*\prime}$	7.12	-1.43	-0.61	0.03
Thioformaldehyde	$^1A_1$	$n^2 \rightarrow \pi^{*2}$	7.37	0.58	-0.71	-0.44
	$^1A_2$	$n, \pi \rightarrow \pi^{*2}$	7.93	-0.74	-0.27	-0.28
	$^3A_2$	$n, \pi \rightarrow \pi^{*2}$	7.43	0.34	-0.20	-0.09
Dithiin	$^1A'$	$\pi^2 \rightarrow \pi^{*2}$	4.91	-0.11	-0.20	0.17
Dithiosuccinimide	$^1A_1$	$n^2 \rightarrow \pi^{*2}$	5.85	0.22	-0.71	-0.36
	$^1A_1$	$n, n' \rightarrow \pi^*, \pi^{*\prime}$	7.13	-2.42	-3.65	0.33
	$^3B_2$	$n, n' \rightarrow \pi^{*2}$	5.86	-1.26	-2.34	0.37
	$^3A_1$	$n, n' \rightarrow \pi^*, \pi^{*\prime}$	6.99	-2.31	-3.49	0.40
Nitromethane	$^3A'$	$n, n' \rightarrow \pi^{*2}$	8.79	-1.48	-2.35	0.60

the additional exchange correction for every integral, as can be seen in Table 5.5. For the less problematic cases like the $^1A_1$ state with $\pi, \pi' \rightarrow \pi^*, \pi^{*\prime}$ character in *o*-benzyne, the R2022 Hamiltonian deviates only 0.04 eV from the NEVPT2 result. In contrast, the original Hamiltonian deviates by 2.99 eV and the R2018 by -0.67 eV. For the more problematic cases, e.g. the $n, n' \rightarrow \pi^*, \pi^{*\prime}$ excitation in the $^1A_1$ state in dithiosuccinimide, the R2022 Hamiltonian overestimates the excitation energy by 0.33 eV, while the original Hamiltonian and the R2018 Hamiltonian underestimate it by -2.42 eV and -3.65 eV, respectively.

As a side effect of the new corrections, the basis set error with smaller basis sets is more pronounced. In the parameterization procedure, the typical basis set is an augmented TZVP basis. Since this basis is not feasible for large molecules, smaller basis sets of valence double-ζ quality are usually used. An investigation of the basis set dependency of 27 $\pi \rightarrow \pi^*$ and $n \rightarrow \pi^*$ excitation energies in the training set revealed that in comparison to the R2016 Hamiltonian the R2022 Hamiltonian has a larger deviation with smaller basis sets, as can be seen in Figure 5.12. For the augmented TZVP basis, the mean deviation from the experiment is 0.01 eV for R2022, while R2016 slightly underestimates with -0.01 eV. Removing the diffuse functions raises the deviation for R2022 to 0.08 eV, while R2016 deviates only by 0.06 eV. Further decreasing the size of the basis set results in an increase of the deviation to 0.17 eV and 0.12 eV for R2022 and R2016, respectively. This might be an unfortunate loss of error cancellation caused by the removal of energetically low-lying doubly excited configurations, which decrease the state energy and counteract the energy increase by a smaller basis.

Overall, the error in doubly excited states is notably reduced by the new R2022

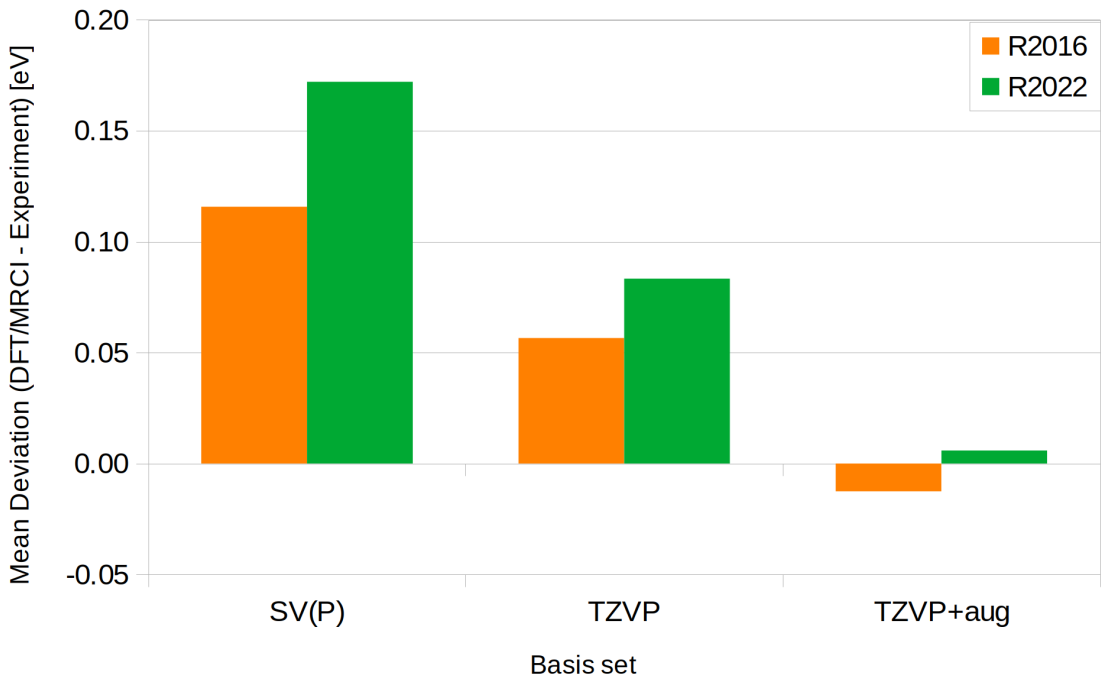

Figure 5.12: Mean deviation from experimental values of 27 vertical excitation energies of $\pi \rightarrow \pi^*$ and $n \rightarrow \pi^*$ singlet transitions included in the training set computed using different basis sets. For details see Paper 1 [1].

Hamiltonian, and the results are comparable to NEVPT2. A drawback of this new Hamiltonian is a more pronounced basis set dependency.

Chapter 6

Application of the R2022 DFT/MRCI Hamiltonian

In the next sections, two groups of molecules with extended π-systems, namely the *para*-oligophenylenes and the substituted anthracene derivatives, are investigated. In context of this thesis, they have been investigated to assess the new R2022 Hamiltonian on highly resolved anion photodetachment-photoelectron (PDPE) spectra. The special feature of this spectroscopy is, that excitation energies to specific singlet and triplet states of the neutral molecule can be measured accurately. The excited states need a significant contribution from a configuration which is build by exciting an electron to the LUMO. Furthermore since these spectra are recorded in the gas phase of the molecules, there are no solvent effects which can otherwise complicate the interpretation. Early studies on α,ω-diphenylpolyenes [121] and α-oligothiophene [122] observed that adiabatic excitation energies calculated with the original Hamiltonian are red-shifted in comparison to the experiment. Furthermore Meissner et al. [53] found in a study on N-methylacridone and N,N'-dimethylquinacridone with the R2016 Hamiltonian, that the experimental spectrum was well reproduced by DFT/MRCI, but the excitation energies seem to be systematically red-shifted by about 0.2 eV. Additionally, a similar shift was observed by Manian et al. [123] in the adiabatic transition energy to the S_1 states of anthracene, tetracene and pentacene in comparison to experimental values. Furthermore, earlier studies on α,ω-diphenylpolyenes[121] and α-oligothiophene[122] found a similar red-shift in combination with the original Hamiltonian. In this chapter the main questions are, whether the R2022 Hamiltonian can accurately reproduce the experimental transition energies, to what extend the red-shift can be observed in this molecules and whether the R2022 Hamiltonian can reduce or remove the red-shift.

6.1 *Para*-Oligophenylenes (Paper 2)

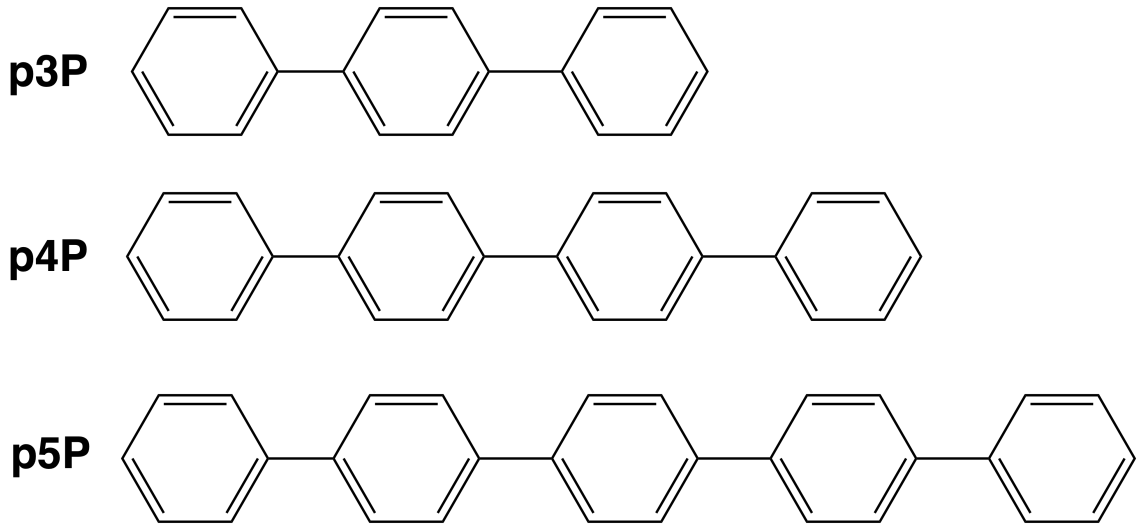

Figure 6.1: Chemical structures of the *para*-oligophenylenes p3P, p4P and p5P.

The molecules *para*-terphenyl (p3P), *para*-quaterphenyl (p4P) and *para*-quinquephenyl (p5P) are *para*-oligophenylenes which are used as UV laser dyes because of their large S_0 - S_1 cross section. Their chemical structures are given in Fig. 6.1. In the neutral ground state (S_0) these molecules have strongly twisted structures, while the dihedral angles between the rings planarize in the anion ground state (D_0) and the excited states and forming a quinoid structure. As a result of these strong geometric differences between the anion and the neutral ground state, the D_0-S_0 excitation has a broad signal in the spectrum. The excited states exhibit significantly smaller geometrical distortions with respect to the anion ground state and therefore have narrower FC profiles. In the longer molecules, especially in p5P, the planarization of the molecule in the excited state affects either the inner or the outer rings so that the structure in the excited states in p5P is almost planar at the inner rings, while the outer rings are twisted or the other way around. In Tab. 6.1, the 0-0 transition energies of the excited states with respect to the neutral ground state for different methods are listed. The red-shift of the R2016 Hamiltonian is also observed in the *para*-oligophenylenes. For the smaller p3P, the magnitude of the shift is about -0.2 to -0.3 eV as in the study by Meissner et al. [53]. For the larger molecules p4P and p5P, the magnitude increases to around -0.4 eV. When the new R2022 Hamiltonian is employed, this shift is reduced, but still observable. For almost all states, the red-shift is halved compared to the R2016 Hamiltonian. For p3P the S_1 state is red-shifted by -0.11 eV instead of -0.27 eV and for the longer molecules, the shift is reduced to -0.22 eV and -0.16 eV for p4P and p5P, respectively. The influence of the R2022 Hamiltonian on the red-shift is therefore similar to the trends observed for the *n*-carotenes in the R2022 paper [1]. Here, the results of the R2016 and

R2022 Hamiltonians deviate more from the experiment with increasing chain length of the carotene. While both Hamiltonians started with adiabatic energies close to the experimental value for mini-5-carotene, for the longer chains the deviation increased to about -0.4 eV for the R2016 Hamiltonian and -0.2 eV for the R2022 Hamiltonian. Interestingly to note is, that the T_1 state of all *para*-oligophenylene has a significantly lower deviation from the experiment than the other states, which is surprising, because the corresponding S_1 state, which is also mainly a transition from the HOMO to the LUMO orbital, is strongly red-shifted. TDDFT with the PBE0 functional follows the same trend as the two DFT/MRCI Hamiltonians. For all three methods, the deviation of the S_1 state from the experimental results increases by 50% between p3P and p4P, while p5P has the same deviation as p4P. Additionally, the deviations of the T_1 state transition energies are constant over all molecules with all methods, namely about -0.15 eV to -0.17 eV for R2016, 0.00 eV to 0.06 eV for R2022 and -0.04 eV to 0.03 eV for TDDFT. Therefore the underlying error has probably a common origin for all three methods. One possible source of error could be the delocalization error in the underlying DFT method. [14] This error causes an overestimation of the delocalization of an electron which in turn underestimates the bond length alternation in extended π-systems. The bond lengths of the S_0 state and various excited states with respect to those in the D_0 state are given in Fig. 6.2. The bond length alternation in the T_1 state is more pronounced than the bond length alternation in the S_1 state, therefore it could be possible that the bond length alternation in the S_1 state is underestimated due to the delocalization error and therefore the geometry of the T_1 state in comparison to the S_1 state geometry is better described and the error smaller in the excitation energies of the T_1 state.

A definitive answer to the question of the origin of this red-shift needs further thorough investigation, which is beyond the scope of this thesis. For the *para*-oligophenylenes, the red-shift is observed for both Hamiltonians. While for the R2016 Hamiltonian it increases up to -0.43 eV, for the R2022 Hamiltonian it is halved in most cases and only increases up to -0.22 eV. Interestingly, the singlet-triplet gaps between the S_1 and T_1 states are almost equal in both Hamiltonians as can be seen in Fig. 6.3. This is due to the fact that the largest change between the two Hamiltonians is the neutral ground state energy. For example, in p5P, the calculated neutral ground state energy with the R2022 Hamiltonian gives a 0.28 eV lower value relative to the R2016 Hamiltonian, while the energy of the S_1 and T_1 states are only 0.02 eV smaller in the R2022 results. Furthermore, the deviation of the singlet-triplet gap from the experiment is smallest for p3P, while the other two molecules have almost the same error. It is therefore not obvious, whether the error depends on the size of the *para*-oligophenylene or stagnates around a constant value.

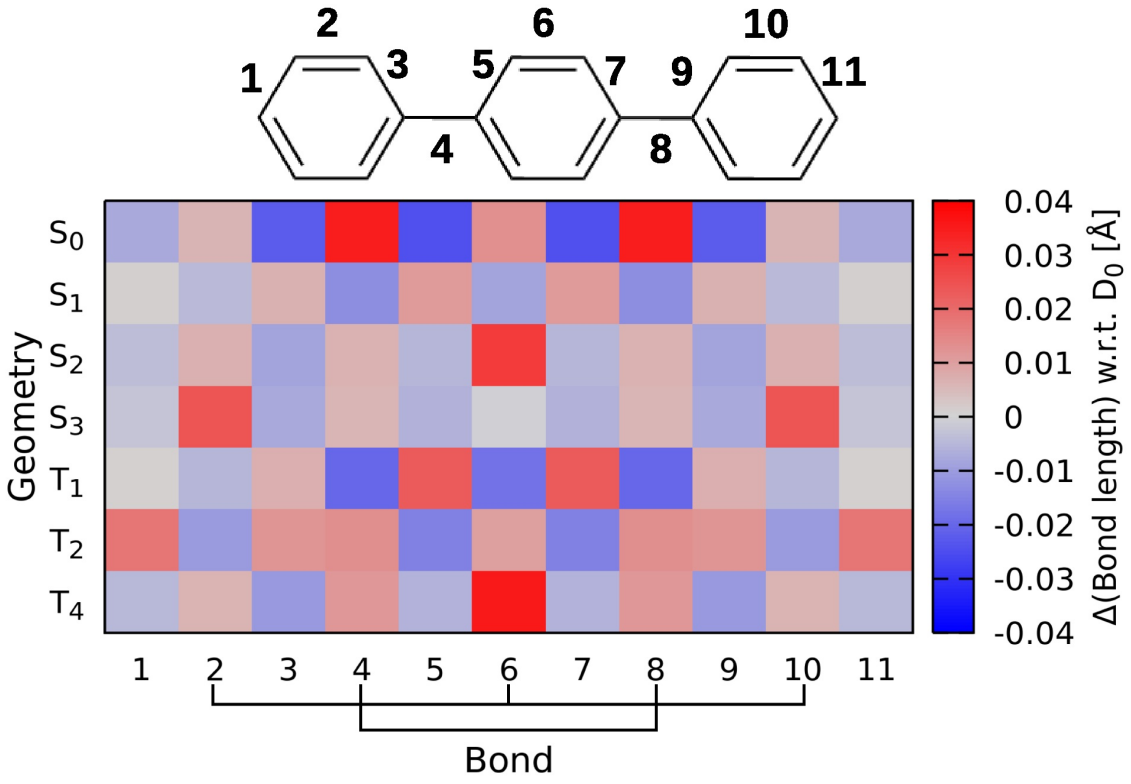

Figure 6.2: Bond length differences of the neutral state geometries with respect to the D_0 anion ground state geometry of p3P. The colour bar at the right side gives the correlation between the colours and the bond length changes in (Å). The bond numbers included in the molecular structure appear also at the x-axis. Bonds involved in the formation of the quinoid structure are connected by a bar on the x-axis.

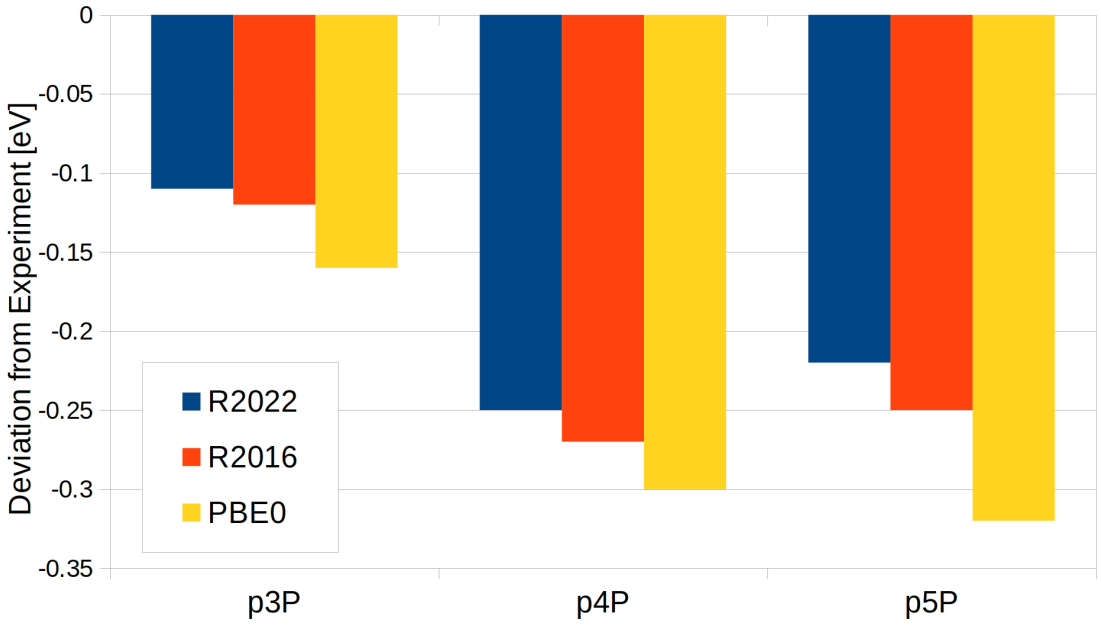

Figure 6.3: Deviation of calculated singlet-triplet gaps from the experimental gap between the S_1 and T_1 states of *para*-oligophenylenes. All values are in eV.

Table 6.1: Experimental electronic state energies E_{exp} for p3P, p4P and p5P and calculated 0-0 transition energies ΔE_{0-0} with respect to the neutral ground state S_0. The calculated transition energies are given as the difference to the experimental electronic state energies. For the PBE0 DFT transition energies, TDDFT and TDADFT were used for singlet and triplet states, respectively. Energies are given in eV.

State		E_{exp}	ΔE_{0-0}^{R2016}	ΔE_{0-0}^{R2022}	ΔE_{0-0}^{PBE0}
p3P					
S_1	1^1A_u	4.02	-0.27	-0.11	-0.19
T_1	1^3A_u	2.60	-0.15	0.00	-0.04
T_2	1^3A_g	3.56	-0.22	-0.11	-0.02
T_3	2^3A_u	3.93	-0.23	-0.12	0.03
p4P					
S_1	1^1B_1	3.87	-0.43	-0.22	-0.34
T_1	1^3B_1	2.48	-0.16	0.03	-0.04
T_2	1^3A	3.26	-0.31	-0.13	-0.07
T_3	3^3A	3.77	-0.39	-0.22	-0.08
p5P					
S_1	1^1A_u	3.65	-0.42	-0.16	-0.29
T_1	1^3A_u	2.34	-0.17	0.06	0.03
T_2	1^3A_g	3.04	-0.31	-0.10	-0.03
T_3	2^3A_u	3.56	-0.34	-0.15	-0.05

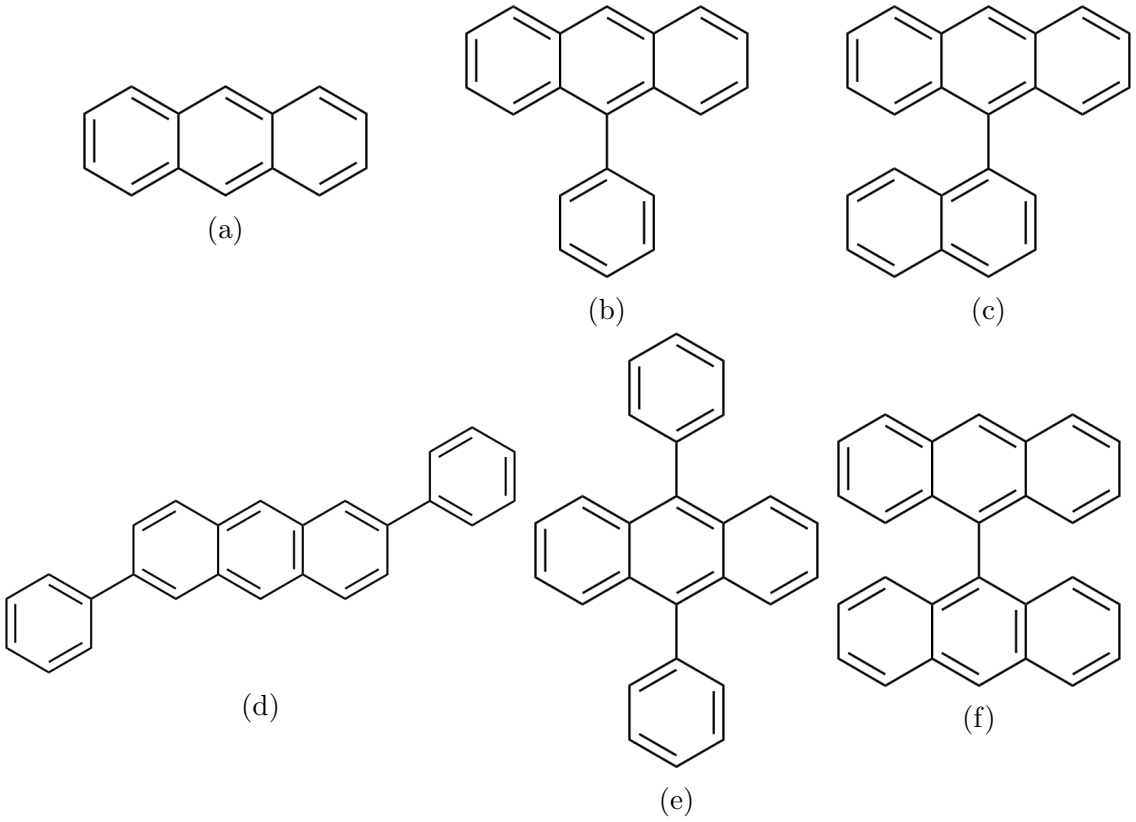

Figure 6.4: Chemical structures of a) anthracene, b) 9-phenylanthracene, c) 9-(1-naphthyl)-anthracene, d) 2,6-diphenylanthracene, e) 9,10-diphenylanthracene and f) 9-9'-bianthracene.

6.2 Substituted Anthracene Derivatives

In this section, the lowest singlet and triplet states of the substituted anthracene derivatives, shown in Fig. 6.4, are investigated. These states are named L_a in the symmetry independent nomenclature introduced by Platt [124]. They are dominated by an excitation of the highest occupied π orbital into the lowest π^* orbital as can be seen in Fig. 6.5 for anthracene. For the other molecules, with the exception of 9,9'-bianthracene, the transition into the excited state is localized on anthracene, while in the case of 9,9'-bianthracene, the excitation is delocalized over both anthracene parts. Like in the former section, their transition energies were calculated

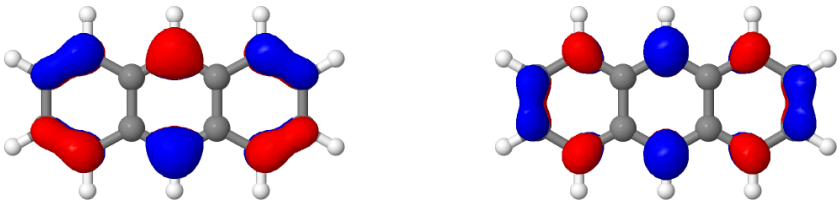

(a) π (b) π^*

Figure 6.5: Orbitals involved in the ^1L_a state of anthracene.

with the DFT/MRCI method with the R2016 and the R2022 Hamiltonians as well as TDDFT with the PBE0 functional. For computational details please see Paper 2. 9-Phenylanthracene, 9-(1-naphthyl)-anthracene and 9,10-diphenylanthracene were calculated by the author of this thesis, while the other three molecules were calculated by Timo Schulz and made available for a statistical analysis in the context of this thesis. The experimental values are taken from the PhD theses of Konieczny [125] and Kosper [126]. The results are presented in Tab. 6.2. In general, the same trends as for the *para*-oligophenylenes are observed. Furthermore for all three methods the 0–0 excitation energies of singlet states deviates significantly more from the experimental values than for the triplet states. TDDFT with the PBE0 functional exhibits larger deviations compared to the results of the *para*-oligophenylenes. The singlet-triplet splitting is hardly affected by the choice of the DFT/MRCI Hamiltonian as can be seen in Fig. 6.6. For anthracene, the singlet-triplet gaps of both Hamiltonians deviate by -0.06 eV in comparison to the experiment, while for the substituted anthracenes the R2022 Hamiltonian gives slightly better results. Interestingly, the error is hardly depending on the place of the substituting group. As soon as a hydrogen is substituted by a group, the error rises from -0.05 eV to -0.12 to -0.15 eV for the DFT/MRCI Hamiltonians. For PBE0/TDDFT the error is approximately -0.25 eV and is independent of the molecule. It is therefore neither the position nor the size of the substitution group which dominates the error in the excitation energies and the singlet-triplet gap. Further investigations are needed to investigate the source of the error. Nevertheless the new Hamiltonian effectively reduces the deviation of the calculated excitation energies in comparison to the former Hamiltonians by about 50% to 67%, which is a satisfactory improvement.

Table 6.2: Experimental electronic state energies E_{exp} for the substituted anthracene derivatives and calculated 0-0 transition energies ΔE_{0-0} with respect to the neutral ground state S_0. The calculated transition energies are given as the difference to the experimental electronic state energies. For the PBE0 DFT transition energies, TDDFT and TDADFT were used for singlet and triplet states, respectively. Energies are given in eV.

State		E_{exp}	ΔE_{0-0}^{R2016}	ΔE_{0-0}^{R2022}	ΔE_{0-0}^{PBE0}
Anthracene					
S_1	1^1B_{2u}	3.43	-0.31	-0.18	-0.41
T_1	1^3B_{2u}	1.87	-0.25	-0.12	-0.17
9-Phenylanthracene					
S_1	2^1A	3.38	-0.38	-0.20	-0.46
T_1	1^3A	1.85	-0.23	-0.06	-0.18
9-(1-Naphthyl)-anthracene					
S_1	1^1A_u	3.38	-0.34	-0.17	-0.45
T_1	1^3A_u	1.85	-0.18	-0.02	-0.17
2,6-Diphenylanthracene					
S_1	1^1A_u	3.21	-0.38	-0.16	-0.39
T_1	1^3A_u	1.80	-0.24	-0.05	-0.16
9,10-Diphenylanthracene					
S_1	1^1B_1	3.25	-0.34	-0.12	-0.38
T_1	1^3B_1	1.78	-0.17	0.03	-0.13
9,9'-Bianthracene					
S_1	2^1A	3.34	-0.39	-0.16	-0.57
T_1	1^3A	1.86	-0.23	-0.03	

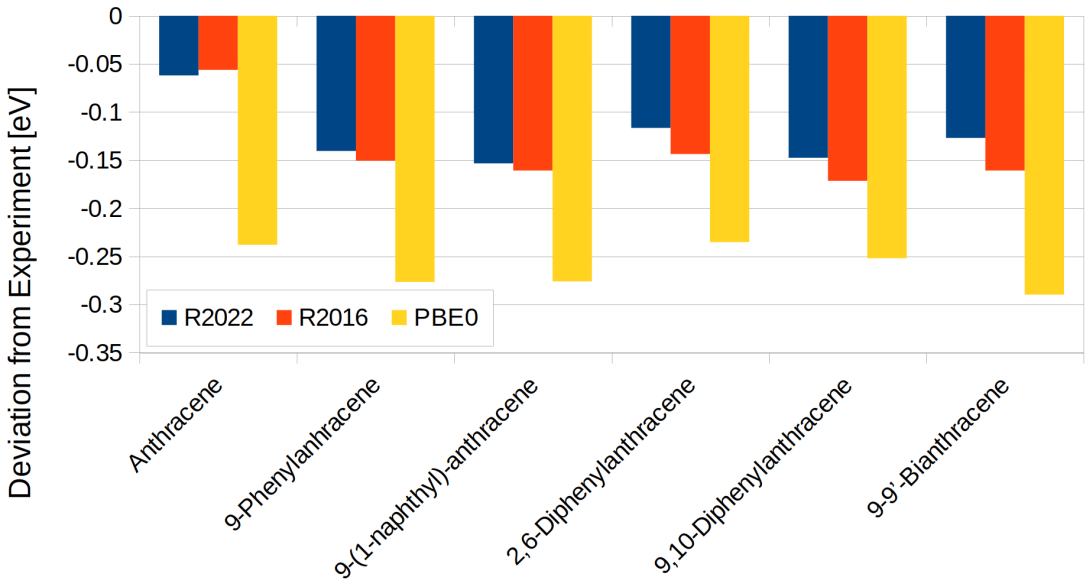

Figure 6.6: Deviation of calculated singlet-triplet gaps from the experimental gap between the S_1 and T_1 states of anthracene and substituted anthracene derivatives. All values are in eV.

Chapter 7

Conclusion

In this thesis the origin of the underestimated double excitation energies, especially for $n^2 \rightarrow \pi^{*2}$ and $n, n' \rightarrow \pi^*, \pi^{*\prime}$ excitations, was investigated. To this end, a multitude of different density functionals with various admixtures of non-local exchange were systematically investigated and a correlation between the admixture of non-local exchange and the accuracy of the DFT/MRCI method was discovered. The most suitable density functional in combination with DFT/MRCI was found to have about 50% non-local exchange, which means that the already used BH-LYP functional is optimal. The reason for this optimal amount of non-local exchange was traced back to the self-interaction error of common density functionals. This error mimics implicitly static electron correlation and improves in this way DFT and TDDFT calculations. Since static electron correlation is already treated by the CI part of the DFT/MRCI method, a small self-interaction error is mandatory to avoid double counting of static correlation. Furthermore commonly used functionals with a smaller amount of non-local exchange like the PBE0 functional did not lead to improved results for doubly excited states. Therefore the underestimation of doubly excited state energies is hardly influenced by the underlying functional. With this in mind the origin of the error was searched for by careful investigation of the energy contributions in the DFT/MRCI Hamiltonian. Three different points were discovered that are important for a good description of doubly excited states:

1. The difference between intra- and interorbital Coulomb interactions, which dominated the error in closed-shell doubly excited states,

2. The missing correction terms to exchange energy contributions between two created electrons (or holes), which dominated the error in open-shell excitations,

3. The relation between the diagonal and off-diagonal elements, which is necessary to describe accurately degenerate states.

The resulting R2022 Hamiltonian improves the RMSD in a test set of doubly excited state excitation energies against NEVPT2 results significantly to 0.32 eV compared to the earlier Hamiltonians which achieve RMSDs of 1.65 eV to 1.84 eV. The performance for singly excited state excitation energies of the former Hamiltonians is maintained, so that the new Hamiltonian can be seen as a general purpose Hamiltonian which builds upon the strength of former Hamiltonians. Furthermore the R2022 Hamiltonian reduces the error in molecules with extended π-systems like carotenoids or polyacenes by about 50% compared to the redesigned Hamiltonians. A drawback of the new Hamiltonian is a more pronounced basis set error with smaller basis sets. This is probably caused by an unfortunate loss of error cancellation, which decreases the state energy and counteracts the energy increase by a smaller basis.

The new Hamiltonian was assessed on a set of experimental high-resolved photodetachment-photoelectron spectra of *para*-oligophenylenes and substituted anthracene derivatives. The results are satisfying and reduce the error by about 50% to 67% in comparison to the R2016 Hamiltonian. Nevertheless the singlet-triplet gaps are not improved by the R2022 Hamiltonian. The reason for this is, that in these molecules the neutral ground state is mainly influenced by the new corrections of the R2022 Hamiltonian, while the singlet and triplet states are hardly affected due to their similar involved dominant configurations. Furthermore the deviation of the singlet excited state energies in these molecules are significantly larger than in the triplet excited state case, not only for the DFT/MRCI results, but also for the TDDFT results with the PBE0 functional. The origin of these differences is currently unknown and needs further investigation.

Currently the new Hamiltonian is tested on other groups of molecules, including covalently linked dimers which can undergo singlet fission. Like already mentioned in the introduction, these molecules are particularly interesting to investigate, because their properties are heavily influenced by doubly excited states and they constitute an interesting group of molecules for use in solar cells. Additionally a new extension to the DFT/MRCI method is being developed, which allows the calculation of odd-electron systems with any number of open shells. This would expand the range of application of the DFT/MRCI method even further to high-spin states.

Bibliography

[1] Dennis R. Dombrowski, Timo Schulz, Martin Kleinschmidt, and Christel M. Marian. R2022: A DFT/MRCI Ansatz with Improved Performance for Double Excitations. *J. Phys. Chem. A*, 127(8):2011–2025, 2023.

[2] Pierre-François Loos, Martial Boggio-Pasqua, Anthony Scemama, Michel Caffarel, and Denis Jacquemin. Reference Energies for Double Excitations. *J. Chem. Theory Comput.*, 15(3):1939–1956, 2019. doi: 10.1021/acs.jctc.8b01205.

[3] Federico J. Hernández and Rachel Crespo-Otero. Modeling Excited States of Molecular Organic Aggregates for Optoelectronics. *Annu. Rev. Phys. Chem.*, 74:547–571, 2023.

[4] Millicent B. Smith and Josef Michl. Singlet Fission. *Chem. Rev.*, 110(11): 6891–6936, 2010.

[5] Victor Gray, Damir Dzebo, Maria Abrahamsson, Bo Albinsson, and Kasper Moth-Poulsen. Triplet–triplet annihilation photon-upconversion: towards solar energy applications. *Phys. Chem. Chem. Phys.*, 16(22):10345–10352, 2014.

[6] Andrew Nattestad, Yuen Yap Cheng, Rowan W MacQueen, Tim F. Schulze, Fletcher W. Thompson, Attila J. Mozer, Burkhard Fückel, Tony Khoury, Maxwell J. Crossley, Klaus Lips, Gorden G. Wallace, and Timothy W. Schmidt. Dye-Sensitized Solar Cell with Integrated Triplet–Triplet Annihilation Upconversion System. *J. Phys. Chem. Lett.*, 4(12):2073–2078, 2013.

[7] Giuseppe M. J. Barca, Andrew T. B. Gilbert, and Peter M. W. Gill. Simple Models for Difficult Electronic Excitations. *J. Chem. Theory Comput.*, 14(3): 1501–1509, 2018.

[8] Giuseppe M. J. Barca, Andrew T. B. Gilbert, and Peter M. W. Gill. Excitation Number: Characterizing Multiply Excited States. *J. Chem. Theory Comput.*, 14(1):9–13, 2018.

[9] Mark E. Casida, Delano P. Chong, et al. Recent Advances In Density Functional Methods, 1995.

[10] E. K. U. Gross, J. F. Dobson, and M. Petersilka. *Density Functional Theory of Time-Dependent Phenomena*, pages 81–172. Springer Berlin Heidelberg, Berlin, Heidelberg, 1996. ISBN 978-3-540-49946-6. doi: 10.1007/BFb0016643. URL `https://doi.org/10.1007/BFb0016643`.

[11] Erich Runge and Eberhard K. U. Gross. Density-Functional Theory for Time-Dependent Systems. *Phys. Rev. Lett.*, 52(12):997, 1984.

[12] Yevhen Horbatenko, Seunghoon Lee, Michael Filatov, and Cheol Ho Choi. How beneficial is the explicit account of doubly-excited configurations in linear response theory? *J. Chem. Theory Comput.*, 17(2):975–984, 2021.

[13] Pragya Verma and Donald G. Truhlar. Status and Challenges of Density Functional Theory. *Trends Chem.*, 2(4):302–318, 2020.

[14] Kyle R. Bryenton, Adebayo A. Adeleke, Stephen G. Dale, and Erin R. Johnson. Delocalization error: The greatest outstanding challenge in density-functional theory. *WIREs Comput Mol Sci*, 13(2):e1631, 2023.

[15] Chen Li, Xiao Zheng, Neil Qiang Su, and Weitao Yang. Localized orbital scaling correction for systematic elimination of delocalization error in density functional approximations. *Natl Sci Rev*, 5(2):203–215, 2018.

[16] David J. Tozer, Roger D. Amos, Nicholas C. Handy, Bjorn O. Roos, and Luis Serrano-Andres. Does density functional theory contribute to the understanding of excited states of unsaturated organic compounds? *Mol. Phys.*, 97(7): 859–868, 1999.

[17] Andreas Dreuw, Jennifer L. Weisman, and Martin Head-Gordon. Long-range charge-transfer excited states in time-dependent density functional theory require non-local exchange. *J. Chem. Phys.*, 119(6):2943–2946, 2003.

[18] Andreas Dreuw and Martin Head-Gordon. Failure of Time-Dependent Density Functional Theory for Long-Range Charge-Transfer Excited States: The Zincbacteriochlorin–Bacteriochlorin and Bacteriochlorophyll–Spheroidene Complexes. *J. Am. Chem. Soc.*, 126(12):4007–4016, 2004.

[19] Yoshihiro Tawada, Takao Tsuneda, Susumu Yanagisawa, Takeshi Yanai, and Kimihiko Hirao. A long-range-corrected time-dependent density functional theory. *J. Chem. Phys.*, 120(18):8425–8433, 2004.

[20] Takeshi Yanai, David P. Tew, and Nicholas C. Handy. A new hybrid exchange–correlation functional using the Coulomb-attenuating method (CAM-B3LYP). *Chem. Phys. Lett.*, 393(1-3):51–57, 2004.

[21] Noriyuki Minezawa and Mark S. Gordon. Optimizing Conical Intersections by Spin- Flip Density Functional Theory: Application to Ethylene. *J. Phys. Chem. A*, 113(46):12749–12753, 2009.

[22] Fan Wang and Tom Ziegler. Time-dependent density functional theory based on a noncollinear formulation of the exchange-correlation potential. *J. Chem. Phys.*, 121(24):12191–12196, 2004.

[23] Miquel Huix-Rotllant, Bhaarathi Natarajan, Andrei Ipatov, C. Muhavini Wawire, Thierry Deutsch, and Mark E. Casida. Assessment of noncollinear spin-flip Tamm–Dancoff approximation time-dependent density-functional theory for the photochemical ring-opening of oxirane. *Phys. Chem. Chem. Phys.*, 12(39):12811–12825, 2010.

[24] Ove Christiansen, Henrik Koch, and Poul Jørgensen. Response functions in the CC3 iterative triple excitation model. *J. Chem. Phys.*, 103(17):7429–7441, 1995.

[25] Henrik Koch, Ove Christiansen, Poul Jørgensen, Alfredo M. Sanchez de Merás, and Trygve Helgaker. The CC3 model: An iterative coupled cluster approach including connected triples. *J. Chem. Phys.*, 106(5):1808–1818, 1997.

[26] Jozef Noga and Rodney J. Bartlett. The full CCSDT model for molecular electronic structure. *J. Chem. Phys.*, 86(12):7041–7050, 1987.

[27] Stanislaw A. Kucharski and Rodney J. Bartlett. Recursive intermediate factorization and complete computational linearization of the coupled-cluster single, double, triple, and quadruple excitation equations. *Theor. Chim. Acta*, 80(4-5):387–405, 1991.

[28] Mark A. Watson and Garnet Kin-Lic Chan. Excited States of Butadiene to Chemical Accuracy: Reconciling Theory and Experiment. *J. Chem. Theory Comput.*, 8(11):4013–4018, 2012.

[29] Björn O. Roos, Peter R. Taylor, and Per E. M. Sigbahn. A complete active space SCF method (CASSCF) using a density matrix formulated super-CI approach. *Chem. Phys.*, 48(2):157–173, 1980.

[30] Kerstin Andersson, Per Aake Malmqvist, Bjoern O. Roos, Andrzej J. Sadlej, and Krzysztof Wolinski. Second-Order Perturbation Theory with a CASSCF Reference Function. *J. Phys. Chem.*, 94(14):5483–5488, 1990.

[31] Celestino Angeli, Renzo Cimiraglia, and Jean-Paul Malrieu. N-electron valence state perturbation theory: a fast implementation of the strongly contracted variant. *Chem. Phys. Lett.*, 350(3-4):297–305, 2001.

[32] Celestino Angeli, Renzo Cimiraglia, Stefano Evangelisti, Thierry Leininger, and Jean-Paul Malrieu. Introduction of n-electron valence states for multireference perturbation theory. *J. Chem. Phys.*, 114(23):10252–10264, 2001.

[33] Celestino Angeli, Renzo Cimiraglia, and Jean-Paul Malrieu. n-electron valence state perturbation theory: A spinless formulation and an efficient implementation of the strongly contracted and of the partially contracted variants. *J. Chem. Phys.*, 117(20):9138–9153, 2002.

[34] Stefan Grimme and Mirko Waletzke. A combination of Kohn–Sham density functional theory and multi-reference configuration interaction methods. *J. Chem. Phys.*, 111(13):5645–5655, 1999.

[35] Igor Lyskov, Martin Kleinschmidt, and Christel M. Marian. Redesign of the DFT/MRCI Hamiltonian. *J. Chem. Phys.*, 144(3):034104, 2016.

[36] Adrian Heil and Christel M. Marian. DFT/MRCI Hamiltonian for odd and even numbers of electrons. *J. Chem. Phys.*, 147(19):194104, 2017.

[37] Adrian Heil, Martin Kleinschmidt, and Christel M. Marian. On the performance of DFT/MRCI Hamiltonians for electronic excitations in transition metal complexes: The role of the damping function. *J. Chem. Phys.*, 149(16): 164106, 2018.

[38] Christel M Marian, Adrian Heil, and Martin Kleinschmidt. The DFT/MCI Method. *Wiley Interdiscip. Rev.: Comput. Mol. Sci.*, 9(2):e1394, 2019.

[39] Christel M. Marian and Natalie Gilka. Performance of the Density Functional Theory/Multireference Configuration Interaction Method on Electronic Excitation of Extended π-systems. *J. Chem. Theory Comput.*, 4(9):1501–1515, 2008. doi: 10.1021/ct8001738.

[40] Martin Kleinschmidt, Christel M. Marian, Mirko Waletzke, and Stefan Grimme. Parallel multireference configuration interaction calculations on mini-β-carotenes and β-carotene. *J. Chem. Phys*, 130:044708, 2009. doi: 10.1063/1.3062842.

[41] Vladimír Lukeš, Niklas Christensson, Franz Milota, Harald F. Kauffmann, and Jürgen Hauer. Electronic ground state conformers of β-carotene and their role in ultrafast spectroscopy. *Chem. Phys. Lett.*, 506(1-3):122–127, 2011.

[42] Oliviero Andreussi, Stefan Knecht, Christel M. Marian, Jacob Kongsted, and Benedetta Mennucci. Carotenoids and Light-Harvesting: From DFT/MRCI to the Tamm–Dancoff Approximation. *J. Chem. Theory Comput.*, 11(2):655–666, 2015.

[43] Stefan Knecht, Christel M. Marian, Jacob Kongsted, and Benedetta Mennucci. On the Photophysics of Carotenoids: A Multireference DFT Study of Peridinin. *J. Phys. Chem. B*, 117(44):13808–13815, 2013.

[44] Riccardo Spezia, Stefan Knecht, and Benedetta Mennucci. Excited state characterization of carbonyl containing carotenoids: a comparison between single and multireference descriptions. *Phys. Chem. Chem. Phys.*, 19(26):17156–17166, 2017.

[45] Vidisha Rai-Constapel, Martin Kleinschmidt, Susanne Salzmann, Luis Serrano-Andrés, and Christel M. Marian. Thioxanthone: on the shape of the first absorption band. *Phys. Chem. Chem. Phys.*, 12(32):9320–9327, 2010.

[46] Jan P. Götze, Dominik Kröner, Shiladitya Banerjee, Bora Karasulu, and Walter Thiel. Carotenoids as a Shortcut for Chlorophyll Soret-to-Q Band Energy Flow. *ChemPhysChem*, 15(15):3392–3401, 2014.

[47] Christel M. Marian, Setsuko Nakagawa, Vidisha Rai-Constapel, Bora Karasulu, and Walter Thiel. Photophysics of Flavin Derivatives Absorbing in the Blue-Green Region: Thioflavins As Potential Cofactors of Photoswitches. *J. Phys. Chem. B*, 118(7):1743–1753, 2014.

[48] Vidisha Rai-Constapel, Torben Villnow, Gerald Ryseck, Peter Gilch, and Christel M. Marian. Chimeric Behavior of Excited Thioxanthone in Protic Solvents: Ii. Theory. *J. Phys. Chem. A*, 118(50):11708–11717, 2014.

[49] Josefin Wilke, Martin Wilke, Christian Brand, J. Dominik Spiegel, Christel M. Marian, and Michael Schmitt. Modulation of the L_a/L_b Mixing in an Indole Derivative: A Position-Dependent Study Using 4-, 5-, and 6-Fluoroindole. *J. Phys. Chem. A*, 121(8):1597–1606, 2017.

[50] Anna Reiffers, Christian Torres Ziegenbein, Luiz Schubert, Janina Diekmann, Kristoffer A. Thom, Ralf Kühnemuth, Axel Griesbeck, Oliver Weingart, and Peter Gilch. On the large apparent Stokes shift of phthalimides. *Phys. Chem. Chem. Phys.*, 21(9):4839–4853, 2019.

[51] Mario Bracker, Mira K. Kubitz, Constantin Czekelius, Christel M. Marian, and Martin Kleinschmidt. Computer-Aided Design of Fluorinated Flavin Derivatives by Modulation of Intersystem Crossing and Fluorescence. *ChemPhotoChem*, 6(7):e202200040, 2022.

[52] Fabian Dinkelbach, Mario Bracker, Martin Kleinschmidt, and Christel M. Marian. Large Inverted Singlet–Triplet Energy Gaps Are Not Always Favorable for Triplet Harvesting: Vibronic Coupling Drives the (Reverse) Intersystem Crossing in Heptazine Derivatives. *J. Phys. Chem. A*, 125(46): 10044–10051, 2021.

[53] Jan Meissner, Bernd Kosper, Christel M. Marian, and Rainer Weinkauf. Lowest Triplet and Singlet States in *N*-Methylacridone and N,N'-Dimethylquinacridone: Theory and Experiment. *J. Phys. Chem. A*, 125(40): 8777–8790, 2021.

[54] Angela Rodriguez-Serrano, Fabian Dinkelbach, and Christel M. Marian. Intersystem crossing processes in the 2CzPN emitter: a DFT/MRCI study including vibrational spin–orbit interactions. *Phys. Chem. Chem. Phys.*, 23(5): 3668–3678, 2021.

[55] Rachel Crespo-Otero and Mario Barbatti. $Cr(CO)_6$ photochemistry: Semiclassical study of UV absorption spectral intensities and dynamics of photodissociation. *J. Chem. Phys.*, 134(16), 2011.

[56] Adrian Heil, Kathleen Gollnisch, Martin Kleinschmidt, and Christel M. Marian. On the photophysics of four heteroleptic iridium(iii) phenylpyridyl complexes investigated by relativistic multi-configuration methods. *Mol. Phys.*, 114(3-4):407–422, 2016.

[57] Jelena Föller, Martin Kleinschmidt, and Christel M. Marian. Phosphorescence or Thermally Activated Delayed Fluorescence? Intersystem Crossing and Radiative Rate Constants of a Three-Coordinate Copper(I) Complex Determined by Quantum-Chemical Methods. *Inorg. Chem.*, 55(15):7508–7516, 2016.

[58] Jelena Föller, Daniel H. Friese, Stefan Riese, Jeremy M. Kaminski, Simon Metz, David Schmidt, Frank Würthner, Christoph Lambert, and Christel M. Marian. On the photophysical properties of Ir^{III}, Pt^{II}, and Pd^{II} (phenylpyrazole)(phenyldipyrrin) complexes. *Phys. Chem. Chem. Phys.*, 22(6):3217–3233, 2020.

[59] Ondřej Mrózek, Mousree Mitra, Bejamin Hupp, Andrey Belyaev, Nora Lüdtke, Dorothee Wagner, Cui Wang, Oliver S. Wenger, Christel M. Marian, and An-

dreas Steffen. An Air-and Moisture-stable Zinc(II) Carbene Dithiolate Dimer Showing Fast Thermally Activated Delayed Fluorescence and Dexter Energy Transfer Catalysis. *Chem. Eur. J.*, 29(23):e202203980, 2023.

[60] Nora Lüdtke, Jelena Föller, and Christel M. Marian. Understanding the luminescence properties of Cu(i) complexes: a quantum chemical perusal. *Phys. Chem. Chem. Phys.*, 22(41):23530–23544, 2020.

[61] Torsten Hölzel, Andrey Belyaev, Meryem Terzi, Laura Stenzel, Markus Gernert, Christel M. Marian, Andreas Steffen, and Christian Ganter. Linear Carbene Pyridine Copper Complexes with Sterically Demanding N, N'-Bis(trityl)imidazolylidene: Syntheses, Molecular Structures, and Photophysical Properties. *Inorg. Chem.*, 60(23):18529–18543, 2021.

[62] Dietrich Püschel, Simon Hédé, Iván Maisuls, Simon-Patrick Höfert, Dennis Woschko, Ralf Kühnemuth, Suren Felekyan, Claus A. M. Seidel, Constantin Czekelius, Oliver Weingart, Cristian A. Strassert, and Christoph Janiak. Enhanced Solid-State Fluorescence of Flavin Derivatives by Incorporation in the Metal-Organic Frameworks MIL-53 (Al) and MOF-5. *Molecules*, 28(6):2877, 2023.

[63] Dietrich Püschel, Julia Wiefermann, Simon Hédé, Tobias Heinen, Leo Pfeifer, Oliver Weingart, Markus Suta, Thomas J. J. Müller, and Christoph Janiak. Molecular design of phenazine-5, 10-diyl-dibenzonitriles and the impact on their thermally activated delayed fluorescence properties. *J. Mater. Chem. C*, 2023.

[64] Hector Miranda-Salinas, Angela Rodriguez-Serrano, Jeremy M. Kaminski, Fabian Dinkelbach, Nakagawa Hiromichi, Yu Kusakabe, Hironori Kaji, Christel M. Marian, and Andrew P. Monkman. Conformational, Host, and Vibrational Effects Giving Rise to Dynamic TADF Behavior in the Through-Space Charge Transfer, Triptycene Bridged Acridine-Triazine Donor Acceptor TADF Molecule TpAT-tFFO. *J. Phys. Chem. C*, 127(18):8607–8617, 2023.

[65] Kleitos Stavrou, Larissa G. Franca, Tobias Böhmer, Luka M. Duben, Christel M. Marian, and Andrew P. Monkman. Unexpected Quasi-Axial Conformer in Thermally Activated Delayed Fluorescence DMAC-TRZ, Pushing Green OLEDs to Blue. *Adv. Funct. Mater.*, page 2300910, 2023.

[66] Wiebke Haselbach, Jeremy M. Kaminski, Laura N. Kloeters, Thomas J. J. Müller, Oliver Weingart, Christel M. Marian, Peter Gilch, and Barbara E. Nogueira de Faria. A Thermally Activated Delayed Fluorescence Emitter

Investigated by Time-Resolved Near-Infrared Spectroscopy. *Chem. Eur. J.*, 29(2):e202202809, 2023.

[67] Julia Wiefermann, Jeremy M. Kaminski, Elisabeth Pankert, Dirk Hertel, Klaus Meerholz, Christel M. Marian, and Thomas J. J. Müller. Highly Luminescent Blue Emitter with Balanced Hybridized Locally and Charge-Transfer Excited-States Emission. *ChemPhotoChem*, 7(3):e202200265, 2023.

[68] Nora Lüdtke, Andreas Steffen, and Christel M. Marian. Finding Design Principles of OLED Emitters through Theoretical Investigations of Zn(II) Carbene Complexes. *Inorg. Chem.*, 61(51):20896–20905, 2022.

[69] Nora Lüdtke, Julia Kuhnt, Tabea Heil, Andreas Steffen, and Christel M. Marian. Revisiting Ligand-to-Ligand Charge Transfer Phosphorescence Emission from Zinc(II) Diimine Bis-Thiolate Complexes: It is Actually Thermally Activated Delayed Fluorescence. *ChemPhotoChem*, 7(1):e202200142, 2023.

[70] Jeremy M. Kaminski, Angela Rodríguez-Serrano, Fabian Dinkelbach, Hector Miranda-Salinas, Andrew P. Monkman, and Christel M. Marian. Vibronic effects accelerate the intersystem crossing processes of the through-space charge transfer states in the triptycene bridged acridine–triazine donor–acceptor molecule TpAT-tFFO. *Chem. Sci.*, 13(23):7057–7066, 2022.

[71] Susanne Salzmann, Mario R. Silva-Junior, Walter Thiel, and Christel M. Marian. Influence of the LOV Domain on Low-Lying Excited States of Flavin: A Combined Quantum-Mechanics/Molecular-Mechanics Investigation. *J. Phys. Chem. B*, 113(47):15610–15618, 2009.

[72] Irina Dokukina and Oliver Weingart. Spectral properties and isomerisation path of retinal in C1C2 channelrhodopsin. *Phys. Chem. Chem. Phys.*, 17(38): 25142–25150, 2015.

[73] Setsuko Nakagawa, Oliver Weingart, and Christel M. Marian. Dual Photochemical Reaction Pathway in Flavin-Based Photoreceptor LOV Domain: A Combined Quantum-Mechanics/Molecular-Mechanics Investigation. *J. Phys. Chem. B*, 121(41):9583–9596, 2017.

[74] Mario R. Silva-Junior, Marko Schreiber, Stephan P. A. Sauer, and Walter Thiel. Benchmarks for electronically excited states: Time-dependent density functional theory and density functional theory based multireference configuration interaction. *J. Chem. Phys.*, 129(10):104103, 2008.

[75] Daniel Escudero and Walter Thiel. Assessing the density functional theory-based multireference configuration interaction (DFT/MRCI) method for transition metal complexes. *J. Chem. Phys.*, 140(19):194105, 05 2014. ISSN 0021-9606. doi: 10.1063/1.4875810. URL `https://doi.org/10.1063/1.4875810`.

[76] Vladimir Jovanović, Igor Lyskov, Martin Kleinschmidt, and Christel M. Marian. On the performance of DFT/MRCI-R and MR-MP2 in spin-orbit coupling calculations on diatomics and polyatomic organic molecules. *Mol. Phys*, 115: 109–137, 2016. doi: 10.1080/00268976.2016.1201600.

[77] Baimei Shi, Dana Nachtigallová, Adélia J. A. Aquino, Francisco B. C. Machado, and Hans Lischka. Excited states and excitonic interactions in prototypic polycyclic aromatic hydrocarbon dimers as models for graphitic interactions in carbon dots. *Phys. Chem. Chem. Phys.*, 21(18):9077–9088, 2019.

[78] Baimei Shi, Dana Nachtigallová, Adélia J. A. Aquino, Francisco B. C. Machado, and Hans Lischka. High-level theoretical benchmark investigations of the UV-vis absorption spectra of paradigmatic polycyclic aromatic hydrocarbons as models for graphene quantum dots. *J. Chem. Phys.*, 150(12), 2019.

[79] Igor Lyskov. *Redesign and Reparameterization of the DFT/MRCI Hamiltonian and its Application to Electronically Excited Linear Polyenes*. PhD thesis, Heinrich-Heine-Universität Düsseldorf, 2016.

[80] Adrian Heil. *Development and Implementation of New DFT/MRCI Hamiltonians for Odd and Even Numbers of Electrons*. PhD thesis, Heinrich-Heine-Universität Düsseldorf, 2019.

[81] Frank Jensen. *Introduction to Computational Chemistry 2nd Edition*. John wiley & sons, 2007.

[82] Attila Szabo and Neil S. Ostlund. *Modern Quantum Chemistry: Introduction to Advanced electronic structure theory*. Dover Publications, 1996.

[83] Dieter Cremer. From configuration interaction to coupled cluster theory: The quadratic configuration interaction approach. *WIREs Comput Mol Sci*, 3(5): 482–503, 2013.

[84] Ross W. Wetmore and Gerald A. Segal. Efficient generation of configuration interaction matrix elements. *Chem. Phys. Lett.*, 36(4):478–483, 1975.

[85] Gerald A. Segal, Ross W. Wetmore, and Kathleen Wolf. Efficient methods for configuration interaction calculations. *Chem. Phys.*, 30(2):269–297, 1978.

[86] Llewellyn H. Thomas. The calculation of atomic fields. In *Math. Proc. Cambridge Philos. Soc.*, volume 23, pages 542–548. Cambridge University Press, 1927.

[87] Enrico Fermi. Eine statistische Methode zur Bestimmung einiger Eigenschaften des Atoms und ihre Anwendung auf die Theorie des periodischen Systems der Elemente. *Z. Phys.*, 48(1-2):73–79, 1928.

[88] Paul A. M. Dirac. Note on Exchange Phenomena in the Thomas Atom. In *Math. Proc. Cambridge Philos. Soc.*, volume 26, pages 376–385. Cambridge University Press, 1930.

[89] Pierre Hohenberg and Walter Kohn. Inhomogeneous electron gas. *Phys. Rev.*, 136(3B):B864, 1964.

[90] Robert G. Parr and Yang Weitao. *Density-Functional Theory of Atoms and Molecules*. Oxford University Press, USA, 1994. ISBN 0195092767.

[91] Walter Kohn and Lu Jeu Sham. Self-consistent equations including exchange and correlation effects. *Phys. Rev.*, 140(4A):A1133, 1965.

[92] Wofram Koch and Max C. Holthausen. *A Chemist's Guide to Density Functional Theory*. WILEY-VCH, 2001.

[93] Dieter Cremer, Michael Filatov, Victor Polo, Elfi Kraka, and Sason Shaik. Implicit and Explicit Coverage of Multi-reference Effects by Density Functional Theory. *Int. J. Mol. Sci.*, 3(6):604–638, 2002.

[94] Chengteh Lee, Weitao Yang, and Robert G Parr. Development of the Colle-Salvetti correlation-energy formula into a functional of the electron density. *Phys. Rev. B*, 37(2):785, 1988.

[95] Dieter Cremer. Density functional theory: coverage of dynamic and non-dynamic electron correlation effects. *Mol. Phys.*, 99(23):1899–1940, 2001.

[96] Axel D. Becke. A new mixing of Hartree–Fock and local density-functional theories. *J. Chem. Phys.*, 98(2):1372–1377, 1993.

[97] Paul A. M. Dirac. Quantum mechanics of many-electron systems. *Proc. R. Soc. London, Ser. A*, 123(792):714–733, 1929.

[98] John C. Slater. A simplification of the Hartree-Fock method. *Phys. Rev.*, 81 (3):385, 1951.

[99] Axel D. Becke. Density-functional exchange-energy approximation with correct asymptotic behavior. *Phys. Rev. A*, 38(6):3098, 1988.

[100] John P. Perdew, Matthias Ernzerhof, and Kieron Burke. Rationale for mixing exact exchange with density functional approximations. *J. Chem. Phys.*, 105 (22):9982–9985, 1996.

[101] Carlo Adamo and Vincenzo Barone. Toward reliable density functional methods without adjustable parameters: The PBE0 model. *J. Chem. Phys.*, 110 (13):6158–6170, 1999.

[102] John P. Perdew, Kieron Burke, and Matthias Ernzerhof. Generalized Gradient Approximation Made Simple. *Phys. Rev. Lett.*, 77(18):3865, 1996.

[103] John P. Perdew and Yue Wang. Accurate and simple analytic representation of the electron-gas correlation energy. *Phys. Rev. B*, 45(23):13244, 1992.

[104] Axel D. Becke. Density-functional thermochemistry. III. The role of exact exchange. *J. Chem. Phys*, 98(7):5648–5652, 04 1993. ISSN 0021-9606. doi: 10.1063/1.464913. URL `https://doi.org/10.1063/1.464913`.

[105] Philip J. Stephens, Frank J. Devlin, Cary F. Chabalowski, and Michael J. Frisch. *Ab Initio* Calculation of Vibrational Absorption and Circular Dichroism Spectra Using Density Functional Force Fields. *J. Phys. Chem.*, 98(45): 11623–11627, 1994.

[106] Seymour H. Vosko, Leslie Wilk, and Marwan Nusair. Accurate spin-dependent electron liquid correlation energies for local spin density calculations: a critical analysis. *Can. J. Phys.*, 58(8):1200–1211, 1980.

[107] Yan Zhao and Donald G. Truhlar. Comparative DFT Study of van der Waals Complexes: Rare-Gas Dimers, Alkaline-Earth Dimers, Zinc Dimer, and Zinc-Rare-Gas Dimers. *J. Phys. Chem. A*, 110(15):5121–5129, 2006.

[108] Yan Zhao and Donald G. Truhlar. Density Functional for Spectroscopy: No Long-Range Self-Interaction Error, Good Performance for Rydberg and Charge-Transfer States, and Better Performance on Average than B3LYP for Ground States. *J. Phys. Chem. A*, 110(49):13126–13130, 2006.

[109] Ulf Ekström, Lucas Visscher, Radovan Bast, Andreas J. Thorvaldsen, and Kenneth Ruud. Arbitrary-order density functional response theory from automatic differentiation. *J. Chem. Theory Comput.*, 6(7):1971–1980, 2010.

[110] Dale R. Lonsdale and Lars Goerigk. The one-electron self-interaction error in 74 density functional approximations: a case study on hydrogenic mono-and dinuclear systems. *Phys. Chem. Chem. Phys.*, 22(28):15805–15830, 2020.

[111] Yves A. Bernard, Yihan Shao, and Anna I. Krylov. General formulation of spin-flip time-dependent density functional theory using non-collinear kernels: Theory, implementation, and benchmarks. *J. Chem. Phys.*, 136(20), 2012.

[112] J. A. Nelder and R. Mead. A Simplex Method for Function Minimization. *Comput. J.*, 7:308–313, 1965. doi: 10.1093/comjnl/7.4.308.

[113] Igor Lyskov, Martin Kleinschmidt, and Christel M. Marian. Redesign of the DFT/MRCI Hamiltonian. *J. Chem. Phys*, 144:034104, 2016. doi: 10.1063/1.4940036.

[114] Adrian Heil and Christel M. Marian. DFT/MRCI Hamiltonian for odd and even numbers of electrons. *J. Chem. Phys*, 147:194104, 2017. doi: 10.1063/1.5003246.

[115] Adrian Heil, Martin Kleinschmidt, and Christel M. Marian. On the performance of DFT/MRCI Hamiltonians for electronic excitations in transition metal complexes: The role of the damping function. *J. Chem. Phys*, 149: 164106, 2018. doi: 10.1063/1.5050476.

[116] TURBOMOLE V7.4 2019, a development of University of Karlsruhe and Forschungszentrum Karlsruhe GmbH, 1989-2007, TURBOMOLE GmbH, since 2007; available from
`http://www.turbomole.com` (visited on 01/23/23).

[117] Sree Ganesh Balasubramani, Guo P. Chen, Sonia Coriani, Michael Diedenhofen, Marius S. Frank, Yannick J. Franzke, Filipp Furche, Robin Grotjahn, Michael E. Harding, Christof Hättig, Arnim Hellweg, Benjamin Helmich-Paris, Christof Holzer, Uwe Huniar, Martin Kaupp, Alireza Marefat Khah, Sarah Karbalaei Khani, Thomas Müller, Fabian Mack, Brian D. Nguyen, Shane M. Parker, Eva Perlt, Dmitrij Rappoport, Kevin Reiter, Saswata Roy, Matthias Rückert, Gunnar Schmitz, Marek Sierka, Enrico Tapavicza, David P. Tew, Christoph van Wüllen, Vamsee K. Voora, Florian Weigend, Artur Wodyński, and Jason M. Yu. TURBOMOLE: Modular program suite for *ab initio* quantum-chemical and condensed-matter simulations. *J. Chem. Phys.*, 152: 184107, 2020. doi: 10.1063/5.0004635. URL `https://doi.org/10.1063/5.0004635`.

[118] Mark E. Casida, Christine Jamorski, Kim C. Casida, and Dennis R. Salahub. Molecular excitation energies to high-lying bound states from time-dependent density-functional response theory: Characterization and correction of the time-dependent local density approximation ionization threshold. *J. Chem. Phys.*, 108(11):4439–4449, 1998.

[119] R. Van Meer, O. V. Gritsenko, and E. J. Baerends. Physical meaning of virtual Kohn–Sham orbitals and orbital energies: an ideal basis for the description of molecular excitations. *J. Chem. Theory Comput.*, 10(10):4432–4441, 2014.

[120] Stefan Grimme. Density functional calculations with configuration interaction for the excited states of molecules. *Chem. Phys. Lett.*, 259(1-2):128–137, 1996.

[121] Ferdinand Vogeler, Swen Siegert, Christel M. Marian, and Rainer Weinkauf. T_1, T_2 State Energies and Electron Affinities of Small α, ω-Diphenylpolyenes Investigated by Anion Photodetachment Photoelectron Spectroscopy and Excited-State Theory. *ChemPhysChem*, 12(10):1948–1956, 2011.

[122] Swen Siegert, Ferdinand Vogeler, Christel M. Marian, and Rainer Weinkauf. Throwing light on dark states of α-oligothiophenes of chain lengths 2 to 6: radical anion photoelectron spectroscopy and excited-state theory. *Phys. Chem. Chem. Phys.*, 13(21):10350–10363, 2011.

[123] A. Manian, R. A. Shaw, I. Lyskov, W. Wong, and S. P. Russo. Modeling radiative and non-radiative pathways at both the Franck–Condon and Herzberg–Teller approximation level. *J. Chem. Phys.*, 155(5), 2021.

[124] John R. Platt. Classification of spectra of cata-condensed hydrocarbons. *J. Chem. Phys.*, 17(5):484–495, 1949.

[125] Paul L. Konieczny. *Anionen-Photodetachment-Photoelektronen-Spektroskopie und Gasphasen UV-Vis-Spektroskopie an konjugierten molekularen Systemen.* PhD thesis, Heinrich-Heine-Universität Düsseldorf, 2017.

[126] Bernd Kosper. *Radical-Anion-Photodetachment-Photoelectron-Spectroscopy: Application to a Variety of Molecules with extended π-Systems.* PhD thesis, Heinrich-Heine-Universität Düsseldorf, 2022.

Included Papers

THE JOURNAL OF PHYSICAL CHEMISTRY A
A JOURNAL OF THE AMERICAN CHEMICAL SOCIETY

pubs.acs.org/JPCA Article

R2022: A DFT/MRCI Ansatz with Improved Performance for Double Excitations

Published as part of The Journal of Physical Chemistry virtual special issue "MQM 2022: The 10th Triennial Conference on Molecular Quantum Mechanics".

Dennis R. Dombrowski, Timo Schulz, Martin Kleinschmidt, and Christel M. Marian*

Cite This: *J. Phys. Chem. A* 2023, 127, 2011−2025 Read Online

ACCESS | Metrics & More | Article Recommendations | Supporting Information

ABSTRACT: A reformulation of the combined density functional theory and multireference configuration interaction method (DFT/MRCI) is presented. Expressions for ab initio matrix elements are used to derive correction terms for a new effective Hamiltonian. On the example of diatomic carbon, the correction terms are derived, focusing on the doubly excited $^1\Delta_g$ state, which was problematic in previous formulations of the method, as were double excitations in general. The derivation shows that a splitting of the parameters for intra- and interorbital interactions is necessary for a concise description of the underlying physics. Results for ^1L_a and ^1L_b states in polyacenes and ^1A_u and ^1A_g states in mini-β-carotenoids suggest that the presented formulation is superior to former effective Hamiltonians. Furthermore, statistical analysis reveals that all the benefits of the previous DFT/MRCI Hamiltonians are retained. Consequently, the here presented formulation should be considered as the new standard for DFT/MRCI calculations.

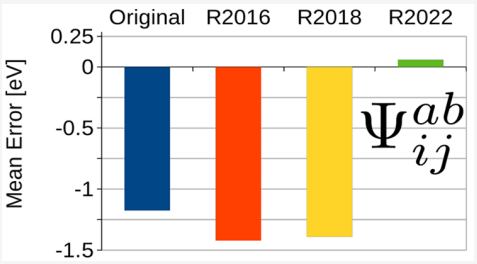

INTRODUCTION

The combined density functional theory and multireference configuration interaction method (DFT/MRCI) is a semi-empirical approach, which makes use of extensive configuration selection and introduces scaling parameters and damping functions to avoid double counting of electron correlation. Since its launch in 1999, it has developed from a powerful electronic structure method for computing spectral properties of singlet and triplet excited states of large molecules into a more general multireference method applicable to states of all spin multiplicities.[1−5] In its original formulation,[1] DFT/MRCI shows great efficiency in the evaluation of singlet and triplet excited states which mainly originate from local one-electron transitions.[6−8] Moreover, it is one of the few methods applicable to large systems that yields the correct ordering of adiabatic states in extended π-systems where double excitations play a significant role.[9−12] The redesigned DFT/MRCI Hamiltonians[2,4,5] extended the application range of the method to excited states of radicals with odd numbers of electrons[13] and to loosely coupled donor−acceptor systems[14−16] that play a central role in energy transfer cassettes and in organic light-emitting diodes based on thermally activated delayed fluorescence. In the course of time, it turned out, however, that certain types of double excitations are not handled well by the DFT/MRCI ansatz. Jovanović et al.[17] described several critical cases, comprising double excitations from nonbonding lone-pair orbitals to π orbitals ($n^2 \rightarrow \pi^{*2}$) and double excitations from different orbitals such as ($n, n' \rightarrow \pi^*\pi^{*\prime}$) or ($\pi, \pi' \rightarrow \pi^*\pi^{*\prime}$). In particular, the energies of doubly excited configurations with four open shells were severely underestimated by the original and redesigned DFT/MRCI Hamiltonians.

However, states of this kind play a key role in singlet fission (SF), the fission of a high-energy singlet exciton into two lower-energy triplet excitons,[18,19] and in triplet−triplet annihilation upconversion (TTA-UC), where low-energy photons are converted to higher-energy photons that can be collected by a solar cell.[20] Both processes are spin-allowed and involve singlet-coupled triplet-pair intermediates, ^{1}(T···T). To accomplish a proper modeling of SF and TTA-UC by quantum chemical methods, a balanced description of singly and doubly excited states is mandatory.[21−25] Doubly excited states also play a pivotal role for the light-harvesting and protective functions of carotenoids in photosynthetic complexes.[26,27] In these compounds, the S_1 state is characterized by a mixture of the two singly excited $\pi_{H-1} \rightarrow \pi_L$ and $\pi_H \rightarrow \pi_{L+1}$ configurations and the doubly excited $\pi_H^2 \rightarrow \pi_L^2$ configuration, while the optically bright S_2 state originates mainly from the $\pi_H \rightarrow \pi_L$ excitation.[28,29] The importance of double excitations is known to increase with growing conjugation lengths N.[30] Experimental results strongly

Received: November 11, 2022
Revised: February 2, 2023
Published: February 17, 2023

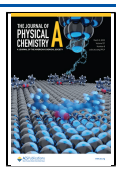

https://doi.org/10.1021/acs.jpca.2c07951
J. Phys. Chem. A 2023, 127, 2011−2025

suggest that in carotenoids with $N \geq 11$, an additional doubly excited dark state is located between S_2 and S_1, which speeds up the deactivation of the S_2 state.[31−35] Furthermore, a proper description of charge transfer states is desirable, since it was recently shown that intramolecular charge transfer (CT) states greatly speed-up the energy transfer to bacteriochlorophyll a.[36]

In this work, we set out for remedying the weaknesses of the previous DFT/MRCI Hamiltonians with regard to double excitations while retaining the good performance for CT, Rydberg, and singly excited states known from the previous formulations.[37−39] We will present a novel ansatz, which differentiates between double excitations involving the same spatial orbital twice and double excitations involving different spatial orbitals. By setting up a relationship between diagonal and off-diagonal corrections only one additional parameter needs to be introduced. After a careful assessment of the new effective Hamiltonian, dubbed R2022, we focus on its performance for two types of extended π-systems, namely, polyacenes and carotenoids, which are well investigated in the literature by other quantum chemical methods.[12,40−44]

THEORY

First we will recapitulate the basic idea of DFT/MRCI before lying focus on the modifications introduced in the R2022 Hamiltonian. In the DFT/MRCI method,[1,3] a Kohn−Sham (KS) one-particle basis and a closed- or single open-shell anchor configuration are used in the construction of the MRCI wave function. An efficient truncation of the CI expansion, without significant loss of accuracy, is achieved by utilizing a simple selection criterion based on orbital energies. The CI wave function is expanded into the basis of configuration state functions (CSFs), denoted $|w\omega\rangle$. Here w denotes the spatial- and ω is the spin-arrangement. To introduce corrections to the MRCI matrix elements, a formulation by Segal, Wetmore, and Wolf[45,46] was chosen. The latter groups the CI matrix into three different cases:

1. Diagonal elements with same spatial occupations

$$\begin{aligned}\langle \omega w|\hat{\mathcal{H}}^{\mathrm{CI}}|\omega w\rangle = {} & E^{\mathrm{HF}} + \sum_i F_{ii}\Delta w_i + \frac{1}{2}\sum_{i\neq j} V_{iijj}\Delta w_i \Delta w_j \\ & + \frac{1}{2}\sum_{i\neq j} V_{ijji}\left(-\frac{1}{2}\Delta w_i \Delta w_j + \frac{1}{2}w_i w_j - w_i + \eta_{ij}^{ji}\right) \\ & + \frac{1}{2}\sum_i V_{iiii}\left(\frac{1}{2}\Delta w_i \Delta w_i + \frac{1}{2}w_i w_i - w_i\right)\end{aligned} \tag{1}$$

2. One-electron occupation differences

$$\begin{aligned}\langle \omega w|\hat{\mathcal{H}}^{\mathrm{CI}}|\omega' w'\rangle = {} & F_{ij}\eta_i^{\ j} + \sum_{k\neq i,j} V_{ikjk}\Delta w'_k \eta_i^{\ j} \\ & + \sum_{k\neq i,j} V_{ikkj}\left(-\frac{1}{2}\Delta w'_k \eta_i^{\ j} + \frac{1}{2}w'_k \eta_i^{\ j} - \eta_i^{\ j} + \eta_{ik}^{kj}\right) \\ & + V_{iiij}\left(\frac{1}{2}\Delta w'_i + \frac{1}{2}w'_i\right)\eta_i^{\ j} \\ & - V_{ijjj}\left(\frac{1}{2}\Delta w'_j + \frac{1}{2}w'_j - 1\right)\eta_i^{\ j}\end{aligned} \tag{2}$$

3. Two-electron occupation differences

$$\langle \omega w|\hat{\mathcal{H}}^{\mathrm{CI}}|\omega'' w''\rangle = (V_{ikjl}\eta_{ik}^{\ jl} + V_{iklj}\eta_{ik}^{\ lj})[(1+\delta_{ik})(1+\delta_{jl})]^{-1} \tag{3}$$

where w_i denotes the occupation number of orbital i in the configuration w, Δw_i is the occupation difference of i with respect to the anchor configuration, η_i^j and η_{ij}^{ji} are the one- and two-electron spin-coupling coefficients, V_{ikjl} is the two-electron integrals $\langle i(1)k(2)|\frac{1}{r_{12}}|j(1)l(2)\rangle$, E^{HF} is the Hartree−Fock energy, F_{ij}^{HF} is the Fock matrix elements, and δ_{ij} is the Kronecker-Delta. In the DFT/MRCI method, a suitable parametrization of the Coulomb- and exchange-integrals for eq 1 as well as an energy-separation dependent scaling of the interacting configurations for eqs 2 and 3 is used to prevent double counting of the dynamical electron correlation. The latter being unquantifiably included in the KS one-particle basis. In the following subsections, we will introduce the corrections applied in DFT/MRCI to these matrix elements.

Diagonal Element Corrections in Previous Hamiltonians. First we concentrate on the corrections to the diagonal matrix elements, which are given in eq 1. They constitute the largest contribution to the MRCI energy because the CI matrix is diagonally dominant. In the DFT/MRCI method, the SCF energy E^{HF} and the diagonal elements of the Fock matrix F_{ii}^{HF}, i.e., the orbital energies in eq 1 are replaced by the KS energy of the anchor configuration E^{KS} and the KS canonical orbital energies F_{ii}^{KS}. Taking the difference of the modified and unmodified elements gives us the expression for a DFT/MRCI diagonal matrix element

$$\begin{aligned}&\langle \omega w|\hat{\mathcal{H}}^{\mathrm{DFT}} - E^{\mathrm{KS}}|\omega w\rangle \\ &= \langle \omega w|\hat{\mathcal{H}}^{\mathrm{CI}}|\omega w\rangle - E^{\mathrm{HF}} - \sum_i \Delta w_i F_{ii}^{\mathrm{HF}} + \sum_i \Delta w_i F_{ii}^{\mathrm{KS}} + \Delta E_{\mathrm{DFTMRCI}}\end{aligned} \tag{4}$$

where $\hat{\mathcal{H}}^{\mathrm{DFT}}$ denotes the modified Hamiltonian and $\Delta E_{\mathrm{DFTMRCI}}$ collects all empirical correction terms. Note that $-E^{\mathrm{HF}}$ and $-\sum_i \Delta w_i F_{ii}^{\mathrm{HF}}$ occur in $\langle \omega w|\hat{\mathcal{H}}^{\mathrm{CI}}|\omega w\rangle$ with opposite signs and cancel out. The two-electron correction terms collected in $\Delta E_{\mathrm{DFTMRCI}}$ constitute the major difference between the DFT/MRCI Hamiltonians and will be presented in the following. For the original Hamiltonian,[1] $\Delta E_{\mathrm{DFTMRCI}}$ is given by

$$\Delta E_{\mathrm{DFTMRCI}} = \frac{1}{n_{\mathrm{exc}}}\sum_{i\in c}^{n_{\mathrm{exc}}}\sum_{j\in a}^{n_{\mathrm{exc}}}(p_J V_{ijij} - {}^m p[N_o]V_{ijji}) \tag{5}$$

with p_J as the parameter for Coulomb- and ${}^m p[N_o]$ as the parameter for exchange-integral scaling. n_{exc} labels the excitation class and c and a denote creation and annihilation operators, respectively. ${}^m p[N_o]$ depends on the number of open shells N_o and takes different forms depending on the multiplicity m. The general idea of the original Hamiltonian is to express the correction term as an averaged sum of single excitation contributions. Note that this is also reflected in the summation over creation and annihilation operators applied to the anchor configuration. This is in contrast to the formulation in eq 1, where the summation is over orbitals. While the summation over operators has been partially retained in the redesigned Hamiltonians, although for different reasons, we chose to return to the summation over orbitals. The reason for this choice will become apparent shortly. In contrast to the original Hamiltonian, the redesigned Hamiltonians R2016,[2] R2017,[4] and R2018[5] correct the integrals according to their occurrence in the ab initio diagonal element. Furthermore, the dependency on a closed-shell anchor configuration and the multiplicity depend-

https://doi.org/10.1021/acs.jpca.2c07951
J. Phys. Chem. A 2023, 127, 2011−2025

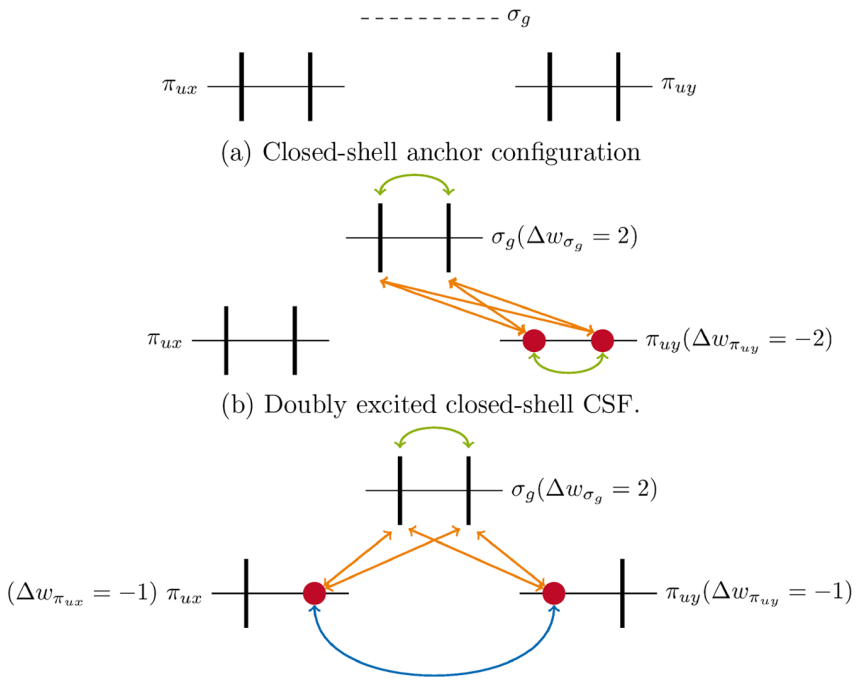

Figure 1. Possible double excitations in the valence orbitals of diatomic carbon. The black, thick, vertical lines symbolize electrons, the red circles symbolize holes. Interorbital interactions between electrons and holes are symbolized with a blue arrow. Intraorbital interactions between electrons or holes are marked with a green arrow, while the interactions between holes and electrons are symbolized with an orange arrow. In the parentheses, the change of occupation number, Δw_i w.r.t. the anchor configuration is given.

ence of the parameters were lifted. The R2017 and R2018 diagonal corrections are given by

$$\Delta E_{\mathrm{DFTMRCI}} = p_J\left(-\sum_{\substack{i,j\in c\\ i>j}}^{n_{\mathrm{exc}}} V_{ijij} - \sum_{\substack{i,j\in a\\ i>j}}^{n_{\mathrm{exc}}} V_{ijij} + \sum_{i\in c}^{n_{\mathrm{exc}}}\sum_{j\in a}^{n_{\mathrm{exc}}} V_{ijij} + \frac{1}{2}\sum_{i\in s}^{n_{\mathrm{single}}} V_{iiii}|\Delta w_i|\right) - p_x\left(\frac{1}{2}\sum_{i\in c}^{n_{\mathrm{exc}}}\sum_{j\in a}^{n_{\mathrm{exc}}} V_{ijji} - \frac{1}{2}\sum_{\substack{i\in c\\ j\in c,s}} V_{ijji} - \frac{1}{2}\sum_{\substack{i\in a\\ j\in a,s}} V_{ijji} + \sum_{\substack{i,j\in o\\ i>j}}^{N_o} V_{ijji}\eta_{ij}^{ji}\right) \tag{6}$$

Here, s denotes an open shell in the anchor configuration and p_x is the exchange integral correction parameter. Since the only difference to the R2016 formulation is the summations over the singly occupied orbitals in the anchor configuration, we refrain from repeating it here.

Derivation of the New Hamiltonian. In the newly proposed R2022 Hamiltonian, the two-electron correction parameters p_J and p_x of the former Hamiltonians are subdivided into cases in which different interactions are considered. The proposed ansatz is motivated by the physical nature of these interactions, which were averaged (eq 5) or not considered (eq 6) in previous formulations. We will illustrate the underlying idea with an example. Consider four electrons in three orbitals and an exemplary double excitation between them. As sketched in the valence MO diagram of diatomic carbon shown in Figure 1, one can roughly divide this situation into two cases, depicted in Figure 1b and c.

In one case, the two particles and holes, both reside in the same spatial orbital, leading to an intraorbital interaction (green arrows in Figure 1b). In the other case, the two particles and holes, reside in different spatial orbitals, leading to an interorbital interaction (blue arrows in Figure 1c). Dynamical correlation effects are expected to be larger in the intraorbital case, since the averaged distance between the interacting quantities is expected to be smaller, hence, the interaction is short-ranged. Therefore, it is advisable to use different scaling parameters for these interactions in the DFT/MRCI Hamiltonian. To derive an expression for such parameters, it is instructive to equip the expressions for the ab inito matrix elements with an arbitrary set of parameters q

$$\begin{aligned}\langle \omega w|\hat{\mathcal{H}}^{\mathrm{DFT}}|\omega w\rangle = {} & \sum_i F_{ii}\Delta w_i + \frac{1}{2}(1-q_J^{he}) \sum_{\substack{i\neq j\\ \Delta w_i\Delta w_j<0}} V_{ijij}\Delta w_i\Delta w_j \\ & + \frac{1}{2}(1-q_J^{hhee}) \sum_{\substack{i\neq j\\ \Delta w_i\Delta w_j>0}} V_{ijij}\Delta w_i\Delta w_j \\ & + \frac{1}{2}(1-q_x^{he}) \sum_{\substack{i\neq j\\ \Delta w_i\Delta w_j<0}} V_{ijji}\left(-\frac{1}{2}\Delta w_i\Delta w_j + \frac{1}{2}w_iw_j - w_i + \eta_{ij}^{ji}\right) + \frac{1}{2}(1-q_x^{hhee}) \sum_{\substack{i\neq j\\ \Delta w_i\Delta w_j>0}} V_{ijji} \\ & \times\left(-\frac{1}{2}\Delta w_i\Delta w_j + \frac{1}{2}w_iw_j - w_i + \eta_{ij}^{ji}\right) \\ & + \frac{1}{2}(1-q_J^{eeee}) \sum_i V_{iiii}\left(\frac{1}{2}\Delta w_i\Delta w_i + \frac{1}{2}w_iw_i - w_i\right)\end{aligned} \tag{7a}$$

https://doi.org/10.1021/acs.jpca.2c07951
J. Phys. Chem. A 2023, 127, 2011−2025

$$\langle \omega w|\hat{\mathcal{H}}^{\mathrm{DFT}}|\omega' w'\rangle = q_1 \cdot \langle \omega w|\hat{\mathcal{H}}^{\mathrm{CI}}|\omega' w'\rangle \tag{7b}$$

where we have split the second and third sums in eq 1 according to the signs of the $\Delta w_i \Delta w_j$ terms in eq 7a because they represent different cases, as illustrated in Figure 1. If two electrons are annihilated in different spatial orbitals, one will always get a positive sign (Figure 1c). This case is labeled *hhee*, where *h* denotes an electron hole and *e* denotes a particle. The other possible case (Figure 1b) in which electrons annihilated in the same spatial orbital, always leads to a negative sign and is labeled *he*.

To yield an expression for the parameters in eq 7, we will investigate the doubly degenerate $1\,^1\Delta_g$ state of diatomic carbon. The valence configuration in its $^1\Sigma_g^+$ ground state is given as $\pi_{u_x}^2 \pi_{u_y}^2 \sigma_g^0$. In a first approximation, one component Θ_1 is built from a linear combination of the two CSFs $|xx\rangle$ and $|yy\rangle$, whose spatial configurations are given by $\pi_{u_x}^2 \pi_{u_y}^0 \sigma_g^2$ and $\pi_{u_x}^0 \pi_{u_y}^2 \sigma_g^2$. The other component Θ_2 contains one CSF $|xy\rangle$, whose spatial configuration is given as $\pi_{u_x}^1 \pi_{u_y}^1 \sigma_g^2$. The energetic degeneracy condition requires $E(\Theta_1) = E(\Theta_2)$. Contained in these two quantities are the matrix elements shown in eq 8 for a generalized Hamiltonian $\hat{\mathcal{H}}^{\mathrm{DFT}}$.

$$\begin{aligned} E(\Theta_1) &= \frac{1}{2}\langle xx|\hat{\mathcal{H}}^{\mathrm{DFT}}|xx\rangle + \frac{1}{2}\langle yy|\hat{\mathcal{H}}^{\mathrm{DFT}}|yy\rangle - \langle xx|\hat{\mathcal{H}}^{\mathrm{DFT}}|yy\rangle \\ &= \langle xx|\hat{\mathcal{H}}^{\mathrm{DFT}}|xx\rangle - \langle xx|\hat{\mathcal{H}}^{\mathrm{DFT}}|yy\rangle \end{aligned} \tag{8a}$$

$$E(\Theta_2) = \langle xy|\hat{\mathcal{H}}^{\mathrm{DFT}}|xy\rangle \tag{8b}$$

The energetic degeneracy condition thus becomes

$$\langle xy|\hat{\mathcal{H}}^{\mathrm{DFT}}|xy\rangle = \langle xx|\hat{\mathcal{H}}^{\mathrm{DFT}}|xx\rangle - \langle xx|\hat{\mathcal{H}}^{\mathrm{DFT}}|yy\rangle \tag{9}$$

where the right-hand side has been simplified, using $\langle xx|\hat{\mathcal{H}}^{\mathrm{DFT}}|xx\rangle = \langle yy|\hat{\mathcal{H}}^{\mathrm{DFT}}|yy\rangle$. Inserting the expressions for $\hat{\mathcal{H}}^{\mathrm{DFT}}$ (eq 7) into eq 9 and using the equality of terms $F_{xx} = F_{yy}$, $V_{x\sigma x\sigma} = V_{y\sigma y\sigma}$, and $V_{x\sigma\sigma x} = V_{y\sigma\sigma y}$ leads to

$$(1 - q_J^{hhee})V_{xyxy} + (1 - q_x^{hhee})V_{xyyx} = (1 - q_J^{eeee})V_{xxxx} - q_1 V_{xyyx} \tag{10}$$

In the ab initio case, the integrals are in a fixed relationship, i.e.,

$$V_{xyxy} + V_{xyyx} = V_{xxxx} - V_{xyyx} \Leftrightarrow V_{xyxy} + 2V_{xyyx} = V_{xxxx} \tag{11}$$

Using this relation, we can eliminate one Coulomb integral in eq 10, giving

$$\begin{aligned} &(1 - q_J^{hhee})V_{xyxy} + (1 - q_x^{hhee})V_{xyyx} = (1 - q_J^{eeee})(V_{xyxy} + 2V_{xyyx}) - q_1 V_{xyyx} \\ &\Leftrightarrow (-q_J^{hhee} + q_J^{eeee})V_{xyxy} = (2\cdot(1 - q_J^{eeee}) - (1 - q_x^{hhee}) - q_1)V_{xyyx} \end{aligned} \tag{12}$$

The degeneracy condition can only be fulfilled if the expressions in the parentheses vanish, yielding the following relations:

$$q_J^{hhee} = q_J^{eeee} \tag{13a}$$

$$q_1 = 1 - 2q_J^{eeee} + q_x^{hhee} = 1 - 2q_J^{hhee} + q_x^{hhee} \tag{13b}$$

The consequences of the equalities in eq 13 are 2-fold. From eq 13a it follows that the parameters scaling the interorbital interactions between two created or two annihilated electrons (blue arrows Figure 1c) need to be treated in the same way as the intraorbital interactions between two created or two annihilated electrons (green arrows Figure 1c). Furthermore, it is evident from eq 13b that a fixed relation between the off-diagonal scaling parameter q_1 in eq 7b and the arbitrary diagonal correction parameters exists. Introducing the canonical KS orbital energies and the KS energy in the spirit of the DFT/MRCI ansatz (eq 4) and returning to the p_J/p_x nomenclature of the former Hamiltonians gives us the final expressions for the diagonal matrix elements of the R2022 Hamiltonian

$$\begin{aligned} \langle \omega w|\hat{\mathcal{H}}^{\mathrm{DFT}}|\omega w\rangle = {} & E^{\mathrm{KS}} + \sum_i F_{ii}^{\mathrm{KS}} \Delta w_i + \frac{1}{2}(1 - p_J^{he}) \sum_{\substack{i\neq j \\ \Delta w_i \Delta w_j < 0}} V_{ijij} \Delta w_i \Delta w_j \\ & + \frac{1}{2}(1 - p_J^{hhee}) \sum_{\substack{i\neq j \\ \Delta w_i \Delta w_j > 0}} V_{ijij} \Delta w_i \Delta w_j \\ & + \frac{1}{2}(1 - p_x^{he}) \sum_{\substack{i\neq j \\ \Delta w_i \Delta w_j < 0}} V_{ijji}\left(-\frac{1}{2}\Delta w_i \Delta w_j + \frac{1}{2} w_i w_j - w_i + \eta_{ij}^{ji}\right) \\ & + \frac{1}{2}(1 - p_x^{hhee}) \sum_{\substack{i\neq j \\ \Delta w_i \Delta w_j > 0}} V_{ijji} \times \left(-\frac{1}{2}\Delta w_i \Delta w_j + \frac{1}{2} w_i w_j - w_i + \eta_{ij}^{ji}\right) \\ & + \frac{1}{2}(1 - p_J^{eeee}) \sum_{i\notin s} V_{iiii}\left(\frac{1}{2}\Delta w_i \Delta w_i + \frac{1}{2} w_i w_i - w_i\right) \\ & + \frac{1}{4}(1 - p_J^{he}) \sum_{i\in s} V_{iiii}|\Delta w_i| + \frac{1}{4} p_x^{he} \sum_{\substack{i\neq j \\ \Delta w_i \Delta w_j < 0 \\ i,j\notin s}} V_{ijji} \Delta w_i \Delta w_j \end{aligned} \tag{14}$$

and a relation between them on the one side and the off-diagonal matrix elements on the other side for the case where the interacting configurations w and w' are energetically degenerate. The last term in eq 14 constitutes a correction term necessary to compute accurate results for triplet states. A thorough discussion of this term is given by Lyskov et al.[2]

To be consistent with the corrections in the diagonal elements, the parameter p_x scaling the matrix elements between different CSFs of the same configuration in the redesigned Hamiltonians is partitioned into p_x^{hhee} and p_x^{he} for R2022 in the same fashion, yielding

$$\begin{aligned} \langle w\omega|\hat{\mathcal{H}}^{\mathrm{DFT}}|w\omega'\rangle = {} & \frac{1}{2}(1 - p_x^{he}) \sum_{\substack{i\neq j \\ \Delta w_i \Delta w_j < 0}} V_{ijji} \eta_{ij}^{ji} + \frac{1}{2}(1 - p_x^{hhee}) \\ & \times \sum_{\substack{i\neq j \\ \Delta w_i \Delta w_j > 0}} V_{ijji} \eta_{ij}^{ji} \end{aligned} \tag{15}$$

Matrix elements coupling different configurations are scaled and damped in the R2022 Hamiltonian according to

$$\langle w\omega|\hat{\mathcal{H}}^{\mathrm{DFT}}|w'\omega'\rangle = p_1 \cdot \exp(-p_2 \cdot \Delta E_{ww'}^4) \cdot \langle w\omega|\hat{\mathcal{H}}^{\mathrm{CI}}|w'\omega'\rangle \tag{16}$$

where

$$p_1 = 1 - 2p_J^{hhee} + p_x^{hhee} \tag{17}$$

and $\Delta E_{ww'}$ denotes the energy difference between the diagonal elements of two interacting configurations. The energy-dependent damping is needed in the first place because interactions between two energetically distant CSFs contribute to the dynamical correlation, which is accounted for in DFT as well. The discussion of the degeneracy requirements for the $^1\Delta_g$ components of the C_2 molecule has taught us, however, that the

https://doi.org/10.1021/acs.jpca.2c07951
J. Phys. Chem. A 2023, 127, 2011−2025

parameter p_1 scaling the off-diagonal DFT/MRCI matrix elements ought not to be treated as an indepedent fit parameter. To avoid symmetry breaking of the $^1\Delta_g$ state, we eliminate p_1 in eq 16 and replace it by diagonal correction parameters yielding the final expression for the off-diagonal R2022 matrix elements

$$\langle w\omega|\hat{\mathcal{H}}^{\mathrm{DFT}}|w'\omega'\rangle = (1 - 2p_J^{hhee} + p_x^{hhee})\cdot\exp(-p_2\cdot\Delta E_{ww'}^4)\cdot\langle w\omega|\hat{\mathcal{H}}^{\mathrm{CI}}|w'\omega'\rangle \tag{18}$$

As the attentive reader might have noticed, the damping function used in eq 18 is similar to the one used in the original Hamiltonian. For the R2018 Hamiltonian, a damping function of the form $p_1\cdot\exp(-p_2\cdot\Delta E_{ww'}^6)$ had been used because the parametrization of the redesigned Hamiltonians in conjunction with an exponential damping depending on $\Delta E_{ww'}^4$ led to a too steep decline in the region of $\Delta E = 0.45E_h$. Comparison of the damping function profiles of the DFT/MRCI Hamiltonians (Figure 2), parametrized for a standard selection threshold E_{sel}

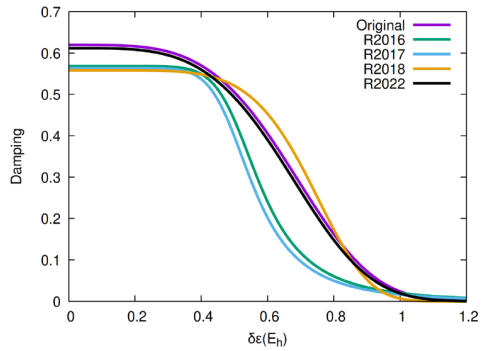

Figure 2. Damping decay for different Hamiltonians for the standard selection threshold $E_{sel} = 1.0E_h$ as a function of the energy difference.

of $1.0E_h$, shows that this is not the case for the R2022 Hamiltonian. Therefore, we decided to switch back to the function used in the original Hamiltonian.

A major advantage of the new formulation is that all terms contributing to the ab initio diagonal elements (eq 1) are corrected, which was not the case for the previous DFT/MRCI Hamiltonians. Let us consider the occurrence of the $V_{\pi_{ux}\pi_{uy}\pi_{uy}\pi_{ux}}$ term, i.e., the exchange interaction between the π electrons in Figure 1c, in the diagonal matrix elements. In this particular case, $w_{\pi_{ux}} = w_{\pi_{uy}} = 1$, and $\Delta w_{\pi_{ux}} = \Delta w_{\pi_{uy}} = -1$, since we start from a closed-shell anchor configuration (Figure 1a). The ab initio matrix element (eq 1) thus becomes

$$\begin{aligned} &V_{\pi_{ux}\pi_{uy}\pi_{uy}\pi_{ux}}\left(-\frac{1}{2}\Delta w_{\pi_{ux}}\Delta w_{\pi_{uy}} + \frac{1}{2}w_{\pi_{ux}}w_{\pi_{uy}} - w_{\pi_{ux}} + \eta_{\pi_{ux}\pi_{uy}}^{\pi_{uy}\pi_{ux}}\right) \\ &= V_{\pi_{ux}\pi_{uy}\pi_{uy}\pi_{ux}}\left(-\frac{1}{2}(-1)(-1) + \frac{1}{2}(1)(1) - (1) + \eta_{\pi_{ux}\pi_{uy}}^{\pi_{uy}\pi_{ux}}\right) \\ &= V_{\pi_{ux}\pi_{uy}\pi_{uy}\pi_{ux}}(-1 + \eta_{\pi_{ux}\pi_{uy}}^{\pi_{uy}\pi_{ux}}) \end{aligned} \tag{19}$$

where the symmetry relations between the integrals have been exploited. Evaluating the correction terms for this same example of the redesigned Hamiltonians of eq 6 shows that only one term

$$-p_x V_{\pi_{ux}\pi_{uy}\pi_{uy}\pi_{ux}}\eta_{\pi_{ux}\pi_{uy}}^{\pi_{uy}\pi_{ux}} \tag{20}$$

contributes, because the occupation numbers and their respective changes are not included in the correction. The missing term in comparison to eq 19 is apparent right away. Carrying out the same calculation for the R2022 Hamiltonian yields

$$\begin{aligned} &-p_x^{hhee}V_{\pi_{ux}\pi_{uy}\pi_{uy}\pi_{ux}}\left(-\frac{1}{2}\Delta w_{\pi_{u_x}}\Delta w_{\pi_{u_y}} + \frac{1}{2}w_{\pi_{u_x}}w_{\pi_{u_y}} - w_{\pi_{u_x}} + \eta_{\pi_{ux}\pi_{uy}}^{\pi_{uy}\pi_{ux}}\right) \\ &= -p_x^{hhee}V_{\pi_{ux}\pi_{uy}\pi_{uy}\pi_{ux}}\left(-\frac{1}{2}(-1)(-1) + \frac{1}{2}(1)(1) - (1) + \eta_{\pi_{ux}\pi_{uy}}^{\pi_{uy}\pi_{ux}}\right) \\ &= -p_x^{hhee}V_{\pi_{ux}\pi_{uy}\pi_{uy}\pi_{ux}}(-1 + \eta_{\pi_{ux}\pi_{uy}}^{\pi_{uy}\pi_{ux}}) \end{aligned} \tag{21}$$

where all integrals occurring in eq 19 are corrected. We want to stress again that, contrary to previous formulations,[1,2,4,5] the corrections in eq 14 are expressed in terms of molecular orbitals instead of annihilated and created electrons. This formulation emphasizes the influence of each term in the diagonal element and ensures that no integral is left uncorrected.

Computational Details. For most of the molecules contained in the fitting or assessment sets, the nuclear coordinates were taken from previous works[2,4,5,10,17,47] (see section S4 of the SI for further information). The geometries of the remaining compounds were optimized using the using the Turbomole package.[48,49] Unless stated otherwise, the optimizations were carried out on the DFT level employing the B3-LYP functional[50−52] together with Grimme's D3 correction[53] with Becke and Johnson damping.[54] The BH-LYP[55] functional in conjunction with a basis of triple-ζ quality, was used to generate the one-particle basis for DFT/MRCI calculations, except for some transition metals and larger molecules. A complete list of the used basis sets can be found in Tables S22−S25 of the SI. The orbital basis for molecules with doublet ground state was generated from restricted open-shell Kohn−Sham (ROKS) DFT calculations using the Dalton program.[56] The frozen (anti)core approximation has been applied throughout, consequently considering only orbitals with an energy ϵ of $-10.0E_h < \epsilon < 2.0E_h$. The reference space was generated iteratively using all configurations with coefficients larger than 0.003, starting from a carefully selected active space. A complete list of the starting active spaces can be found in Tables S27 and S28 of the SI. The number of selected configurations and CSFs is given in Tables S27 and S28 for the standard and tight selection thresholds, respectively.

Reference values for the assessment of the critical double excitation cases were generated using the second order fully internally contracted n-electron valence state perturbation theory (FIC-NEVPT2)[57−59] based on a complete-active space self-consistent field (CASSCF) wave function,[60−62] as implemented in the Orca 5.0[63] program. For all FIC-NEVPT2 calculations, the resolution of the identity (RI-JK) approximation was used. The auxiliary basis sets were generated using the AutoAux generation procedure.[64] In the state-averaging procedure, the required number of states from one irrep is used together with the ground state. The CAS spaces were set up to contain the most important orbitals as determined by a foregoing DFT/MRCI calculation. Further details on the CAS spaces can be found in Table S19 of the SI.

RESULTS AND DISCUSSION

Parameter Optimization. The parameters were optimized as described in ref 5. Using the Nelder−Mead simplex algorithm,[65] five parameters were fitted to give the lowest root mean-square deviation (RMSD) in the fitting set. The former fitting set was altered to reduce the computation time and to correct for errors, e.g., some doublet states were removed since

https://doi.org/10.1021/acs.jpca.2c07951
J. Phys. Chem. A 2023, 127, 2011−2025

their use in the parametrization was found to barely influence the resulting parameters, as one can see from the parameter differences in Table S1 between R2016 and R2017. All corrections made are indicated in the respective tables in the SI. To tune the newly introduced parameters for doubly excited states, 12 theoretical best estimates (TBEs) from Loos et al.[47] as well as two experimental energies of doubly excited states in hexatriene[66] and the magnesium atom[67] were added, leading to a training set comprising 55 singlet and 29 triplet states. A detailed list of all used states can be found in Tables S9−S18 of the SI. As in the case of the former Hamiltonians, two different parameter sets for the standard (E_{sel} = 1.0E_h) and the tight selection threshold (E_{sel} = 0.8E_h) were optimized (Table 1).

Table 1. Parameter Sets Optimized for the Standard and Tight Selection Thresholds of E_{sel} = 1.0E_h and E_{sel} = 0.8E_h

E_{sel} (E_h)	p_2	p_J^{he}	p_J^{hhee}	p_x^{he}	p_x^{hhee}
1.0	3.4673	0.5085	0.4649	0.3426	0.5416
0.8	4.5957	0.5051	0.4610	0.3375	0.5414

Note that the effective selection threshold T_{sel} for the inclusion of a configuration in the CI space is determined by adding the E_{sel} value to the excitation energy of the highest root in the reference space. Typical values for T_{sel} range between 1.2 and 1.35E_h for the standard parameter set and between 1.0 and 1.15E_h for the tight selection threshold.

The RMSDs and mean deviations of all states in the fitting set and its subsets are displayed in Figures 3 and 4. The corresponding numerical values are listed in Table S3 of the SI. The RMSDs and mean deviations of the singlet vertical excitations of all Hamiltonians are almost equal, with R2022 being slightly better than the other two. For triplet excited states, the performance of R2022 is marginally inferior. For the doubly excited states, R2022 vastly improves the performance of DFT/MRCI, lowering the RMSD from around 0.6 eV in R2016 and R2018 to 0.28 eV. Especially the description of $n^2 \rightarrow \pi^{*2}$ excitations are improved w.r.t. the other redesigned Hamiltonians. The largest differences are found in the excited state manifold of the C_2 molecule. Here, the two components of the $1^1\Delta_g$ state are at 0.77 and 0.85 eV in R2016, the energies being fairly similar for R2018, 1.86 and 2.28 eV for the original Hamiltonian, and 1.76 and 1.76 eV in R2022, while the TBE is at an excitation energy of 2.09 eV. Because the DFT/MRCI method is parametrized against experimental band maxima, in contrast to the TBEs from ab initio calculations of ref 68, it is expected and acceptable that the TBEs of the doubly excited state energies are slightly underestimated by the R2022 Hamiltonian. For the tight parameter set, the RMSDs are marginally inferior (Figure S1 and Table S4 of the SI).

General Assessment. Over the course of the development of R2016, R2017, and R2018, three different assessment sets had been assembled.[2,4,5] These contain 97 singlet and 63 triplet states of small metal-free compounds, 150 doublet states, and 67 states of transition metal complexes. To compare the performance of R2022 with the former Hamiltonians, all used states of these sets were combined, recomputed, and re-evaluated for all Hamiltonians. The RMSDs and mean deviations are visualized in Figures 5 and 6. A detailed list can be found in the SI (Tables S5−S8). We will start our analysis with the singlet and triplet assessment set by Lyskov et al.[2] The set contains $\pi \rightarrow \pi^*$, $n \rightarrow \pi^*$ as well as Rydberg vertical transition energies in small organic compounds and oxides. In comparison to the original set, some states were discarded, because they were already included in the parametrization set, leading to a total of 89 singlet and 50 triplet excitations. The overall performance remains the same for singlet and triplet states, which are dominated by singly excited configurations. For the doublet test set of Heil and Marian[4] the situation is similar. The set contains experimental values from photoelectron and electron absorption spectroscopy. Here R2022 performs as good as the other Hamiltonians without any outliers. Following the suggestion by Heil and Marian,[4] the transition metal complexes were subdivided into organometallic compounds, carrying organic ligands, and inorganic compounds comprising transition metal oxides, halides, cyanides and carbonyl complexes. The only modification to the inorganic assessment set is the exclusion of the CrF_6 molecule, since it is controversial whether this molecule is stable or not.[69,70] For the inorganic transition metal complexes, the results obtained with R2022 are improved w.r.t. R2018. This is mainly caused by a better description of the $\pi \rightarrow d^*/\pi^*$ ligand-to-metal charge

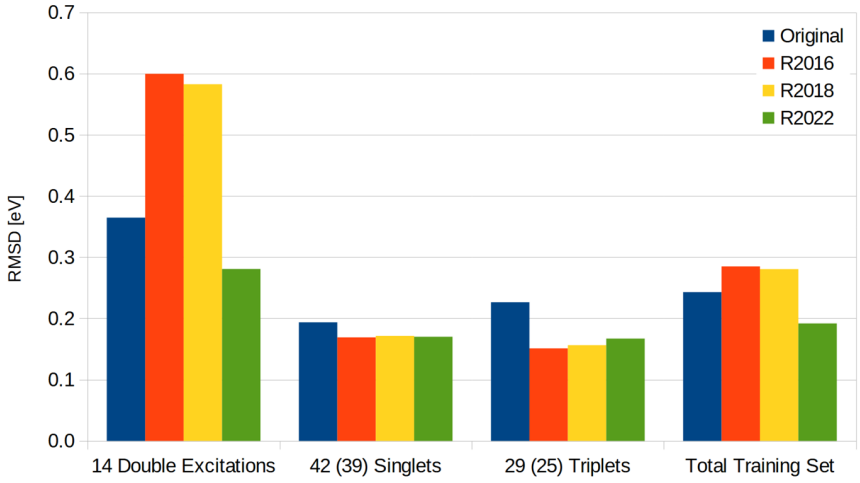

Figure 3. RMSD of the states in the fitting set sorted by type for the standard selection threshold of E_{sel} = 1.0E_h. R2016, R2018, and values for the original Hamiltonian are given for comparison. Doubly excited states are not included in the singlet or triplet subset. Values in brackets are the number of states for the original Hamiltonian, where dimer states were excluded. All values in eV.

https://doi.org/10.1021/acs.jpca.2c07951
J. Phys. Chem. A 2023, 127, 2011−2025

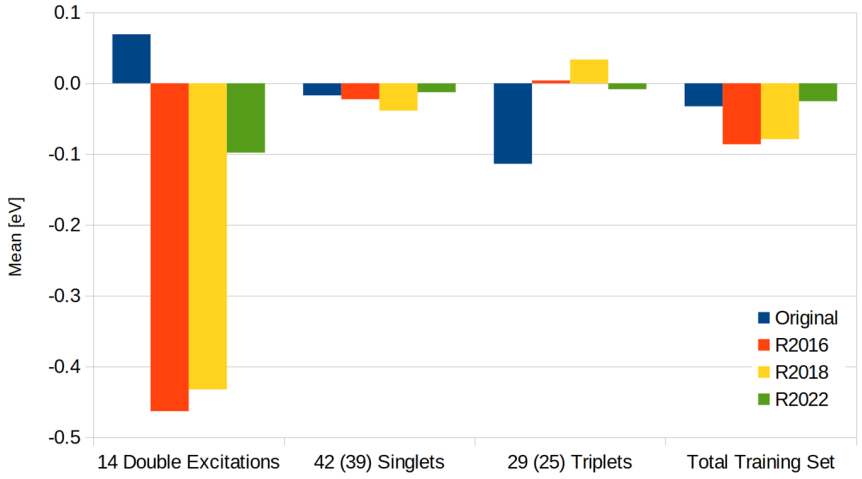

Figure 4. Mean deviation of the states in the fitting set sorted by type for the standard selection threshold of $E_{sel} = 1.0E_h$. R2016, R2018, and values for the original Hamiltonian are given for comparison. Doubly excited states are not included in the singlet or triplet subset. Values in brackets are the number of states for the original Hamiltonian, where dimer states were excluded. All values in eV.

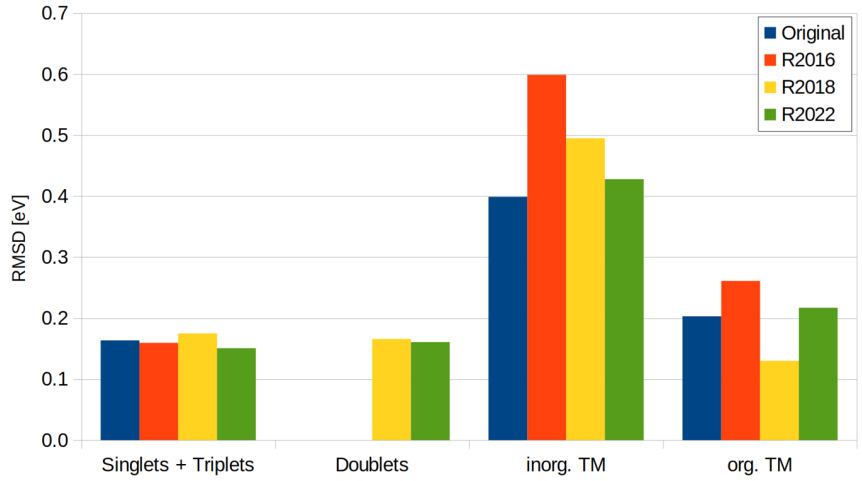

Figure 5. RMSD of the states in the assessment set sorted by type for the standard selection threshold of $\Delta E = 1.0E_h$. R2016, R2018, and values for the original Hamiltonian are given for comparison. Doubly excited states are not included in the singlet or triplet subset. All values in eV.

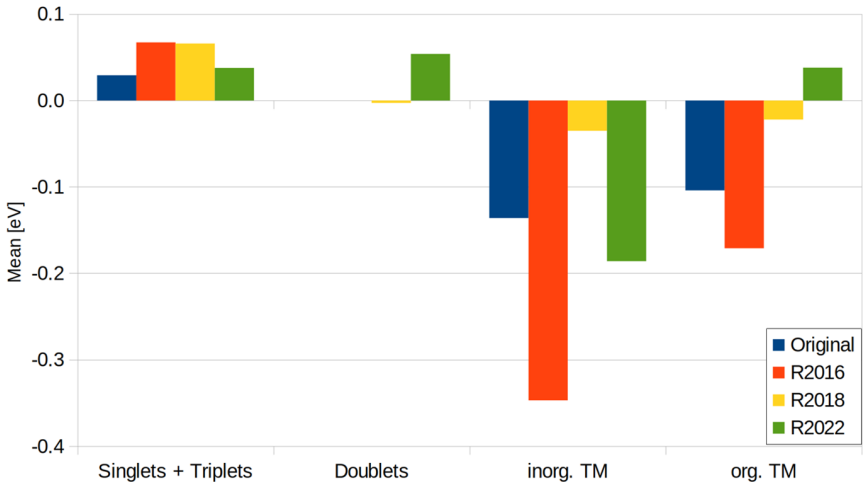

Figure 6. Mean deviation of the states in the assessment set sorted by type for the standard selection threshold of $\Delta E = 1.0E_h$. R2016, R2018, and values for the original Hamiltonian are given for comparison. Doubly excited states are not included in the singlet or triplet subset. All values in eV.

https://doi.org/10.1021/acs.jpca.2c07951
J. Phys. Chem. A 2023, 127, 2011−2025

transfer (LMCT) states in MnO_4^-, which could not be assigned in the R2018 assessment because of low-lying double excitations. In the case of organometallics, R2022 tends to slightly overestimate the excitation energy, which can be seen from the mean value given as 0.06 eV. This is in contrast to the marginal underestimation of the R2018 Hamiltonian, which yielded a mean value of −0.03 eV. Comparing the RMSDs for the two Hamiltonians, we find a comparable performance, with 0.19 eV for the R2022 and 0.14 eV for the R2018 Hamiltonian, respectively. All in all, the R2022 Hamiltonian performs better for the standard selection threshold as the previous Hamiltonians.

Basis Set Dependence of the DFT/MRCI Results. As stated above, typically an augmented TZVP basis set was used in the parametrization of the Hamiltonian. For large molecules, it might be necessary to choose smaller basis sets of valence double-ζ qualitiy, for example. The performance of the R2016 and R2022 Hamiltonians in conjunction with smaller basis sets was investigated for 27 $\pi \rightarrow \pi^*$ and $n \rightarrow \pi^*$ transitions taken from our training set. The used states are highlighted in Table S9. As can be seen in Figure 7, the here proposed R2022 Hamiltonian overestimates the vertical excitation energy by about 0.2 eV when a small basis set is used. The better performance of the R2016 Hamiltonian based on the SV(P) orbitals might be a bias to energy lowering by inclusion of doubly excited configurations in the former Hamiltonians. This bias can also lead to intruder states in the reference space, analogous to intruder states found in CAS-PT methods.[71−73] An extreme example can be found in the C_{60} molecule, whose spectra computed with the tight parameter set and various Hamiltonians, as well as two different basis sets, are shown in Figures S8−S10. The computed states were assigned according to the irreducible representations of the I_h ground state geometry and are shown in Table S21. The intruding doubly excited configurations in the reference space of R2016 lead to the unfortunate circumstance that only the first bright state is accessible, while the rest of the spectrum is spoiled with doubly substituted configurations of open shell character, preventing an assignment of higher excited states. Results obtained with the R2022 Hamiltonian do suffer from this problem as well, however not nearly as severely, and the second bright state is accessible. However, the state energies computed at the ground state geometry are overestimated by ≈0.6 eV using the R2022 Hamiltonian, compared to experimental band maxima. On the contrary the R2016 Hamiltonian shows good agreement with the energetic position of the experimental first bright state. We interpret this circumstance as an unfortunate loss of error cancellation in the new Hamiltonian. Although this does not fully explain the large deviation, a detailed analysis is subject of future work and will not be discussed here.

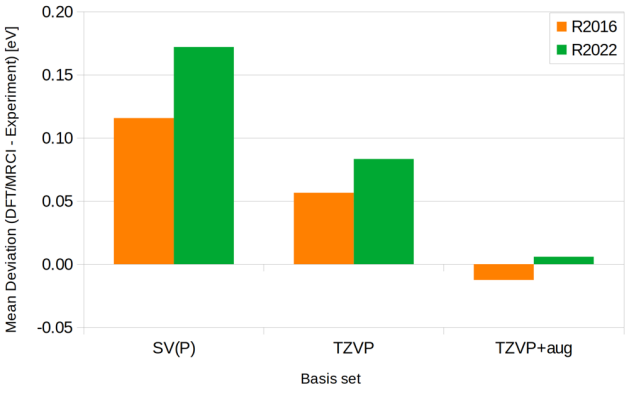

Figure 7. Mean deviation from experiment of 27 vertical excitation energies of $\pi \rightarrow \pi^*$ and $n \rightarrow \pi^*$ singlet transitions included in the training set computed using different basis sets. The used states were highlighted in Table S9.

Performance for Doubly Excited States. To assess the performance of the R2022 Hamiltonian for doubly excited states, it is useful to study its effect on the critical cases reported by Jovanović et al.[17] We decided to compare our results with vertical excitation energies calculated with NEVPT2, because this method was shown to give accurate excitation energies for doubly excited states.[47] As laid out in the Theory section, doubly excited states can be grouped into closed- and open-shell excitations (Figure 1).

Regarding the particular case of the C_2 molecule, we have shown that it is advisible to differentiate between intra- and interorbital interactions. While the original Hamiltonian does not consider the intraorbital interactions directly in its corrections, the redesigned Hamiltonians treat them on an equal footing as the interorbital ones and miss some corrections in open-shell cases (eq 20). Among the DFT/MRCI Hamiltonians, the here proposed R2022 Hamiltonian is the only one ensuring a balanced description of these cases per

Table 2. Vertical Excitation Energies in eV of Doubly Excited States[a]

molecule	state	character	NEVPT2	original	R2018	R2022
o-benzyne	$^1A_1$	$\pi, \pi' \rightarrow \pi^*, \pi^{*\prime}$	7.23	−2.99	−0.67	0.04
	$^1B_2$	$\pi, \pi' \rightarrow \pi^*, \pi^{*\prime}$	8.15	−2.41	−0.75	−0.04
	$^3A_1$	$\pi, \pi' \rightarrow \pi^*, \pi^{*\prime}$	7.12	−1.43	−0.61	0.03
thioformaldehyde	$^1A_1$	$n^2 \rightarrow \pi^{*2}$	7.37	0.58	−0.71	−0.44
	$^1A_2$	$n, \pi \rightarrow \pi^{*2}$	7.93	−0.74	−0.27	−0.28
	$^3A_2$	$n, \pi \rightarrow \pi^{*2}$	7.43	0.34	−0.20	−0.09
dithiosuccinimide	$^1A_1$	$n^2 \rightarrow \pi^{*2}$	5.85	0.22	−0.71	−0.36
	$^1A_1$	$n, n' \rightarrow \pi^*, \pi^{*\prime}$	7.13	−2.42	−3.65	0.33
	$^3B_2$	$n, n' \rightarrow \pi^{*2}$	5.86	−1.26	−2.34	0.37
	$^3A_1$	$n, n' \rightarrow \pi^*, \pi^{*\prime}$	6.99	−2.31	−3.49	0.40
nitromethane	$^3A'$	$n, n' \rightarrow \pi^{*2}$	8.79	−1.48	−2.35	0.60
dithiin	$^1A_1$	$\pi^2 \rightarrow \pi^{*2}$	4.91	−0.11	−0.20	0.17

[a]For the DFT/MRCI Hamiltonians the difference ΔE to the NEVPT2 results are given.

https://doi.org/10.1021/acs.jpca.2c07951
J. Phys. Chem. A 2023, 127, 2011−2025

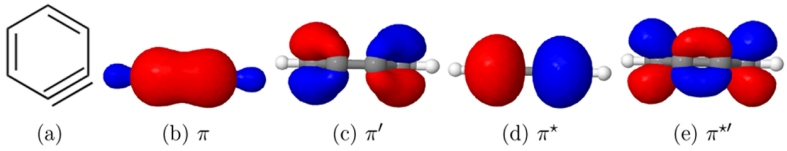

Figure 8. Chemical structure of *o*-benzyne and molecular orbitals involved in the $\pi, \pi' \rightarrow \pi^*, \pi^{*\prime}$ double excitation. The isosurface plots were generated with a cutoff of 0.05.

construction. As one can see from the results in Table 2, the new ansatz performs very well with regard to NEVPT2. A striking feature of the R2022 results is the drastically reduced number of outliers, compared to the other Hamiltonians. As can be seen from Table 2, the results obtained for the former DFT/MRCI Hamiltonians deviate strongly for the open-shell excitations, e.g., $\pi, \pi' \rightarrow \pi^*, \pi^{*\prime}$ in *o*-benzyne, while the difference to NEVPT2 is less in the closed-shell cases, e.g., $\pi^2 \rightarrow \pi^{*2}$ in dithiin. The R2022 Hamiltonian is of equal quality in both cases.

Comparing open-shell singlet and triplet excitations, e.g., the $^1A_1$ and $^3A_1$ exciations in *o*-benzyne in Table 2, it can be seen that the original Hamiltonian deviates less for the triplet state. This behavior is explained considering that the multiplicity-specific parameter sets are used for singlet and triplet excitations in the original Hamiltonian. Nevertheless, the deviations are large in the open-shell cases. These stem from the dependency of its diagonal exchange corrections on the number of open shells and the excitation class, as exemplified on the $^3B_2$ and $^3A_1$ exciations in dithiosuccinimide. The first is a state with two open shells N_o, while the latter has four open shells. The underestimation of the $^3A_1$ excitation is with −2.31 eV, almost twice as large as for the $^3B_2$ excitation. Considering the correction factor for diagonal elements in the original formulation $^3p_0[N_o] = \alpha N_o$ for triplets, we see that the increased error nicely corresponds to the N_o factor. A detailed discussion of the dependency of open shells in the original Hamiltonian can be found in the works of Lyskov et al.[2] or Jovanović et al.[17] The large deviations of the R2018 Hamiltonian in the dithiosuccinimide open-shell $^1A_1$ ($n, n' \rightarrow \pi^*, \pi^{*\prime}$) excitation can be explained by the missing exchange integral correction as outlined in the discussion of eq 20. We will illustrate this problem by comparing this case with the $\pi, \pi' \rightarrow \pi^*, \pi^{*\prime}$ excitation of *o*-benzyne, where the value computed with R2018 does not deviate as much. The excitation in *o*-benzyne occurs between the in-plane π/π^* orbitals and the out-of-plane $\pi'/\pi^{*\prime}$ orbitals, respectively, which are shown in Figure 8. Because the densities of the involved orbitals have negligible overlap, the interaction between a created electron in the out-of plane $\pi^{*\prime}$ orbital and the annihilated electron in the in-plane π-orbital will be close to zero. Analogously, the interaction between the created holes/particles will be close to zero. Therefore, the missing correction for the exchange intergrals does not influence the energy significantly.

In contrast, the exchange interaction of two electrons in the two *n* orbitals of dithiosuccinimide (Figure 9) will be much larger, because the associated densities overlap strongly. Therefore, the missing correction has a major impact on the excitation energy, which is found indeed.

The missing correction term is even more obvious considering the triplet excited states, e.g., $^3A_1$ excitation in dithiosuccinimide. This ought to be expected since electron exchange plays a larger role in these cases. Calculating the mean absolute errors (MAEs) for the cases in Table 2 yields a value of 0.26 eV for R2022, while for the original and the R2018

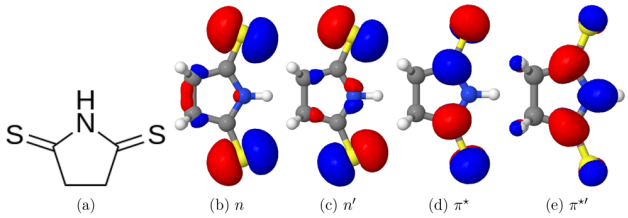

Figure 9. Chemical structure of dithiosuccinimide and molecular orbitals involved in the $n, n \rightarrow \pi^*, \pi^*$ excitation. The isosurface plots were generated with a cutoff of 0.05.

Hamitonians, the values are 1.34 and 1.39 eV, respectively. The RMSD of R2022 for all critical cases is 0.32 eV. The RMSDs for the original and R2018 Hamiltonians amount to 1.65 and 1.84 eV, respectively. Overall, we observe that the R2022 Hamiltonian notably reduces errors in doubly excited states and gives results comparable to NEVPT2, thus vastly outperforming the former Hamiltonians.

Extended π Systems. Polyacenes and carotenoids can be systematically extended to study the influence of doubly excited configurations on the energies of states. We will use the symmetry independent nomenclature introduced by Platt,[74] ^1L_a and ^1L_b, for the excited states of the investigated polyacenes. In the ^1L_a wave function, the $\pi_H \rightarrow \pi_L$ contribution prevails.[75,76] Its dominance remains essentially unaffected with increasing number of rings. Consequently, one would expect it to show a similar behavior as a particle in a box. This is indeed the case as can be seen from the curve generated from experimental values[9] shown Figure 10. The R2022 Hamiltonian reproduces this trend perfectly. Although the state does not change its main character, the R2016 curve starts to deviate from the experimental curve with increasing chain length. Clearly, the number of doubly excited configurations will increase with system size. Their

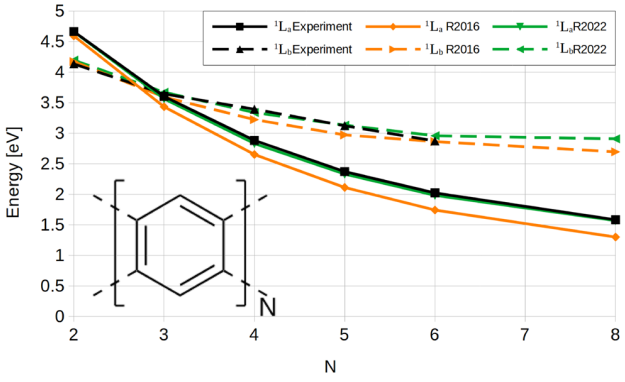

Figure 10. Calculated vertical excitation energies of polyacenes as a function of the number of rings *N*. Geometries and experimental values were taken from ref 9. The TZVP AO-basis was used for the DFT/MRCI calculation.

https://doi.org/10.1021/acs.jpca.2c07951
J. Phys. Chem. A 2023, 127, 2011−2025

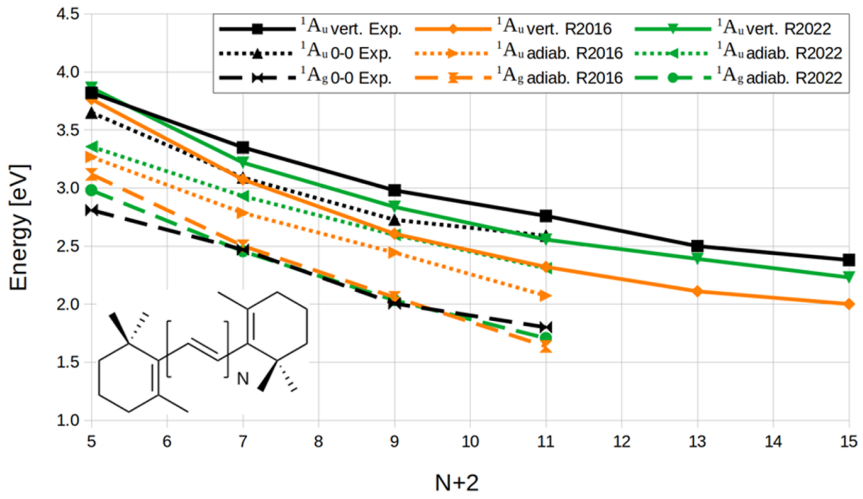

Figure 11. Calculated vertical and adiabatic excitation energies of *n*-carotenes as a function of the conjugation length *N*+2. Geometries and experimental values for mini-5-carotene to *β*-carotene were taken from ref 10. For M13 and M15, the geometries were optimized as described in ref 10 with B3-LYP/def-SV(P), and the experimental results were taken from ref 77. The def-SV(P) AO-basis was used for the DFT/MRCI calculation. The chemical structures of the molecules can be found in the SI, Figure S6.

diagonal elements are underestimated for the R2016 Hamiltonian, as outlined in the Theory section, thus explaining the increasing deviation from experiment. Comparing the R2022 energies of the ^1L_b state with the experimental curve, we find an excellent match again. This underpins the success of the new design strategy followed in this work.

Turning to carotenoids, we find a similar situation. Here, the low lying 2 ^1A_g state, which shows a pronounced double excitation character, and the optically bright 1 ^1A_u state, which is dominated by the $\pi_H \rightarrow \pi_L$ excitation, are investigated. The calculated vertical and adiabatic energies and the experimental values[10] are shown in Figure 11. On the abscissa, the conjugation length is given as $N + 2$, where N is the number of conjugated bonds in the polyene chain. This is done to stress that the double bonds in the terminal ionone groups are included. As discussed for the previous case, larger deviations with increasing number of double bonds are observed for former DFT/MRCI Hamiltonians, exemplified for the R2016 Hamiltonian in Figure 11. The deviations from experiment are approximately cut in half with the R2022 Hamiltonian, reducing the mean of the deviation from −0.23 to −0.10 eV.

To further support these findings and test the new Hamiltonian on a realistic example, the two extended carotenoids *β*-apo-8′-carotenal (BAC) and fucoxanthin (Fx) were investigated. Their chemical structures are shown in Figure 12. Both are found in the light-harvesting complexes of algae,

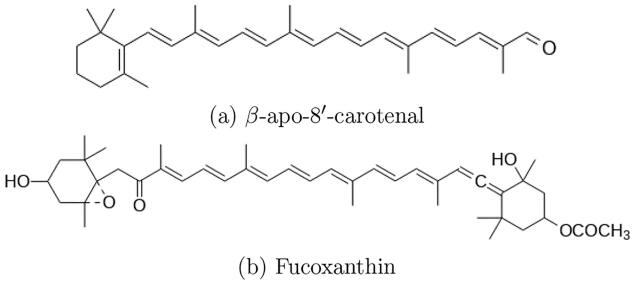

Figure 12. Chemical structures of *β*-apo-8′-carotenal and fucoxanthin.

showing efficient carotenoid to porphyrin energy transfer. A terminal allenic bond, a conjugated carbonyl group, an epoxy group and a backbone of eight conjugated double bonds bestow Fx a unique chemical structure and photophysics. In addition to the polyene-typical states, FX and BAC exhibit a low-lying $n \rightarrow \pi^*$ state close to the bright S_2 state due to the terminal aldehyde group on the polyene chain in the molecule. Here we want to give a very brief overview of the lowest excited states calculated at the ground state structure, since an exhaustive exploration of the excited state manifold is out of the scope of this work.

In Table 3, a comparison of excitation energies and oscillator strengths computed with R2016 and the newly developed R2022 Hamiltonian is shown. Difference density plots of the bright $\pi \rightarrow \pi^*$ and $n \rightarrow \pi^*$ states are displayed in Figure 13. The S_1 state exhibits strong contributions from doubly excited configurations, of which the $(\pi_H^2 \rightarrow \pi_L^2)$ excitation dominates and is delocalized along the polyene backbone. The bright S_2 state is mainly described by a $\pi_H \rightarrow \pi_L$ configuration and has a transition dipole directed along the polyene backbone.

In cyclohexane solution, the band maximum of this state is located at 2.61 eV in BAC.[79] As can be seen from Table 3 and the spectrum shown in Figure 14, the vertical excitation energy calculated with the R2016 Hamiltonian underestimates this value by around 0.2 eV. This is in line with the results shown in Figure 11 for *β*-carotenoids. The R2022 vertical excitation energy agrees well with the experimental result. Noteworthy is the ordering of the S_3 and S_4 states, which is reversed in R2016 and R2022. The S_3 state in the R2022 treatment results from a promotion of an electron from the in-plane nonbonding orbital at the carbonyl group to the polyene backbone and lies 0.2 eV above the S_2 state. A doubly excited state with two open shells consisting of $\pi_{H-1}\pi_H \rightarrow \pi_L^2$ and $\pi_H^2 \rightarrow \pi_L\pi_{L+1}$ is located 0.15 eV above the S_3 state. When the R2016 Hamiltonian is employed instead, this state is lowered in energy due to the open shell character of the double excitation and falls below the $n \rightarrow \pi^*$ state, which has the same energy in both Hamiltonians. For Fx, the situation is similar, as can be seen from Figure 15. The S_1 and S_2 states have the same character as in BAC and are located on the polyene backbone, too. Vertically, they are 0.2 and 0.1 eV

https://doi.org/10.1021/acs.jpca.2c07951
J. Phys. Chem. A 2023, 127, 2011−2025

Table 3. Vertical Excitation Energies and Oscillator Strengths of β-Apo-8′-Carotenal (BAC) and Fucoxanthin (Fx)[a]

molecule	state	character	R2016 (eV)	f (L)	R2022 (eV)	f (L)	exp. (eV)
β-apo-8′-carotenal	S_1	$\pi^2 \rightarrow \pi^{*2}$	2.14	0.26	2.41	0.35	
	S_2	$\pi \rightarrow \pi^*$	2.42	3.14	2.62	3.25	2.61[b]
	S_3	$n \rightarrow \pi^*$	2.83	0.00	2.82	0.00	
	S_4	$\pi, \pi' \rightarrow \pi^{*2}$	2.74	0.04	2.97	0.03	
fucoxanthin	S_1	$\pi^2 \rightarrow \pi^{*2}$	2.38	0.38	2.61	0.64	∼2.4[c]
	S_2	$\pi \rightarrow \pi^*$	2.56	3.25	2.74	3.11	2.74,[c] 2.76[d]
	S_3	$n \rightarrow \pi^*$	2.89	0.00	2.86	0.01	
	S_4	$\pi, \pi' \rightarrow \pi^{*2}$	3.00	0.00	3.19	0.00	

[a]Ground state geometry of Fx was taken from ref 78, while the geometry of BAC was optimized with B3LYP/def-SV(P). [b]Ref 79. [c]Ref 80. [d]Ref 81.

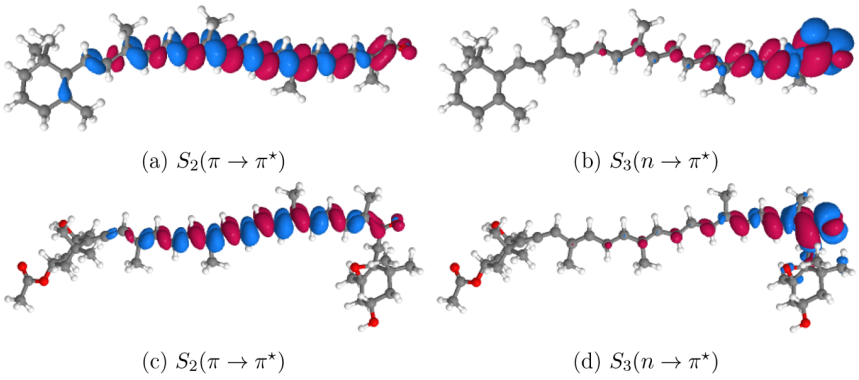

Figure 13. Difference densitiy plots (isosurface value of 0.001) between the ground and excited states of β-apo-8′-carotenal (top) and fucoxanthin (bottom). Blue (red) indicates a negative (positive) difference density. The state ordering was assigned on the basis of the R2022 results.

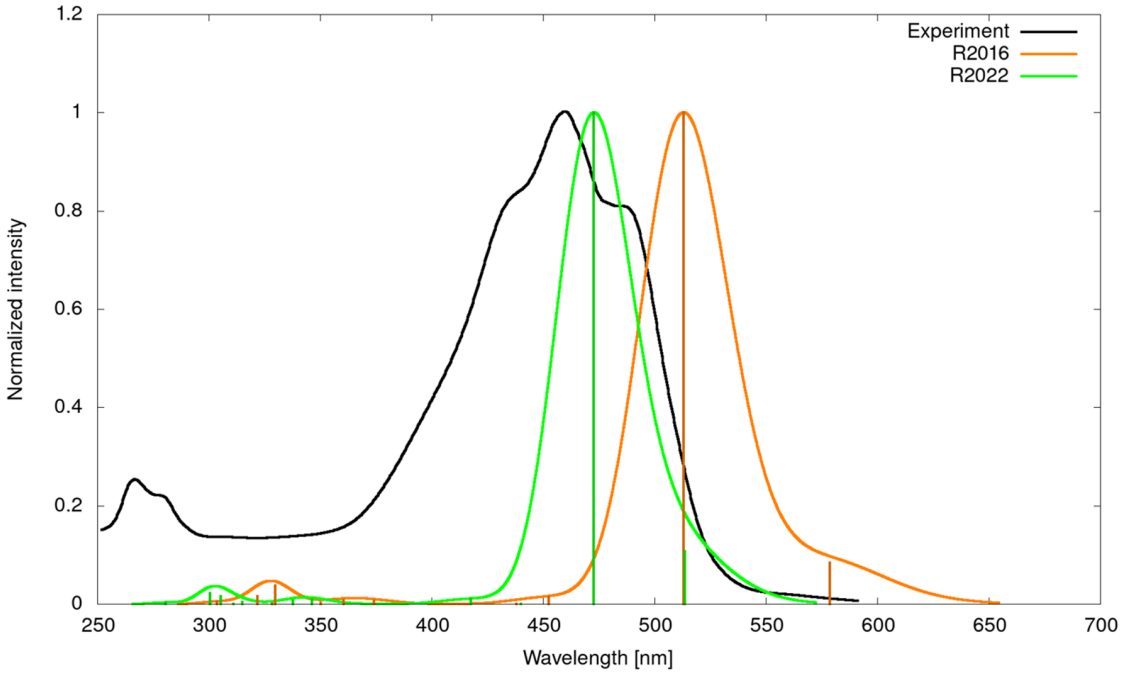

Figure 14. Calculated and experimental absorption spectrum of β-apo-8′-carotenal in cyclohexane solution. The calculated line spectrum was broadened by a Gaussian of 750 cm^{-1} full width at half-maximum. Note that the experimental spectrum, extracted from ref 79, shows a pronounced C−C stretching vibrational progression.

higher in energy compared to the states in BAC. The S_2 band maximum in tetrahydrofuran was experimentally determined at 2.74 eV[80] and in isopropanol at 2.76 eV.[81] Premvardhan et al.[80] estimated the energetic position of the dark S_1 state to be roughly around 2.4 eV from fluoresence studies. It is better predicted by R2016, contrary to the expectations. Since the R2016 Hamiltonian tends to underestimate these states in all previously discussed cases, this good agreement might be fortuitous. In comparison to BAC, the state ordering of the S_3 and S_4 states do not change. The S_3 state is the $n \rightarrow \pi^*$ transition

https://doi.org/10.1021/acs.jpca.2c07951
J. Phys. Chem. A 2023, 127, 2011−2025

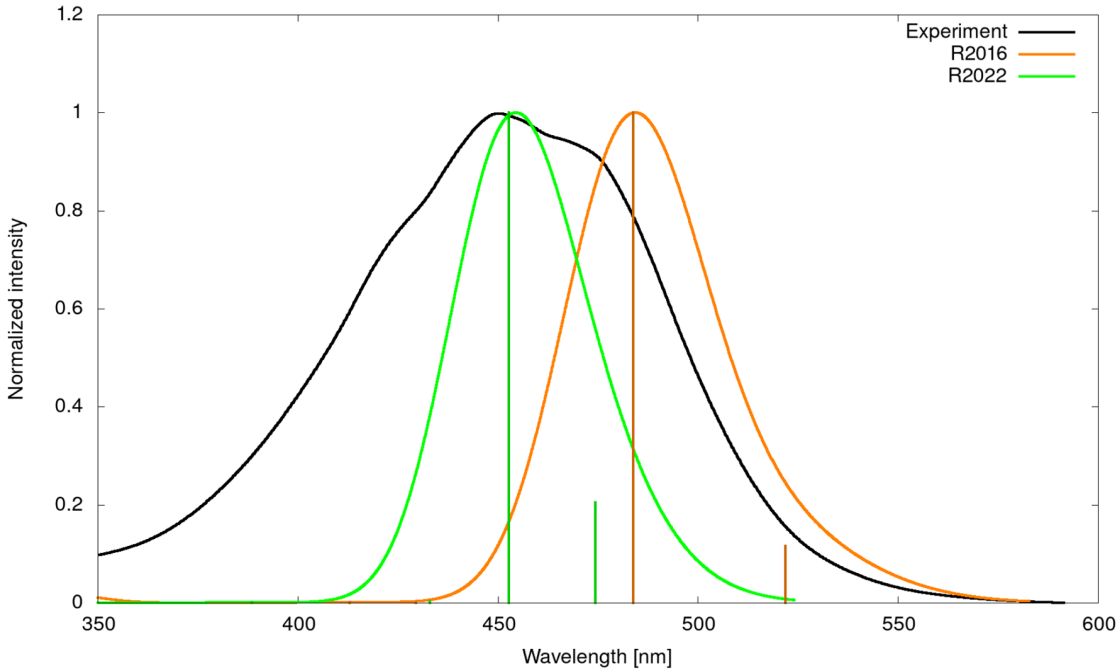

Figure 15. Calculated and experimental absorption spectrum of fucoxanthin in isopropanol solution. The calculated line spectrum was broadened by a Gaussian of 750 cm^{-1} full width at half-maximum. Note that the experimental spectrum, extracted from ref 81, shows a pronounced C−C stretching vibrational progression.

originating from the carbonyl group to the polyene backbone, while the S_4 is again the doubly excited $\pi_{H-1}\pi_H \rightarrow \pi_L^2$ state.

The phenalene derivatives heptazine and cycl[3.3.3]azine show an interesting excited state behavior. Due to the bipartite charge distribution in the HOMO and LUMO orbitals (Figure 16), the exchange interaction between π_H and π_L electrons

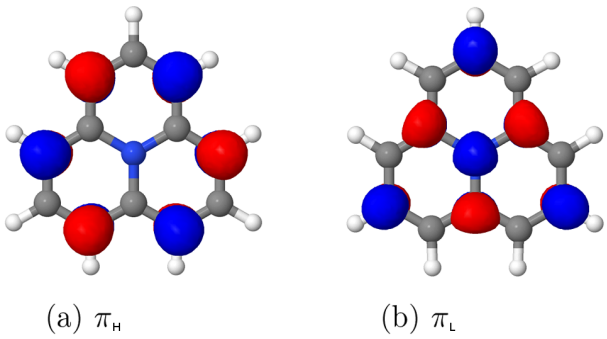

Figure 16. Frontier molecular orbitals of cycl[3.3.3]azine.

nearly vanishes, yielding a small S_1-T_1 gap. It was argued that double excitation contributions preferentially lower the S_1 energy and hence push it energetically below the T_1 state.[82−85] The inverted S_1-T_1 gap causes the reverse intersystem crossing to be a downhill process and therefore no thermal activation is needed. Results for heptazine, computed using the R2016 Hamiltonian were recently published by our group.[83] In this work we want to verify that an inverted S_1-T_1 gap is obtained with the new R2022 Hamiltonian as well. In Table 4, the excitation energies and resulting S_1-T_1 gaps computed at the ground state geometry of the respective molecules are given. The transitions are all dominated by single excitations of $\pi_H \rightarrow \pi_L$ character. As can be seen, the choice of the Hamiltonian hardly influences the determined S_1-T_1 gap in both molecules. However, the state energies are raised by approximately 0.15 eV, when using the R2022 Hamiltonian. This is might be a consequence of the different basis set behavior of the R2016 and R2022 Hamiltonian (vide supra).

These presented cases nicely illustrate the improvements gained with the new ansatz chosen in the R2022 Hamiltonian for double exciations. At the same time, they demonstrate that the good performance of the previous Hamiltonians for singly excited states is retained.

Table 4. Vertical Excitation Energies of Heptazine and Cycl[3.3.3]azine Calculated with Different Methods[a]

method	E_{S_1}	E_{T_1}	ΔE_{ST}
heptazine			
R2016	2.59	2.60	−0.01
R2022	2.74	2.78	−0.04
ADC(2)	2.57	2.85	−0.28
EOM-CCSD	2.78	2.96	−0.18
TDDFT/B3LYP	2.82	2.60	0.22
TDDFT/PBE0	2.92	2.68	0.24
cycl[3.3.3]azine			
R2016	0.96	0.97	−0.01
R2022	1.09	1.12	−0.03
ADC(2)	1.04	1.20	−0.16
EOM-CCSD	1.09	1.19	−0.10
TDDFT/B3LYP	1.26	1.05	0.21
TDDFT/PBE0	1.28	1.05	0.23

[a]The ADC(2), EOM-CCSD, and TDDFT results for heptazine and cycl[3.3.3]azine are taken from refs 82 and 84, respectively. All values in eV. The geometry of heptazine was taken from ref 83, while the geometry of cycl[3.3.3]azine was optimized with B3-LYP/TZVP.

https://doi.org/10.1021/acs.jpca.2c07951
J. Phys. Chem. A 2023, 127, 2011−2025

CONCLUSION

In this work, a new ansatz for the modification of the DFT/MRCI Hamiltonian has been presented. The ansatz remedies former errors made in the description of doubly excited and degenerate states. Especially the large underestimations of the $n^2 \rightarrow \pi^{*2}$ and $n, n' \rightarrow \pi^*, \pi^{*\prime}$ excitations in small organic compounds are removed, which is the largest improvement w.r.t. former approaches. Furthermore, it has been shown that for extended π-systems, specifically polyacenes and β-carotenoids, the description of the low-lying excited states gets much better. The experimental trends for the polyacenes are matched excellently, while the trends for the carotenoids are better reproduced compared to the redesigned Hamiltonians. The most important point to emphasize is that the new R2022 Hamiltonian leads to a balanced correction of ab initio CI-matrix elements, while losing nothing of the simplicity and strength of the DFT/MRCI method. This improvement is achieved with a moderate number of five parameters that have been derived in such a way that the underlying physics is reflected in the corrections at variance with former effective Hamiltonians used in DFT/MRCI. By requiring that the spatial components of the $^1\Delta$ state of C_2 remain degenerate, a fixed relationship between diagonal and off-diagonal scaling parameters was derived. As in previous formulations, the parametrization is independent of the particular chemical element and covers the most common multiplicities found in excited-state processes. Since the R2022 retains the same excellent performance for singly excited states as previous Hamiltonians, we conclude that the here presented formulation should be considered as the new standard for DFT/MRCI calculations. However, for small basis sets it might happen that the new ansatz overestimates excitation energies, although it was parametrized on experimental band maxima. A systematic study of the basis set behavior of the new Hamiltonian and DFT/MRCI in general is ongoing and will be the subject of future work.

ASSOCIATED CONTENT

Supporting Information

The Supporting Information is available free of charge at https://pubs.acs.org/doi/10.1021/acs.jpca.2c07951.

Statistical data, training data set, assessment data set, computational details, chemical structures of carotenoids, cycl[3.3.3]azine and heptazine, excitation energies, and spectra of C_{60} (PDF)

AUTHOR INFORMATION

Corresponding Author

Christel M. Marian − *Institute of Theoretical and Computational Chemistry, Heinrich-Heine-University Düsseldorf, 40225 Düsseldorf, Germany;* orcid.org/0000-0001-7148-0900; Email: christel.marian@hhu.de

Authors

Dennis R. Dombrowski − *Institute of Theoretical and Computational Chemistry, Heinrich-Heine-University Düsseldorf, 40225 Düsseldorf, Germany*

Timo Schulz − *Institute of Theoretical and Computational Chemistry, Heinrich-Heine-University Düsseldorf, 40225 Düsseldorf, Germany*

Martin Kleinschmidt − *Institute of Theoretical and Computational Chemistry, Heinrich-Heine-University Düsseldorf, 40225 Düsseldorf, Germany*

Complete contact information is available at: https://pubs.acs.org/10.1021/acs.jpca.2c07951

Notes

The authors declare no competing financial interest.

ACKNOWLEDGMENTS

Financial support by the Deutsche Forschungsgemeinschaft (DFG), Projects MA1051/14-2 and MA1051/19-1, is gratefully acknowledged.

REFERENCES

(1) Grimme, S.; Waletzke, M. A combination of Kohn-Sham density functional theory and multi-reference configuration interaction methods. *J. Chem. Phys.* **1999**, *111*, 5645−5655.

(2) Lyskov, I.; Kleinschmidt, M.; Marian, C. M. Redesign of the DFT/MRCI Hamiltonian. *J. Chem. Phys.* **2016**, *144*, 034104.

(3) Marian, C. M.; Heil, A.; Kleinschmidt, M. The DFT/MRCI method. *WIREs Comput. Mol. Sci.* **2019**, *9*, e1394.

(4) Heil, A.; Marian, C. M. DFT/MRCI Hamiltonian for odd and even numbers of electrons. *J. Chem. Phys.* **2017**, *147*, 194104.

(5) Heil, A.; Kleinschmidt, M.; Marian, C. M. On the performance of DFT/MRCI Hamiltonians for electronic excitations in transition metal complexes: The role of the damping function. *J. Chem. Phys.* **2018**, *149*, 164106.

(6) Grimme, S. *Rev. Comput. Chem.*; Wiley-Blackwell, 2004; Chapter 3, pp 153−218.

(7) Parusel, A. B. J.; Grimme, S. A Theoretical Study of the Excited States of Chlorophyll a and Pheophytin a. *J. Phys. Chem. B* **2000**, *104*, 5395−5398.

(8) Parusel, A. B. J.; Grimme, S. DFT/MRCI calculations on the excited states of porphyrin, hydroporphyrins, tetrazaporphyrins and metalloporphyrins. *J. Porphyr. Phthalocya.* **2001**, *05*, 225−232.

(9) Marian, C. M.; Gilka, N. Performance of the Density Functional Theory/Multireference Configuration Interaction Method on Electronic Excitation of Extended π-Systems. *J. Chem. Theory Comput.* **2008**, *4*, 1501−1515.

(10) Kleinschmidt, M.; Marian, C. M.; Waletzke, M.; Grimme, S. Parallel multireference configuration interaction calculations on mini-β-carotenes and β-carotene. *J. Chem. Phys.* **2009**, *130*, 044708.

(11) Knecht, S.; Marian, C. M.; Kongsted, J.; Mennucci, B. On the photophysics of carotenoids: A multireference DFT study of peridinin. *J. Phys. Chem. B* **2013**, *117*, 13808−13815.

(12) Andreussi, O.; Knecht, S.; Marian, C. M.; Kongsted, J.; Mennucci, B. Carotenoids and Light-Harvesting: From DFT/MRCI to the Tamm-Dancoff Approximation. *J. Chem. Theory Comput.* **2015**, *11*, 655−666.

(13) Heil, A.; Marian, C. M. DFT/MRCI-R2018 study of the photophysics of the zinc(II) tripyrrindione radical: non-Kasha emission? *Phys. Chem. Chem. Phys.* **2019**, *21*, 19857−19867.

(14) Spiegel, J. D.; Kleinschmidt, M.; Larbig, A.; Tatchen, J.; Marian, C. M. Quantum-Chemical Studies on Excitation Energy Transfer Processes in BODIPY-Based Donor-Acceptor Systems. *J. Chem. Theory Comput.* **2015**, *11*, 4316−4327.

(15) Lyskov, I.; Marian, C. M. Climbing up the ladder: Intermediate triplet states promote the reverse intersystem crossing in the efficient TADF emitter ACRSA. *J. Phys. Chem. C* **2017**, *121*, 21145−21153.

(16) Kaminski, J. M.; Rodriguez-Serrano, A.; Dinkelbach, F.; Miranda-Salinas, H.; Monkman, A. P.; Marian, C. M. Vibronic effects accelerate the intersystem crossing processes of the through-space charge transfer states in the triptycene bridged acridine-triazine donor-acceptor molecule TpAT-tFFO. *Chem. Sci.* **2022**, *13*, 7057−7066.

(17) Jovanović, V.; Lyskov, I.; Kleinschmidt, M.; Marian, C. M. On the performance of DFT/MRCI-R and MR-MP2 in spin-orbit coupling calculations on diatomics and polyatomic organic molecules. *Mol. Phys.* **2017**, *115*, 109−137.

(18) Smith, M. B.; Michl, J. Singlet Fission. *Chem. Rev.* **2010**, *110*, 6891−6936.

(19) Smith, M. B.; Michl, J. Recent Advances in Singlet Fission. *Annu. Rev. Phys. Chem.* **2013**, *64*, 361−386.
(20) Gray, V.; Dzebo, D.; Abrahamsson, M.; Albinsson, B.; Moth-Poulsen, K. Triplet-triplet annihilation photon-upconversion: Towards solar energy applications. *Phys. Chem. Chem. Phys.* **2014**, *16*, 10345−10352.
(21) Zimmerman, P. M.; Bell, F.; Casanova, D.; Head-Gordon, M. Mechanism for Singlet Fission in Pentacene and Tetracene: From Single Exciton to Two Triplets. *J. Am. Chem. Soc.* **2011**, *133*, 19944−19952.
(22) Casanova, D. Theoretical Modeling of Singlet Fission. *Chem. Rev.* **2018**, *118*, 7164−7207.
(23) Feng, X.; Krylov, A. I. On couplings and excimers: Lessons from studies of singlet fission in covalently linked tetracene dimers. *Phys. Chem. Chem. Phys.* **2016**, *18*, 7751−7761.
(24) Feng, X.; Casanova, D.; Krylov, A. I. Intra- and Intermolecular Singlet Fission in Covalently Linked Dimers. *J. Phys. Chem. C* **2016**, *120*, 19070−19077.
(25) C. A. Valente, D.; do Casal, M. T.; Barbatti, M.; Niehaus, T. A.; Aquino, A. J. A.; Lischka, H.; Cardozo, T. M. Excitonic and charge transfer interactions in tetracene stacked and T-shaped dimers. *J. Chem. Phys.* **2021**, *154*, 044306.
(26) Polívka, T.; Sundström, V. Ultrafast Dynamics of Carotenoid Excited States-From Solution to Natural and Artificial Systems. *Chem. Rev.* **2004**, *104*, 2021−2072.
(27) Hashimoto, H.; Uragami, C.; Yukihira, N.; Gardiner, A. T.; Cogdell, R. J. Understanding/unravelling carotenoid excited singlet states. *J. R. Soc. Interface* **2018**, *15*, 20180026.
(28) Tavan, P.; Schulten, K. The low-lying electronic excitations in long polyenes:A PPP-MRD-CI study. *J. Chem. Phys.* **1986**, *85*, 6602−6609.
(29) Tavan, P.; Schulten, K. Electronic excitations in finite and infinite polyenes. *Phys. Rev. B* **1987**, *36*, 4337−4358.
(30) Kurashige, Y.; Nakano, H.; Nakao, Y.; Hirao, K. The $\pi \rightarrow \pi^*$ excited states of long linear polyenes studied by the CASCI-MRMP method. *Chem. Phys. Lett.* **2004**, *400*, 425−429.
(31) Sashima, T.; Koyama, Y.; Yamada, T.; Hashimoto, H. The $1B_u^+$, $1B_u^-$, and $2A_g^-$ energies of crystalline lycopene, β-carotene, and mini-9-β-carotene as determined by resonance-Raman excitation profiles: Dependence of the $1B_u^-$ state energy on the conjugation length. *J. Phys. Chem. A* **2000**, *104*, 5011−5019.
(32) Fujii, R.; Inaba, T.; Watanabe, Y.; Koyama, Y.; Zhang, J.-P. Two different pathways of internal conversion in carotenoids depending on the length of the conjugated chain. *Chem. Phys. Lett.* **2003**, *369*, 165−172.
(33) Fujii, R.; Fujino, T.; Inaba, T.; Nagae, H.; Koyama, Y. Internal conversion of $1B_u^+ \rightarrow 1B_u^- \rightarrow 2A_g^-$ and fluorescence from the $1B_u^-$ state in all-trans-neurosporene as probed by up-conversion spectroscopy. *Chem. Phys. Lett.* **2004**, *384*, 9−15.
(34) Ostroumov, E.; Müller, M. G.; Marian, C. M.; Kleinschmidt, M.; Holzwarth, A. R. Electronic Coherence Provides a Direct Proof for Energy-Level Crossing in Photoexcited Lutein and β-Carotene. *Phys. Rev. Lett.* **2009**, *103*, 108302.
(35) Marek, M. S.; Buckup, T.; Motzkus, M. Direct Observation of a Dark State in Lycopene Using Pump-DFWM. *J. Phys. Chem. B* **2011**, *115*, 8328−8337.
(36) Yukihira, N.; Uragami, C.; Horiuchi, K.; Kosumi, D.; Gardiner, A. T.; Cogdell, R. J.; Hashimoto, H. Intramolecular charge-transfer enhances energy transfer efficiency in carotenoid-reconstituted light-harvesting 1 complex of purple photosynthetic bacteria. *Commun. Chem.* **2022**, *5*, 135.
(37) Diedrich, C.; Grimme, S. Systematic Investigation of Modern Quantum Chemical Methods to Predict Electronic Circular Dichroism Spectra. *J. Phys. Chem. A* **2003**, *107*, 2524−2539.
(38) Röder, A.; de Oliveira, N.; Grollau, F.; Mestdagh, J.-M.; Gaveau, M.-A.; Briant, M. Vacuum-Ultraviolet Absorption Spectrum of 3-Methoxyacrylonitrile. *J. Phys. Chem. A* **2020**, *124*, 9470−9477.
(39) Stojanović, L.; Alyoubi, A. O.; Aziz, S. G.; Hilal, R. H.; Barbatti, M. UV excitations of halons. *J. Chem. Phys.* **2016**, *145*, 184306.
(40) Khokhlov, D.; Belov, A. Ab Initio Study of Low-Lying Excited States of Carotenoid-Derived Polyenes. *J. Phys. Chem. A* **2020**, *124*, 5790−5803.
(41) Khokhlov, D.; Belov, A. Low-Lying Excited States of Natural Carotenoids Viewed by Ab Initio Methods. *J. Phys. Chem. A* **2022**, *126*, 4376−4391.
(42) Casanova, D.; Head-Gordon, M. Restricted active space spin-flip configuration interaction approach: theory, implementation and examples. *Phys. Chem. Chem. Phys.* **2009**, *11*, 9779−9790.
(43) Bettinger, H. F.; Tönshoff, C.; Doerr, M.; Sanchez-Garcia, E. Electronically Excited States of Higher Acenes up to Nonacene: A Density Functional Theory/Multireference Configuration Interaction Study. *J. Chem. Theory Comput.* **2016**, *12*, 305−312.
(44) Yang, Y.; Davidson, E. R.; Yang, W. Nature of ground and electronic excited states of higher acenes. *Proc. Natl. Acad. Sci. U.S.A.* **2016**, *113*, E5098−E5107.
(45) Segal, G. A.; Wetmore, R. W.; Wolf, K. Efficient methods for configuration interaction calculations. *Chem. Phys.* **1978**, *30*, 269−297.
(46) Wetmore, R. W.; Segal, G. A. Efficient generation of configuration interaction matrix elements. *Chem. Phys. Lett.* **1975**, *36*, 478−483.
(47) Loos, P.-F.; Boggio-Pasqua, M.; Scemama, A.; Caffarel, M.; Jacquemin, D. Reference Energies for Double Excitations. *J. Chem. Theory Comput.* **2019**, *15*, 1939−1956.
(48) TURBOMOLE V7.4 2019, a development of University of Karlsruhe and Forschungszentrum Karlsruhe GmbH, 1989−2007, TURBOMOLE GmbH, 2007; available from http://www.turbomole.com (visited on 01/23/23).
(49) Balasubramani, S. G.; Chen, G. P.; Coriani, S.; Diedenhofen, M.; Frank, M. S.; Franzke, Y. J.; Furche, F.; Grotjahn, R.; Harding, M. E.; Hättig, C.; et al. TURBOMOLE: Modular program suite for ab initio quantum-chemical and condensed-matter simulations. *J. Chem. Phys.* **2020**, *152*, 184107.
(50) Becke, A. D. Density-functional thermochemistry. III. The role of exact exchange. *J. Chem. Phys.* **1993**, *98*, 5648−5652.
(51) Stephens, P. J.; Devlin, F. J.; Chabalowski, C. F.; Frisch, M. J. *Ab initio* calculation of vibrational absorption and circular dichroism spectra using density functional force fields. *J. Phys. Chem.* **1994**, *98*, 11623−11627.
(52) Lee, C.; Yang, W.; Parr, R. G. Development of the Colle-Salvetti correlation-energy formula into a functional of the electron density. *Phys. Rev. B* **1988**, *37*, 785.
(53) Grimme, S.; Antony, J.; Ehrlich, S.; Krieg, H. A consistent and accurate ab initio parametrization of density functional dispersion correction (DFT-D) for the 94 elements H-Pu. *J. Chem. Phys.* **2010**, *132*, 154104.
(54) Grimme, S.; Ehrlich, S.; Goerigk, L. Effect of the damping function in dispersion corrected density functional theory. *J. Comput. Chem.* **2011**, *32*, 1456−1465.
(55) Becke, A. D. A new mixing of Hartree-Fock and local density-functional theories. *J. Chem. Phys.* **1993**, *98*, 1372−1377.
(56) Aidas, K.; Angeli, C.; Bak, K. L.; Bakken, V.; Bast, R.; Boman, L.; Christiansen, O.; Cimiraglia, R.; Coriani, S.; Dahle, P.; et al. The Dalton quantum chemistry program system. *WIREs Comput. Mol. Sci.* **2014**, *4*, 269−284.
(57) Angeli, C.; Cimiraglia, R.; Evangelisti, S.; Leininger, T.; Malrieu, J.-P. Introduction of n-electron valence states for multireference perturbation theory. *J. Chem. Phys.* **2001**, *114*, 10252−10264.
(58) Angeli, C.; Cimiraglia, R.; Malrieu, J.-P. n-electron valence state perturbation theory: A spinless formulation and an efficient implementation of the strongly contracted and of the partially contracted variants. *J. Chem. Phys.* **2002**, *117*, 9138−9153.
(59) Angeli, C.; Pastore, M.; Cimiraglia, R. New perspectives in multireference perturbation theory: the n-electron valence state approach. *Theor. Chem. Acc.* **2007**, *117*, 743−754.
(60) Roos, B. O.; Taylor, P. R.; Sigbahn, P. E. A complete active space SCF method (CASSCF) using a density matrix formulated super-CI approach. *Chem. Phys.* **1980**, *48*, 157−173.

https://doi.org/10.1021/acs.jpca.2c07951
J. Phys. Chem. A 2023, 127, 2011−2025

(61) Siegbahn, P. E.; Almlöf, J.; Heiberg, A.; Roos, B. O. The complete active space SCF (CASSCF) method in a Newton−Raphson formulation with application to the HNO molecule. *J. Chem. Phys.* **1981**, *74*, 2384−2396.
(62) Siegbahn, P.; Heiberg, A.; Roos, B.; Levy, B. A Comparison of the Super-CI and the Newton-Raphson Scheme in the Complete Active Space SCF Method. *Phys. Scr.* **1980**, *21*, 323.
(63) Neese, F.; Wennmohs, F.; Becker, U.; Riplinger, C. The ORCA quantum chemistry program package. *J. Chem. Phys.* **2020**, *152*, 224108.
(64) Stoychev, G. L.; Auer, A. A.; Neese, F. Automatic generation of auxiliary basis sets. *J. Chem. Theory Comput.* **2017**, *13*, 554−562.
(65) Nelder, J. A.; Mead, R. A Simplex Method for Function Minimization. *Comput. J.* **1965**, *7*, 308−313.
(66) Manna, S.; Chaudhuri, R. K.; Chattopadhyay, S. Taming the excited states of butadiene, hexatriene, and octatetraene using state specific multireference perturbation theory with density functional theory orbitals. *J. Chem. Phys.* **2020**, *152*, 244105.
(67) Martin, W. C.; Zalubas, R. Energy levels of magnesium, Mg I through Mg XII. *J. Phys. Chem. Ref. Data* **1980**, *9*, 1.
(68) Véril, M.; Scemama, A.; Caffarel, M.; Lipparini, F.; Boggio-Pasqua, M.; Jacquemin, D.; Loos, P.-F. QUESTDB: A database of highly accurate excitation energies for the electronic structure community. *WIREs Comput. Mol. Sci.* **2021**, *11*, e1517.
(69) Nikitin, M. I.; Malkerova, I. P.; Kayumova, D. B.; Alikhanyan, A. S. Enthalpies of Formation of Chromium Fluorides. II. Higher Fluorides CrF_4, CrF_5, and CrF_6. *Russ. J. Inorg. Chem.* **2021**, *66*, 1519−1526.
(70) Schlöder, T.; Brosi, F.; Freyh, B. J.; Vent-Schmidt, T.; Riedel, S. New Evidence in an Old Case: The Question of Chromium Hexafluoride Reinvestigated. *Inorg. Chem.* **2014**, *53*, 5820−5829.
(71) Roos, B. O.; Andersson, K. Multiconfigurational perturbation theory with level shift - the Cr_2 potential revisited. *Chem. Phys. Lett.* **1995**, *245*, 215−223.
(72) Forsberg, N.; Malmqvist, P.-Å. Multiconfiguration perturbation theory with imaginary level shift. *Chem. Phys. Lett.* **1997**, *274*, 196−204.
(73) Battaglia, S.; Fransén, L.; Fdez. Galván, I.; Lindh, R. Regularized CASPT2: an Intruder-State-Free Approach. *J. Chem. Theory Comput.* **2022**, *18*, 4814−4825.
(74) Platt, J. R. Classification of Spectra of Cata-Condensed Hydrocarbons. *J. Chem. Phys.* **1949**, *17*, 484−495.
(75) Parac, M.; Grimme, S. A TDDFT study of the lowest excitation energies of polycyclic aromatic hydrocarbons. *Chem. Phys.* **2003**, *292*, 11−21.
(76) Grimme, S.; Parac, M. Substantial Errors from Time-Dependent Density Functional Theory for the Calculation of Excited States of Large π Systems. *ChemPhysChem* **2003**, *4*, 292−295.
(77) Yoshizawa, M.; Aoki, H.; Ue, M.; Hashimoto, H. Ultrafast relaxation kinetics of excited states in a series of mini-and macro-β-carotenes. *Phys. Rev. B* **2003**, *67*, 174302.
(78) Spezia, R.; Knecht, S.; Mennucci, B. Excited state characterization of carbonyl containing carotenoids: a comparison between single and multireference descriptions. *Phys. Chem. Chem. Phys.* **2017**, *19*, 17156−17166.
(79) Pang, Y.; Fleming, G. R. Branching relaxation pathways from the hot S_2 state of 8′-apo-β-caroten-8′-al. *Phys. Chem. Chem. Phys.* **2010**, *12*, 6782−6788.
(80) Premvardhan, L.; Sandberg, D. J.; Fey, H.; Birge, R. R.; Büchel, C.; van Grondelle, R. The charge-transfer properties of the S2 state of fucoxanthin in solution and in fucoxanthin chlorophyll-a/c2 protein (FCP) based on stark spectroscopy and molecular-orbital theory. *J. Phys. Chem. B* **2008**, *112*, 11838−11853.
(81) West, R. G.; Fuciman, M.; Staleva-Musto, H.; Šebelík, V.; Bína, D.; Durchan, M.; Kuznetsova, V.; Polívka, T. Equilibration dependence of fucoxanthin S1 and ICT signatures on polarity, proticity, and temperature by multipulse femtosecond absorption spectroscopy. *J. Phys. Chem. B* **2018**, *122*, 7264−7276.
(82) Ehrmaier, J.; Rabe, E. J.; Pristash, S. R.; Corp, K. L.; Schlenker, C. W.; Sobolewski, A. L.; Domcke, W. Singlet-triplet inversion in heptazine and in polymeric carbon nitrides. *J. Phys. Chem. A* **2019**, *123*, 8099−8108.
(83) Dinkelbach, F.; Bracker, M.; Kleinschmidt, M.; Marian, C. M. Large Inverted Singlet-Triplet Energy Gaps Are Not Always Favorable for Triplet Harvesting: Vibronic Coupling Drives the (Reverse) Intersystem Crossing in Heptazine Derivatives. *J. Phys. Chem. A* **2021**, *125*, 10044−10051.
(84) de Silva, P. Inverted singlet-triplet gaps and their relevance to thermally activated delayed fluorescence. *J. Phys. Chem. Lett.* **2019**, *10*, 5674−5679.
(85) Sobolewski, A. L.; Domcke, W. Are heptazine-based organic light-emitting diode chromophores thermally activated delayed fluorescence or inverted singlet−triplet systems? *J. Phys. Chem. Lett.* **2021**, *12*, 6852−6860.

https://doi.org/10.1021/acs.jpca.2c07951
J. Phys. Chem. A 2023, 127, 2011−2025

R2022: A DFT/MRCI Ansatz with Improved Performance for Double Excitations Supporting Information

Dennis R. Dombrowski, Timo Schulz, Martin Kleinschmidt, and Christel M. Marian*

Institute of Theoretical and Computational Chemistry, Heinrich-Heine-University Düsseldorf, 40225 Düsseldorf, Germany

E-mail: christel.marian@hhu.de

Contents

S1 Parameters and statistical data

Table S1: Parameter sets optimized for the standard selection threshold of E_{sel} = 1.0 E_h. $p[0]$ refers to the original Hamiltonian, p_J and p_x to the Hamiltonians R2016 to R2018 and p_J^{he}, p_J^{hhee}, p_x^{he} and p_x^{hhee} to the new R2022 Hamiltonian.

Reference		p_1	p_2	p_j, p_j^{he}	p_j^{hhee}	p_x, $p[0]$, p_x^{he}	p_x^{hhee}	α
Original	Singlet	0.6195	3.2719	0.5102	-	0.5945	-	0.1058
	Triplet			0.4930	-	-	-	0.0563
R2016		0.5682	18.2960	0.5079	-	0.3559	-	-
R2017		0.5639	22.0912	0.5030	-	0.3587	-	-
R2018		0.5584	4.4717	0.5089	-	0.3624	-	-
R2022		-	3.4641	0.5088	0.4659	0.3430	0.5424	-

Table S2: Parameter sets optimized for the tight standard selection threshold of $E_{sel} = 0.8\ E_h$. $p[0]$ refers to the original Hamiltonian, p_J and p_x to the Hamiltonians R2016 to R2018 and p_J^{he}, p_J^{hhee}, p_x^{he} and p_x^{hhee} to the new R2022 Hamiltonian.

Reference		p_1	p_2	p_j, p_j^{he}	p_j^{hhee}	p_x, $p[0]$, p_x^{he}	p_x^{hhee}	α
Original	Singlet	0.6290	8.0000	0.5030	-	0.6110	-	0.1190
	Triplet			0.4860	-	-	-	0.0630
R2016		0.5798	50.0000	0.5035	-	0.3681	-	-
R2017		0.5735	26.5414	0.5008	-	0.3570	-	-
R2018		0.5777	11.4991	0.5058	-	0.3596	-	-
R2022		-	4.5958	0.5051	0.4610	0.3375	0.5414	-

Table S3: RMSD of the states in the fitting set sorted by type for the selection threshold of $E_{sel} = 1.0\ E_h$. $p[0]$. R2016 and R2018 values are given for comparison. Doubly excited states are not included in the singlet or triplet subset. All values in eV.

Subset	R2016	R2018	R2022
Singlets	0.169	0.172	0.171
Triplets	0.151	0.156	0.168
Doubly excited states	0.600	0.583	0.281
Total	0.285	0.281	0.192

Table S4: RMSD of the states in the fitting set sorted by type for the tight selection threshold of $E_{sel} = 0.8\ E_h$. $p[0]$. R2016 and R2018 values are given for comparison. Doubly excited states are not included in the singlet or triplet subset. All values in eV.

Subset	R2016	R2018	R2022
Singlets	0.199	0.170	0.183
Triplets	0.166	0.170	0.184
Doubly excited states	0.639	0.609	0.348
Total	0.310	0.292	0.219

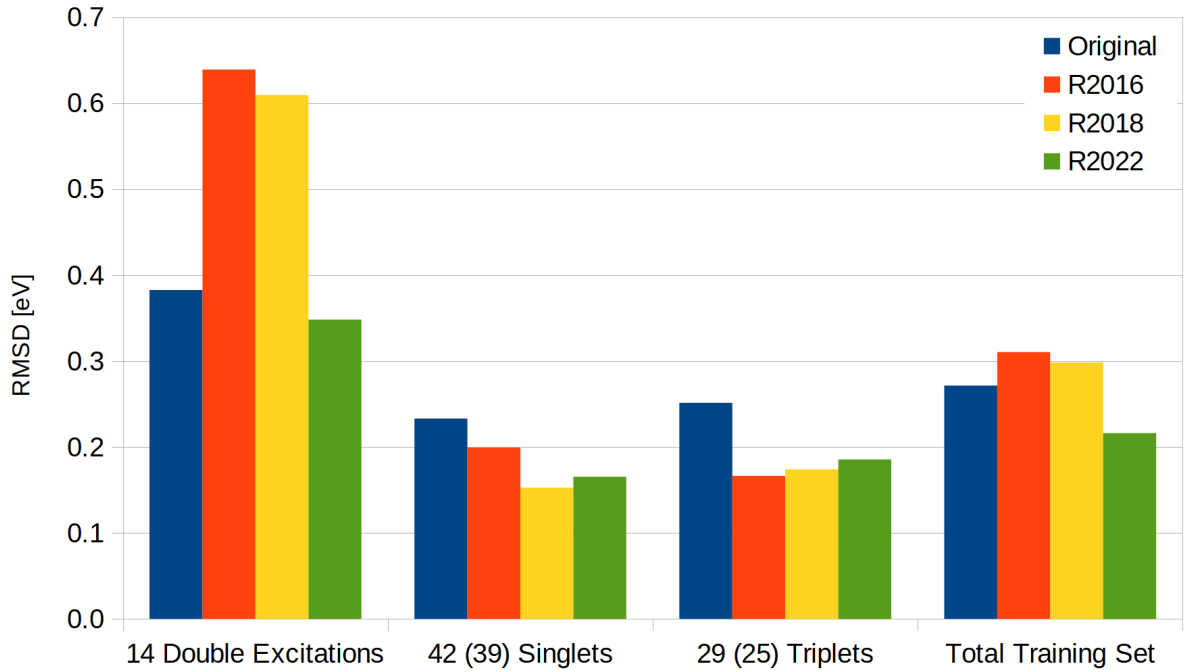

Figure S1: RMSD of the states in the fitting set sorted by type for the tight selection threshold of E_{sel} = 0.8 E_h. Original, R2016 and R2018 values are given for comparison. Doubly excited states are not included in the singlet or triplet subset. Values in brackets are the number of states for the Original Hamiltonian, where dimer states were excluded. All values in eV.

Table S5: Root-mean-square deviation (RMSD), mean absolute error (MAE), mean deviation and minimal and maximal deviation for the singlet and triplet assessment set.

$\Delta E_{sel}(E_h)$	Hamiltonian	RMSD (eV)	MAE (eV)	Mean (eV)	Min (eV)	Max (eV)
1.0	Original	0.164	0.131	0.029	-0.370	0.360
	R2016	0.159	0.117	0.067	-0.280	0.390
	R2018	0.175	0.133	0.066	-0.310	0.489
	R2022	0.151	0.114	0.038	-0.301	0.365
0.8	Original	0.178	0.148	-0.016	-0.395	0.349
	R2016	0.166	0.131	0.033	-0.359	0.395
	R2018	0.153	0.117	0.044	-0.301	0.407
	R2022	0.158	0.124	0.026	-0.320	0.380

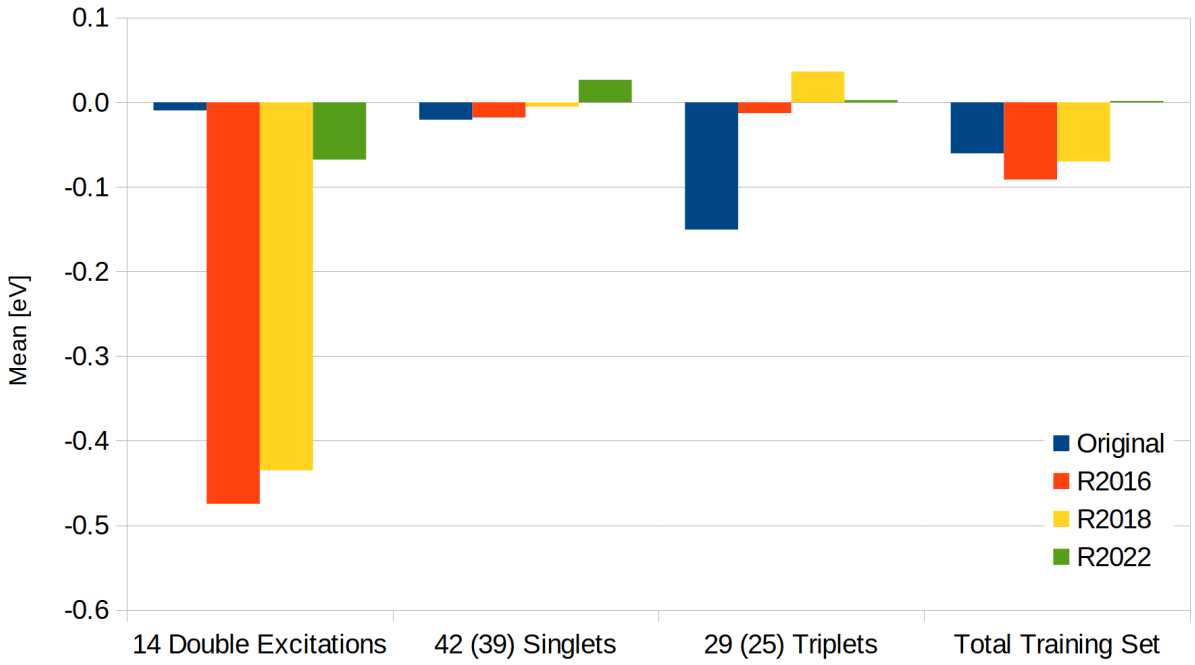

Figure S2: Mean deviation of the states in the fitting set sorted by type for the tight selection threshold of E_{sel} = 0.8 E_h. Original, R2016 and R2018 values are given for comparison. Doubly excited states are not included in the singlet or triplet subset. Values in brackets are the number of states for the Original Hamiltonian, where dimer states were excluded. All values in eV.

Table S6: Root-mean-square deviation (RMSD), mean absolute error (MAE), mean deviation and minimal and maximal deviation for the doublet assessment set. Note that R2016 is missing, because doublet states cannot be described on this level of theory.

$\Delta E_{sel}(E_h)$	Hamiltonian	RMSD (eV)	MAE (eV)	Mean (eV)	Min (eV)	Max (eV)
1.0	R2017	0.166	0.130	-0.007	-0.440	0.420
	R2018	0.166	0.128	-0.003	-0.525	0.428
	R2022	0.161	0.117	0.054	-0.455	0.443
0.8	R2017	0.167	0.131	0.000	-0.450	0.420
	R2018	0.167	0.130	0.006	-0.472	0.495
	R2022	0.165	0.119	0.063	-0.473	0.443

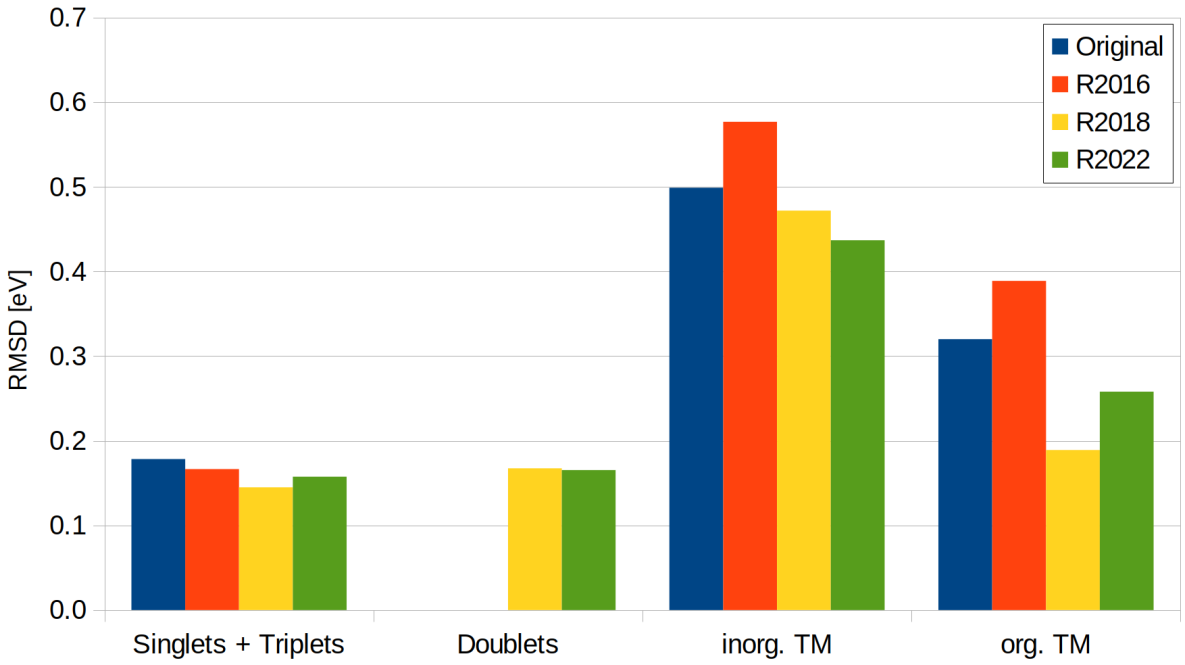

Figure S3: RMSD of the states in the assessment set sorted by type for the tight selection threshold of $E_{sel} = 0.8\ E_h$. R2016, R2018 and values for the original Hamiltonian are given for comparison. Doubly excited states are not included in the singlet or triplet subset. All values are given in eV.

Table S7: Root-mean-square deviation (RMSD), mean absolute error (MAE), mean deviation and minimal and maximal deviation for the inorganic transition metal complexes.

$\Delta E_{sel}(E_h)$	Hamiltonian	RMSD (eV)	MAE (eV)	Mean (eV)	Min (eV)	Max (eV)
1.0	Original	0.40	0.32	-0.14	-0.88	0.33
	R2016	0.60	0.41	-0.35	-1.31	0.42
	R2018	0.50	0.40	-0.04	-1.10	0.85
	R2022	0.43	0.31	-0.19	-1.05	0.34
0.8	Original	0.50	0.31	-0.34	-1.04	0.48
	R2016	0.58	0.35	-0.4	-1.26	0.35
	R2018	0.47	0.35	-0.21	-1.14	0.34
	R2022	0.44	0.31	-0.23	-1.00	0.25

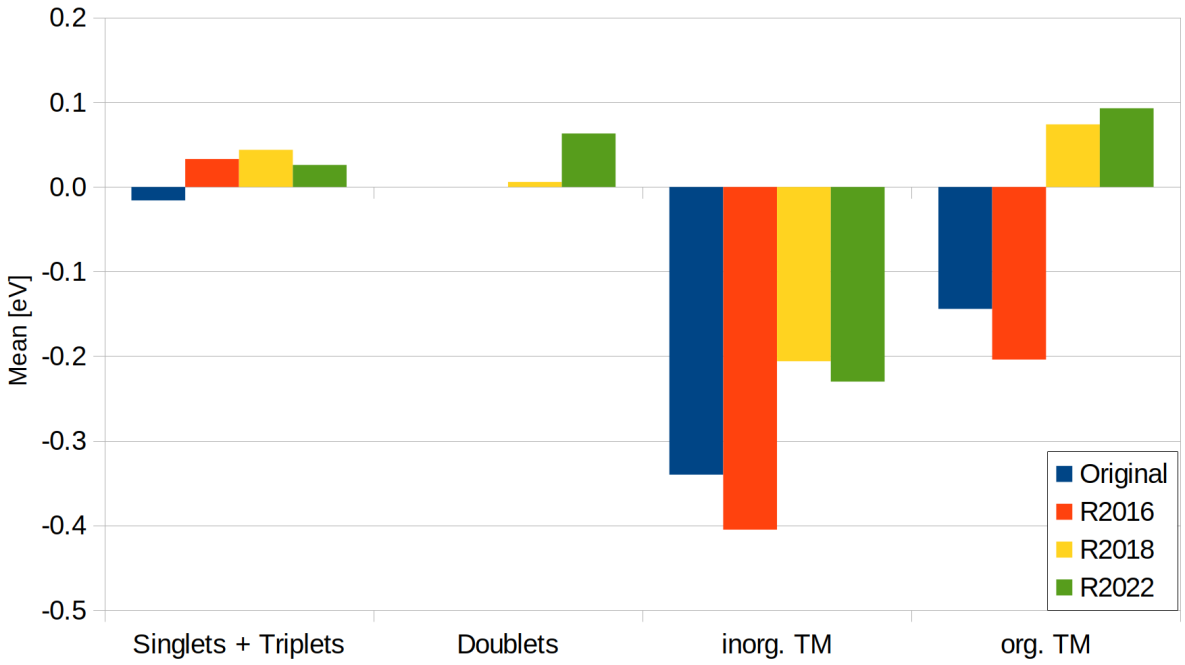

Figure S4: Mean deviation of the states in the assessment set sorted by type for the tight selection threshold of $E_{sel} = 0.8\ E_h$. R2016, R2018 and values for the original Hamiltonian are given for comparison. Doubly excited states are not included in the singlet or triplet subset. All values are given in eV.

Table S8: Root-mean-square deviation (RMSD), mean absolute error (MAE), mean deviation and minimal and maximal deviation for the organic transition metal complexes.

$\Delta E_{sel}(E_h)$	Hamiltonian	RMSD (eV)	MAE (eV)	Mean (eV)	Min (eV)	Max (eV)
1.0	Original	0.20	0.14	-0.10	-0.47	0.20
	R2016	0.26	0.15	-0.17	-0.62	0.28
	R2018	0.13	0.10	-0.02	-0.40	0.20
	R2022	0.20	0.16	0.06	-0.35	0.30
0.8	Original	0.32	0.21	-0.14	-1.06	0.29
	R2016	0.39	0.24	-0.20	-1.16	0.32
	R2018	0.19	0.14	0.07	-0.36	0.40
	R2022	0.26	0.20	0.09	-0.41	0.59

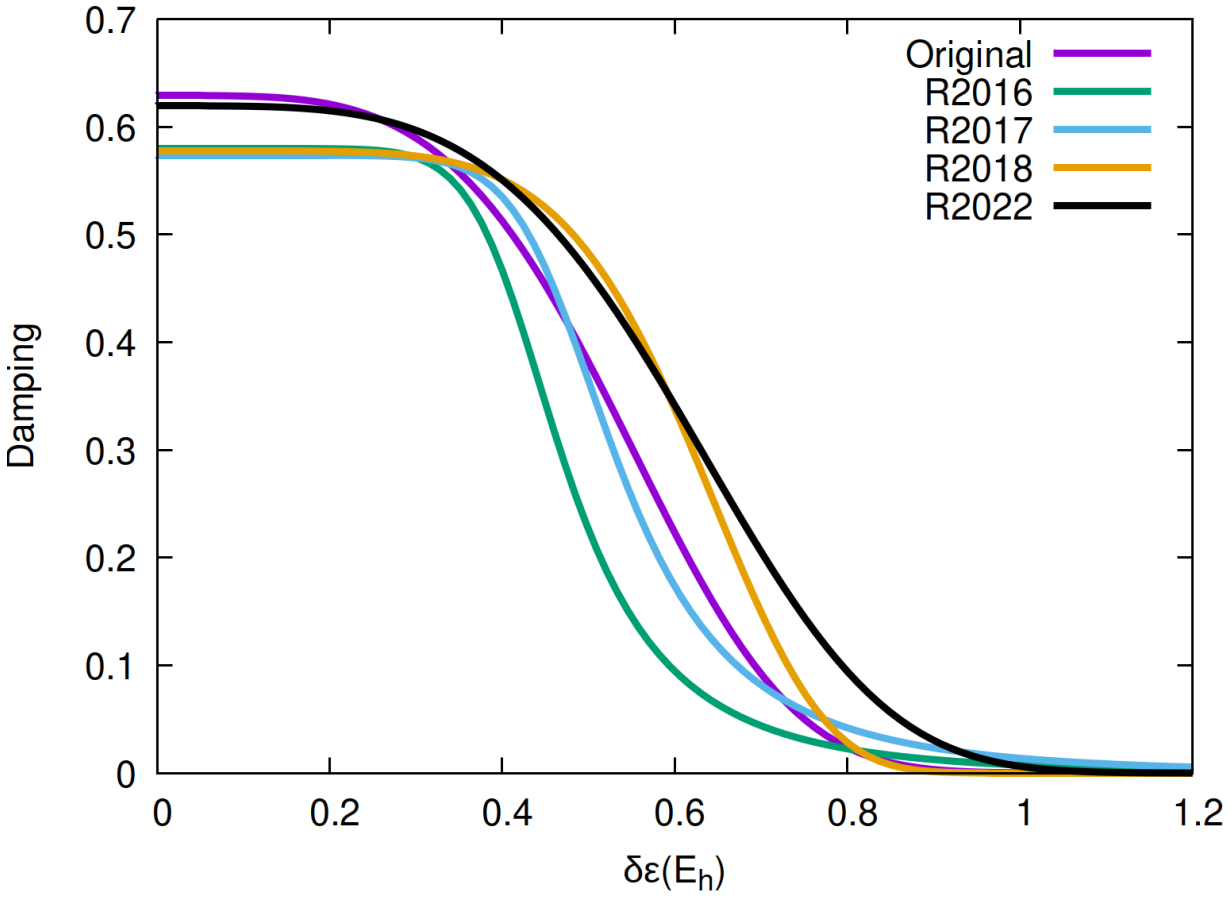

Figure S5: Damping decay for different Hamiltonians for the parameters obtained with a tight selection threshold of $E_{sel} = 0.8\ E_h$ as a function of the energy difference. Note, that for the Original and R2016 Hamiltonials, the damping function parameter p_2 was fixed during the parametrization, while in the other cases it is optimized.

S2 The training data set

Table S9: Molecular states employed in the parameters optimization. Vertical excitation energies for the standard selection threshold of Original, R2016, R2018 and R2022 Hamiltonians in comparison with experimental data. All energies are given in eV.

Molecule	State		Exp./ TBE	Ref.	Original	R2016	R2018	R2022
Acetaldehyde	$1^1A''$	$n \rightarrow \pi^\star$	4.27[b]	1	4.00	4.09	4.04	4.18
	$1^3A''$	$n \rightarrow \pi^\star$	3.97	1	3.58	3.78	3.74	3.87
Acetone	1^1A_2	$n \rightarrow \pi^\star$	4.37[b]	2	4.11	4.26	4.21	4.12
	1^1B_2	$n \rightarrow Ry$	6.35	2	6.54	6.47	6.30	6.42
	1^3A_2	$n \rightarrow \pi^\star$	4.16	2	3.70	3.97	3.93	3.82
Acrolein	$6^1A'$	$\pi^2 \rightarrow \pi^{\star 2}$	7.87	3,4	7.41	7.64	7.64	7.49
	$1^1A''$	$n \rightarrow \pi^\star$	3.75[b]	5	3.38	3.58	3.54	3.50
	$1^3A''$	$n \rightarrow \pi^\star$	3.05	6	3.12	3.33	3.30	3.25
Benzene	1^1E_{2g}	$\pi^2 \rightarrow \pi^{\star 2}$	8.28	3,4	7.69	7.97	8.02	7.94
					7.71	8.07	8.11	7.94
	1^1B_{3u}	$\pi \rightarrow \pi^\star$	4.90[b]	7	5.03	4.99	5.02	5.00
	1^1B_{2u}	$\pi \rightarrow \pi^\star$	6.25[b]	8	6.23	6.12	6.14	6.13
	2^1B_{3u}	$\pi \rightarrow \pi^\star$	6.95[b]	8	7.02	6.91	6.82	6.97
	1^3B_{2u}	$\pi \rightarrow \pi^\star$	3.89	9	4.12	4.13	4.12	4.13
	2^3B_{3u}	$\pi \rightarrow \pi^\star$	5.59	8	5.51	5.49	5.51	5.52
Beryllium	1^1D	$2s^2 \rightarrow 2p^2$	7.15	3,4	6.74	7.16	7.27	6.94
					6.74	7.16	7.27	6.94
					6.74	7.19	7.29	6.97

Continued on next page

Molecule	State		Exp./ TBE	Ref.	Original	R2016	R2018	R2022
					7.22	7.19	7.29	6.97
					7.22	7.19	7.29	6.97
Butadiene	2^1A_g	$\pi \rightarrow \pi^\star$	6.27	10	6.16	6.26	6.34	6.20
	1^1B_u	$\pi \rightarrow \pi^\star$	5.91[b]	11	5.89	5.75	5.72	5.79
	1^3B_u	$\pi \rightarrow \pi^\star$	3.24	11	3.13	3.18	3.22	3.16
	1^3A_g	$\pi \rightarrow \pi^\star$	4.92	11	4.84	4.99	5.05	4.91
Carbon	$1^1\Delta_g$	$\pi^2 \rightarrow \sigma^2$	2.09	3,4	1.84	0.77	0.83	1.76
dimer					2.25	0.84	0.92	1.76
	$2^1\Sigma_g^+$	$\pi^2 \rightarrow \sigma^2$	2.42	3,4	2.56	1.37	1.42	2.12
CO	2^1A	$n \rightarrow \pi^\star$	8.39[b]	12	8.12	8.16	8.09	8.10
Carbon	$1^1\Delta_g$	$\pi^2 \rightarrow \sigma^2$	5.22	3,4	4.98	5.09	5.12	5.70
trimer					5.32	5.13	5.15	5.71
	$2^1\Sigma_g^+$	$\pi^2 \rightarrow \sigma^2$	5.91	3,4	5.78	5.50	5.53	6.18
Cu^+	1^1D	$d \rightarrow s$	3.26[a]	13	3.25	3.24	3.22	3.24
	1^1F	$d \rightarrow p$	8.92[a]	13	8.57	8.57	8.59	8.54
	1^1D	$d \rightarrow p$	9.09[a]	13	8.72	8.72	8.73	8.70
	1^1P	$d \rightarrow p$	9.12[a]	13	9.04	9.00	9.01	9.01
	1^3D	$d \rightarrow s$	2.81[a]	13	2.65	2.84	2.81	2.83
	1^3P	$d \rightarrow p$	8.33[a]	13	8.06	8.23	8.25	8.19
	1^3F	$d \rightarrow p$	8.54[a]	13	8.25	8.41	8.43	8.38
	1^3D	$d \rightarrow p$	8.86[a]	13	8.56	8.68	8.69	8.67
Cyclopentadiene	1^1B_2	$\pi \rightarrow \pi^\star$	5.22[b]	11	5.39	5.29	5.27	5.32
	1^3B_2	$\pi \rightarrow \pi^\star$	3.15	11	3.11	3.16	3.20	3.15

Continued on next page

Molecule	State		Exp./ TBE	Ref.	Original	R2016	R2018	R2022
Ethylene	1^1B_{1u}	$\pi \rightarrow Ry$	7.11	14	7.23	7.20	7.15	7.19
	1^3B_{2u}	$\pi \rightarrow \pi^\star$	4.36	15	4.25	4.36	4.42	4.31
Ethylene	2^1A	$\pi, \pi \rightarrow \pi^\star\pi^\star$	$2 \times \mathrm{E}(1^3\mathrm{B_{2u}})$			8.71	8.88	8.67
dimer	3^3A	$\pi, \pi \rightarrow \pi^\star\pi^\star$	$2 \times \mathrm{E}(1^3\mathrm{B_{2u}})$			8.71	8.88	8.68
Formaldehyde	4^1A_1	$n^2 \rightarrow \pi^{\star 2}$	10.35	3,4	11.19	9.36	9.37	10.00
	1^1A_2	$n \rightarrow \pi^\star$	3.79[b]	1	3.73	3.83	3.78	3.76
	1^1B_1	$n \rightarrow Ry$	7.09	16	7.20	7.11	6.97	7.10
	2^1B_1	$n \rightarrow Ry$	7.97	16	7.96	7.93	7.80	7.90
	1^3A_2	$n \rightarrow \pi^\star$	3.50	1	3.29	3.49	3.45	3.42
Formaldehyde	2^1A	$n, n \rightarrow \pi^\star, \pi^\star$	$2 \times \mathrm{E}(1^3\mathrm{A_2})$			7.09	7.09	7.07
dimer	5^1A	$n, n \rightarrow \pi^\star, \pi^\star$	$2 \times \mathrm{E}(1^1\mathrm{A_2})$			7.80	7.77	7.79
	1^3A	$n, n \rightarrow \pi^\star, \pi^\star$	$2 \times \mathrm{E}(1^3\mathrm{A_2})$			7.09	7.09	7.06
	4^3A	$n, n \rightarrow \pi^\star, \pi^\star$	$\mathrm{E}(1^3\mathrm{A_2}) + \mathrm{E}(1^1\mathrm{A_2})$			7.44	7.43	7.43
	5^3A	$n, n \rightarrow \pi^\star, \pi^\star$	$\mathrm{E}(1^3\mathrm{A_2}) + \mathrm{E}(1^1\mathrm{A_2})$			7.44	7.43	7.43
Furan	1^1B_1	$\pi \rightarrow \pi^\star$	6.04[b]	17	6.15	6.09	6.05	6.10
	3^1A_1	$\pi \rightarrow \pi^\star$	7.82	18	7.95	7.90	7.77	7.90
	1^3B_1	$\pi \rightarrow \pi^\star$	3.99	18	3.82	3.94	4.02	3.88
	1^3A_1	$\pi \rightarrow \pi^\star$	5.22	18	4.99	5.15	5.22	5.06
Glyoxal	2^1A_g	$n^2 \rightarrow \pi^{\star 2}$	5.61	3,4	5.72	5.07	5.09	5.68
	1^1A_u	$n \rightarrow \pi^\star$	2.80[b]	19	2.66	2.70	2.71	2.71
	1^1B_g	$n \rightarrow \pi^\star$	4.20[b]	19	3.83	3.97	4.00	3.92
	1^3A_u	$n \rightarrow \pi^\star$	2.50	19	2.26	2.37	2.39	2.38
Hexatriene	2^1A_g	$\pi^2 \rightarrow \pi^{\star 2}$	5.21	20	4.94	5.18	5.23	5.05

Continued on next page

Molecule	State		Exp./ TBE	Ref.	Original	R2016	R2018	R2022
Magnesium	3^3P	$2s^2 \rightarrow 2p^2$	7.17	21	7.67	6.95	7.00	6.93
					7.67	6.95	7.01	6.93
					7.67	6.95	7.01	6.93
Naphtaline	1^1B_{3u}	$\pi \rightarrow \pi^\star$	3.97[b]	22	4.16	4.18	4.20	4.19
	1^1B_{2u}	$\pi \rightarrow \pi^\star$	4.45[b]	22	4.62	4.55	4.56	4.61
	2^1B_{3u}	$\pi \rightarrow \pi^\star$	5.89[b]	22	5.86	5.76	5.72	5.86
	2^1B_{2u}	$\pi \rightarrow \pi^\star$	6.14[b]	22	6.18	6.09	6.08	6.18
Nitrobenzene	2^1A_1	$\pi \rightarrow \pi^\star$	5.11[b]	23	4.75	4.78	4.80	4.84
Nitromethane	$2^1A'$	$\pi \rightarrow \pi^\star$	6.25[b]	24	6.31	6.34	6.26	6.34
Nitrosomethane	$2^1A'$	$n^2 \rightarrow \pi^{\star 2}$	4.76	3,4	5.07	4.23	4.09	4.95
Nitroxyl	$2^1A'$	$n^2 \rightarrow \pi^{\star 2}$	4.33	3,4	4.63	3.63	3.66	4.55
Pyridine	1^1B_2	$n \rightarrow \pi^\star$	4.78[b]	25	4.76	4.86	4.86	4.84
	1^1B_1	$\pi \rightarrow \pi^\star$	4.99[b]	26	5.18	5.13	5.15	5.15
	2^1A_1	$\pi \rightarrow \pi^\star$	6.38[b]	26	6.42	6.31	6.35	6.33
Pyrrole	1^3B_1	$\pi \rightarrow Ry$	4.21	18	4.04	4.21	4.30	4.12
Ruthenocene	a^1E_{1g}	$d \rightarrow d^\star\pi^\star$	4.54	27	4.16	4.05	4.19	4.30
	b^1E_{1g}	$d \rightarrow d^\star\pi^\star$	3.22	27	3.03	3.04	3.20	3.22
Styrene	$2^1A'$	$\pi \rightarrow \pi^\star$	4.43[b]	28	4.49	4.53	4.56	4.52
	$1^3A'$	$\pi \rightarrow \pi^\star$	3.40	28	3.15	3.18	3.24	3.19
Tetrazine	1^1B_{1u}	$n \rightarrow \pi^\star$	2.25[b]	29	2.36	2.36	2.37	2.46
	1^1A_u	$n \rightarrow \pi^\star$	3.42[b]	30	3.60	3.61	3.66	3.74
	1^1B_{3u}	$\pi \rightarrow \pi^\star$	4.97[b]	31	5.25	5.11	5.17	5.18
	1^3B_{1u}	$n \rightarrow \pi^\star$	1.69	31	1.85	1.85	1.89	1.94

Continued on next page

Molecule	State		Exp./ TBE	Ref.	Original	R2016	R2018	R2022
	1^3A_u	$n \rightarrow \pi^\star$	2.95	29	3.39	3.37	3.42	3.46
Thio-	1^1A_2	$n \rightarrow \pi^\star$	2.03[b]	32	2.18	2.22	2.22	2.22
formaldehyde	1^3A_2	$n \rightarrow \pi^\star$	1.80	32	1.86	1.95	1.94	1.96
Thiophene	2^1A_1	$\pi \rightarrow \pi^\star$	5.43	11	5.52	5.48	5.49	5.48
	1^3B_1	$\pi \rightarrow \pi^\star$	3.74	11	3.75	3.77	3.79	3.77
	1^3A_1	$\pi \rightarrow \pi^\star$	4.62	18	4.56	4.58	4.61	4.60
Water	1^1B_2	$n \rightarrow Ry$	7.40	33	7.50	7.52	7.40	7.40

[a] Changed in comparison to the R2018 training set.

[b] State was used in the basis set study.

Table S10: Molecular states employed in the parameters optimization. Vertical excitation energies for the tight selection threshold of Original, R2016, R2018 and R2022 Hamiltonians in comparison with experimental data. All energies are given in eV.

Molecule	State		Exp./ TBE	Ref.	Original	R2016	R2018	R2022
Acetaldehyde	$1^1A''$	$n \rightarrow \pi^\star$	4.27	1	4.02	4.12	4.03	4.17
	$1^3A''$	$n \rightarrow \pi^\star$	3.97	1	3.60	3.81	3.73	3.86
Acetone	1^1A_2	$n \rightarrow \pi^\star$	4.37	2	4.16	4.31	4.19	4.12
	1^1B_2	$n \rightarrow Ry$	6.35	2	6.70	6.66	6.41	6.49
	1^3A_2	$n \rightarrow \pi^\star$	4.16	2	3.73	4.00	3.90	3.80
Acrolein	$6^1A'$	$\pi^2 \rightarrow \pi^{\star 2}$	7.87	3,4	7.33	7.58	7.62	7.53
	$1^1A''$	$n \rightarrow \pi^\star$	3.75	5	3.38	3.58	3.55	3.49
	$1^3A''$	$n \rightarrow \pi^\star$	3.05	6	3.14	3.33	3.30	3.25
Benzene	1^1E_{2g}	$\pi^2 \rightarrow \pi^{\star 2}$	8.28	3,4	7.55	7.82	7.93	7.91
					7.59	7.93	8.02	7.92
	1^1B_{3u}	$\pi \rightarrow \pi^\star$	4.90	7	5.04	4.94	4.99	5.01
	1^1B_{2u}	$\pi \rightarrow \pi^\star$	6.25	8	6.08	5.93	6.10	6.11
	2^1B_{3u}	$\pi \rightarrow \pi^\star$	6.95	8	7.09	6.97	6.89	7.02
	1^3B_{2u}	$\pi \rightarrow \pi^\star$	3.89	9	4.09	4.10	4.14	4.13
	2^3B_{3u}	$\pi \rightarrow \pi^\star$	5.59	8	5.40	5.36	5.49	5.49
Beryllium	1^1D	$2s^2 \rightarrow 2p^2$	7.15	3,4	6.45	6.96	7.12	6.88
					6.45	6.96	7.12	6.88
					6.46	6.99	7.15	6.91
					6.98	6.99	7.15	6.91
					6.98	6.99	7.15	6.91

Continued on next page

Molecule	State		Exp./ TBE	Ref.	Original	R2016	R2018	R2022
Butadiene	2^1A_g	$\pi \rightarrow \pi^\star$	6.27	10	6.10	6.26	6.26	6.19
	1^1B_u	$\pi \rightarrow \pi^\star$	5.91	11	5.80	5.67	5.73	5.80
	1^3B_u	$\pi \rightarrow \pi^\star$	3.24	11	3.06	3.13	3.16	3.14
	1^3A_g	$\pi \rightarrow \pi^\star$	4.92	11	4.77	4.94	5.03	4.89
Carbon	$1^1\Delta_g$	$\pi^2 \rightarrow \sigma^2$	2.09	3,4	1.59	0.57	0.78	1.66
dimer	$2^1\Sigma_g^+$				2.02	0.65	0.86	1.66
		$\pi^2 \rightarrow \sigma^2$	2.42	3,4	2.31	1.17	1.39	2.04
CO	2^1A	$n \rightarrow \pi^\star$	8.39	12	8.06	8.14	8.13	8.13
Carbon	$1^1\Delta_g$	$\pi^2 \rightarrow \sigma^2$	5.22	3,4	4.83	5.03	5.08	5.87
trimer					5.22	5.05	5.08	5.90
	$2^1\Sigma_g^+$	$\pi^2 \rightarrow \sigma^2$	5.91	3,4	5.67	5.42	5.50	6.41
Cu^+	1^1D		3.26[a]	13	3.25	3.33	3.20	3.22
	1^1F		8.92[a]	13	8.52	8.53	8.54	8.51
	1^1D		9.09[a]	13	8.67	8.67	8.69	8.67
	1^1P		9.12[a]	13	8.98	8.96	8.98	8.98
	1^3D		2.81[a]	13	2.68	2.97	2.80	2.81
	1^3P		8.33[a]	13	8.02	8.18	8.20	8.15
	1^3F		8.54[a]	13	8.20	8.37	8.38	8.34
	1^3D		8.86[a]	13	8.52	8.64	8.65	8.64
Cyclopentadiene	1^1B_2	$\pi \rightarrow \pi^\star$	5.22	11	5.30	5.23	5.27	5.32
	1^3B_2	$\pi \rightarrow \pi^\star$	3.15	11	3.03	3.13	3.15	3.11
Ethylene	1^1B_{1u}	$\pi \rightarrow Ry$	7.11	14	7.21	7.20	7.18	7.18
	1^3B_{2u}	$\pi \rightarrow \pi^\star$	4.36	15	4.15	4.29	4.33	4.26

Continued on next page

Molecule	State		Exp./ TBE	Ref.	Original	R2016	R2018	R2022
Ethylene	2^1A	$\pi,\pi \rightarrow \pi^\star\pi^\star$	$2 \times \mathrm{E}(1^3\mathrm{B}_{2u})$			8.64	8.80	8.71
dimer	3^3A	$\pi,\pi \rightarrow \pi^\star\pi^\star$	$2 \times \mathrm{E}(1^3\mathrm{B}_{2u})$			8.65	8.81	8.71
Formaldehyde	4^1A_1	$n^2 \rightarrow \pi^{\star 2}$	10.35	3,4	11.18	9.41	9.31	9.99
	1^1A_2	$n \rightarrow \pi^\star$	3.79	1	3.75	3.85	3.76	3.74
	1^1B_1	$n \rightarrow Ry$	7.09	16	7.31	7.22	7.05	7.14
	2^1B_1	$n \rightarrow Ry$	7.97	16	8.03	8.00	7.87	7.92
	1^3A_2	$n \rightarrow \pi^\star$	3.50	1	3.30	3.50	3.42	3.39
Formaldehyde	2^1A	$n,n \rightarrow \pi^\star,\pi^\star$	$2 \times \mathrm{E}(1^3\mathrm{A}_2)$			7.15	7.15	7.10
dimer	5^1A	$n,n \rightarrow \pi^\star,\pi^\star$	$2 \times \mathrm{E}(1^1\mathrm{A}_2)$			7.90	7.90	7.88
	1^3A	$n,n \rightarrow \pi^\star,\pi^\star$	$2 \times \mathrm{E}(1^3\mathrm{A}_2)$			7.15	7.16	7.10
	4^3A	$n,n \rightarrow \pi^\star,\pi^\star$	$\mathrm{E}(1^3\mathrm{A}_2) + \mathrm{E}(1^1\mathrm{A}_2)$			7.52	7.53	7.49
	5^3A	$n,n \rightarrow \pi^\star,\pi^\star$	$\mathrm{E}(1^3\mathrm{A}_2) + \mathrm{E}(1^1\mathrm{A}_2)$			7.52	7.53	7.49
Furan	1^1B_1	$\pi \rightarrow \pi^\star$	6.04	17	6.12	6.09	6.06	6.11
	3^1A_1	$\pi \rightarrow \pi^\star$	7.82	18	8.03	7.98	7.87	7.95
	1^3B_1	$\pi \rightarrow \pi^\star$	3.99	18	3.74	3.89	3.93	3.84
	1^3A_1	$\pi \rightarrow \pi^\star$	5.22	18	4.91	5.09	5.14	5.02
Glyoxal	2^1A_g	$n^2 \rightarrow \pi^{\star 2}$	5.61	3,4	5.79	5.20	5.13	5.73
	1^1A_u	$n \rightarrow \pi^\star$	2.80	19	2.66	2.73	2.68	2.69
	1^1B_g	$n \rightarrow \pi^\star$	4.20	19	3.82	3.99	3.95	3.90
	1^3A_u	$n \rightarrow \pi^\star$	2.50	19	2.26	2.41	2.35	2.37
Hexatriene	2^1A_g	$\pi^2 \rightarrow \pi^{\star 2}$	5.21	20	4.87	5.11	5.15	5.04
Magnesium	3^3P	$2s^2 \rightarrow 2p^2$	7.17	21	7.50	6.82	6.92	6.90
					7.50	6.82	6.92	6.90

Continued on next page

Molecule	State		Exp./ TBE	Ref.	Original	R2016	R2018	R2022
					7.50	6.82	6.92	6.90
Naphtaline	1^1B_{3u}	$\pi \rightarrow \pi^\star$	3.97	22	4.17	4.18	4.19	4.21
	1^1B_{2u}	$\pi \rightarrow \pi^\star$	4.45	22	4.17	4.48	4.55	4.61
	2^1B_{3u}	$\pi \rightarrow \pi^\star$	5.89	22	5.90	5.84	5.77	5.91
	2^1B_{2u}	$\pi \rightarrow \pi^\star$	6.14	22	6.17	6.10	6.13	6.21
Nitrobenzene	2^1A_1	$\pi \rightarrow \pi^\star$	5.11	23	4.73	4.72	4.79	4.86
Nitromethane	$2^1A'$	$\pi \rightarrow \pi^\star$	6.25	24	6.29	6.49	6.29	6.40
Nitrosomethane	$2^1A'$	$n^2 \rightarrow \pi^{\star 2}$	4.76	3,4	5.11	4.35	4.10	4.98
Nitroxyl	$2^1A'$	$n^2 \rightarrow \pi^{\star 2}$	4.33	3,4	4.53	3.73	3.56	4.53
Pyridine	1^1B_2	$n \rightarrow \pi^\star$	4.78	25	4.76	4.86	4.87	4.85
	1^1B_1	$\pi \rightarrow \pi^\star$	4.99	26	5.18	5.12	5.11	5.16
	2^1A_1	$\pi \rightarrow \pi^\star$	6.38	26	6.26	6.13	6.29	6.32
Pyrrole	1^3B_1	$\pi \rightarrow Ry$	4.21	18	3.96	4.16	4.20	4.07
Ruthenocene	a^1E_{1g}	$d \rightarrow d^\star\pi^\star$	4.54	27	4.22	4.06	4.35	4.35
	b^1E_{1g}	$d \rightarrow d^\star\pi^\star$	3.22	27	3.00	3.03	3.31	3.25
Styrene	$2^1A'$	$\pi \rightarrow \pi^\star$	4.43	28	4.51	4.53	4.55	4.55
	$1^3A'$	$\pi \rightarrow \pi^\star$	3.40	28	3.12	3.17	3.24	3.20
Tetrazine	1^1B_{1u}	$n \rightarrow \pi^\star$	2.25	29	2.35	2.35	2.40	2.46
	1^1A_u	$n \rightarrow \pi^\star$	3.42	30	3.65	3.63	3.66	3.76
	1^1B_{3u}	$\pi \rightarrow \pi^\star$	4.97	31	5.25	5.15	5.10	5.21
	1^3B_{1u}	$n \rightarrow \pi^\star$	1.69	31	1.86	1.82	1.88	1.94
	1^3A_u	$n \rightarrow \pi^\star$	2.95	29	3.42	3.32	3.40	3.47
Thio-	1^1A_2	$n \rightarrow \pi^\star$	2.03	32	2.09	2.13	2.18	2.18

Continued on next page

Molecule	State		Exp./ TBE	Ref.	Original	R2016	R2018	R2022
formaldehyde	1^3A_2	$n \rightarrow \pi^\star$	1.80	32	1.81	1.88	1.91	1.93
Thiophene	2^1A_1	$\pi \rightarrow \pi^\star$	5.43	11	5.51	5.47	5.46	5.50
	1^3B_1	$\pi \rightarrow \pi^\star$	3.74	11	3.69	3.73	3.76	3.75
	1^3A_1	$\pi \rightarrow \pi^\star$	4.62	18	4.50	4.52	4.58	4.58
Water	1^1B_2	$n \rightarrow Ry$	7.40	33	7.99	7.50	7.46	7.41

[a] Changed in comparison to the R2018 training set.

S3 The assessment data set

Table S11: Selected molecules and vertical absorption energies for the standard selection threshold (in eV) of singlet and triplet states used for benchmarking. In comparison to the R2016 assessment set, 1,3-butadiene, benzene, furan and acetone as well as some states of the marked molecules were removed.

Molecule	State		Exp.	Ref.	Original	R2016	R2018	R2022
Carbon dioxide	$1^1\Delta_u$	$\pi \rightarrow \pi^\star$	8.60	34	8.75	8.80	8.62	8.69
					8.78	8.85	8.65	8.75
Carbon disulfide	$1^3\Delta_u$	$\pi \rightarrow \pi^\star$	3.36	34	3.40	3.37	3.38	3.42
					3.62	3.57	3.58	3.64
	$1^1\Delta_u$	$\pi \rightarrow \pi^\star$	3.91	34	3.97	3.97	3.98	3.98
					4.02	4.02	4.03	4.01
	$1^1\Pi_g$	$\pi \rightarrow \pi^\star$	6.79	34	6.71	6.69	6.66	6.76
Carbonyl sulfide	$1^3\Sigma_u^+$	$\pi \rightarrow \pi^\star$	4.94	34	4.86	4.95	4.99	4.94
	$1^1\Delta_u$	$\pi \rightarrow \pi^\star$	5.53	34	5.64	5.66	5.70	5.56
					5.66	5.67	5.70	5.61
	$1^1\Pi_g$	$\pi \rightarrow Ry$	7.36	34	7.29	7.31	7.29	7.30
	$1^1\Sigma_u^+$	$\pi \rightarrow \pi^\star$	8.02	34	8.26	8.11	7.96	8.20
Sulfur dioxide	1^3B_2	$n \rightarrow \pi^\star$	3.40	34	3.23	3.27	3.29	3.34
	1^1A_2	$n \rightarrow \pi^\star$	4.31	34	4.28	4.29	4.27	4.35
Ethylene[a]	1^1B_{3u}	$\pi \rightarrow \pi^\star$	7.60	34	7.64	7.51	7.45	7.55
	2^1B_{3g}	$\sigma \rightarrow \pi^\star$	8.25	34	8.21	8.25	8.26	8.23
	2^1B_{1u}	$\pi \rightarrow Ry$	8.91	34	8.94	8.89	8.83	8.89
Propene	$1^3A\prime$	$\pi \rightarrow \pi^\star$	4.28	34	4.14	4.35	4.43	4.23
	$1^1A''$	$\pi \rightarrow Ry$	6.60	34	6.61	6.64	6.59	6.59

Continued on next page

Molecule	State		Exp.	Ref.	Original	R2016	R2018	R2022
	$2^1A\prime$	$\pi \rightarrow \pi^\star$	7.17	34	7.22	7.16	7.11	7.17
iso-butene	1^3A_1	$\pi \rightarrow \pi^\star$	4.22	34	4.04	4.30	4.37	4.14
	1^1B_1	$\pi \rightarrow Ry$	6.10	34	6.26	6.29	6.23	6.24
	2^1A_1	$\pi \rightarrow \pi^\star$	6.71	34	6.69	6.67	6.62	6.65
	3^1A_1	$\pi \rightarrow \pi^\star$	7.78	34	7.88	7.88	7.80	7.87
cis-2-Butene	2^3B_2	$\pi \rightarrow \pi^\star$	4.21	34	4.27	4.41	4.46	4.33
	1^1B_2	$\pi \rightarrow \pi^\star$	7.10	34	7.40	7.32	7.27	7.33
trans-2-Butene	1^3B_u	$\pi \rightarrow \pi^\star$	4.24	34	4.18	4.37	4.43	4.26
	1^1A_u	$\pi \rightarrow Ry$	6.30	34	6.31	6.33	6.27	6.29
	1^1B_u	$\pi \rightarrow \pi^\star$	6.95	34	7.12	7.06	7.01	7.07
Trimethylethylene	$1^3A\prime$	$\pi \rightarrow \pi^\star$	4.16	34	4.02	4.31	4.38	4.13
	$1^1A''$	$\pi \rightarrow Ry$	5.76	34	5.87	5.91	5.84	5.85
	$2^1A\prime$	$\pi \rightarrow \pi^\star$	6.47	34	6.59	6.60	6.54	6.57
	$3^1A\prime$	$\pi \rightarrow \pi^\star$	6.97	34	7.20	7.19	7.13	7.18
Tetramethylethylene	1^3A	$\pi \rightarrow \pi^\star$	4.10	34	4.07	4.27	4.32	4.15
	2^1A	$\pi \rightarrow Ry$	5.55	34	5.67	5.70	5.61	5.65
	5^1A	$\pi \rightarrow \pi^\star$	6.57	34	6.65	6.64	6.49	6.54
Fluoroethylene	$1^3A\prime$	$\pi \rightarrow \pi^\star$	4.40	34	4.34	4.46	4.53	4.40
	$1^1A''$	$\pi \rightarrow Ry$	7.02	34	7.09	7.09	7.06	7.06
	$2^1A\prime$	$\pi \rightarrow \pi^\star$	7.50	34	7.66	7.53	7.48	7.57
	$3^1A''$	$\pi \rightarrow Ry$	8.08	34	7.88	7.89	7.86	7.86
	$5^1A''$	$\pi \rightarrow Ry$	8.87	34	9.02	8.98	8.94	8.98
1,1-Difluoroethylene	1^3A_1	$\pi \rightarrow \pi^\star$	4.63	34	4.47	4.68	4.76	4.56
	1^1B_2	$\pi \rightarrow Ry$	6.95	34	6.98	6.99	6.96	6.96

Continued on next page

Molecule	State		Exp.	Ref.	Original	R2016	R2018	R2022
	2^1A_1	$\pi \rightarrow \pi^\star$	7.50	34	7.67	7.59	7.54	7.60
	1^1A_2	$\pi \rightarrow Ry$	8.23	34	7.93	7.98	7.97	7.93
cis-1,2-Difluoroethylene	1^3B_1	$\pi \rightarrow \pi^\star$	4.43	34	4.43	4.53	4.60	4.48
	1^1B_2	$\pi \rightarrow Ry$	6.52	34	6.43	6.48	6.49	6.43
	1^1B_1	$\pi \rightarrow \pi^\star$	7.82	34	7.96	7.80	7.76	7.86
	2^1A_1	$\pi \rightarrow Ry$	8.38	34	8.29	8.24	8.21	8.25
	3^1B_2	$\pi \rightarrow Ry$	9.01	34	8.81	8.79	8.79	8.78
trans-1,2-Difluoroethylene	1^3B_u	$\pi \rightarrow \pi^\star$	4.18	34	4.27	4.37	4.43	4.33
	1^1B_g	$\pi \rightarrow Ry$	6.44	34	6.60	6.70	6.71	6.60
	1^1B_u	$\pi \rightarrow \pi^\star$	7.39	34	7.68	7.53	7.48	7.58
Trifluoroethylene	$1^3A\prime$	$\pi \rightarrow \pi^\star$	4.43	34	4.39	4.61	4.70	4.48
	$1^1A''$	$\pi \rightarrow Ry$	6.56	34	6.47	6.56	6.59	6.48
	$2^1A\prime$	$\pi \rightarrow \pi^\star$	7.65	34	7.85	7.77	7.74	7.79
	$3^1A''$	$\pi \rightarrow Ry$	7.98	34	7.79	7.78	7.78	7.78
	$4^1A''$	$\pi \rightarrow Ry$	8.74	34	8.77	8.78	8.78	8.76
Tetrafluoroethylene	1^3B_{2u}	$\pi \rightarrow \pi^\star$	4.68	34	4.85	4.84	4.91	4.87
	1^1B_{1u}	$\pi \rightarrow Ry$	6.62	34	6.81	6.80	6.82	6.80
	6^1B_{2u}	$\pi \rightarrow \pi^\star$	8.84	34	8.79	8.58	8.53	8.66
Chlorotrifluoroethylene	$1^3A\prime$	$\pi \rightarrow \pi^\star$	4.43	34	4.41	4.51	4.56	4.46
	$2^1A''$	$\pi \rightarrow Ry$	6.51	34	6.54	6.59	6.57	6.55
Chloroethylene	$1^3A\prime$	$\pi \rightarrow \pi^\star$	4.08	34	4.08	4.22	4.25	4.14
	$2^1A\prime$	$\pi \rightarrow \pi^\star$	6.72	34	6.82	6.73	6.63	6.75
Acetylene	$1^3\Sigma_u^+$	$\pi \rightarrow \pi^\star$	5.20	34	5.23	5.43	5.53	5.32
	$1^3\Delta_u$	$\pi \rightarrow \pi^\star$	6.00	34	5.72	5.87	5.97	5.80

Continued on next page

Molecule	State		Exp.	Ref.	Original	R2016	R2018	R2022
					5.81	6.05	6.15	5.95
	$1^1\Pi_u$	$\pi \rightarrow Ry$	8.16	34	7.96	7.91	7.89	7.91
Propyne	$1^3A\prime$	$\pi \rightarrow \pi^\star$	5.20	34	5.16	5.48	5.56	5.27
	$2^3A\prime$	$\pi \rightarrow \pi^\star$	5.80	34	5.62	5.89	5.97	5.72
	$3^1A\prime$	$\pi \rightarrow Ry$	7.18	34	6.91	6.94	6.89	6.89
1-Butyne	$1^3A\prime$	$\pi \rightarrow \pi^\star$	5.20	34	5.11	5.45	5.51	5.22
	$2^3A\prime$	$\pi \rightarrow \pi^\star$	5.80	34	5.57	5.85	5.92	5.67
3,3,3-Trifluoropropyne	$1^3A\prime$	$\pi \rightarrow \pi^\star$	5.00	34	5.27	5.39	5.49	5.33
	$2^3A\prime$	$\pi \rightarrow \pi^\star$	5.80	34	5.75	5.81	5.92	5.80
	$3^1A\prime$	$\pi \rightarrow Ry$	8.80	34	8.55	8.52	8.54	8.51
trans-1,3-Pentadiene	$1^3A\prime$	$\pi \rightarrow \pi^\star$	3.14	34	3.14	3.19	3.23	3.17
	$2^3A\prime$	$\pi \rightarrow \pi^\star$	4.87	34	4.83	4.99	5.06	4.90
	$1^1A''$	$\pi \rightarrow \pi^\star$	5.80	34	5.83	5.81	5.78	5.81
cis-2-*trans*-4-Hexadiene	$1^3A\prime$	$\pi \rightarrow \pi^\star$	3.11	34	3.12	3.17	3.20	3.15
	$2^3A\prime$	$\pi \rightarrow \pi^\star$	4.80	34	4.93	5.02	5.08	4.90
	$2^1A\prime$	$\pi \rightarrow \pi^\star$	5.69	34	5.71	5.61	5.58	5.64
1,3-Cyclohexadiene	1^3B	$\pi \rightarrow \pi^\star$	2.94	34	2.89	2.95	3.00	2.93
	1^1B	$\pi \rightarrow \pi^\star$	4.94	34	5.06	4.96	4.94	4.99
1,5-Hexadiene	1^3A	$\pi \rightarrow \pi^\star$	4.25	34	4.00	4.29	4.39	4.12
1,4-Cyclohexadiene	1^3B_{2g}	$\pi \rightarrow \pi^\star$	4.29	34	4.15	4.35	4.43	4.26
	1^1B_{3g}	$\pi \rightarrow \pi^\star$	6.15	34	6.27	6.30	6.26	6.26
	3^1B_{3g}	$\pi \rightarrow \pi^\star$	7.95	34	7.88	7.89	7.80	7.86
Propadiene	1^3A_1	$\pi \rightarrow \pi^\star$	4.28	34	4.38	4.61	4.67	4.47
	2^1A_1	$\pi \rightarrow \pi^\star$	7.24	34	7.16	7.14	7.10	7.12

Continued on next page

Molecule	State		Exp.	Ref.	Original	R2016	R2018	R2022
Fluorobenzene	1^3A_1	$\pi \rightarrow \pi^\star$	3.90	34	4.16	4.19	4.21	4.17
	2^3B_1	$\pi \rightarrow \pi^\star$	5.72	34	5.63	5.61	5.64	5.64
	1^1B_1	$\pi \rightarrow \pi^\star$	4.78	34	5.02	5.00	5.01	5.00
	2^1A_1	$\pi \rightarrow \pi^\star$	6.23	34	6.26	6.15	6.17	6.16
o-Difluorobenzene	1^3B_1	$\pi \rightarrow \pi^\star$	3.92	34	4.17	4.19	4.23	4.18
	2^3A_1	$\pi \rightarrow \pi^\star$	5.67	34	5.65	5.63	5.66	5.66
	2^1A_1	$\pi \rightarrow \pi^\star$	4.76	34	5.04	5.01	5.03	5.01
	1^1B_1	$\pi \rightarrow \pi^\star$	6.22	34	6.30	6.19	6.21	6.20
1,3,5-Trifluorobenzene	1^3A_1	$\pi \rightarrow \pi^\star$	3.95	34	4.23	4.25	4.25	4.24
	2^3B_2	$\pi \rightarrow \pi^\star$	5.62	34	5.61	5.59	5.61	5.62
	1^1B_2	$\pi \rightarrow \pi^\star$	4.87	34	5.13	5.12	5.12	5.11
	2^1A_1	$\pi \rightarrow \pi^\star$	6.20	34	6.34	6.24	6.26	6.25
1,2,3,4-Tetrafluorobenzene	1^3B_1	$\pi \rightarrow \pi^\star$	3.95	34	4.19	4.20	4.24	4.19
	2^1A_1	$\pi \rightarrow \pi^\star$	4.85	34	5.07	5.04	5.06	5.05
	1^1B_1	$\pi \rightarrow \pi^\star$	6.43	34	6.37	6.27	6.28	6.28
1,2,4,5-Tetrafluorobenzene	1^3B_{2u}	$\pi \rightarrow \pi^\star$	4.00	34	4.18	4.18	4.17	4.19
	1^1B_{3u}	$\pi \rightarrow \pi^\star$	4.69	34	4.97	4.95	4.95	4.95
	1^1B_{2u}	$\pi \rightarrow \pi^\star$	6.30	34	6.40	6.28	6.30	6.31
Pentafluorobenzene	1^3A_1	$\pi \rightarrow \pi^\star$	3.90	34	4.26	4.22	4.25	4.22
	1^1B_1	$\pi \rightarrow \pi^\star$	4.79	34	5.09	5.07	5.08	5.07
	2^1A_1	$\pi \rightarrow \pi^\star$	6.36	34	6.44	6.38	6.34	6.35
Hexafluorobenzene	1^3B_{2u}	$\pi \rightarrow \pi^\star$	3.86	34	4.18	4.15	4.14	4.18
	1^1B_{3u}	$\pi \rightarrow \pi^\star$	4.80	34	5.15	5.10	5.13	5.12
	1^1B_{2u}	$\pi \rightarrow \pi^\star$	6.36	34	6.51	6.38	6.40	6.40

Continued on next page

Molecule	State		Exp.	Ref.	Original	R2016	R2018	R2022
Thiophene[a]	3^1A_1	$\pi \rightarrow \pi^\star$	7.05	34	7.10	7.11	7.05	7.07
Pyrrole[a]	1^1A_2	$\pi \rightarrow Ry$	5.22	34	5.11	5.07	5.03	5.07
	1^1B_1	$\pi \rightarrow \pi^\star$	5.98	34	6.01	5.98	5.95	5.98
Azomethane	1^3B_g	$n \rightarrow \pi^\star$	2.75	34	2.62	2.79	2.80	2.76
	1^1B_g	$\pi \rightarrow \pi^\star$	3.50	34	3.44	3.48	3.43	3.44
	2^1B_u	$n \rightarrow Ry$	6.71	34	6.92	6.97	6.80	6.94
	3^1B_u	$\pi \rightarrow \pi^\star$	7.80	34	8.07	8.02	7.93	8.02
Azo-tert-butane	1^3B_g	$n \rightarrow \pi^\star$	2.67	34	2.30	2.61	2.61	2.44
	1^3B_u	$\pi \rightarrow \pi^\star$	4.90	34	4.70	5.08	5.14	4.82
	1^1B_g	$n \rightarrow \pi^\star$	3.37	34	3.10	3.28	3.23	3.12
	3^1B_u	$n \rightarrow Ry$	7.30	34	7.39	7.53	7.24	7.39
Nitromethane[a]	$2^1A''$	$n \rightarrow \pi^\star$	4.45	34	4.35	4.36	4.41	4.39
Thiophosgene	1^3A_1	$\pi \rightarrow \pi^\star$	3.10	34	3.08	3.10	3.11	3.11
	1^1A_2	$n \rightarrow \pi^\star$	2.61	34	2.65	2.68	2.69	2.68
	1^1A_1	$\pi \rightarrow \pi^\star$	4.89	34	4.91	4.88	4.82	4.85
1,3-Cyclopentadiene	1^3B_2	$\pi \rightarrow \pi^\star$	3.10	34	3.11	3.16	3.20	3.15
	1^1B_2	$\pi \rightarrow \pi^\star$	5.26	34	5.39	5.29	5.27	5.32
Pyridine	1^1A_2	$n \rightarrow \pi^\star$	5.43	35	5.39	5.43	5.41	5.45
Pyrazine	1^3B_{1u}	$n \rightarrow \pi^\star$	3.33	35	3.55	3.61	3.65	3.64
	1^3B_{2g}	$n \rightarrow \pi^\star$	4.59	35	4.87	4.96	5.00	4.96
	1^1B_{1u}	$n \rightarrow \pi^\star$	3.83	35	4.03	4.04	4.05	4.08
	1^1B_{2g}	$n \rightarrow \pi^\star$	5.19	35	5.33	5.45	5.47	5.45
Pyrimidine	1^1A_2	$n \rightarrow \pi^\star$	4.62	26	4.83	4.86	4.86	4.91
s-Triazine	1^1B_2	$n \rightarrow \pi^\star$	4.59	26	4.62	4.66	4.67	4.71

Continued on next page

Molecule	State		Exp.	Ref.	Original	R2016	R2018	R2022
Acetamide	$1^1A''$	$n \rightarrow \pi^\star$	5.44	36	5.27	5.43	5.38	5.28
Nitrobenzene	1^1A_2	$n \rightarrow \pi^\star$	3.65	37	3.32	3.52	3.60	3.55
Dithiosuccinimide	1^3B_1	$n \rightarrow \pi^\star$	2.63	38	2.44	2.58	2.58	2.55
	1^1B_1	$n \rightarrow \pi^\star$	2.77	38	2.65	2.73	2.72	2.70
	1^1A_2	$n \rightarrow \pi^\star$	3.04	38	2.84	2.93	2.93	2.89

[a] Some states were removed in comparison to the R2016 assessment set.

Table S12: Selected molecules and vertical absorption energies for the tight selection threshold (in eV) of singlet and triplet states used for benchmarking. In comparison to the R2016 assessment set, 1,3-butadiene, benzene, furan and acetone as well as some states of the marked molecules were removed.

Molecule	State		Exp.	Ref.	Original	R2016	R2018	R2022
Carbon dioxide	$1^1\Delta_u$	$\pi \rightarrow \pi^\star$	8.60	34	8.82	8.94	8.62	8.72
					8.84	8.97	8.63	8.77
Carbon disulfide	$1^3\Delta_u$	$\pi \rightarrow \pi^\star$	3.36	34	3.31	3.33	3.44	3.43
					3.54	3.53	3.65	3.66
	$1^1\Delta_u$	$\pi \rightarrow \pi^\star$	3.91	34	3.92	3.92	4.05	4.02
					3.93	3.92	4.08	4.04
	$1^1\Pi_g$	$\pi \rightarrow \pi^\star$	6.79	34	6.77	6.74	6.81	6.83
Carbonyl sulfide	$1^3\Sigma_u^+$	$\pi \rightarrow \pi^\star$	4.94	34	4.75	4.82	4.97	4.91
	$1^1\Delta_u$	$\pi \rightarrow \pi^\star$	5.53	34	5.50	5.50	5.64	5.57
					5.53	5.53	5.66	5.61
	$1^1\Pi_g$	$\pi \rightarrow Ry$	7.36	34	7.25	7.26	7.31	7.30
	$1^1\Sigma_u^+$	$\pi \rightarrow \pi^\star$	8.02	34	8.29	8.09	8.09	8.26
Sulfur dioxide	1^3B_2	$n \rightarrow \pi^\star$	3.40	34	3.17	3.25	3.25	3.30
	1^1A_2	$n \rightarrow \pi^\star$	4.31	34	4.27	4.33	4.27	4.34
Ethylene[a]	1^1B_{3u}	$\pi \rightarrow \pi^\star$	7.60	34	7.55	7.44	7.46	7.56
	2^1B_{3g}	$\sigma \rightarrow \pi^\star$	8.25	34	8.17	8.24	8.22	8.20
	2^1B_{1u}	$\pi \rightarrow Ry$	8.91	34	8.92	8.89	8.87	8.89
Propene	$1^3A\prime$	$\pi \rightarrow \pi^\star$	4.28	34	4.05	4.29	4.32	4.17
	$1^1A''$	$\pi \rightarrow Ry$	6.60	34	6.62	6.66	6.61	6.59
	$2^1A\prime$	$\pi \rightarrow \pi^\star$	7.17	34	7.18	7.13	7.12	7.17
iso-butene	1^3A_1	$\pi \rightarrow \pi^\star$	4.22	34	3.97	4.24	4.25	4.08

Continued on next page

Molecule	State		Exp.	Ref.	Original	R2016	R2018	R2022
	1^1B_1	$\pi \rightarrow Ry$	6.10	34	6.29	6.33	6.26	6.25
	2^1A_1	$\pi \rightarrow \pi^\star$	6.71	34	6.68	6.68	6.63	6.66
	3^1A_1	$\pi \rightarrow \pi^\star$	7.78	34	7.93	7.91	7.84	7.89
cis-2-Butene	2^3B_2	$\pi \rightarrow \pi^\star$	4.21	34	4.18	4.34	4.37	4.28
	1^1B_2	$\pi \rightarrow \pi^\star$	7.10	34	7.33	7.27	7.28	7.34
trans-2-Butene	1^3B_u	$\pi \rightarrow \pi^\star$	4.24	34	4.09	4.30	4.33	4.21
	1^1A_u	$\pi \rightarrow Ry$	6.30	34	6.33	6.36	6.31	6.30
	1^1B_u	$\pi \rightarrow \pi^\star$	6.95	34	7.07	7.03	7.02	7.07
Trimethylethylene	$1^3A\prime$	$\pi \rightarrow \pi^\star$	4.16	34	3.95	4.24	4.26	4.07
	$1^1A''$	$\pi \rightarrow Ry$	5.76	34	5.91	5.95	5.87	5.86
	$2^1A\prime$	$\pi \rightarrow \pi^\star$	6.47	34	6.61	6.63	6.57	6.58
	$3^1A\prime$	$\pi \rightarrow \pi^\star$	6.97	34	7.21	7.22	7.16	7.19
Tetramethylethylene	1^3A	$\pi \rightarrow \pi^\star$	4.10	34	4.00	4.20	4.23	4.10
	2^1A	$\pi \rightarrow Ry$	5.55	34	5.71	5.74	5.67	5.66
	5^1A	$\pi \rightarrow \pi^\star$	6.57	34	6.61	6.62	6.54	6.56
Fluoroethylene	$1^3A\prime$	$\pi \rightarrow \pi^\star$	4.40	34	4.23	4.39	4.43	4.35
	$1^1A''$	$\pi \rightarrow Ry$	7.02	34	7.06	7.08	7.06	7.05
	$2^1A\prime$	$\pi \rightarrow \pi^\star$	7.50	34	7.57	7.48	7.48	7.57
	$3^1A''$	$\pi \rightarrow Ry$	8.08	34	7.86	7.88	7.87	7.84
	$5^1A''$	$\pi \rightarrow Ry$	8.87	34	9.00	8.98	8.97	8.98
1,1-Difluoroethylene	1^3A_1	$\pi \rightarrow \pi^\star$	4.63	34	4.37	4.61	4.64	4.49
	1^1B_2	$\pi \rightarrow Ry$	6.95	34	6.97	7.00	6.96	6.95
	2^1A_1	$\pi \rightarrow \pi^\star$	7.50	34	7.63	7.58	7.55	7.61
	1^1A_2	$\pi \rightarrow Ry$	8.23	34	7.90	7.97	7.95	7.91

Continued on next page

Molecule	State		Exp.	Ref.	Original	R2016	R2018	R2022
cis-1,2-Difluoroethylene	1^3B_1	$\pi \rightarrow \pi^\star$	4.43	34	4.32	4.45	4.50	4.43
	1^1B_2	$\pi \rightarrow Ry$	6.52	34	6.37	6.45	6.46	6.40
	1^1B_1	$\pi \rightarrow \pi^\star$	7.82	34	7.85	7.74	7.76	7.86
	2^1A_1	$\pi \rightarrow Ry$	8.38	34	8.27	8.24	8.23	8.25
	3^1B_2	$\pi \rightarrow Ry$	9.01	34	8.76	8.77	8.78	8.77
trans-1,2-Difluoroethylene	1^3B_u	$\pi \rightarrow \pi^\star$	4.18	34	4.16	4.29	4.35	4.27
	1^1B_g	$\pi \rightarrow Ry$	6.44	34	6.54	6.65	6.66	6.57
	1^1B_u	$\pi \rightarrow \pi^\star$	7.39	34	7.57	7.45	7.48	7.58
Trifluoroethylene	$1^3A\prime$	$\pi \rightarrow \pi^\star$	4.43	34	4.28	4.54	4.57	4.42
	$1^1A''$	$\pi \rightarrow Ry$	6.56	34	6.41	6.53	6.53	6.45
	$2^1A\prime$	$\pi \rightarrow \pi^\star$	7.65	34	7.79	7.74	7.73	7.79
	$3^1A''$	$\pi \rightarrow Ry$	7.98	34	7.76	7.78	7.77	7.76
	$4^1A''$	$\pi \rightarrow Ry$	8.74	34	8.74	8.76	8.76	8.75
Tetrafluoroethylene	1^3B_{2u}	$\pi \rightarrow \pi^\star$	4.68	34	4.72	4.78	4.83	4.82
	1^1B_{1u}	$\pi \rightarrow Ry$	6.62	34	6.75	6.77	6.79	6.78
	6^1B_{2u}	$\pi \rightarrow \pi^\star$	8.84	34	8.65	8.48	8.54	8.67
Chlorotrifluoroethylene	$1^3A\prime$	$\pi \rightarrow \pi^\star$	4.43	34	4.31	4.44	4.49	4.42
	$2^1A''$	$\pi \rightarrow Ry$	6.51	34	6.53	6.57	6.57	6.54
Chloroethylene	$1^3A\prime$	$\pi \rightarrow \pi^\star$	4.08	34	3.99	4.16	4.18	4.09
	$2^1A\prime$	$\pi \rightarrow \pi^\star$	6.72	34	6.81	6.73	6.67	6.77
Acetylene	$1^3\Sigma_u^+$	$\pi \rightarrow \pi^\star$	5.20	34	5.14	5.38	5.39	5.25
	$1^3\Delta_u$	$\pi \rightarrow \pi^\star$	6.00	34	5.62	5.82	5.83	5.74
					5.72	6.00	6.01	5.89
	$1^1\Pi_u$	$\pi \rightarrow Ry$	8.16	34	7.96	7.95	7.88	7.90

Continued on next page

Molecule	State		Exp.	Ref.	Original	R2016	R2018	R2022
Propyne	$1^3A\prime$	$\pi \rightarrow \pi^\star$	5.20	34	5.09	5.43	5.42	5.22
	$2^3A\prime$	$\pi \rightarrow \pi^\star$	5.80	34	5.54	5.84	5.83	5.67
	$3^1A\prime$	$\pi \rightarrow Ry$	7.18	34	6.94	7.00	6.89	6.89
1-Butyne	$1^3A\prime$	$\pi \rightarrow \pi^\star$	5.20	34	5.05	5.40	5.38	5.17
	$2^3A\prime$	$\pi \rightarrow \pi^\star$	5.80	34	5.50	5.81	5.79	5.61
3,3,3-Trifluoropropyne	$1^3A\prime$	$\pi \rightarrow \pi^\star$	5.00	34	5.16	5.33	5.39	5.29
	$2^3A\prime$	$\pi \rightarrow \pi^\star$	5.80	34	5.63	5.75	5.82	5.75
	$3^1A\prime$	$\pi \rightarrow Ry$	8.80	34	8.49	8.51	8.53	8.50
trans-1,3-Pentadiene	$1^3A\prime$	$\pi \rightarrow \pi^\star$	3.14	34	3.08	3.15	3.19	3.15
	$2^3A\prime$	$\pi \rightarrow \pi^\star$	4.87	34	4.76	4.94	5.02	4.88
	$1^1A''$	$\pi \rightarrow \pi^\star$	5.80	34	5.82	5.80	5.79	5.81
cis-2-*trans*-4-Hexadiene	$1^3A\prime$	$\pi \rightarrow \pi^\star$	3.11	34	3.06	3.14	3.16	3.13
	$2^3A\prime$	$\pi \rightarrow \pi^\star$	4.80	34	4.75	4.96	5.03	4.88
	$2^1A\prime$	$\pi \rightarrow \pi^\star$	5.69	34	5.64	5.56	5.59	5.65
1,3-Cyclohexadiene	1^3B	$\pi \rightarrow \pi^\star$	2.94	34	2.83	2.92	2.95	2.91
	1^1B	$\pi \rightarrow \pi^\star$	4.94	34	4.98	4.90	4.94	4.99
1,5-Hexadiene	1^3A	$\pi \rightarrow \pi^\star$	4.25	34	3.91	4.24	4.32	4.07
1,4-Cyclohexadiene	1^3B_{2g}	$\pi \rightarrow \pi^\star$	4.29	34	4.06	4.29	4.35	4.21
	1^1B_{3g}	$\pi \rightarrow \pi^\star$	6.15	34	6.27	6.31	6.28	6.26
	3^1B_{3g}	$\pi \rightarrow \pi^\star$	7.95	34	7.92	7.93	7.87	7.88
Propadiene	1^3A_1	$\pi \rightarrow \pi^\star$	4.28	34	4.30	4.56	4.57	4.43
	2^1A_1	$\pi \rightarrow \pi^\star$	7.24	34	7.15	7.12	7.09	7.12
Fluorobenzene	1^3A_1	$\pi \rightarrow \pi^\star$	3.90	34	4.12	4.15	4.17	4.15
	2^3B_1	$\pi \rightarrow \pi^\star$	5.72	34	5.52	5.48	5.62	5.61

Continued on next page

Molecule	State		Exp.	Ref.	Original	R2016	R2018	R2022
	1^1B_1	$\pi \rightarrow \pi^\star$	4.78	34	5.05	4.99	4.98	5.02
	2^1A_1	$\pi \rightarrow \pi^\star$	6.23	34	6.11	5.97	6.13	6.15
o-Difluorobenzene	1^3B_1	$\pi \rightarrow \pi^\star$	3.92	34	4.13	4.14	4.18	4.16
	2^3A_1	$\pi \rightarrow \pi^\star$	5.67	34	5.54	5.49	5.63	5.63
	2^1A_1	$\pi \rightarrow \pi^\star$	4.76	34	5.05	4.97	4.99	5.03
	1^1B_1	$\pi \rightarrow \pi^\star$	6.22	34	6.15	6.00	6.17	6.19
1,3,5-Trifluorobenzene	1^3A_1	$\pi \rightarrow \pi^\star$	3.95	34	4.20	4.23	4.23	4.22
	2^3B_2	$\pi \rightarrow \pi^\star$	5.62	34	5.50	5.46	5.59	5.59
	1^1B_2	$\pi \rightarrow \pi^\star$	4.87	34	5.14	5.12	5.10	5.13
	2^1A_1	$\pi \rightarrow \pi^\star$	6.20	34	6.19	6.06	6.21	6.24
1,2,3,4-Tetrafluorobenzene	1^3B_1	$\pi \rightarrow \pi^\star$	3.95	34	4.14	4.14	4.18	4.17
	2^1A_1	$\pi \rightarrow \pi^\star$	4.85	34	5.08	5.01	5.02	5.06
	1^1B_1	$\pi \rightarrow \pi^\star$	6.43	34	6.22	6.07	6.24	6.26
1,2,4,5-Tetrafluorobenzene	1^3B_{2u}	$\pi \rightarrow \pi^\star$	4.00	34	4.16	4.17	4.18	4.18
	1^1B_{3u}	$\pi \rightarrow \pi^\star$	4.69	34	4.98	4.92	4.92	4.96
	1^1B_{2u}	$\pi \rightarrow \pi^\star$	6.30	34	6.25	6.09	6.26	6.29
Pentafluorobenzene	1^3A_1	$\pi \rightarrow \pi^\star$	3.90	34	4.19	4.19	4.20	4.20
	1^1B_1	$\pi \rightarrow \pi^\star$	4.79	34	5.10	5.05	5.05	5.09
	2^1A_1	$\pi \rightarrow \pi^\star$	6.36	34	6.28	6.13	6.30	6.33
Hexafluorobenzene	1^3B_{2u}	$\pi \rightarrow \pi^\star$	3.86	34	4.16	4.12	4.17	4.18
	1^1B_{3u}	$\pi \rightarrow \pi^\star$	4.80	34	5.15	5.03	5.08	5.13
	1^1B_{2u}	$\pi \rightarrow \pi^\star$	6.36	34	6.35	6.17	6.36	6.39
Thiophene[a]	3^1A_1	$\pi \rightarrow \pi^\star$	7.05	34	7.13	7.15	7.08	7.10
Pyrrole[a]	1^1A_2	$\pi \rightarrow Ry$	5.22	34	5.13	5.12	5.05	5.07

Continued on next page

Molecule	State		Exp.	Ref.	Original	R2016	R2018	R2022
	1^1B_1	$\pi \rightarrow \pi^\star$	5.98	34	6.03	6.03	5.95	5.98
Azomethane	1^3B_g	$n \rightarrow \pi^\star$	2.75	34	2.58	2.77	2.76	2.73
	1^1B_g	$\pi \rightarrow \pi^\star$	3.50	34	3.42	3.48	3.42	3.43
	2^1B_u	$n \rightarrow Ry$	6.71	34	7.04	7.10	6.91	6.98
	3^1B_u	$\pi \rightarrow \pi^\star$	7.80	34	8.06	8.02	7.97	8.05
Azo-tert-butane	1^3B_g	$n \rightarrow \pi^\star$	2.67	34	2.28	2.59	2.54	2.40
	1^3B_u	$\pi \rightarrow \pi^\star$	4.90	34	4.63	5.01	5.01	4.76
	1^1B_g	$n \rightarrow \pi^\star$	3.37	34	3.10	3.28	3.21	3.11
	3^1B_u	$n \rightarrow Ry$	7.30	34	7.60	7.69	7.45	7.49
Nitromethane[a]	$2^1A''$	$n \rightarrow \pi^\star$	4.45	34	4.24	4.27	4.34	4.35
Thiophosgene	1^3A_1	$\pi \rightarrow \pi^\star$	3.10	34	2.98	3.03	3.08	3.08
	1^1A_2	$n \rightarrow \pi^\star$	2.61	34	2.58	2.62	2.65	2.65
	1^1A_1	$\pi \rightarrow \pi^\star$	4.89	34	4.86	4.85	4.83	4.87
1,3-Cyclopentadiene	1^3B_2	$\pi \rightarrow \pi^\star$	3.10	34	3.04	3.14	3.16	3.12
	1^1B_2	$\pi \rightarrow \pi^\star$	5.26	34	5.30	5.23	5.26	5.31
Pyridine	1^1A_2	$n \rightarrow \pi^\star$	5.43	35	5.46	5.48	5.43	5.49
Pyrazine	1^3B_{1u}	$n \rightarrow \pi^\star$	3.33	35	3.54	3.58	3.62	3.63
	1^3B_{2g}	$n \rightarrow \pi^\star$	4.59	35	4.87	4.98	5.00	4.97
	1^1B_{1u}	$n \rightarrow \pi^\star$	3.83	35	4.00	4.03	4.06	4.09
	1^1B_{2g}	$n \rightarrow \pi^\star$	5.19	35	5.31	5.46	5.46	5.47
Pyrimidine	1^1A_2	$n \rightarrow \pi^\star$	4.62	26	4.87	4.90	4.87	4.93
s-Triazine	1^1B_2	$n \rightarrow \pi^\star$	4.59	26	4.66	4.69	4.72	4.73
Acetamide	$1^1A''$	$n \rightarrow \pi^\star$	5.44	36	5.32	5.49	5.36	5.28
Nitrobenzene	1^1A_2	$n \rightarrow \pi^\star$	3.65	37	3.35	3.46	3.53	3.54

Continued on next page

Molecule	State		Exp.	Ref.	Original	R2016	R2018	R2022
Dithiosuccinimide	1^3B_1	$n \rightarrow \pi^\star$	2.63	38	2.41	2.55	2.57	2.53
	1^1B_1	$n \rightarrow \pi^\star$	2.77	38	2.62	2.69	2.71	2.68
	1^1A_2	$n \rightarrow \pi^\star$	3.04	38	2.80	2.88	2.91	2.86

[a] Some states were removed in comparison to the R2016 assessment set.

Table S13: Selected molecules and vertical absorption energies for the standard selection threshold (in eV) of doublet states used for benchmarking.

Molecule	State		Exp.	Ref.	R2017	R2018	R2022
p-Benzosemiquionone anion	1^2B_{1u}	$\pi \rightarrow \pi^\star$	2.87	39	2.69	2.69	2.67
	1^2A_u	$\pi \rightarrow \pi^\star$	3.22	39	3.09	3.03	3.08
	2^2B_{1u}	$\pi \rightarrow Ry$	3.92	39	3.81	3.72	3.82
Perylene cation	1^2B_{3g}	$\pi \rightarrow \pi^\star$	1.56	40	1.68	1.71	1.81
	1^2B_{2g}	$\pi \rightarrow \pi^\star$	1.69	40	1.64	1.70	1.74
	2^2B_{3g}	$\pi \rightarrow \pi^\star$	1.93	40	1.85	1.90	1.99
	2^2B_{2g}	$\pi \rightarrow \pi^\star$	2.32	40	2.22	2.24	2.35
	3^2B_{3g}	$\pi \rightarrow \pi^\star$	3.73[a]	40	3.42	3.49	3.75
Fluoroene cation	1^2B_1	$\pi \rightarrow \pi^\star$	0.86	41	0.88	0.89	0.96
	2^2A_2	$\pi \rightarrow \pi^\star$	1.18	41	1.07	1.08	1.15
	2^2B_1	$\pi \rightarrow \pi^\star$	1.93	41	1.95	1.97	2.01
	1^2B_2	$\sigma \rightarrow \pi^\star$	3.13	41	3.23	3.20	3.25
	3^2B_1	$\pi \rightarrow \pi^\star$	3.64	41	3.63	3.64	3.67
	4^2B_1	$\pi \rightarrow \pi^\star$	4.08	41	3.83	3.88	3.91
Tetrathiafulvalene	1^2B_{2g}	$\pi \rightarrow \pi^\star$	2.14	42	2.22	2.22	2.25
	1^2B_{3g}	$\pi \rightarrow \pi^\star$	2.51	42	2.93	2.94	2.95
	2^2B_{2g}	$\pi \rightarrow \pi^\star$	2.86	42	3.01	2.99	3.06
	2^2B_{3g}	$\pi \rightarrow \pi^\star$	3.67	42	3.71	3.73	3.77
1,5-Hexadiene-3-yne	1^2B_u	$n \rightarrow \pi^\star$	1.16	43	1.32	1.34	1.37
	1^2B_g	$\pi \rightarrow \pi^\star$	2.19	43	2.06	2.06	2.07
	2^2A_u	$\pi \rightarrow \pi^\star$	3.20	43	3.25	3.31	3.35
	1^2A_g	$n \rightarrow \pi^\star$	4.14[a]	43	4.26	4.24	4.24

Continued on next page

Molecule	State		Exp.	Ref.	R2017	R2018	R2022
	2^2B_u	$\pi \rightarrow \pi^\star$	4.44	43	4.44	4.39	4.43
	4^2A_g	$\pi \rightarrow \pi^\star$	6.14	43	6.30	6.28	6.00
	6^2A_g	$\pi \rightarrow \pi^\star$	7.19	43	7.11	7.16	7.05
all-*trans* 1,3,5,7-octatetraene cation	1^2A_u	$\pi \rightarrow \pi^\star$	1.67	44	1.75	1.77	1.75
	2^2A_u	$\pi \rightarrow \pi^\star$	2.77	44	2.77	2.75	2.83
	2^2B_g	$\pi \rightarrow \pi^\star$	2.97	44	2.84	2.88	2.94
all-*trans* 1,3,5,7-octatetraene	1^2A_u	$\pi \rightarrow \pi^\star$	1.82	45	1.76	1.76	1.77
	2^2B_g	$\pi \rightarrow \pi^\star$	3.10	45	2.89	2.90	2.96
	1^2A_g	$\pi \rightarrow \pi^\star$	3.93	45	4.16	4.10	4.11
o-Xylylene	1^2B	$\pi \rightarrow \pi^\star$	1.90	46	1.96	2.01	1.97
	2^2A	$\pi \rightarrow \pi^\star$	2.35	46	2.42	2.43	2.47
	2^2B	$\pi \rightarrow \pi^\star$	2.79	46	2.87	2.86	2.94
	3^2A	$\pi \rightarrow \pi^\star$	3.74	46	4.04	3.99	4.04
	4^2B	$\pi \rightarrow \pi^\star$	4.40	46	4.62	4.57	4.59
Styrene	$2^2A''$	$\pi \rightarrow \pi^\star$	0.80	46	0.75	0.74	0.79
	$3^2A''$	$\pi \rightarrow \pi^\star$	2.09	46	2.18	2.19	2.21
	$1^2A'$	$n/\sigma \rightarrow \pi^\star$	3.04	46	3.40	3.35	3.40
	$2^2A'$	$n/\sigma \rightarrow \pi^\star$	3.70	46	3.58	3.53	3.59
	$3^2A'$	$n/\sigma \rightarrow \pi^\star$	4.38	46	4.31	4.26	4.31
Carbazole	1^2A_2	$\pi \rightarrow \pi^\star$	0.39	47	0.26	0.28	0.33
	2^2A_2	$\pi \rightarrow \pi^\star$	1.46	47	1.43	1.46	1.50
	2^2B_2	$\pi \rightarrow \pi^\star$	2.15	47	2.03	2.06	2.11
	3^2B_2	$\pi \rightarrow \pi^\star$	3.19	47	3.21	3.26	3.30
Dibenzofuran	1^2B_2	$\pi \rightarrow \pi^\star$	0.25	47	0.20	0.20	0.29

Continued on next page

Molecule	State		Exp.	Ref.	R2017	R2018	R2022
	2^2A_2	$\pi \rightarrow \pi^\star$	1.26	47	1.01	1.02	1.09
	2^2B_2	$\pi \rightarrow \pi^\star$	1.97	47	1.84	1.86	1.90
	1^2A_1	$n/\sigma \rightarrow \pi^\star$	3.12	47	3.51	3.48	3.53
Dichlorodifluoromethane	1^2A_2	$n \rightarrow \pi^\star$	0.30	48	0.19	0.21	0.22
	1^2B_2	$n \rightarrow \pi^\star$	0.90	48	0.61	0.64	0.62
	1^2A_1	$n \rightarrow \pi^\star$	1.20	48	1.35	1.39	1.38
Adenine	$1^2A'$	$n/\sigma \rightarrow \pi^\star$	0.98	49	0.95	0.89	0.94
	$2^2A''$	$\pi \rightarrow \pi^\star$	1.07	49	1.21	1.20	1.25
	$2^2A'$	$n/\sigma \rightarrow \pi^\star$	1.98	49	1.87	1.81	1.88
	$3^2A''$	$\pi \rightarrow \pi^\star$	2.04	49	2.11	2.06	2.15
	$3^2A'$	$n/\sigma \rightarrow \pi^\star$	2.88	49	2.72	2.69	2.72
Fluorobenzene	1^2A_2	$\pi \rightarrow \pi^\star$	0.40	50	0.38	0.38	0.41
	1^2B_1	$\pi \rightarrow \pi^\star$	2.90	50	3.10	3.05	3.11
	2^2B_2	$n/\sigma \rightarrow \pi^\star$	2.90	50	2.95	2.98	2.98
	1^2A_1	$n/\sigma \rightarrow \pi^\star$	3.60	50	3.70	3.66	3.71
	2^2B_1	$n/\sigma \rightarrow \pi^\star$	4.50	50	4.78	4.68	4.74
	3^2B_1	$n/\sigma \rightarrow \pi^\star$	5.20	50	5.28	5.25	5.29
	2^2A_1	$n/\sigma \rightarrow \pi^\star$	5.80	50	5.68	5.64	5.67
2,3-Benzofluoroene cation/tnoteb	$2^2A''$	$\pi \rightarrow \pi^\star$	0.80	50	0.70	0.72	0.79
	$4^2A''$	$\pi \rightarrow \pi^\star$	1.72	50	1.79	1.81	1.88
	$6^2A''$	$\pi \rightarrow \pi^\star$	2.70	50	2.83	2.90	2.93
Tetracene cation	1^2B_{3g}	$\pi \rightarrow \pi^\star$	1.43	51	1.49	1.52	1.59
	1^2B_{2g}	$\pi \rightarrow \pi^\star$	1.65	51	1.61	1.66	1.69
	2^2B_{3g}	$\pi \rightarrow \pi^\star$	3.14[a]	51	2.77	2.83	3.21

Continued on next page

Molecule	State		Exp.	Ref.	R2017	R2018	R2022
1,2,4,5-Tetrafluorobenzene	1^2B_{3g}	$\pi \rightarrow \pi^\star$	0.70	50	0.61	0.61	0.64
	1^2B_{1u}	$\pi \rightarrow \pi^\star$	3.00	50	2.85	2.89	2.88
	1^2B_{3u}	$n \rightarrow \pi^\star$	4.20	50	4.30	4.20	4.28
	1^2A_g	$n \rightarrow \pi^\star$	4.20	50	4.13	4.07	4.13
	1^2B_{1g}	$n \rightarrow \pi^\star$	5.10	50	5.19	5.05	5.14
1,2,3,4-Tetrafluorobenzene	1^2B_2	$\pi \rightarrow \pi^\star$	0.00	50	0.32	0.32	0.34
	2^2B_2	$\pi \rightarrow \pi^\star$	2.70	50	2.81	2.84	2.84
	1^2A_1	$n \rightarrow \pi^\star$	3.90	50	4.13	4.02	4.09
	1^2B_1	$n \rightarrow \pi^\star$	3.90	50	3.96	3.90	3.96
	2^2A_1	$n \rightarrow \pi^\star$	4.80	50	4.95	4.86	4.93
Ethylfluoride	$1^2A'$	$n/\sigma \rightarrow \pi^\star$	0.50	50	0.06	0.07	0.04
	$2^2A'$	$n/\sigma \rightarrow \pi^\star$	1.60	50	1.48	1.37	1.49
	$2^2A''$	$\pi \rightarrow \pi^\star$	2.10	50	2.12	2.00	2.12
	$3^2A'$	$n/\sigma \rightarrow \pi^\star$	3.60	50	3.17	3.08	3.20
	$3^2A''$	$\pi \rightarrow \pi^\star$	4.70	50	4.88	4.78	4.90
	$4^2A'$	$n/\sigma \rightarrow \pi^\star$	4.70	50	4.42	4.38	4.48
	$5^2A'$	$n/\sigma \rightarrow \pi^\star$	8.60	50	8.51	8.41	8.53
Hydroxyl radical	$A^2\Sigma^+$	$\sigma \rightarrow \pi^\star$	4.09	52	4.05	4.04	4.05
	$B^2\Sigma^+$	$\sigma \rightarrow Ry$	8.65	52	8.45	8.22	8.54
Acenaphthylene cation	1^2A_2	$\pi \rightarrow \pi^\star$	0.80	53	0.70	0.69	0.76
	2^2B_2	$\pi \rightarrow \pi^\star$	1.15	53	1.12	1.11	1.19
	2^2A_2	$\pi \rightarrow \pi^\star$	2.53	53	2.51	2.53	2.56
Acenaphthene cation	2^2B_1	$\pi \rightarrow \pi^\star$	2.10	51	2.02	2.04	2.07
	2^2A_2	$\pi \rightarrow \pi^\star$	2.92	51	2.75	2.78	2.77

Continued on next page

Molecule	State		Exp.	Ref.	R2017	R2018	R2022
Bithiophene cation	2^2A_u	$\pi \rightarrow \pi^\star$	2.10	54	2.13	2.16	2.16
	3^2A_u	$\pi \rightarrow \pi^\star$	2.92	54	2.93	2.93	3.01
Phenanthrene cation	2^2A_2	$\pi \rightarrow \pi^\star$	1.38	55	1.49	1.50	1.56
	2^2B_2	$\pi \rightarrow \pi^\star$	1.95	55	2.01	2.04	2.09
	3^2B_2	$\pi \rightarrow \pi^\star$	2.63	55	2.60	2.66	2.72
	3^2A_2	$\pi \rightarrow \pi^\star$	2.91	55	3.15	3.20	3.23
	3^2A_2	$\pi \rightarrow \pi^\star$	3.13	55	3.29	3.37	3.23
	4^2A_2	$\pi \rightarrow \pi^\star$	3.59	55	3.45	3.52	3.58
Beryllium monohydride	$A^2\Pi$	$n \rightarrow \pi^\star$	2.48	52	2.40	2.39	2.36
	$B^2\Pi$	$n \rightarrow Ry$	6.32	52	6.33	6.33	6.35
Ethylenyl[b]	$1^2A''$	$\pi \rightarrow n^\star$	3.08	56	3.04	3.13	3.10
	$6^2A'$	$\sigma \rightarrow n^\star$	7.37	56	7.25	7.27	7.33
Nitric Oxide	$A^2\Sigma^+$	$\pi \rightarrow Ry$	5.92	51	6.06	5.84	5.98
	$D^2\Sigma^+$	$\pi \rightarrow Ry$	7.03	51	7.11	6.95	7.08
Nitrogen dioxide	2^2B_1	$\pi \rightarrow \pi^\star$	5.22	57	4.83	5.01	5.19
	2^2A_1	$n/\sigma \rightarrow Ry$	7.50	57	7.37	7.35	7.41
	4^2B_1	$n/\sigma \rightarrow Ry$	8.60	57	8.63	8.58	8.67
	3^2B_2	$n/\sigma \rightarrow Ry$	8.60	57	8.74	8.69	8.81
	4^2A_1	$n/\sigma \rightarrow Ry$	8.60	57	8.68	8.62	8.74
	7^2B_1	$n/\sigma \rightarrow Ry$	9.66	57	9.31	9.31	9.79
Azulene cation	2^2A_2	$\pi \rightarrow \pi^\star$	2.58	51	2.77	2.81	2.84
	3^2B_2	$\pi \rightarrow \pi^\star$	3.37	51	3.38	3.41	3.51
Azulene	1^2B_2	$\pi \rightarrow \pi^\star$	1.07	49	1.11	1.10	1.15
	2^2A_2	$\pi \rightarrow \pi^\star$	2.64	49	2.64	2.68	2.73

Continued on next page

Molecule	State		Exp.	Ref.	R2017	R2018	R2022
	3^2B_2	$\pi \rightarrow \pi^\star$	3.42	49	3.28	3.32	3.41
Pentacene cation	1^2B_{1u}	$\pi \rightarrow \pi^\star$	1.26	51	1.17	1.21	1.28
	1^2A_u	$\pi \rightarrow \pi^\star$	1.30	51	1.27	1.30	1.39
	2^2A_u	$\pi \rightarrow \pi^\star$	2.91[a]	51	2.57	2.63	2.92
Terthiophene cation	1^2B_2	$\pi \rightarrow \pi^\star$	1.46	54	1.52	1.53	1.58
	3^2B_2	$\pi \rightarrow \pi^\star$	2.25	54	2.24	2.25	2.32
Styrene cation	$3^2A''$	$\pi \rightarrow \pi^\star$	2.14	58	2.26	2.28	2.28
	$5^2A''$	$\pi \rightarrow \pi^\star$	3.75	58	3.75	3.80	3.96
Ovalene cation[b]	1^2A_u	$\pi \rightarrow \pi^\star$	1.10	51	1.25	1.31	1.43
	1^2B_{1u}	$\pi \rightarrow \pi^\star$	1.27	51	1.49	1.56	1.64
	3^2B_{1u}	$\pi \rightarrow \pi^\star$	2.21	51	2.17	2.25	2.36
Hexacene	1^2B_{3g}	$\pi \rightarrow \pi^\star$	1.11	59	1.07	1.10	1.21
	1^2B_{1u}	$\pi \rightarrow \pi^\star$	1.70	59	1.68	1.78	1.88
	2^2A_u	$\pi \rightarrow \pi^\star$	2.12	59	1.97	2.04	2.14
	2^2B_{2g}	$\pi \rightarrow \pi^\star$	2.92	59	2.91	3.02	2.65
	3^2B_{3g}	$\pi \rightarrow \pi^\star$	2.92	59	2.77	2.86	2.96
	3^2A_u	$\pi \rightarrow \pi^\star$	3.51	59	3.35	3.47	3.55
	6^2B_{1u}	$\pi \rightarrow \pi^\star$	3.51	59	3.79	3.93	3.73
	6^2B_{3g}	$\pi \rightarrow \pi^\star$	3.86	59	3.79	3.91	3.95
Phenoxyl	1^2B_1	$\pi \rightarrow \pi^\star$	1.10	60	0.90	0.90	0.89
	1^2A_2	$\pi \rightarrow \pi^\star$	1.92	60	2.29	2.31	2.30
	2^2B_2	$\pi \rightarrow \pi^\star$	3.12	60	3.33	3.36	3.32
	2^2A_2	$\pi \rightarrow \pi^\star$	4.20	60	4.40	4.39	4.46
	4^2B_2	$\pi \rightarrow \pi^\star$	5.18	60	5.17	5.19	5.27

Continued on next page

Molecule	State		Exp.	Ref.	R2017	R2018	R2022
	3^2A_2	$\pi \rightarrow \pi^\star$	5.95	60	5.72	5.80	6.21
Phenyl	1^2B_2	$\pi \rightarrow \pi^\star$	2.43	61	2.65	2.67	2.66
	3^2A_1	$\pi \rightarrow \pi^\star$	5.27	61	4.94	5.04	5.15
	3^2B_1	$\pi \rightarrow \pi^\star$	5.86	61	5.69	5.76	5.84

[a] Changed in comparisson to the R2017 training set.

[b] Some states were removed in comparison to the R2017 assessment set.

Table S14: Selected molecules and vertical absorption energies for the tight selection threshold (in eV) of doublet states used for benchmarking.

Molecule	State		Exp.	Ref.	R2017	R2018	R2022
p-Benzosemiquionone anion	1^2B_{1u}	$\pi \rightarrow \pi^\star$	2.87	39	2.68	2.67	2.67
	1^2A_u	$\pi \rightarrow \pi^\star$	3.22	39	3.10	3.06	3.10
	2^2B_{1u}	$\pi \rightarrow Ry$	3.92	39	3.84	3.78	3.85
Perylene cation	1^2B_{3g}	$\pi \rightarrow \pi^\star$	1.56	40	1.70	1.68	1.80
	1^2B_{2g}	$\pi \rightarrow \pi^\star$	1.69	40	1.66	1.65	1.72
	2^2B_{3g}	$\pi \rightarrow \pi^\star$	1.93	40	1.87	1.86	1.98
	2^2B_{2g}	$\pi \rightarrow \pi^\star$	2.32	40	2.25	2.22	2.36
	3^2B_{3g}	$\pi \rightarrow \pi^\star$	3.73[a]	40	3.45	3.40	3.76
Fluoroene cation	1^2B_1	$\pi \rightarrow \pi^\star$	0.86	41	0.88	0.89	0.96
	2^2A_2	$\pi \rightarrow \pi^\star$	1.18	41	1.06	1.08	1.15
	2^2B_1	$\pi \rightarrow \pi^\star$	1.93	41	1.95	1.97	2.01
	1^2B_2	$\sigma \rightarrow \pi^\star$	3.13	41	3.24	3.25	3.28
	3^2B_1	$\pi \rightarrow \pi^\star$	4.08	41	3.81	3.84	3.89
	4^2B_1	$\pi \rightarrow \pi^\star$	3.64	41	3.63	3.63	3.68
Tetrathiafulvalene	1^2B_{2g}	$\pi \rightarrow \pi^\star$	2.14	42	2.22	2.21	2.24
	1^2B_{3g}	$\pi \rightarrow \pi^\star$	2.51	42	2.93	2.93	2.95
	2^2B_{2g}	$\pi \rightarrow \pi^\star$	2.86	42	3.01	3.00	3.07
	2^2B_{3g}	$\pi \rightarrow \pi^\star$	3.67	42	3.71	3.72	3.77
1,5-Hexadiene-3-yne	1^2B_u	$n \rightarrow \pi^\star$	1.16	43	1.31	1.33	1.35
	1^2B_g	$\pi \rightarrow \pi^\star$	2.19	43	2.05	2.04	2.06
	2^2A_u	$\pi \rightarrow \pi^\star$	3.20	43	3.22	3.25	3.33
	1^2A_g	$n \rightarrow \pi^\star$	4.14[a]	43	4.26	4.23	4.26

Continued on next page

Molecule	State		Exp.	Ref.	R2017	R2018	R2022
	2^2B_u	$\pi \rightarrow \pi^\star$	4.44	43	4.45	4.42	4.45
	4^2A_g	$\pi \rightarrow \pi^\star$	6.14	43	6.33	6.34	6.03
	6^2A_g	$\pi \rightarrow \pi^\star$	7.19	43	7.13	7.18	7.07
all-*trans* 1,3,5,7-octatetraene cation	1^2A_u	$\pi \rightarrow \pi^\star$	1.67	44	1.73	1.74	1.73
	2^2A_u	$\pi \rightarrow \pi^\star$	2.77	44	2.78	2.77	2.84
	2^2B_g	$\pi \rightarrow \pi^\star$	2.97	44	2.83	2.84	2.92
all-*trans* 1,3,5,7-octatetraene	1^2A_u	$\pi \rightarrow \pi^\star$	1.82	45	1.75	1.74	1.76
	2^2B_g	$\pi \rightarrow \pi^\star$	3.10	45	2.87	2.86	2.94
	1^2A_g	$\pi \rightarrow \pi^\star$	3.93	45	4.16	4.13	4.13
o-Xylylene	1^2B	$\pi \rightarrow \pi^\star$	1.90	46	1.94	1.96	1.94
	2^2A	$\pi \rightarrow \pi^\star$	2.35	46	2.41	2.42	2.47
	2^2B	$\pi \rightarrow \pi^\star$	2.79	46	2.88	2.87	2.95
	3^2A	$\pi \rightarrow \pi^\star$	3.74	46	4.05	4.03	4.06
	4^2B	$\pi \rightarrow \pi^\star$	4.40	46	4.63	4.63	4.62
Styrene	$2^2A''$	$\pi \rightarrow \pi^\star$	0.80	46	0.74	0.74	0.79
	$3^2A''$	$\pi \rightarrow \pi^\star$	2.09	46	2.17	2.18	2.21
	$1^2A'$	$n/\sigma \rightarrow \pi^\star$	3.04	46	3.40	3.39	3.42
	$2^2A'$	$n/\sigma \rightarrow \pi^\star$	3.70	46	3.59	3.58	3.61
	$3^2A'$	$n/\sigma \rightarrow \pi^\star$	4.38	46	4.32	4.31	4.34
Carbazole	1^2A_2	$\pi \rightarrow \pi^\star$	0.39	47	0.25	0.27	0.32
	2^2A_2	$\pi \rightarrow \pi^\star$	1.46	47	1.42	1.45	1.49
	2^2B_2	$\pi \rightarrow \pi^\star$	2.15	47	2.02	2.05	2.11
	3^2B_2	$\pi \rightarrow \pi^\star$	3.19	47	3.20	3.23	3.29
Dibenzofuran	1^2B_2	$\pi \rightarrow \pi^\star$	0.25	47	0.20	0.21	0.28

Continued on next page

Molecule	State		Exp.	Ref.	R2017	R2018	R2022
	2^2A_2	$\pi \rightarrow \pi^\star$	1.26	47	1.00	1.02	1.09
	2^2B_2	$\pi \rightarrow \pi^\star$	1.97	47	1.83	1.85	1.90
	1^2A_1	$n/\sigma \rightarrow \pi^\star$	3.12	47	3.53	3.52	3.55
Dichlorodifluoromethane	1^2A_2	$n \rightarrow \pi^\star$	0.30	48	0.18	0.20	0.21
	1^2B_2	$n \rightarrow \pi^\star$	0.90	48	0.60	0.61	0.61
	1^2A_1	$n \rightarrow \pi^\star$	1.20	48	1.34	1.36	1.37
Adenine	$1^2A'$	$n/\sigma \rightarrow \pi^\star$	0.98	49	0.96	0.92	0.96
	$2^2A''$	$\pi \rightarrow \pi^\star$	1.07	49	1.21	1.20	1.25
	$2^2A'$	$n/\sigma \rightarrow \pi^\star$	1.98	49	1.88	1.85	1.90
	$3^2A''$	$\pi \rightarrow \pi^\star$	2.04	49	2.12	2.08	2.17
	$3^2A'$	$n/\sigma \rightarrow \pi^\star$	2.88	49	2.74	2.72	2.75
Fluorobenzene	1^2A_2	$\pi \rightarrow \pi^\star$	0.40	50	0.38	0.38	0.40
	1^2B_1	$\pi \rightarrow \pi^\star$	2.90	50	3.10	3.09	3.12
	2^2B_2	$n/\sigma \rightarrow \pi^\star$	2.90	50	2.92	2.93	2.95
	1^2A_1	$n/\sigma \rightarrow \pi^\star$	3.60	50	3.71	3.71	3.73
	2^2B_1	$n/\sigma \rightarrow \pi^\star$	4.50	50	4.80	4.76	4.77
	3^2B_1	$n/\sigma \rightarrow \pi^\star$	5.20	50	5.29	5.28	5.31
	2^2A_1	$n/\sigma \rightarrow \pi^\star$	5.80	50	5.69	5.68	5.69
2,3-Benzofluoroene cation[b]	$2^2A''$	$\pi \rightarrow \pi^\star$	0.80	50	0.70	0.72	0.79
	$4^2A''$	$\pi \rightarrow \pi^\star$	1.72	50	1.79	1.81	1.89
	$6^2A''$	$\pi \rightarrow \pi^\star$	2.70	50	2.84	2.88	2.93
Tetracene cation	1^2B_{3g}	$\pi \rightarrow \pi^\star$	1.43	51	1.50	1.52	1.59
	1^2B_{2g}	$\pi \rightarrow \pi^\star$	1.65	51	1.61	1.64	1.68
	2^2B_{3g}	$\pi \rightarrow \pi^\star$	3.14[a]	51	2.93	3.00	3.24

Continued on next page

Molecule	State		Exp.	Ref.	R2017	R2018	R2022
1,2,4,5-Tetrafluorobenzene	1^2B_{3g}	$\pi \rightarrow \pi^\star$	0.70	50	0.61	0.61	0.63
	1^2B_{1u}	$\pi \rightarrow \pi^\star$	3.00	50	2.83	2.85	2.86
	1^2B_{3u}	$n \rightarrow \pi^\star$	4.20	50	4.32	4.29	4.30
	1^2A_g	$n \rightarrow \pi^\star$	4.20	50	4.14	4.13	4.16
	1^2B_{1g}	$n \rightarrow \pi^\star$	5.10	50	5.21	5.16	5.19
1,2,3,4-Tetrafluorobenzene	1^2B_2	$\pi \rightarrow \pi^\star$	0.00	50	0.32	0.32	0.34
	2^2B_2	$\pi \rightarrow \pi^\star$	2.70	50	2.78	2.80	2.83
	1^2A_1	$n \rightarrow \pi^\star$	3.90	50	4.13	4.10	4.11
	1^2B_1	$n \rightarrow \pi^\star$	3.90	50	3.95	3.95	3.98
	2^2A_1	$n \rightarrow \pi^\star$	4.80	50	4.95	4.94	4.97
Ethylfluoride	$1^2A'$	$n/\sigma \rightarrow \pi^\star$	0.50	50	0.05	0.05	0.03
	$2^2A'$	$n/\sigma \rightarrow \pi^\star$	1.60	50	1.49	1.45	1.51
	$2^2A''$	$\pi \rightarrow \pi^\star$	2.10	50	2.13	2.08	2.15
	$3^2A'$	$n/\sigma \rightarrow \pi^\star$	3.60	50	3.18	3.13	3.21
	$3^2A''$	$\pi \rightarrow \pi^\star$	4.70	50	4.89	4.83	4.93
	$4^2A'$	$n/\sigma \rightarrow \pi^\star$	4.70	50	4.43	4.41	4.48
	$5^2A'$	$n/\sigma \rightarrow \pi^\star$	8.60	50	8.52	8.46	8.56
Hydroxyl radical	$A^2\Sigma^+$	$\sigma \rightarrow \pi^\star$	4.09	52	4.05	4.05	4.05
	$B^2\Sigma^+$	$\sigma \rightarrow Ry$	8.65	52	8.46	8.36	8.58
Acenaphthylene cation	1^2A_2	$\pi \rightarrow \pi^\star$	0.80	53	0.71	0.70	0.77
	2^2B_2	$\pi \rightarrow \pi^\star$	1.15	53	1.12	1.12	1.20
	2^2A_2	$\pi \rightarrow \pi^\star$	2.53	53	2.51	2.52	2.56
Acenaphthene cation	2^2B_1	$\pi \rightarrow \pi^\star$	2.10	51	2.01	2.02	2.06
	2^2A_2	$\pi \rightarrow \pi^\star$	2.92	51	2.73	2.75	2.75

Continued on next page

Molecule	State		Exp.	Ref.	R2017	R2018	R2022
Bithiophene cation	2^2A_u	$\pi \rightarrow \pi^\star$	2.10	54	2.12	2.13	2.15
	3^2A_u	$\pi \rightarrow \pi^\star$	2.92	54	2.94	2.94	3.02
Phenanthrene cation	2^2A_2	$\pi \rightarrow \pi^\star$	1.38	55	1.49	1.50	1.57
	2^2B_2	$\pi \rightarrow \pi^\star$	1.95	55	2.02	2.04	2.10
	3^2B_2	$\pi \rightarrow \pi^\star$	2.63	55	2.61	2.65	2.72
	3^2A_2	$\pi \rightarrow \pi^\star$	2.91	55	3.18	3.21	3.25
	3^2A_2	$\pi \rightarrow \pi^\star$	3.13	55	3.33	3.40	3.25
	4^2A_2	$\pi \rightarrow \pi^\star$	3.59	55	3.48	3.53	3.63
Beryllium monohydride	$A^2\Pi$	$n \rightarrow \pi^\star$	2.48	52	2.39	2.38	2.36
	$B^2\Pi$	$n \rightarrow Ry$	6.32	52	6.34	6.33	6.36
Ethylenyl[b]	$1^2A''$	$\pi \rightarrow n^\star$	3.08	56	3.02	3.07	3.07
	$6^2A'$	$\sigma \rightarrow n^\star$	7.37	56	7.23	7.24	7.32
Nitric Oxide	$A^2\Sigma^+$	$\pi \rightarrow Ry$	5.92	51	6.11	5.99	6.06
	$D^2\Sigma^+$	$\pi \rightarrow Ry$	7.03	51	7.15	7.07	7.15
Nitrogen dioxide	2^2B_1	$\pi \rightarrow \pi^\star$	5.22	57	4.80	4.90	5.14
	2^2A_1	$n/\sigma \rightarrow Ry$	7.50	57	7.38	7.38	7.44
	4^2B_1	$n/\sigma \rightarrow Ry$	8.60	57	8.66	8.64	8.73
	3^2B_2	$n/\sigma \rightarrow Ry$	8.60	57	8.78	8.77	8.88
	4^2A_1	$n/\sigma \rightarrow Ry$	8.60	57	8.72	8.71	8.80
	7^2B_1	$n/\sigma \rightarrow Ry$	9.66	57	9.34	9.33	9.81
Azulene cation	2^2A_2	$\pi \rightarrow \pi^\star$	2.58	51	2.76	2.78	2.83
	3^2B_2	$\pi \rightarrow \pi^\star$	3.37	51	3.36	3.38	3.50
Azulene	1^2B_2	$\pi \rightarrow \pi^\star$	1.07	49	1.10	1.10	1.15
	2^2A_2	$\pi \rightarrow \pi^\star$	2.64	49	2.63	2.65	2.71

Continued on next page

Molecule	State		Exp.	Ref.	R2017	R2018	R2022
	3^2B_2	$\pi \rightarrow \pi^\star$	3.42	49	3.27	3.29	3.40
Pentacene cation	1^2B_{1u}	$\pi \rightarrow \pi^\star$	1.26	51	1.16	1.19	1.26
	1^2A_u	$\pi \rightarrow \pi^\star$	1.30	51	1.27	1.29	1.39
	2^2A_u	$\pi \rightarrow \pi^\star$	2.91[a]	51	2.61	2.66	2.94
Terthiophene cation	1^2B_2	$\pi \rightarrow \pi^\star$	1.46	54	1.52	1.52	1.57
	3^2B_2	$\pi \rightarrow \pi^\star$	2.25	54	2.25	2.25	2.33
Styrene cation	$3^2A''$	$\pi \rightarrow \pi^\star$	2.14	58	2.25	2.26	2.28
	$5^2A''$	$\pi \rightarrow \pi^\star$	3.75	58	3.73	3.76	3.96
Ovalene cation[b]	1^2A_u	$\pi \rightarrow \pi^\star$	1.10	51	1.26	1.30	1.42
	1^2B_{1u}	$\pi \rightarrow \pi^\star$	1.27	51	1.49	1.53	1.63
	3^2B_{1u}	$\pi \rightarrow \pi^\star$	2.21	51	2.19	2.25	2.37
Hexacene	1^2B_{3g}	$\pi \rightarrow \pi^\star$	1.11	59	1.07	1.09	1.20
	1^2B_{1u}	$\pi \rightarrow \pi^\star$	1.70	59	1.69	1.78	1.89
	2^2A_u	$\pi \rightarrow \pi^\star$	2.12	59	1.99	2.03	2.15
	2^2B_{2g}	$\pi \rightarrow \pi^\star$	2.92	59	2.96	3.06	2.90
	3^2B_{3g}	$\pi \rightarrow \pi^\star$	2.92	59	2.81	2.87	2.97
	3^2A_u	$\pi \rightarrow \pi^\star$	3.51	59	3.42	3.51	3.59
	6^2B_{1u}	$\pi \rightarrow \pi^\star$	3.51	59	3.88	4.00	3.78
	6^2B_{3g}	$\pi \rightarrow \pi^\star$	3.86	59	3.86	3.96	4.00
Phenoxyl	1^2B_1	$\pi \rightarrow \pi^\star$	1.10	60	0.89	0.88	0.88
	1^2A_2	$\pi \rightarrow \pi^\star$	1.92	60	2.27	2.29	2.29
	2^2B_2	$\pi \rightarrow \pi^\star$	3.12	60	3.31	3.32	3.30
	2^2A_2	$\pi \rightarrow \pi^\star$	4.20	60	4.41	4.41	4.48
	4^2B_2	$\pi \rightarrow \pi^\star$	5.18	60	5.19	5.20	5.30

Continued on next page

Molecule	State		Exp.	Ref.	R2017	R2018	R2022
	3^2A_2	$\pi \rightarrow \pi^\star$	5.95	60	5.75	5.80	6.25
Phenyl	1^2B_2	$\pi \rightarrow \pi^\star$	2.43	61	2.63	2.65	2.65
	3^2A_1	$\pi \rightarrow \pi^\star$	5.27	61	4.93	4.99	5.14
	3^2B_1	$\pi \rightarrow \pi^\star$	5.86	61	5.67	5.73	5.82

[a] Changed in comparisson to the R2017 training set.

[b] Some states were removed in comparison to the R2017 assessment set.

Table S15: Selected inorganic molecules and vertical absorption energies for the standard selection threshold (in eV) used for benchmarking.

Molecule	State		Exp.	Ref.	Original	R2016	R2018	R2022
MoF_6	$^1T_{1u}$	$\pi \rightarrow d/\pi^\star$	5.90	62	5.12	4.86	5.03	5.06
		$\pi \rightarrow d/\pi^\star$	5.90		5.13	4.86	5.02	5.06
		$\pi \rightarrow d/\pi^\star$	5.90		5.13	4.86	5.02	5.06
	$^1T_{1u}$	$\pi \rightarrow d/\pi^\star$	6.54	62	5.66	5.24	5.44	5.49
		$\pi \rightarrow d/\pi^\star$	6.54		5.66	5.24	5.44	5.49
		$\pi \rightarrow d/\pi^\star$	6.54		5.66	5.24	5.44	5.49
	$^1T_{1u}$	$\pi \rightarrow d/\pi^\star$	7.12	62	6.33	5.81	6.05	6.11
		$\pi \rightarrow d/\pi^\star$	7.12		6.33	5.81	6.05	6.11
		$\pi \rightarrow d/\pi^\star$	7.12		6.33	5.81	6.05	6.11
$Mo(CO)_6$	$^1T_{1u}$	$d/\pi \rightarrow \pi^\star$	4.32	63	4.46	4.33	4.41	4.44
		$d/\pi \rightarrow \pi^\star$	4.32		4.46	4.33	4.41	4.44
		$d/\pi \rightarrow \pi^\star$	4.32		4.46	4.33	4.41	4.44
	$^1T_{1u}$	$d/\pi \rightarrow \pi^\star$	5.44	63	5.71	5.45	5.54	5.63
		$d/\pi \rightarrow \pi^\star$	5.44		5.70	5.45	5.53	5.63
		$d/\pi \rightarrow \pi^\star$	5.44		5.70	5.45	5.53	5.63
$Cr(CO)_6$	$^1T_{1u}$	$d/\pi \rightarrow \pi^\star$	4.43	63	4.73	4.60	4.72	4.64
		$d/\pi \rightarrow \pi^\star$	4.43		4.73	4.60	4.72	4.64
		$d/\pi \rightarrow \pi^\star$	4.43		4.73	4.60	4.72	4.64
	$^1T_{1u}$	$d/\pi \rightarrow \pi^\star$	5.41	63	5.72	5.54	5.66	5.57
		$d/\pi \rightarrow \pi^\star$	5.41		5.72	5.54	5.66	5.57
		$d/\pi \rightarrow \pi^\star$	5.41		5.72	5.54	5.67	5.57
$Ni(CO)_4$	$^1T_2$	$\sigma/d \rightarrow \pi^\star$	4.54	64	4.39	4.08	4.90	4.34

Continued on next page

Molecule	State		Exp.	Ref.	Original	R2016	R2018	R2022
		$\sigma/d \rightarrow \pi^\star$	4.54		4.40	4.10	4.91	4.37
		$\sigma/d \rightarrow \pi^\star$	4.54		4.40	4.10	4.91	4.37
	$^1T_2$	$\sigma/d \rightarrow \pi^\star$	5.17	64	5.42	4.65	5.56	5.06
		$\sigma/d \rightarrow \pi^\star$	5.17		5.45	4.67	5.56	5.07
		$\sigma/d \rightarrow \pi^\star$	5.17		5.45	4.67	5.56	5.07
$Co(H2O)_6^{2+}$	$^3T_g(t_g^5e_g^1)$	$\pi/d \rightarrow \sigma^\star d^\star$	0.99	65	0.88	1.36	1.43	1.12
		$\pi/d \rightarrow \sigma^\star d^\star$	0.99		0.91	1.37	1.47	1.15
		$\pi/d \rightarrow \sigma^\star d^\star$	0.99		0.85	1.41	1.42	1.19
	$^3T_g(t_g^5e_g^1)$	$\pi/d \rightarrow \sigma^\star d^\star$	1.55	65	1.36	1.75	1.84	1.60
		$\pi/d \rightarrow \sigma^\star d^\star$	1.55		1.32	1.79	1.81	1.65
		$\pi/d \rightarrow \sigma^\star d^\star$	1.55		1.37	1.80	1.86	1.67
	$^1T_g(t_g^5e_g^1)$	$\pi/d \rightarrow \sigma^\star d^\star$	2.06	65	1.72	1.97	2.04	1.74
		$\pi/d \rightarrow \sigma^\star d^\star$	2.06		1.75	1.99	2.05	1.76
		$\pi/d \rightarrow \sigma^\star d^\star$	2.06		1.70	2.00	2.03	1.79
	$^1T_g(t_g^5e_g^1)$	$\pi/d \rightarrow \sigma^\star d^\star$	3.09	65	2.65	2.80	2.85	2.72
		$\pi/d \rightarrow \sigma^\star d^\star$	3.09		2.62	2.81	2.83	2.75
		$\pi/d \rightarrow \sigma^\star d^\star$	3.09		2.67	2.83	2.86	2.77
$Co(NH_3)_6^{3+}$	$^1T_{1g}$	$d \rightarrow \sigma^\star d^\star$	2.70	66	2.66	2.68	2.89	2.69
		$d \rightarrow \sigma^\star d^\star$	2.70		2.68	2.70	2.90	2.71
		$d \rightarrow \sigma^\star d^\star$	2.70		2.68	2.70	2.91	2.71
	$^1T_{2g}$	$d \rightarrow \sigma^\star d^\star$	3.40	66	3.62	3.57	3.76	3.71
		$d \rightarrow \sigma^\star d^\star$	3.40		3.63	3.58	3.76	3.72
		$d \rightarrow \sigma^\star d^\star$	3.40		3.65	3.59	3.77	3.74
$Rh(NH_3)_6^{3+}$	$^1T_{1g}$	$d \rightarrow \sigma^\star d^\star$	3.96	66	3.77	3.77	3.82	3.78

Continued on next page

Molecule	State		Exp.	Ref.	Original	R2016	R2018	R2022
		$d \rightarrow \sigma^\star d^\star$	3.96		3.78	3.78	3.83	3.79
		$d \rightarrow \sigma^\star d^\star$	3.96		3.80	3.80	3.84	3.81
	$^1T_{2g}$	$d \rightarrow \sigma^\star d^\star$	4.88	66	4.47	4.44	4.47	4.49
		$d \rightarrow \sigma^\star d^\star$	4.88		4.49	4.45	4.48	4.51
		$d \rightarrow \sigma^\star d^\star$	4.88		4.51	4.45	4.48	4.53
MnO_4^-	$^1T_2$	$\pi \rightarrow d/\pi^\star$	2.40	67	2.47	1.80	2.70	2.31
		$\pi \rightarrow d/\pi^\star$	2.40		2.54	1.80	2.70	2.45
		$\pi \rightarrow d/\pi^\star$	2.40		2.54	1.85	2.71	2.45
	$^1T_2$	$\pi \rightarrow d/\pi^\star/\sigma^\star$	3.60	67	3.74			3.55
		$\pi \rightarrow d/\pi^\star/\sigma^\star$	3.60		3.75			3.58
		$\pi \rightarrow d/\pi^\star/\sigma^\star$	3.60		3.75			3.58
	$^1T_2$	$\pi \rightarrow d/\pi^\star$	4.10	67	4.33	3.85	4.95	4.24
		$\pi \rightarrow d/\pi^\star$	4.10		4.33	3.93	4.95	4.25
		$\pi \rightarrow d/\pi^\star$	4.10		4.33	3.93	4.95	4.25
	$^1T_2$	$\pi \rightarrow d/\pi^\star$	5.50	67	5.73			5.50
		$\pi \rightarrow d/\pi^\star$	5.50		5.83			5.56
		$\pi \rightarrow d/\pi^\star$	5.50		5.83			5.56
TcO_4^-	$^1T_2$	$\pi \rightarrow d/\pi^\star$	4.35	68	3.92	3.54	4.04	3.81
		$\pi \rightarrow d/\pi^\star$	4.35		3.95	3.58	4.06	3.90
		$\pi \rightarrow d/\pi^\star$	4.35		3.95	3.58	4.06	3.90
	$^1T_2$	$d/\pi \rightarrow d^\star/\pi^\star$	5.10	68	4.88	4.44	4.99	4.78
		$d/\pi \rightarrow d^\star/\pi^\star$	5.10		4.90	4.44	4.97	4.82
		$d/\pi \rightarrow d^\star/\pi^\star$	5.10		4.90	4.48	4.97	4.82
	$^1T_2$	$d/\pi \rightarrow d^\star/\pi^\star/\sigma^\star$	6.60	69	5.92	5.62	6.16	5.85

Continued on next page

Molecule	State		Exp.	Ref.	Original	R2016	R2018	R2022
		$d/\pi \rightarrow d^\star/\pi^\star/\sigma^\star$	6.60		5.91	5.62	6.15	5.85
		$d/\pi \rightarrow d^\star/\pi^\star/\sigma^\star$	6.60		5.91	5.64	6.15	5.87

Table S16: Selected inorganic molecules and vertical absorption energies for the tight selection threshold (in eV) used for benchmarking.

Molecule	State		Exp.	Ref.	Original	R2016	R2018	R2022
MoF_6	$^1T_{1u}$	$\pi \rightarrow d/\pi^\star$	5.90	62	5.25	4.99	4.94	5.06
		$\pi \rightarrow d/\pi^\star$	5.90		5.25	4.99	4.94	5.07
		$\pi \rightarrow d/\pi^\star$	5.90		5.25	4.99	4.94	5.07
	$^1T_{1u}$	$\pi \rightarrow d/\pi^\star$	6.54	62	5.87	5.45	5.40	5.54
		$\pi \rightarrow d/\pi^\star$	6.54		5.87	5.45	5.40	5.54
		$\pi \rightarrow d/\pi^\star$	6.54		5.87	5.45	5.40	5.54
	$^1T_{1u}$	$\pi \rightarrow d/\pi^\star$	7.12	62	6.58	6.02	6.05	6.16
		$\pi \rightarrow d/\pi^\star$	7.12		6.58	6.02	6.05	6.16
		$\pi \rightarrow d/\pi^\star$	7.12		6.58	6.02	6.05	6.16
$Mo(CO)_6$	$^1T_{1u}$	$d/\pi \rightarrow \pi^\star$	4.32	63	4.33	4.24	4.38	4.42
		$d/\pi \rightarrow \pi^\star$	4.32		4.33	4.24	4.38	4.42
		$d/\pi \rightarrow \pi^\star$	4.32		4.33	4.24	4.38	4.42
	$^1T_{1u}$	$d/\pi \rightarrow \pi^\star$	5.44	63	5.65	5.43	5.57	5.66
		$d/\pi \rightarrow \pi^\star$	5.44		5.65	5.43	5.57	5.66
		$d/\pi \rightarrow \pi^\star$	5.44		5.65	5.43	5.57	5.66
$Cr(CO)_6$	$^1T_{1u}$	$d/\pi \rightarrow \pi^\star$	4.43	63	4.57	4.22	4.67	4.65
		$d/\pi \rightarrow \pi^\star$	4.43		4.57	4.22	4.67	4.65
		$d/\pi \rightarrow \pi^\star$	4.43		4.57	4.22	4.67	4.65
	$^1T_{1u}$	$d/\pi \rightarrow \pi^\star$	5.41	63	5.58	5.15	5.67	5.63
		$d/\pi \rightarrow \pi^\star$	5.41		5.58	5.15	5.67	5.63
		$d/\pi \rightarrow \pi^\star$	5.41		5.58	5.15	5.67	5.63
$Ni(CO)_4$	$^1T_2$	$\sigma/d \rightarrow \pi^\star$	4.54	64	4.31	3.84	4.42	4.20

Continued on next page

Molecule	State		Exp.	Ref.	Original	R2016	R2018	R2022
		$\sigma/d \rightarrow \pi^\star$	4.54		4.32	3.86	4.44	4.23
		$\sigma/d \rightarrow \pi^\star$	4.54		4.32	3.86	4.44	4.23
	$^1T_2$	$\sigma/d \rightarrow \pi^\star$	5.17	64	5.62	4.87	5.24	5.03
		$\sigma/d \rightarrow \pi^\star$	5.17		5.65	4.90	5.25	5.04
		$\sigma/d \rightarrow \pi^\star$	5.17		5.65	4.90	5.25	5.04
$Co(H2O)_6^{2+}$	$^3T_g(t_g^5e_g^1)$	$\pi/d \rightarrow \sigma^\star d^\star$	0.99	65	0.78	1.29	1.28	1.05
		$\pi/d \rightarrow \sigma^\star d^\star$	0.99		0.81	1.31	1.30	1.07
		$\pi/d \rightarrow \sigma^\star d^\star$	0.99		0.84	1.34	1.33	1.11
	$^3T_g(t_g^5e_g^1)$	$\pi/d \rightarrow \sigma^\star d^\star$	1.55	65	1.26	1.70	1.69	1.54
		$\pi/d \rightarrow \sigma^\star d^\star$	1.55		1.30	1.75	1.74	1.58
		$\pi/d \rightarrow \sigma^\star d^\star$	1.55		1.33	1.77	1.76	1.61
	$^1T_g(t_g^5e_g^1)$	$\pi/d \rightarrow \sigma^\star d^\star$	2.06	65	1.59	1.88	1.89	1.66
		$\pi/d \rightarrow \sigma^\star d^\star$	2.06		1.62	1.89	1.91	1.68
		$\pi/d \rightarrow \sigma^\star d^\star$	2.06		1.66	1.92	1.93	1.72
	$^1T_g(t_g^5e_g^1)$	$\pi/d \rightarrow \sigma^\star d^\star$	3.09	65	2.58	2.74	2.73	2.66
		$\pi/d \rightarrow \sigma^\star d^\star$	3.09		2.53	2.77	2.76	2.70
		$\pi/d \rightarrow \sigma^\star d^\star$	3.09		2.60	2.79	2.78	2.72
$Co(NH_3)_6^{3+}$	$^1T_{1g}$	$d \rightarrow \sigma^\star d^\star$	2.70	66	2.48	2.59	2.64	2.58
		$d \rightarrow \sigma^\star d^\star$	2.70		2.50	2.61	2.66	2.60
		$d \rightarrow \sigma^\star d^\star$	2.70		2.51	2.62	2.66	2.61
	$^1T_{2g}$	$d \rightarrow \sigma^\star d^\star$	3.40	66	3.46	3.50	3.55	3.62
		$d \rightarrow \sigma^\star d^\star$	3.40		3.46	3.50	3.56	3.63
		$d \rightarrow \sigma^\star d^\star$	3.40		3.48	3.52	3.57	3.65
$Rh(NH_3)_6^{3+}$	$^1T_{1g}$	$d \rightarrow \sigma^\star d^\star$	3.96	66	3.67	3.71	3.74	3.73

Continued on next page

Molecule	State		Exp.	Ref.	Original	R2016	R2018	R2022
		$d \rightarrow \sigma^\star d^\star$	3.96		3.68	3.72	3.75	3.74
		$d \rightarrow \sigma^\star d^\star$	3.96		3.71	3.74	3.77	3.77
	$^1T_{2g}$	$d \rightarrow \sigma^\star d^\star$	4.88	66	4.38	4.38	4.41	4.46
		$d \rightarrow \sigma^\star d^\star$	4.88		4.41	4.40	4.43	4.48
		$d \rightarrow \sigma^\star d^\star$	4.88		4.42	4.41	4.44	4.49
MnO_4^-	$^1T_2$	$\pi \rightarrow d/\pi^\star$	2.40	67	1.52	1.14	2.09	2.20
		$\pi \rightarrow d/\pi^\star$	2.40		1.72	1.39	2.09	2.30
		$\pi \rightarrow d/\pi^\star$	2.40		1.72	1.39	2.11	2.30
	$^1T_2$	$\pi \rightarrow d/\pi^\star/\sigma^\star$	3.60	67	2.93			3.48
		$\pi \rightarrow d/\pi^\star/\sigma^\star$	3.60		2.93			3.48
		$\pi \rightarrow d/\pi^\star/\sigma^\star$	3.60		2.93			3.50
	$^1T_2$	$\pi \rightarrow d/\pi^\star$	4.10	67	3.40	3.29	4.26	4.19
		$\pi \rightarrow d/\pi^\star$	4.10		3.40	3.44	4.26	4.20
		$\pi \rightarrow d/\pi^\star$	4.10		3.42	3.44	4.42	4.20
	$^1T_2$	$\pi \rightarrow d/\pi^\star$	5.50	67	5.14			5.40
		$\pi \rightarrow d/\pi^\star$	5.50		5.14			5.48
		$\pi \rightarrow d/\pi^\star$	5.50		5.14			5.48
TcO_4^-	$^1T_2$	$\pi \rightarrow d/\pi^\star$	4.35	68	3.55	3.70	3.82	3.75
		$\pi \rightarrow d/\pi^\star$	4.35		3.63	3.74	3.86	3.83
		$\pi \rightarrow d/\pi^\star$	4.35		3.63	3.74	3.86	3.83
	$^1T_2$	$d/\pi \rightarrow d^\star/\pi^\star$	5.10	68	4.52	4.68	4.81	4.70
		$d/\pi \rightarrow d^\star/\pi^\star$	5.10		4.57	4.68	4.82	4.75
		$d/\pi \rightarrow d^\star/\pi^\star$	5.10		4.57	4.69	4.82	4.75
	$^1T_2$	$d/\pi \rightarrow d^\star/\pi^\star/\sigma^\star$	6.60	69	5.56	5.84	6.00	5.81

Continued on next page

Molecule	State		Exp.	Ref.	Original	R2016	R2018	R2022
		$d/\pi \rightarrow d^\star/\pi^\star/\sigma^\star$	6.60		5.56	5.84	6.00	5.81
		$d/\pi \rightarrow d^\star/\pi^\star/\sigma^\star$	6.60		5.58	5.85	6.00	5.82

Table S17: Selected metal organic molecules and vertical absorption energies for the standard selection threshold (in eV) used for benchmarking.

Molecule	State		Exp.	Ref.	Original	R2016	R2018	R2022
$Ru(bpy)_3$	band max.	$d \rightarrow \pi^\star$	2.88	70	2.92	2.81	2.92	3.17
		$d \rightarrow d^\star$	4.00	70	3.94	4.28	3.94	3.97
		$\pi \rightarrow \pi^\star$	4.38	70	4.37	4.26	4.41	4.66
		$d \rightarrow \pi^\star$	5.02	70	4.98	4.86	5.08	5.30
$Ru(tpy)(bpy)(py)^{2+}$	band max.	$d \rightarrow \pi^\star$	2.66	71	2.76	2.67	2.77	3.00
		$d \rightarrow \pi^\star$	2.99	71	3.02	3.04	3.14	3.37
		$d \rightarrow \pi^\star$	3.99	71	4.04	3.92	4.09	4.32
		$d/\pi \rightarrow \pi^\star$	4.40	71	4.38	4.32	4.49	4.71
		$d/\pi \rightarrow \pi^\star$	5.30	71	5.02	5.02	5.23	5.44
$Rh(bpy)_3^{3+}$	band max.	$\pi \rightarrow \pi^\star$	3.88	72	3.89	3.82	3.99	4.22
		$\pi \rightarrow \pi^\star$	4.04	72	3.94	3.88	4.05	4.25
		$d/\pi \rightarrow \pi^\star$	5.15	72	5.12	5.10	5.32	5.56
$Rh(phen)_3^{3+}$	band max.	$\pi \rightarrow \pi^\star$	4.44	73	4.44	4.35	4.53	4.73
$Rh(tpy)(bpy)(py)^{2+}$	band max.	$\pi \rightarrow \pi^\star$	3.46	74	3.50	3.56	3.60	3.91
		$\pi \rightarrow \pi^\star$	3.65	74	3.85	3.91	3.73	4.24
		$\pi \rightarrow \pi^\star$	4.00	74	4.08	4.11	4.08	4.48
		$d/\pi \rightarrow \pi^\star$	4.37	74	4.28	4.31	4.29	4.68
ZnP	1^1E_u	$\pi \rightarrow \pi^\star$	2.18	75	2.19	2.17	2.20	2.32
		$\pi \rightarrow \pi^\star$	2.18		2.19	2.17	2.20	2.32
	2^1E_u	$\pi \rightarrow \pi^\star$	3.13	75	3.25	3.18	3.19	3.46
		$\pi \rightarrow \pi^\star$	3.13		3.25	3.18	3.19	3.46
	4^1E_u	$\pi \rightarrow \pi^\star$	4.07	75	4.04	4.02	4.15	3.93

Continued on next page

Molecule	State		Exp.	Ref.	Original	R2016	R2018	R2022
		$\pi \rightarrow \pi^\star$	4.07		4.04	4.02	4.15	3.93
ZnTBP	1^1E_u	$\pi \rightarrow \pi^\star$	1.98	76	1.93	1.89	1.95	2.14
		$\pi \rightarrow \pi^\star$	1.98		1.93	1.89	1.95	2.14
	2^1E_u	$\pi \rightarrow \pi^\star$	3.06	76	3.03	2.94	3.01	3.30
		$\pi \rightarrow \pi^\star$	3.06		3.03	2.94	3.01	3.30
	3^1E_u	$\pi \rightarrow \pi^\star$	3.87	76	3.73	3.68	3.81	4.01
		$\pi \rightarrow \pi^\star$	3.87		3.73	3.68	3.81	4.01
	8^1E_u	$\pi \rightarrow \pi^\star$	4.89	76	4.61	4.55	4.76	4.96
		$\pi \rightarrow \pi^\star$	4.89		4.61	4.55	4.76	4.96
ZnPC	1^1E_u	$\pi \rightarrow \pi^\star$	1.89	77	1.81	1.82	1.84	2.06
		$\pi \rightarrow \pi^\star$	1.89		1.81	1.82	1.84	2.06
	2^1E_u	$\pi \rightarrow \pi^\star$	3.71	77	3.50	3.53	3.72	3.63
		$\pi \rightarrow \pi^\star$	3.71		3.50	3.53	3.72	3.63
	3^1E_u	$\pi \rightarrow \pi^\star$	3.74	77	3.60	3.60	3.67	3.92
		$\pi \rightarrow \pi^\star$	3.74		3.60	3.60	3.67	3.92
	1^1A_{2u}	$\pi \rightarrow \pi^\star$	3.99	77	3.91	3.90	4.10	4.30
Ferrocene	a^3E_{1g}	$d \rightarrow d^\star/\pi^\star$	2.34	27	2.04	1.97	2.15	2.29
		$d \rightarrow d^\star/\pi^\star$	2.34		2.04	1.97	2.15	2.29
	a^1E_{1g}	$d \rightarrow d^\star/\pi^\star$	2.98	78	2.92	2.72	2.93	3.14
		$d \rightarrow d^\star/\pi^\star$	2.98		2.92	2.72	2.93	3.14
	$^1E_{2g}$	$d \rightarrow d^\star/\pi^\star$	2.70	78	2.69	2.51	2.69	2.83
		$d \rightarrow d^\star/\pi^\star$	2.70		2.69	2.51	2.69	2.83
	b^1E_{1g}	$d \rightarrow d^\star/\pi^\star$	3.82	78	3.99	3.72	4.02	3.64
		$d \rightarrow d^\star/\pi^\star$	3.82		3.99	3.72	4.02	3.65

Continued on next page

Molecule	State		Exp.	Ref.	Original	R2016	R2018	R2022
Ruthenocene[a]	a^1E_{1g}	$d \rightarrow d^\star/\pi^\star$	3.66	27	3.55	3.49	3.62	3.68
		$d \rightarrow d^\star/\pi^\star$	3.66		3.55	3.49	3.62	3.68
	$^1E_{2g}$	$d \rightarrow d^\star/\pi^\star$	4.03	27	3.56	3.48	3.63	3.72
		$d \rightarrow d^\star/\pi^\star$	4.03		3.56	3.48	3.63	3.72
Cobaltocene	a^3E_{1g}	$d \rightarrow d^\star/\pi^\star$	2.70	27	2.26	2.08	2.43	2.29
		$d \rightarrow d^\star/\pi^\star$	2.70		2.26	2.08	2.43	2.29
	a^1E_{1g}	$d \rightarrow d^\star/\pi^\star$	3.01	27	2.57	2.53	2.86	2.69
		$d \rightarrow d^\star/\pi^\star$	3.01		2.57	2.53	2.86	2.69
	$^1E_{2g}$	$d \rightarrow d^\star/\pi^\star$	3.27	27	2.85	2.77	3.12	2.95
		$d \rightarrow d^\star/\pi^\star$	3.27		2.85	2.77	3.12	2.95
	b^1E_{1g}	$d \rightarrow d^\star/\pi^\star$	4.12	27	4.08	3.79	4.19	4.04
		$d \rightarrow d^\star/\pi^\star$	4.12		4.08	3.79	4.19	4.04

[a] Some states were removed in comparison to the R2018 assessment set.

Table S18: Selected metal organic molecules and vertical absorption energies for the tight selection threshold (in eV) used for benchmarking.

Molecule	State		Exp.	Ref.	Original	R2016	R2018	R2022
$Ru(bpy)_3$	band max.	$d \rightarrow \pi^\star$	2.88	70	2.97	2.91	2.93	3.17
		$d \rightarrow d^\star$	4.00	70	4.09	4.28	4.15	3.97
		$\pi \rightarrow \pi^\star$	4.38	70	4.43	4.37	4.40	4.66
		$d \rightarrow \pi^\star$	5.02	70	4.92	4.92	5.09	5.30
$Ru(tpy)(bpy)(py)^{2+}$	band max.	$d \rightarrow \pi^\star$	2.66	71	2.82	2.73	2.80	3.00
		$d \rightarrow \pi^\star$	2.99	71	3.09	3.11	3.16	3.37
		$d \rightarrow \pi^\star$	3.99	71	4.15	4.01	4.13	4.32
		$d/\pi \rightarrow \pi^\star$	4.40	71	4.40	4.40	4.51	4.71
		$d/\pi \rightarrow \pi^\star$	5.30	71	5.04	5.04	5.31	5.44
$Rh(bpy)_3^{3+}$	band max.	$\pi \rightarrow \pi^\star$	3.88	72	3.86	3.89	3.92	4.22
		$\pi \rightarrow \pi^\star$	4.04	72	3.92	3.96	3.99	4.25
		$d/\pi \rightarrow \pi^\star$	5.15	72	5.17	5.25	5.38	5.56
$Rh(phen)_3^{3+}$	band max.	$\pi \rightarrow \pi^\star$	4.44	73	4.37	4.35	4.53	4.73
$Rh(tpy)(bpy)(py)^{2+}$	band max.	$\pi \rightarrow \pi^\star$	3.46	74	3.51	3.64	3.64	3.91
		$\pi \rightarrow \pi^\star$	3.65	74	3.83	3.97	4.03	4.24
		$\pi \rightarrow \pi^\star$	4.00	74	4.08	4.18	4.26	4.48
		$d/\pi \rightarrow \pi^\star$	4.37	74	4.31	4.44	4.48	4.68
ZnP	1^1E_u	$\pi \rightarrow \pi^\star$	2.18	75	2.16	2.17	2.22	2.32
		$\pi \rightarrow \pi^\star$	2.18		2.16	2.17	2.22	2.32
	2^1E_u	$\pi \rightarrow \pi^\star$	3.13	75	3.28	3.24	3.28	3.46
		$\pi \rightarrow \pi^\star$	3.13		3.28	3.24	3.28	3.46
	4^1E_u	$\pi \rightarrow \pi^\star$	4.07	75	4.02	4.04	4.26	3.93

Continued on next page

Molecule	State		Exp.	Ref.	Original	R2016	R2018	R2022
		$\pi \rightarrow \pi^\star$	4.07		4.02	4.04	4.26	3.93
ZnTBP	1^1E_u	$\pi \rightarrow \pi^\star$	1.98	76	1.89	1.91	1.93	2.14
		$\pi \rightarrow \pi^\star$	1.98		1.89	1.91	1.93	2.14
	2^1E_u	$\pi \rightarrow \pi^\star$	3.06	76	3.03	3.00	3.05	3.30
		$\pi \rightarrow \pi^\star$	3.06		3.03	3.00	3.05	3.30
	3^1E_u	$\pi \rightarrow \pi^\star$	3.87	76	3.68	3.68	3.81	4.01
		$\pi \rightarrow \pi^\star$	3.87		3.68	3.68	3.81	4.01
	8^1E_u	$\pi \rightarrow \pi^\star$	4.89	76	4.59	4.57	4.79	4.96
		$\pi \rightarrow \pi^\star$	4.89		4.59	4.57	4.79	4.96
ZnPC	1^1E_u	$\pi \rightarrow \pi^\star$	1.89	77	1.81	1.82	1.85	2.06
		$\pi \rightarrow \pi^\star$	1.89		1.81	1.82	1.85	2.06
	2^1E_u	$\pi \rightarrow \pi^\star$	3.71	77	3.50	3.53	3.77	3.63
		$\pi \rightarrow \pi^\star$	3.71		3.50	3.53	3.77	3.63
	3^1E_u	$\pi \rightarrow \pi^\star$	3.74	77	3.60	3.60	3.73	3.92
		$\pi \rightarrow \pi^\star$	3.74		3.60	3.60	3.73	3.92
	1^1A_{2u}	$\pi \rightarrow \pi^\star$	3.99	77	3.91	3.90	4.24	4.30
Ferrocene	a^3E_{1g}	$d \rightarrow d^\star/\pi^\star$	2.34	27	2.24	1.97	2.54	2.29
		$d \rightarrow d^\star/\pi^\star$	2.34		2.24	1.97	2.54	2.29
	a^1E_{1g}	$d \rightarrow d^\star/\pi^\star$	2.98	78	3.10	2.73	3.25	3.14
		$d \rightarrow d^\star/\pi^\star$	2.98		3.10	2.73	3.25	3.14
	$^1E_{2g}$	$d \rightarrow d^\star/\pi^\star$	2.70	78	2.99	2.50	3.10	2.83
		$d \rightarrow d^\star/\pi^\star$	2.70		2.99	2.50	3.10	2.83
	b^1E_{1g}	$d \rightarrow d^\star/\pi^\star$	3.82	78	3.54	3.62	4.17	3.64
		$d \rightarrow d^\star/\pi^\star$	3.82		3.54	3.62	4.17	3.65

Continued on next page

Molecule	State		Exp.	Ref.	Original	R2016	R2018	R2022
Ruthenocene[a]	a^1E_{1g}	$d \rightarrow d^\star/\pi^\star$	3.66	27	3.57	3.48	3.81	3.68
		$d \rightarrow d^\star/\pi^\star$	3.66		3.57	3.48	3.81	3.68
	$^1E_{2g}$	$d \rightarrow d^\star/\pi^\star$	4.03	27	3.59	3.44	3.78	3.72
		$d \rightarrow d^\star/\pi^\star$	4.03		3.59	3.44	3.78	3.72
Cobaltocene	a^3E_{1g}	$d \rightarrow d^\star/\pi^\star$	2.70	27	1.95	1.68	2.47	2.29
		$d \rightarrow d^\star/\pi^\star$	2.70		1.95	1.68	2.47	2.29
	a^1E_{1g}	$d \rightarrow d^\star/\pi^\star$	3.01	27	2.47	2.37	3.18	2.69
		$d \rightarrow d^\star/\pi^\star$	3.01		2.47	2.37	3.18	2.69
	$^1E_{2g}$	$d \rightarrow d^\star/\pi^\star$	3.27	27	2.21	2.11	2.91	2.95
		$d \rightarrow d^\star/\pi^\star$	3.27		2.21	2.11	2.91	2.95
	b^1E_{1g}	$d \rightarrow d^\star/\pi^\star$	4.12	27	3.62	3.39	4.23	4.04
		$d \rightarrow d^\star/\pi^\star$	4.12		3.62	3.39	4.23	4.04

[a] Some states were removed in comparison to the R2018 assessment set.

Table S19: NEVPT2 vertical excitation energies, states used in state averaging of complete active space self consistent field (CASSCF) wave function, and active spaces. Numbers in parentheses denote the number of electrons and the number of orbitals used to generate the active space.

Molecule	State	Active space (#El, #MOs)	States used for averaging	Vertical excitation energy [eV]
o-Benzyne	$^1A_1$	(8, 8)	$3\ ^1A_1$	7.23
	$^1B_2$	(8, 8)	$1\ ^1A_1, 2\ ^1B_2$	8.15
	$^3A_1$	(8, 8)	$1\ ^1A_1, 3\ ^3A_1$	7.12
Thioformaldehyde	$^1A_1$	(8, 9)	$5\ ^1A_1$	7.37
	$^1A_2$	(8, 9)	$1\ ^1A_1, 4\ ^1A_2$	7.93
	$^3A_2$	(8, 9)	$1\ ^1A_1, 3\ ^3A_2$	7.43
Dithiosuccinimide	$^1A_1$	(10, 7)	$4\ ^1A_1$	5.85
	$^1A_1$	(10, 7)	$4\ ^1A_1$	7.13
	$^3B_2$	(10, 7)	$1\ ^1A_1, 2\ ^3B_2$	5.86
	$^3A_1$	(10, 7)	$1\ ^1A_1, 3\ ^3A_1$	6.99
Nitromethane	$^3A'$	(8, 9)	$1\ ^1A', 7\ ^1A'$	8.79
Dithiin	$^1A_1$	(8, 7)	$4\ ^1A_1$	4.91

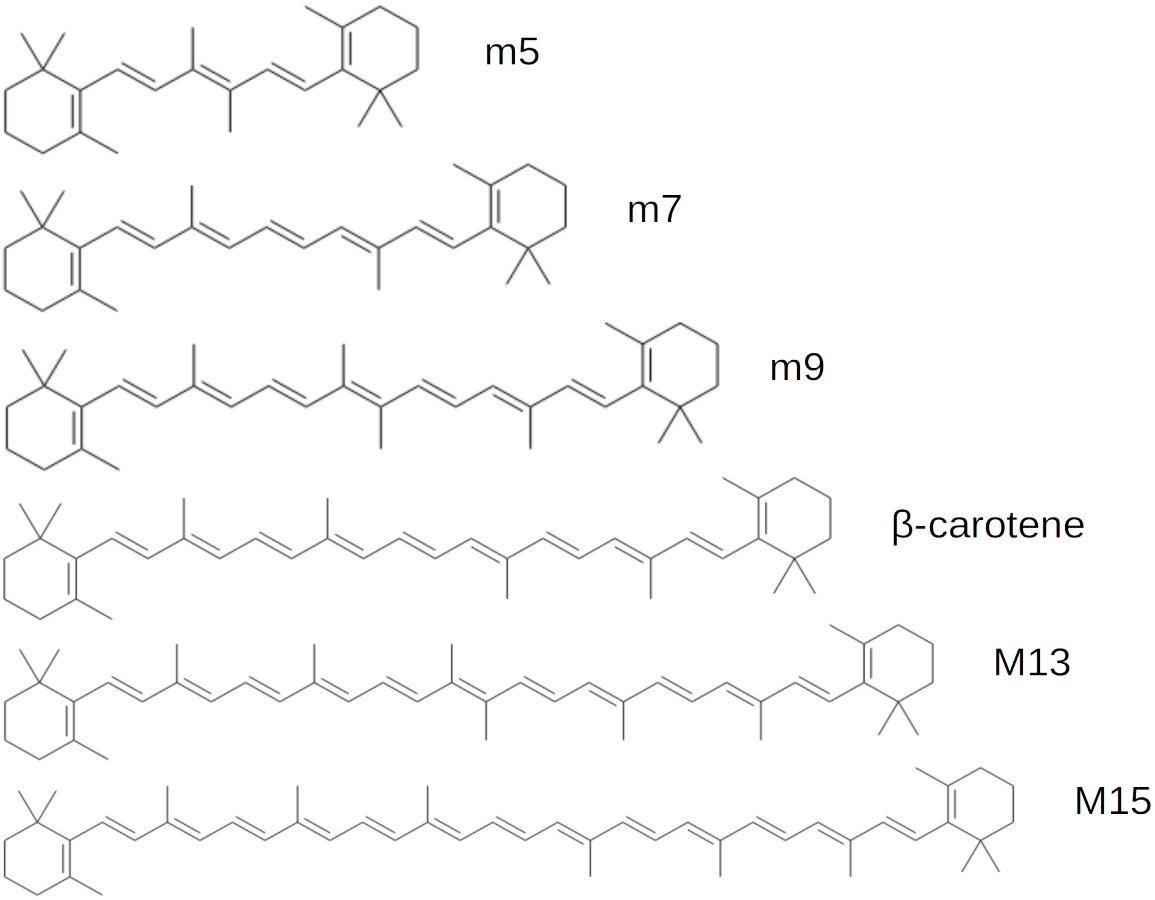

Figure S6: Chemical structure of β-carotenoids. A capital M denotes *macro*-, a lowercase m *mini*-carotenoids.

Figure S7: Chemical structure of cycl[3.3.3]azine (left) and heptazine (right).

Table S20: Gaussian basis functions placed in the center of C_{60}. Functions were taken from the augmented Sadlej basis sets[79] of Casida et al.[80]

l	Exponent	Coefficient
0	0.047900	1.0000
0	0.014700	1.0000
0	0.004480	1.0000
1	0.038568	1.0000
1	0.012000	1.0000
1	0.004480	1.0000
2	0.121940	0.6535
2	0.038658	0.8636
2	0.012000	1.0000
3	0.038658	0.8636
3	0.012000	1.0000

Table S21: Computed and experimental transition energies of C_{60} at the ground state geometry in eV. Numbers given in parentheses denote oscillator strengths. Band codes used by Leach et al.[82] and Catalán[83] are given in brackets. Leading configurations (LC) refer to orbitals in I_h symmetry. Italic numbers refer to energies calculated with the direct symmetry-adapted cluster-configuration interaction (SAC-CI) method[84] by Fukuda and Ehara[85].

$\rightarrow 1^1A_g$	Exp.	R2022	R2016	LC R2022	LC R2016
1^1G_g	1.82 - 1.91[82]	2.43	1.94	H→L	H→L
		2.48	1.98		
	1.75	2.49	1.98		
		2.50	1.99		
1^1T_{2g}	2.0 - 2.04[82,83,88]	2.52	2.01	H→L	H→L
	$[\gamma_0 - \gamma_5]$	2.52	2.01		
	1.90	2.54	2.02		
1^1T_{1g}	2.0 - 2.04[82,83,88]	2.55	2.04	H→L	H→L
	$[\gamma_0 - \gamma_5]$	2.56	2.05		

Continued on next page

$\rightarrow 1^1A_g$	Exp.	R2022	R2016	LC R2022	LC R2016
	1.94	2.56	2.05		
1^1H_{1g}	2.24^{86a}; 2.26^{87b}	2.72	2.19	H→L	H→L
		2.72	2.20		
		2.76	2.22		
	2.09	2.76	2.23		
		2.78	2.24		
1^1T_{2u}[e]	2.98^{86}	3.49 ($< 1^{-4}$)	2.95 ($< 1^{-4}$)	H→L+1, H-1→L	H→L+1, H-1→L
		3.50 ($< 1^{-4}$)	2.95 ($< 1^{-4}$)		
	2.98	3.50 ($< 1^{-4}$)	2.96 ($< 1^{-4}$)		
2^1T_{1u}	3.04-$3.07^{82,83,86}$	3.66 ($< 1^{-4}$)	3.09 ($< 1^{-4}$)	H→L+1	H → L+1
	(0.0030^{89})(0.0015^{82})	3.66 ($< 1^{-4}$)	3.09 ($< 1^{-4}$)		
	[$A_0 - A_1$]	3.67 ($< 1^{-4}$)	3.12 ($< 1^{-4}$)		
1^1H_u	*3.30*	3.69 ($< 1^{-4}$)	3.10 ($< 1^{-4}$)	H→L+1	H→L+1
		3.70	3.13		
		3.70	3.13		
		3.70 ($< 1^{-4}$)	3.13 ($< 1^{-4}$)		
		3.70 ($< 1^{-4}$)	3.14 ($< 1^{-4}$)		
1^1A_u[c]	-	3.75	3.18	H→L+1	H→L+1
1^1T_{2u}[c]	*3.38*	3.86 ($< 1^{-4}$)	3.27 ($< 1^{-4}$)	H-1→L, H-2→L	H-2→L
		3.86 ($< 1^{-4}$)	3.27 ($< 1^{-4}$)		
		3.87 ($< 1^{-4}$)	3.28 ($< 1^{-4}$)		

Continued on next page

$\rightarrow 1^1A_g$	Exp.	R2022	R2016	LC R2022	LC R2016
1^1G_u	*3.38*	3.91	3.31	H-2→L, H-1→L	H-2→L, H-1→L
		3.98 (0.0039)	3.37 (0.0013)		
		3.98 (0.0005)	3.37 (0.0067)		
		3.99 (0.0007)	3.38 (0.0003)		
3^1T_{1u}	3.29,[82] *3.67* (0.003[89]) [B_0]	3.99 (0.0338)	3.37 (0.0172)	H→L+1	H-2→L, H→L+1
		4.00 (0.0381)	3.38 (0.0175)		
		4.00 (0.0398)	3.38 (0.0181)		
2^1H_u	*3.50*	4.00 (0.0069)	3.39 (0.0173)	H-1→L, H-2→L	H-1→L, H-2→L, H →L+1
		4.01 (0.0005)	3.40 (0.0090)		
		4.02 (0.0022)	3.40 (0.0042)		
		4.02	3.40		
		4.02	3.41		
3^1H_u	*3.68*	4.02 (0.0003)	3.41 ($< 10^{-4}$)	H-1→L	H-1→L
		4.03 (0.0002)	3.42 (0.0021)		
		4.04 ($< 10^{-4}$)	3.42 (0.0002)		
		4.05	3.45		
		4.06	3.45		
2^1G_u	*3.69*	4.09	3.47 (0.0003)	H-1→L, H→L+1	H-1→L
		4.11 ($< 10^{-4}$)	3.47		
		4.11 ($< 10^{-4}$)	3.47 ($< 10^{-4}$)		
		4.11 (0.0004)	3.48 ($< 10^{-4}$)		

Continued on next page

$\rightarrow 1^1A_g$	Exp.	R2022	R2016	LC R2022	LC R2016
		4.17 (0.0004)	3.55 (0.0003)		
2^1T_{2u}	*3.74*	4.17 (0.0001)	3.56 (0.0003)	H-2→L	H-1 → L,
		4.18 (0.0002)	3.56 (0.0002)		H-2 → L
	3.78,[82] 3.84,[83] *3.90*	4.36 (0.4150)	3.75 (0.3564)		
5^1T_{1u}	(0.3700[82]) (0.3980[89])	4.37 (0.3971)	3.76 (0.3444)	H-1→L	H-1 → L
	[C]	4.37 (0.3972)	3.76 (0.3425)		

[a] Assigned to ^1H_u by authors.

[b] Assigned to superposition of $^1T_{1g}$,$^1T_{2g}$,^1G_g by authors.

[c] G_u state of Fukuda and Ehara[85]. Assignment controversial with DFT/MRCI results.

[d] H: highest occupied molecular orbital, L: lowest unoccupied molecular orbital

[e] 1^1T_{2u} state of Fukuda and Ehara[85]. Assigned to $2^1G_u, 2^1H_u$ by Bulliard et al.[86], triplet state by Abouaf et al.[87].

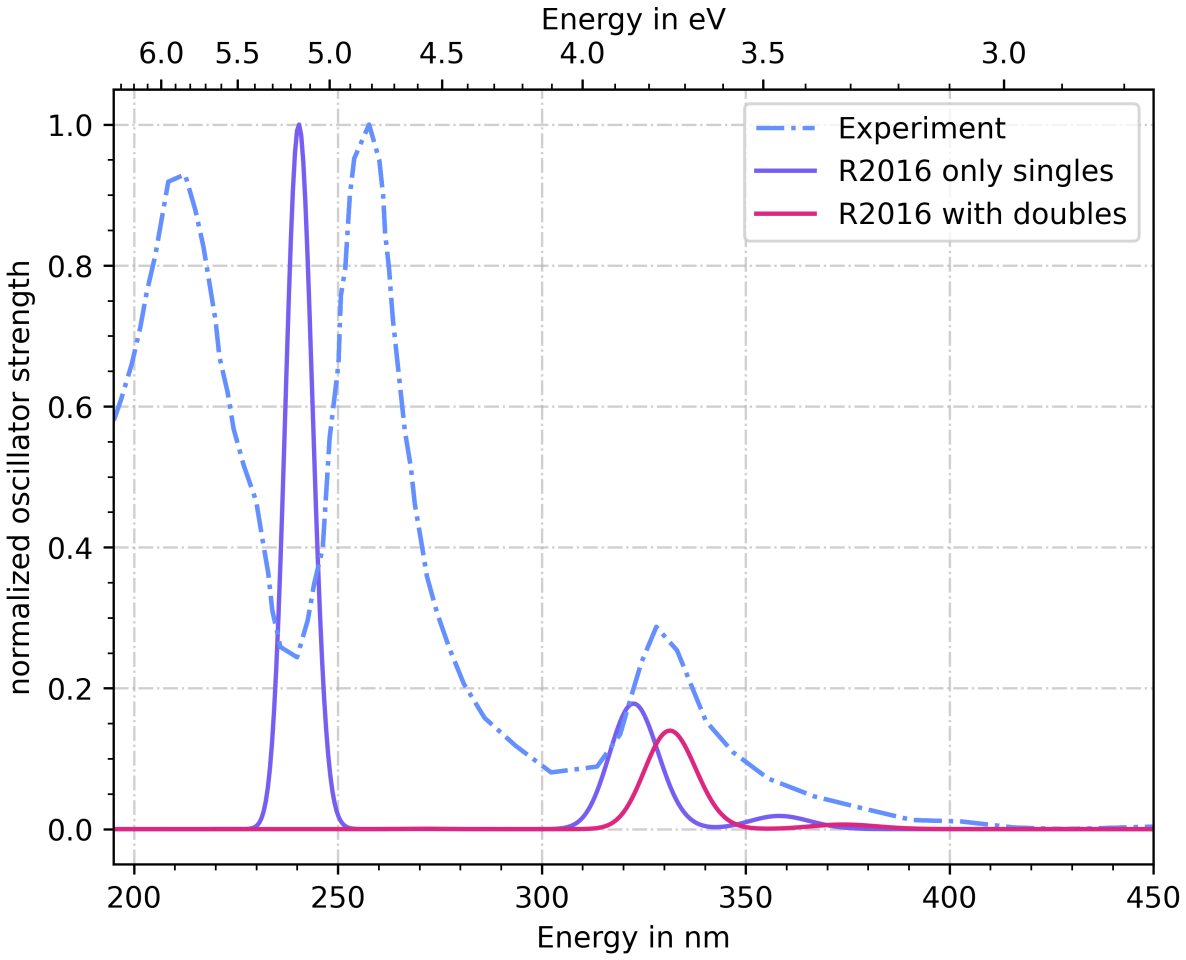

Figure S8: Absorption spectra for different reference spaces computed with the R2016 Hamiltonian. The tight parameter set and a SV(P) basis set were used. The basis was augmented by placing diffuse functions given in Table S20 in the center of mass of C_{60}. Energies were broadened with Gaussian functions with full-width at half maximum of 0.25 eV. The intensities were normalized to the maximum of the R2016 with singles spectrum.

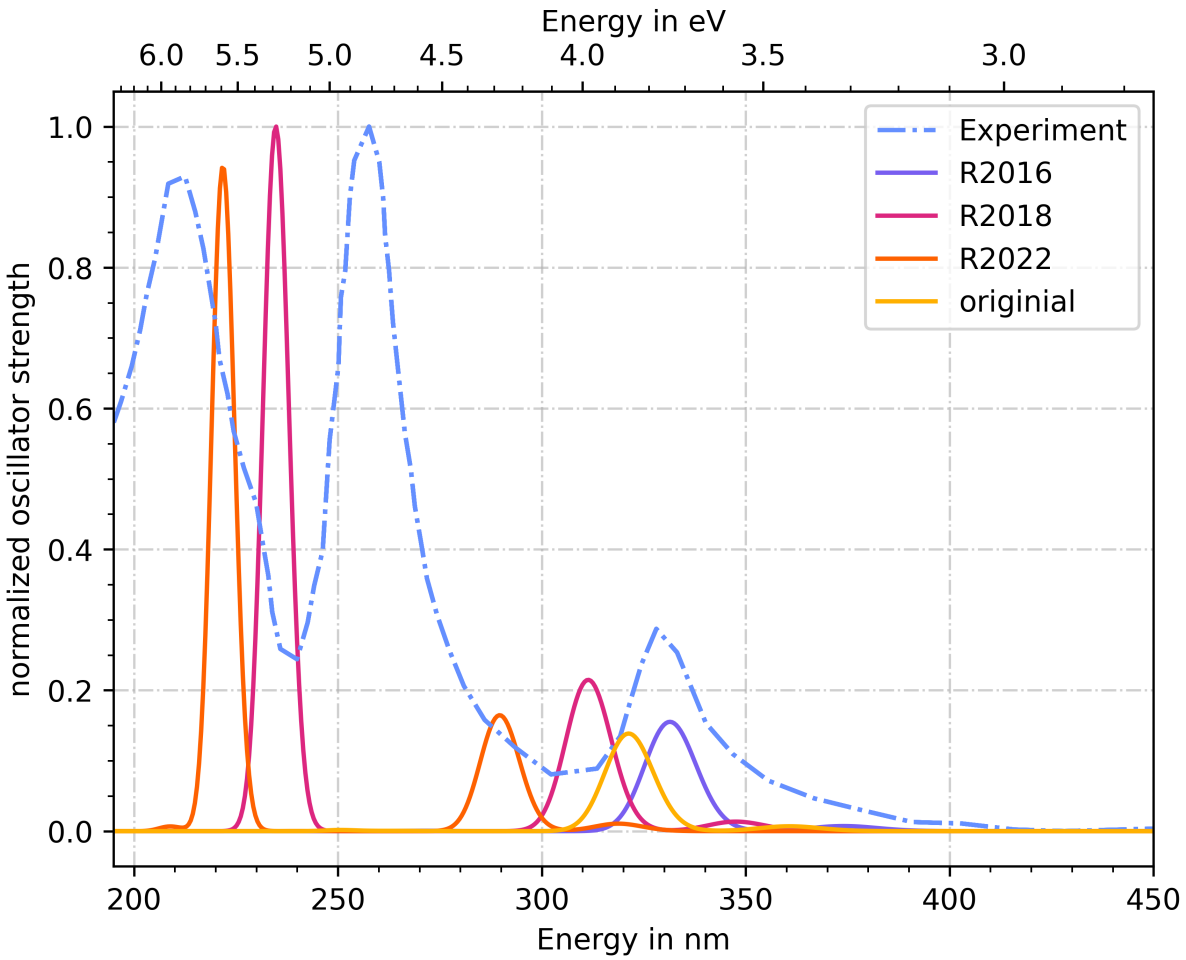

Figure S9: Transition energies computed at the ground state geometry of C_{60} using different DFT/MRCI Hamiltonians. The one-particle basis was generated using an augmented def2-SV(P)[81] basis set. For augmentation the functions given in Table S20 were placed in the center of mass of C_{60}. Energies were broadened with Gaussian functions with full-width at half maximum of 0.25 eV The intensities were normalized to the maximum value of the R2018 calculations.

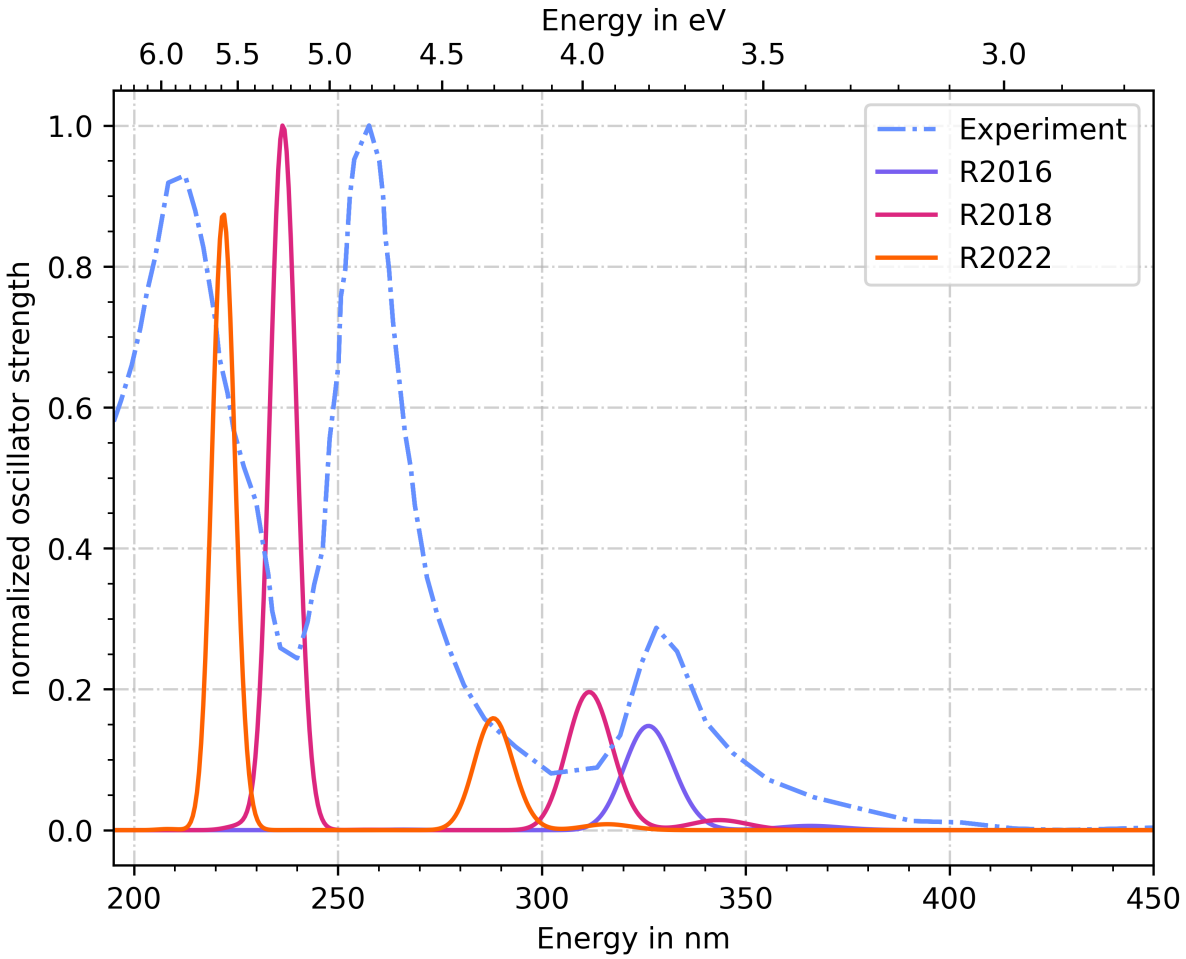

Figure S10: Transition energies computed at the ground state geometry of C_{60} using different DFT/MRCI Hamiltonians. The one-particle basis was generated using the def2-TZVP[81] basis set. Energies were broadened with gaussian functions with full-width at half maximum of 0.25 eV The intensities were normalized to the maximum value of the R2018 calculations.

S4 Further technical details of the calculations

For all molecules added to the newly designed double excitation training set the geometries from Ref. 90 were taken. The geometries of the singlet and triplet states of the assessment set containing small organic molecules were taken from Ref. 91. For molecules with a doublet ground state, the geometries were taken from Ref. 92. The geometries for the transition metal complexes are taken from Ref. 93. The geometries of the critical cases were taken from Ref. 94. The geometries for polyacenes and mini-carotenes were taken from Ref. 95 and 96.

Table S22: Basis, auxiliary basis and starting reference space used in the parameterization set.

Molecule	Atom	**Basis**	**AuxBasis**	**ECP**	$(\mathbf{n_{el.}};\mathbf{n_{orb.}};\mathbf{n_{exc.}})$
Acetaldehyde	H	TZVP	TZVP		(10;10;2)
	o	TZVP+aug	TZVP		
	c	TZVP+aug	TZVP		
Aceton	h	TZVP	TZVP		(10;10;2)
	o	TZVP+aug	TZVP		
	c	TZVP+aug	TZVP		
Acrolein	h	TZVP	TZVP		(10;10;2)
	o	TZVP+aug	TZVP		
	c	TZVP+aug	TZVP		
Benzene	h	TZVP	TZVP		(10;10;2)
	c	TZVP+aug	TZVP		
Beryllium	be	aug-cc-pVTZ	aug-cc-pVTZ		(2;13;2)
Butadiene	h	TZVP	TZVP		(10;10;2)
	c	TZVP+aug	TZVP		
Carbon dimer	c	aug-cc-pVTZ	TZVP		(8;10;2)
Carbon monoxide	o	TZVP+aug	TZVP		(10;11;2)
	c	TZVP+aug	TZVP		
Carbon trimer	c	aug-cc-pVTZ	aug-cc-pVTZ		(8;10;2)
Cu^+	cu	cc-pVDZ-PP	TZVP	defpp-ecp	(0;0;0)
Cyclopentadiene	h	TZVP	TZVP		(10;11;2)
	c	TZVP+aug	TZVP		

Continued on next page

Molecule	Atom	**Basis**	**AuxBasis**	**ECP**	$(\mathbf{n_{el.}};\mathbf{n_{orb.}};\mathbf{n_{exc.}})$
Ethylene	h	TZVP	TZVP		(10;10;2)
	c	TZVP+aug	TZVP		
Ethylene dimer	h	TZVP	TZVP		(12;12;2)
	c	TZVP+aug	TZVP		
Formaldehyde	h	TZVP	TZVP		(10;10;2)
	o	TZVP+aug	TZVP		
	c	TZVP+aug	TZVP		
Formaldehyde dimer	h	TZVP	TZVP		(12;14;2)
	o	TZVP+aug	TZVP		
	c	TZVP+aug	TZVP		
Formamide	h	TZVP	TZVP		(10;10;2)
	n	TZVP+aug	TZVP		
	o	TZVP+aug	TZVP		
	c	TZVP+aug	TZVP		
Furan	h	TZVP	TZVP		(10;10;2)
	o	TZVP+aug	TZVP		
	c	TZVP+aug	TZVP		
Glyoxal	h	TZVP	TZVP		(10;10;2)
	o	TZVP+aug	TZVP		
	c	TZVP+aug	TZVP		
Hexatriene	h	TZVP	TZVP		(10;10;2)
	c	TZVP+aug	TZVP		
Magnesium	mg	def2-TZVPD	def2-TZVPD		(2;13;2)

Continued on next page

Molecule	Atom	**Basis**	**AuxBasis**	**ECP**	$(\mathbf{n_{el.}};\mathbf{n_{orb.}};\mathbf{n_{exc.}})$
Naphtaline	h	TZVP	TZVP		(10;10;2)
	c	TZVP+aug	TZVP		
Nitrobenzene	h	TZVP	TZVP		(10;11;2)
	n	TZVP+aug	TZVP		
	o	TZVP+aug	TZVP		
	c	TZVP+aug	TZVP		
Nitromethane	h	TZVP	TZVP		(10;10;2)
	n	TZVP+aug	TZVP		
	o	TZVP+aug	TZVP		
	c	TZVP+aug	TZVP		
Nitrosomethane	h	aug-cc-pVTZ	aug-cc-pVTZ		(12;11;2)
	n	aug-cc-pVTZ	aug-cc-pVTZ		
	o	aug-cc-pVTZ	aug-cc-pVTZ		
	c	aug-cc-pVTZ	aug-cc-pVTZ		
Nitroxyl	h	aug-cc-pVTZ	aug-cc-pVTZ		(10;10;2)
	n	aug-cc-pVTZ	aug-cc-pVTZ		
	o	aug-cc-pVTZ	aug-cc-pVTZ		
Pyrazine	h	TZVP	TZVP		(10;10;2)
	n	TZVP+aug	TZVP		
	c	TZVP+aug	TZVP		
Pyridine	h	TZVP	TZVP		(10;10;2)
	n	TZVP+aug	TZVP		
	c	TZVP+aug	TZVP		

Continued on next page

Molecule	Atom	**Basis**	**AuxBasis**	**ECP**	$(\mathbf{n_{el.}};\mathbf{n_{orb.}};\mathbf{n_{exc.}})$
Pyrrole	h	TZVP	TZVP		(10;10;2)
	n	TZVP+aug	TZVP		
	c	TZVP+aug	TZVP		
Styrene	h	TZVP	TZVP		(10;10;2)
	c	TZVP+aug	TZVP		
Tetrazine	h	TZVP	TZVP		(10;11;2)
	n	TZVP+aug	TZVP		
	c	TZVP+aug	TZVP		
Thioformaldehyde	h	TZVP	TZVP		(10;10;2)
	c	TZVP+aug	TZVP		
	s	TZVP+aug	TZVP		
Thiophene	h	TZVP	TZVP		(10;10;2)
	c	TZVP+aug	TZVP		
	s	TZVP+aug	TZVP		
Water	h	aug-cc-pVTZ	aug-cc-pVTZ		(8;8;2)
	o	aug-cc-pVTZ	aug-cc-pVTZ		

Table S23: Basis, auxiliary basis (AuxBasis) and starting reference space used in the benchmarking of singlet and triplet states.

Molecule	Atom	**Basis**	**AuxBasis**	**ECP**	$(\mathbf{n_{el.}};\mathbf{n_{orb.}};\mathbf{n_{exc.}})$
1,1-Difluoroethylene	h	TZVP+aug	TZVP		(10;10;2)
	c	TZVP+aug	TZVP		
	f	TZVP+aug	TZVP		
1,2,3,4-Tetrafluorobenzene	h	TZVP+aug	TZVP		(10;10;2)
	c	TZVP+aug	TZVP		
	f	TZVP+aug	TZVP		
1,2,4,5-Tetrafluorobenzene	h	TZVP+aug	TZVP		(10;10;2)
	c	TZVP+aug	TZVP		
	f	TZVP+aug	TZVP		
1,3,5-Trifluorobenzene	h	TZVP+aug	TZVP		(10;10;2)
	c	TZVP+aug	TZVP		
	f	TZVP+aug	TZVP		
1,3-Butadiene	h	TZVP+aug	TZVP		(10;10;2)
	c	TZVP+aug	TZVP		
1,3-Cyclohexadiene	h	TZVP+aug	TZVP		(10;10;2)
	c	TZVP+aug	TZVP		
1,3-Cyclopentadiene	h	TZVP+aug	TZVP		(10;10;2)
	c	TZVP+aug	TZVP		
1,3-Pentadiene	h	TZVP+aug	TZVP		(10;10;2)
	c	TZVP+aug	TZVP		
1,4-Cyclohexadiene	h	TZVP+aug	TZVP		(10;10;2)
	c	TZVP+aug	TZVP		

Continued on next page

Molecule	Atom	**Basis**	**AuxBasis**	**ECP**	$(\mathbf{n_{el.}}; \mathbf{n_{orb.}}; \mathbf{n_{exc.}})$
1,5-Hexadiene	h	TZVP+aug	TZVP		(10;10;2)
	c	TZVP+aug	TZVP		
1-Butyne	h	TZVP+aug	TZVP		(10;10;2)
	c	TZVP+aug	TZVP		
3,3,3-Trifluoropropyne	h	TZVP+aug	TZVP		(10;10;2)
	c	TZVP+aug	TZVP		
	f	TZVP+aug	TZVP		
Acetamide	h	TZVP+aug	TZVP		(10;10;2)
	n	TZVP+aug	TZVP		
	o	TZVP+aug	TZVP		
	c	TZVP+aug	TZVP		
Acetone	h	TZVP+aug	TZVP		(10;10;2)
	o	TZVP+aug	TZVP		
	c	TZVP+aug	TZVP		
Acetylene	h	TZVP+aug	TZVP		(10;10;2)
	c	TZVP+aug	TZVP		
Azo-tert-butane	h	TZVP+aug	TZVP		(10;10;2)
	n	TZVP+aug	TZVP		
	c	TZVP+aug	TZVP		
Azomethane	h	TZVP+aug	TZVP		(10;10;2)
	n	TZVP+aug	TZVP		
	c	TZVP+aug	TZVP		
Benzene	h	TZVP+aug	TZVP		(10;10;2)
	c	TZVP+aug	TZVP		

Continued on next page

Molecule	Atom	**Basis**	**AuxBasis**	**ECP**	($\mathbf{n_{el.}}$;$\mathbf{n_{orb.}}$;$\mathbf{n_{exc.}}$)
Chloroethylene	h	TZVP+aug	TZVP		(10;10;2)
	c	TZVP+aug	TZVP		
	cl	TZVP+aug	TZVPP		
Chlorotrifluoroethylene	c	TZVP+aug	TZVP		(10;10;2)
	f	TZVP+aug	TZVP		
	cl	TZVP+aug	TZVPP		
cis-1-2-difluoroethylene	h	TZVP+aug	TZVP		(10;10;2)
	c	TZVP+aug	TZVP		
	f	TZVP+aug	TZVP		
cis-2-butene	h	TZVP+aug	TZVP		(10;10;2)
	c	TZVP+aug	TZVP		
cis-2-*trans*-4-hexadiene	h	TZVP+aug	TZVP		(10;10;2)
	c	TZVP+aug	TZVP		
Carbon dioxide	o	TZVP+aug	TZVP		(10;10;2)
	c	TZVP+aug	TZVP		
Carbonyl sulfide	o	TZVP+aug	TZVP		(10;10;2)
	c	TZVP+aug	TZVP		
	s	TZVP+aug	TZVPP		
Carbon disulfide	c	TZVP+aug	TZVP		(10;10;2)
	s	TZVP+aug	TZVPP		
Dithiosuccinimide	h	TZVP+aug	TZVP		(10;10;2)
	n	TZVP+aug	TZVP		
	c	TZVP+aug	TZVP		
	s	TZVP+aug	TZVP		

Continued on next page

Molecule	Atom	**Basis**	**AuxBasis**	**ECP**	$(\mathbf{n_{el.}};\mathbf{n_{orb.}};\mathbf{n_{exc.}})$
Ethylene	h	TZVP+aug	TZVP		(10;10;2)
	c	TZVP+aug	TZVP		
Fluorobenzene	h	TZVP+aug	TZVP		(10;10;2)
	c	TZVP+aug	TZVP		
	f	TZVP+aug	TZVP		
Fluoroethylene	h	TZVP+aug	TZVP		(10;10;2)
	c	TZVP+aug	TZVP		
	f	TZVP+aug	TZVP		
Furan	h	TZVP+aug	TZVP		(10;10;2)
	o	TZVP+aug	TZVP		
	c	TZVP+aug	TZVP		
Hexafluorobenzene	c	TZVP+aug	TZVP		(10;10;2)
	f	TZVP+aug	TZVP		
iso-butene	h	TZVP+aug	TZVP		(10;10;2)
	c	TZVP+aug	TZVP		
Nitrobenzene	h	TZVP+aug	TZVP		(10;10;2)
	n	TZVP+aug	TZVP		
	o	TZVP+aug	TZVP		
	c	TZVP+aug	TZVP		
Nitromethane	h	TZVP+aug	TZVP		(10;10;2)
	n	TZVP+aug	TZVP		
	o	TZVP+aug	TZVP		
	c	TZVP+aug	TZVP		

Continued on next page

Molecule	Atom	**Basis**	**AuxBasis**	**ECP**	($\mathbf{n_{el.}}$; $\mathbf{n_{orb.}}$; $\mathbf{n_{exc.}}$)
o-Difluorobenzene	h	TZVP+aug	TZVP		(10;10;2)
	c	TZVP+aug	TZVP		
	f	TZVP+aug	TZVP		
Pentafluorobenzene	h	TZVP+aug	TZVP		(10;10;2)
	n	TZVP+aug	TZVP		
	c	TZVP+aug	TZVP		
	f	TZVP+aug	TZVP		
Propadiene	h	TZVP+aug	TZVP		(10;10;2)
	c	TZVP+aug	TZVP		
Propene	h	TZVP+aug	TZVP		(10;10;2)
	c	TZVP+aug	TZVP		
Propyne	h	TZVP+aug	TZVP		(10;10;2)
	c	TZVP+aug	TZVP		
Pyrazine	h	TZVP+aug	TZVP		(10;10;2)
	n	TZVP+aug	TZVP		
	c	TZVP+aug	TZVP		
Pyridine	h	TZVP+aug	TZVP		(10;10;2)
	n	TZVP+aug	TZVP		
	c	TZVP+aug	TZVP		
Pyrimidine	h	TZVP+aug	TZVP		(10;10;2)
	n	TZVP+aug	TZVP		
	c	TZVP+aug	TZVP		
Pyrrole	h	TZVP+aug	TZVP		(10;10;2)
	n	TZVP+aug	TZVP		

Continued on next page

Molecule	Atom	**Basis**	**AuxBasis**	**ECP**	$(\mathbf{n_{el.}};\mathbf{n_{orb.}};\mathbf{n_{exc.}})$
	c	TZVP+aug	TZVP		
s-Triazine	h	TZVP+aug	TZVP		(10;10;2)
	n	TZVP+aug	TZVP		
	c	TZVP+aug	TZVP		
Sulfur dioxide	o	TZVP+aug	TZVP		(10;10;2)
	s	TZVP+aug	TZVPP		
Tetrafluoroethylene	c	TZVP+aug	TZVP		(10;10;2)
	f	TZVP+aug	TZVP		
Tetramethylethylene	h	TZVP+aug	TZVP		(10;10;2)
	c	TZVP+aug	TZVP		
Thiophene	h	TZVP+aug	TZVP		(10;10;2)
	c	TZVP+aug	TZVP		
	s	TZVP+aug	TZVPP		
Thiophosgene	c	TZVP+aug	TZVP		(10;10;2)
	s	TZVP+aug	TZVPP		
	cl	TZVP+aug	TZVPP		
trans-1-2-difluoroethylene	h	TZVP+aug	TZVP		(10;10;2)
	c	TZVP+aug	TZVP		
	f	TZVP+aug	TZVP		
trans-2-butene	h	TZVP+aug	TZVP		(10;10;2)
	c	TZVP+aug	TZVP		
Trifluoroethylene	h	TZVP+aug	TZVP		(10;10;2)
	c	TZVP+aug	TZVP		
	f	TZVP+aug	TZVP		

Continued on next page

Molecule	Atom	**Basis**	**AuxBasis**	**ECP**	$(\mathbf{n_{el.}};\mathbf{n_{orb.}};\mathbf{n_{exc.}})$
Trimethylethylene	h	TZVP+aug	TZVP		(10;10;2)
	c	TZVP+aug	TZVP		

Table S24: Basis, auxiliary basis (AuxBasis) and starting reference space used in the benchmarking of doublet states.

Molecule	Atom	**Basis**	**AuxBasis**	**ECP**	$(\mathbf{n_{el.}};\mathbf{n_{orb.}};\mathbf{n_{exc.}})$
1,2,3,4-Tetrafluorobenzene	h	TZVP+aug	TZVP		(11;12;2)
	c	TZVP+aug	TZVP		
	f	TZVP+aug	TZVP		
1,2,4,5,Tetrafluorobenzene	h	TZVP+aug	TZVP		(9;10;2)
	c	TZVP+aug	TZVP		
	f	TZVP+aug	TZVP		
1,3,5,7,Octatetraene	h	TZVP+aug	TZVP		(9;10;2)
	c	TZVP+aug	TZVP		
1,5-Hexadiene-3-yne	h	TZVP+aug	TZVP		(11;12;2)
	c	TZVP+aug	TZVP		
2,3-Benzofluorene cation	h	def2-TZVPD	def2-TZVPD		(13;14;2)
	c	def2-TZVPD	def2-TZVPD		
Acenaphthene cation	h	TZVP+aug	TZVP		(9;10;2)
	c	TZVP+aug	TZVP		
Acenaphthylene cation	h	TZVP+aug	TZVP		(9;10;2)
	c	TZVP+aug	TZVP		
Adenine	h	TZVP+aug	TZVP		(9;10;2)
	n	TZVP+aug	TZVP		
	c	TZVP+aug	TZVP		
Azulene	h	TZVP+aug	TZVP		(11;12;2)
	c	TZVP+aug	TZVP		
Azulene cation	h	TZVP+aug	TZVP		(11;14;2)

Continued on next page

Molecule	Atom	**Basis**	**AuxBasis**	**ECP**	($\mathbf{n_{el.}}$;$\mathbf{n_{orb.}}$;$\mathbf{n_{exc.}}$)
	c	TZVP+aug	TZVP		
Beryllium monohydride	h	QZVPP	QZVPP		(3;16;2)
	be	QZVPP	QZVPP		
Bithiophene cation	h	def2-TZVPD	def2-TZVPD		(9;10;2)
	c	def2-TZVPD	def2-TZVPD		
	s	def2-TZVPD	TZVP		(9;10;2)
Ethylenyl	h	TZVP+aug	TZVP		(11;12;2)
	c	TZVP+aug	TZVP		
all-*trans* 1-3-5-7-octatetraene cation	h	TZVP+aug	TZVP		(9;10;2)
	c	TZVP+aug	TZVP		
Dichlorodifluoromethane	c	TZVP+aug	TZVP		(9;10;2)
	f	TZVP+aug	TZVP		
	cl	TZVP+aug	TZVP		
Carbazole	h	TZVP+aug	TZVP		(13;14;2)
	n	TZVP+aug	TZVP		
	c	TZVP+aug	TZVP		
Dibenzofuran	h	TZVP+aug	TZVP		(11;12;2)
	o	TZVP+aug	TZVP		
	c	TZVP+aug	TZVP		
Ethylfluoride	h	TZVP+aug	TZVP		(9;10;2)
	c	TZVP+aug	TZVP		
	f	TZVP+aug	TZVP		
Fluorene cation	h	TZVP+aug	TZVP		(9;10;2)
	c	TZVP+aug	TZVP		

Continued on next page

Molecule	Atom	**Basis**	**AuxBasis**	**ECP**	($\mathbf{n_{el.}}$;$\mathbf{n_{orb.}}$;$\mathbf{n_{exc.}}$)
Fluorobenzene	h	TZVP+aug	TZVP		(9;10;2)
	c	TZVP+aug	TZVP		
	f	TZVP+aug	TZVP		
Hexacene	h	def2-TZVP	def2-TZVP		(11;12;2)
	c	def2-TZVP	def2-TZVP		
NO	n	TZVP+aug	TZVP		(11;12;2)
	o	TZVP+aug	TZVP		
NO2	n	TZVP+aug	TZVP		(11;11;2)
	o	TZVP+aug	TZVP		
Naphthalene cation	h	TZVP+aug	TZVP		(11;11;2)
	c	TZVP+aug	TZVP		
Hydroxyl radical	h	TZVP+aug	TZVP		(7;12;2)
	o	TZVP+aug	TZVP		
Ovalene cation	h	def-SV(P)	def-SV(P)		(11;12;2)
	c	def-SV(P)	def-SV(P)		
Pentacene cation	h	def2-TZVP	def2-TZVP		(11;12;2)
	c	def2-TZVP	def2-TZVP		
Perylene cation	h	def2-TZVPD	def2-TZVPD		(11;12;2)
	c	def2-TZVPD	def2-TZVPD		
Phenanthrene	h	TZVP+aug	TZVP		(9;10;2)
	c	TZVP+aug	TZVP		
Phenoxyl	h	TZVP+aug	TZVP		(11;11;2)
	o	TZVP+aug	TZVP		
	c	TZVP+aug	TZVP		

Continued on next page

Molecule	Atom	**Basis**	**AuxBasis**	**ECP**	($\mathbf{n_{el.}}$;$\mathbf{n_{orb.}}$;$\mathbf{n_{exc.}}$)
Phenyl	h	TZVP+aug	TZVP		(9;10;2)
	c	TZVP+aug	TZVP		
Styrene	h	TZVP+aug	TZVP		(11;12;2)
	c	TZVP+aug	TZVP		
Styrene cation	h	TZVP+aug	TZVP		(9;10;2)
	c	TZVP+aug	TZVP		
Terthiophene cation	h	def2-TZVPD	TZVP		(9;10;2)
	c	def2-TZVPD	TZVP		
	s	def2-TZVPD	TZVP		
Tetracene cation	h	def2-TZVPD	def2-TZVPD		(9;10;2)
	c	def2-TZVPD	def2-TZVPD		
Tetrathiafulvalene cation	h	def2-TZVPD	def2-TZVPD		(9;10;2)
	c	def2-TZVPD	def2-TZVPD		
	s	def2-TZVPD	def2-TZVPD		
o-Benzoquinone	h	def-SV(P)	def-SV(P)		(9;10;2)
	o	def-SV(P)	def-SV(P)		
	c	def-SV(P)	def-SV(P)		
o-Xylylene	h	TZVP+aug	TZVP		(9;10;2)
	c	TZVP+aug	TZVP		
p-Benzosemiquinone	h	TZVP+aug	TZVP		(11;11;2)
	o	TZVP+aug	TZVP		
	c	TZVP+aug	TZVP		
p-Xylylene	h	TZVP+aug	TZVP		(11;11;2)
	c	TZVP+aug	TZVP		

Table S25: Basis, auxiliary basis and starting reference space used in the benchmarking of states in organic transition metal complexes.

Molecule	Atom	**Basis**	**AuxBasis**	**ECP**	$(\mathbf{n_{el.}};\mathbf{n_{orb.}};\mathbf{n_{exc.}})$
Cobaltocene	h	SV(P)	SV(P)		(16;18;1)
	co	ecp-10-mdf	def-SVP	ecp-10-mdf	
	c	SV(P)	SV(P)		
Ferrocene	h	SV(P)	SV(P)		(14;16;1)
	fe	ecp-10-mdf	def-SVP	ecp-10-mdf	
	c	SV(P)	SV(P)		
ZnP	h	def-SV(P)	def-SV(P)		(14;18;1)
	n	def-SV(P)	def-SV(P)		
	c	def-SV(P)	def-SV(P)		
	zn	10-mdf 6s5p3d	def-TZVP	defpp-ecp	
ZnPC	h	def-SV(P)	def-SV(P)		(18;17;1)
	n	def-SV(P)	def-SV(P)		
	c	def-SV(P)	def-SV(P)		
	zn	10-mdf 6s5p3d	def-TZVP	defpp-ecp	
ZnTBP	h	def-SV(P)	def-SV(P)		(18;17;1)
	n	def-SV(P)	def-SV(P)		
	c	def-SV(P)	def-SV(P)		
	zn	10-mdf 6s5p3d	def-TZVP	defpp-ecp	

Table S26: Basis, auxiliary basis and starting reference space used in the benchmarking of states in inorganic transition metal complexes.

Molecule	Atom	**Basis**	**AuxBasis**	**ECP**	$(\mathbf{n_{el.}};\mathbf{n_{orb.}};\mathbf{n_{exc.}})$
$Co(H_2O)_6^{2+}$	h	def2-SVP	def2-SVP		(10;10;2)
	co	ecp-10-mdf	TZVP	ecp-10-mdf	
	o	def2-TZVPD	def2-TZVPD		
$Co(NH_3)_6^{3+}$)	h	def2-SVP	def2-SVP		(16;14;2)
	co	ecp-10-mdf	TZVP	ecp-10-mdf	
	n	def2-TZVPD	def2-TZVPD		
$Cr(CO)_6$	cr	ecp-10-mdf	TZVP	ecp-10-mdf	(10;10;2)
	o	def2-TZVPD	def2-TZVPD		
	c	def2-TZVPD	def2-TZVPD		
MnO_4^-	o	def2-TZVPD	def2-TZVPD		(12;12;2)
	mn	ecp-10-mdf	TZVP	ecp-10-mdf	
$Mo(CO)_6$	o	def2-TZVPD	def2-TZVPD		(10;10;2)
	c	def2-TZVPD	def2-TZVPD		
	mo	ecp-28-mwb-TZVP	ecp-28-mwb-TZVP	ecp-28-mwb	
MoF_6	f	def2-TZVPD	def2-TZVPD		(12;10;2)
	mo	ecp-28-mwb-TZVP	ecp-28-mwb-TZVP	def-ecp	
$NiCO_4$	o	def2-TZVPD	def2-TZVPD		(10;10;2)
	tc	ecp-28-mwb-TZVP	ecp-28-mwb-TZVP	def-ecp	
$Rh(NH_3)_6^{3+}$)	h	def2-SVP	def2-SVP		(12;12;2)
	n	def2-TZVPD	def2-TZVPD		
	rh	ecp-28-mwb-TZVP	ecp-28-mwb-TZVP	def-ecp	

Continued on next page

Molecule	Atom	**Basis**	**AuxBasis**	**ECP**	($\mathbf{n_{el.}}$;$\mathbf{n_{orb.}}$;$\mathbf{n_{exc.}}$)
TcO_4^-	o	def2-TZVPD	def2-TZVPD		(10;10;2)
	tc	ecp-28-mwb-TZVP	ecp-28-mwb-TZVP	def-ecp	

Table S27: Number of configurations and CSFs used in calculation with the standard selection threshold.

Molecule	Multiplicity	Configurations	CSFs
Training set			
Acetaldehyde	1	5200	8456
	3	2001	4585
Acetone	1	11459	19637
	3	2816	6974
Acrolein	1	14628	25873
	3	4813	11727
Benzene	1	93288	231605
	3	22808	74022
Beryllium	1	360	360
Butadiene	1	12684	23339
	3		
Carbon dimer	1	2317	3708
Carbon monoxide	1	516	714
Carbon trimer	1	7262	13294
Cu cation	1	1641	3091
	3		
Cyclopentadiene	1	15476	28069
	3	6132	16788
Ethylene	1	742	1128
	3		
Ethylene dimer	1	60848	125175

Continued on next page

Molecule	Multiplicity	Configurations	CSFs
	3		
Formaldehyde	1	2723	4344
	3		
Formaldehyde dimer	1	18730	34071
	3		
Furan	1	12417	22252
	3		
Glyoxal	1	12199	21558
	3		
Hexatriene	1	139395	309373
Magnesium	1	201	201
	3		
Naphtaline	1	121734	278775
Nitrobenzene	1	33757	70393
Nitromethane	1	2972	4794
Nitrosomethane	1	7737	12846
Nitroxyl	1	1335	1966
Pyridine	1	36490	71110
Pyrrole	1	5388	9504
	3		
Ruthenocene	1	55203	145549
Styrene	1	60177	122473
	3		
Tetrazine	1	17289	33690

Continued on next page

Molecule	Multiplicity	Configurations	CSFs
	3		
Thioformaldehyde	1	1463	2334
	3		
Thiophene	1	11061	21567
	3		
Water	1	254	337
Assessment Singlets and Triplets			
Carbon dioxide	1	1916	2985
Carbon disulfide	1	11759	21784
	3	7252	18176
Carbonyl sulfide	1	4167	6658
	3	2755	5897
Sulfur dioxide	1	4918	8228
	3	2510	5442
Ethylene	1	5178	8659
Propene	1	11699	20173
	3	6964	15896
iso-butene	1	39826	76493
	3	27262	71412
cis-2-Butene	1	34671	65260
	3	21579	54337
trans-2-Butene	1	41483	80614
	3	27793	73169

Continued on next page

Molecule	Multiplicity	Configurations	CSFs
Trimethylethylene	1	67993	132204
	3	35490	91480
Tetramethylethylene	1	122363	245686
	3	60213	161349
Fluoroethylene	1	5218	8477
	3	2691	5771
1,1-Difluoroethylene	1	7387	12251
	3	6129	14129
cis-1,2-Difluoroethylene	1	10789	18379
	3	5330	12160
trans-1,2-Difluoroethylene	1	10544	17917
	3	6440	14918
Trifluoroethylene	1	10485	17729
	3	4056	9002
Tetrafluoroethylene	1	17647	30550
	3	12819	31161
Chlorotrifluoroethylene	1	17701	30683
	3	10824	25822
Chloroethylene	1	9657	16765
	3	5848	13374
Acetylene	1	4398	7345
	3	2355	4903
Propyne	1	8474	14360
	3	4361	9491

Continued on next page

Molecule	Multiplicity	Configurations	CSFs
1-Butyne	1	23414	42914
	3	12169	29223
3,3,3-Trifluoropropyne	1	14274	24382
	3	5630	12582
trans-1,3-Pentadiene	1	60605	120421
	3	26853	68537
cis-2-*trans*-4-Hexadiene	1	76128	146696
	3	50837	135873
1,3-Cyclohexadiene	1	79974	161063
	3	46332	126168
1,5-Hexadiene	1	82415	163189
	3	63711	180689
1,4-Cyclohexadiene	1	114063	244979
	3	95122	301992
Propadiene	1	9309	16124
	3	5589	12521
Fluorobenzene	1	107980	225138
	3	47412	130022
o-Difluorobenzene	1	115824	236351
	3	49520	133722
1,3,5-Trifluorobenzene	1	62570	115930
	3	57299	154331
1,2,3,4-Tetrafluorobenzene	1	128582	253907
	3	52134	137724

Continued on next page

Molecule	Multiplicity	Configurations	CSFs
1,2,4,5-Tetrafluorobenzene	1	86997	164460
	3	82785	229819
Pentafluorobenzene	1	133573	260570
	3	55477	146077
Hexafluorobenzene	1	156689	307313
	3	100971	281753
Thiophene	1	74818	161422
Pyrrole	1	67367	142787
Azomethane	1	25223	47053
	3	13999	34609
Azo-tert-butane	1	494251	1056589
	3	443421	1416973
Nitromethane	1	7367	12365
Thiophosgene	1	35878	75099
	3	16540	44386
1,3-Cyclopentadiene	1	67302	140629
	3	29169	77443
Pyridine	1	71093	147880
Pyrazine	1	55232	112345
	3	46742	138936
Pyrimidine	1	42068	81580
s-Triazine	1	32896	61615
Acetamide	1	10416	17686
Nitrobenzene	1	124130	258614

Continued on next page

Molecule	Multiplicity	Configurations	CSFs
Dithiosuccinimide	1	177581	416644
	3	118588	412248
Assessment Doublets			
p-Benzosemiquionone anion	2	631553	2978532
Perylene cation	2	1813714	8950990
Fluoroene cation	2	903711	3634133
Tetrathiafulvalene	2	401037	1629215
1,5-Hexadiene-3-yne	2	48380	149131
all-*trans* 1,3,5,7-octatetraene cation	2	127603	422476
all-*trans* 1,3,5,7-octatetraene	2	142549	478344
o-Xylylene	2	78610	246605
Styrene	2	88119	281553
Carbazole	2	681438	2650764
Dibenzofuran	2	633785	2437434
Dichlorodifluoromethane	2	8832	23528
Adenine	2	103929	339971
Fluorobenzene	2	41907	123781
2,3-Benzofluoroene cation	2	403138	1617458
Tetracene cation	2	357873	1483898
1,2,4,5-Tetrafluorobenzene	2	55013	161950
1,2,3,4-Tetrafluorobenzene	2	52637	151338
Ethylfluoride	2	4524	11175
Hydroxyl radical	2	232	419

Continued on next page

Molecule	Multiplicity	Configurations	CSFs
Acenaphthylene cation	2	337837	1285924
Acenaphthene cation	2	305488	1118836
Bithiophene cation	2	251636	917084
Phenanthrene cation	2	256633	959202
Beryllium monohydride	2	366	621
Ethylenyl	2	4028	9873
Nitric Oxide	2	559	1093
Nitrogen dioxide	2	3492	8826
Azulene cation	2	282028	1022968
Azulene	2	272497	983082
Pentacene cation	2	782751	3678047
Terthiophene cation	2	1758604	7894448
Styrene cation	2	100304	325763
Ovalene cation	2	1572938	8453795
Hexacene	2	1460149	7322133
Phenoxyl	2	159364	575867
Phenyl	2	144006	528714
Inorganic transition metals			
MoF_6	1	102251	237302
$Mo(CO)_6$	1	1276470	3403966
$Cr(CO)_6$	1	1025574	2640556
$Ni(CO)_4$	1	422176	1078793
$Co(H_2O)_6$	1	8826	15528

Continued on next page

Molecule	Multiplicity	Configurations	CSFs
	3	4969	12605
$Co(NH_3)_6$	1	28857	51825
$Rh(NH_3)_6$	1	41249	75651
MnO_4^-	1	159536	444294
TcO_4^-	1	184730	516960
Metal organic compounds			
$Ru(bpy)_3$	1	7236748	25182505
$Ru(tpy)(bpy)(py)^{2+}$	1	9652907	34503231
$Rh(bpy)_3$ $^{3+}$	1	7023082	23890349
$Rh(phen)_3$ $^{3+}$	1	10617753	38410460
$Rh(tpy)(bpy)(py)^{2+}$	1	7259178	24864421
ZnP	1	810644	2358688
ZnTBP	1	14410603	55061944
ZnPC	1	9422196	34225740
Ferrocene	1	127472	295926
	3	122448	442020
Ruthenocene	1	277149	735864
Cobaltocene	1	63887	125217
	3	58269	168863
Doubly excited states			
o-Benzyne	1	15021	28294
	3	10102	26260

Continued on next page

Molecule	Multiplicity	Configurations	CSFs
Thioformaldehyde	1	11485	23372
	3	6227	17159
Dithiosuccinimide	1	43813	92811
	3	42840	138577
Nitromethane	1	8603	14688
	3	8296	20104
Dithiin	1	14481	29432
Polyacenes			
Naphthalene	1	44648	94710
Anthracene	1	99924	228338
Tetracene	1	242852	609860
Pentacene	1	565583	1555798
Hexacene	1	1025799	2999711
Octacene	1	4575413	16038673
Carotenoids			
mini-5-carotene			
S_0 Geometry	1	1468069	3295869
S_1 Geometry	1	1411524	3276190
T_1 Geometry	1	1493171	3545397
mini-7-carotene			
S_0 Geometry	1	2737987	6794866
S_2 Geometry	1	2550635	6434429

Continued on next page

Molecule	Multiplicity	Configurations	CSFs
T_1 Geometry	1	2701055	6898372
mini-9-carotene			
S_0 Geometry	1	5247047	14071912
S_2 Geometry	1	4836635	13112084
T_1 Geometry	1	5155513	14183629
β-carotene			
S_0 Geometry	1	7883166	22544828
S_2 Geometry	1	7454223	21615285
T_1 Geometry	1	7904280	23251985
M13	1	10829563	31829723
M15	1	16311941	51165333
β-apo-8′-carotenal	1	2263990	5947723
Fucoxanthin	1	9725345	26316875

Table S28: Number of configurations and CSFs used in calculation with the tight selection threshold.

Molecule	Multiplicity	Configurations	CSFs
Training set			
Acetaldehyde	1	1640	2461
	3	611	1225
Acetone	1	3096	4915
	3	820	1832
Acrolein	1	4073	6426
	3	1270	2682
Benzene	1	20999	40714
	3	5360	13084
Beryllium	1	252	252
Butadiene	1	3416	5397
	3	2046	4380
Carbon dimer	1	929	1355
Carbon monoxide	1	170	199
Carbon trimer	1	2507	3870
Cu cation	1	756	1226
	3	705	1625
Cyclopentadiene	1	3971	6354
	3	1715	3843
Ethylene	1	279	386
	3	135	229
Ethylene dimer	1	14552	24595

Continued on next page

Molecule	Multiplicity	Configurations	CSFs
	3	11106	26000
Formaldehyde	1	1138	1673
	3	90	164
Formaldehyde dimer	1	5153	8321
	3	5051	11353
Furan	1	3459	5511
	3	2533	5521
Glyoxal	1	3742	5922
	3	378	762
Hexatriene	1	28809	50818
Magnesium	1	150	150
	3	152	152
Naphtaline	1	23521	42970
Nitrobenzene	1	7107	12235
Nitromethane	1	852	1227
Nitrosomethane	1	2351	3544
Nitroxyl	1	552	757
Pyridine	1	8060	13309
Pyrrole	1	1410	2202
	3	1382	2990
Ruthenocene	1	10629	20718
Styrene	1	12341	21105
	3	6602	15346
Tetrazine	1	4515	7468

Continued on next page

Molecule	Multiplicity	Configurations	CSFs
	3	1973	4619
Thioformaldehyde	1	538	759
	3	209	411
Thiophene	1	2843	4664
	3	4494	10278
Water	1	119	144
Assessment Singlets and Triplets			
Carbon dioxide	1	607	812
Carbon disulfide	1	3394	5339
	3	2096	4330
Carbonyl sulfide	1	1421	2097
	3	875	1571
Sulfur dioxide	1	1789	2730
	3	775	1445
Ethylene	1	1901	2847
Propene	1	3495	5484
	3	1984	4012
iso-butene	1	10601	17705
	3	7040	16170
cis-2-Butene	1	9092	15059
	3	5443	12201
trans-2-Butene	1	10933	18272
	3	7079	16267

Continued on next page

Molecule	Multiplicity	Configurations	CSFs
Trimethylethylene	1	16040	27334
	3	7886	18164
Tetramethylethylene	1	26245	45637
	3	12309	29331
Fluoroethylene	1	1704	2544
	3	812	1402
1,1-Difluoroethylene	1	2196	3335
	3	1776	3542
cis-1,2-Difluoroethylene	1	3325	5237
	3	1517	2933
trans-1,2-Difluoroethylene	1	3239	5094
	3	1846	3698
Trifluoroethylene	1	2871	4439
	3	1085	1773
Tetrafluoroethylene	1	4625	7439
	3	3245	6897
Chlorotrifluoroethylene	1	4425	6937
	3	2557	5001
Chloroethylene	1	2961	4604
	3	1720	3432
Acetylene	1	1762	2611
	3	935	1655
Propyne	1	2651	4038
	3	1275	2365

Continued on next page

Molecule	Multiplicity	Configurations	CSFs
1-Butyne	1	6273	10127
	3	3056	6334
3,3,3-Trifluoropropyne	1	3519	5380
	3	1180	1850
trans-1,3-Pentadiene	1	13750	23085
	3	5668	12490
cis-2-*trans*-4-Hexadiene	1	14933	25182
	3	9576	22068
1,3-Cyclohexadiene	1	16350	27646
	3	9138	20856
1,5-Hexadiene	1	17171	29182
	3	13285	31485
1,4-Cyclohexadiene	1	23466	40888
	3	19578	47988
Propadiene	1	2833	4339
	3	1683	3301
Fluorobenzene	1	23072	39999
	3	9882	22524
o-Difluorobenzene	1	24480	42393
	3	9938	22402
1,3,5-Trifluorobenzene	1	12397	20369
	3	11349	25769
1,2,3,4-Tetrafluorobenzene	1	25930	44725
	3	9825	21561

Continued on next page

Molecule	Multiplicity	Configurations	CSFs
1,2,4,5-Tetrafluorobenzene	1	16877	28209
	3	16280	38188
Pentafluorobenzene	1	26158	44967
	3	10135	22019
Hexafluorobenzene	1	30403	52647
	3	19290	45432
Thiophene	1	16836	29004
Pyrrole	1	16347	28367
Azomethane	1	6932	11368
	3	3637	7833
Azo-tert-butane	1	89737	162768
	3	78606	206174
Nitromethane	1	2217	3349
Thiophosgene	1	9126	15484
	3	4119	9089
1,3-Cyclopentadiene	1	15871	26972
	3	6502	14484
Pyridine	1	15458	26415
Pyrazine	1	11273	18824
	3	10526	24612
Pyrimidine	1	9655	15933
s-Triazine	1	8256	13580
Acetamide	1	2850	4390
Nitrobenzene	1	23821	40987

Continued on next page

Molecule	Multiplicity	Configurations	CSFs
Dithiosuccinimide	1	31104	57135
	3	21213	53691
Assessment Doublets			
p-Benzosemiquionone anion	2	115191	414554
Perylene cation	2	229044	851120
Fluoroene cation	2	139093	443837
Tetrathiafulvalene	2	62879	199869
1,5-Hexadiene-3-yne	2	11331	28416
all-*trans* 1,3,5,7-octatetraene cation	2	24628	63373
all-*trans* 1,3,5,7-octatetraene	2	27895	73922
o-Xylylene	2	16252	39567
Styrene	2	17673	44469
Carbazole	2	106446	327654
Dibenzofuran	2	102144	313203
Dichlorodifluoromethane	2	2610	5231
Adenine	2	19555	51179
Fluorobenzene	2	9941	23417
2,3-Benzofluoroene cation	2	55166	171093
Tetracene cation	2	47277	148548
1,2,4,5-Tetrafluorobenzene	2	12748	29363
1,2,3,4-Tetrafluorobenzene	2	12082	27223
Ethylfluoride	2	1436	2730
Hydroxyl radical	2	134	235

Continued on next page

Molecule	Multiplicity	Configurations	CSFs
Acenaphthylene cation	2	57018	170600
Acenaphthene cation	2	50034	143344
Bithiophene cation	2	42531	122191
Phenanthrene cation	2	37353	108537
Beryllium monohydride	2	187	311
Ethylenyl	2	1499	3150
Nitric Oxide	2	259	449
Nitrogen dioxide	2	1440	3117
Azulene cation	2	50837	144666
Azulene	2	49514	140730
Pentacene cation	2	100436	352168
Terthiophene cation	2	222489	761194
Styrene cation	2	20074	51778
Ovalene cation	2	183216	733524
Hexacene	2	164095	603797
Phenoxyl	2	31319	90608
Phenyl	2	30576	88931
Inorganic transition metals			
MoF_6	1	23811	45532
$Mo(CO)_6$	1	190146	397441
$Cr(CO)_6$	1	145898	290028
$Ni(CO)_4$	1	73824	148383
$Co(H_2O)_6$	1	2341	3528

Continued on next page

Molecule	Multiplicity	Configurations	CSFs
	3	1328	2670
$Co(NH_3)_6$	1	5249	8026
$Rh(NH_3)_6$	1	9305	15325
MnO_4^-	1	34690	74647
TcO_4^-	1	35574	73538
Metal organic compounds			
$Ru(bpy)_3$	1	1027951	2699577
$Ru(tpy)(bpy)(py)^{2+}$	1	929388	2409101
$Rh(bpy)_3^{3+}$	1	707678	1751572
$Rh(phen)_3^{3+}$	1	1256090	3421817
$Rh(tpy)(bpy)(py)^{2+}$	1	743096	1872308
ZnP	1	100829	218682
ZnTBP	1	1396985	3905313
ZnPC	1	898105	2378862
Ferrocene	1	22286	39647
	3	22218	57102
Ruthenocene	1	46505	92529
Cobaltocene	1	12809	21989
	3	11447	27741
Buckminster fullerene			
C_{60}	1	9309939	37950226

References

(1) Walzl, K.; Koerting, C.; Kuppermann, A. Electron-impact spectroscopy of acetaldehyde. *J. Chem. Phys.* **1987**, *87*, 3796–3803.

(2) St. John III, W. M.; Estler, R. C.; Doering, J. P. Low-energy electron impact study of acetone. *J. Chem. Phys.* **1974**, *61*, 763–767.

(3) Loos, P.-F.; Boggio-Pasqua, M.; Scemama, A.; Caffarel, M.; Jacquemin, D. Reference energies for double excitations. *J. Theor. Comput. Chem.* **2019**, *15*, 1939–1956.

(4) Veril, M.; Scemama, A.; Caffarel, M.; Lipparini, F.; Boggio-Pasqua, M.; Jacquemin, D.; Loos, P.-F. QUESTDB: A database of highly accurate excitation energies for the electronic structure community. *Wiley Interdiscip. Rev. Comput. Mol. Sci.* **2021**, *11*, e1517.

(5) Becker, R. S.; Inuzuka, K.; King, J. Acrolein: Spectroscopy, Photoisomerization, and Theoretical Considerations. *J. Chem. Phys.* **1970**, *52*, 5164–5170.

(6) Hollas, J. The electronic absorption spectrum of acrolein vapour. *Spectrochim. Acta* **1963**, *19*, 1425–1441.

(7) Hiraya, A.; Shobatake, K. Direct absorption spectra of jet-cooled benzene in 130–260 nm. *J. Chem. Phys.* **1991**, *94*, 7700–7706.

(8) Frueholz, R. P.; Flicker, W. M.; Mosher, O. A.; Kuppermann, A. Electronic spectroscopy of benzene and the fluorobenzenes by variable angle electron impact. *J. Chem. Phys.* **1979**, *70*, 3057–3070.

(9) Doering, J. Electronic energy levels of benzene below 7 eV. *J. Chem. Phys.* **1977**, *67*, 4065–4070.

(10) Price, W. C.; Walsh, A. D. The absorption spectra of conjugated dienes in the vacuum ultra-violet (1). *Proc. R. Soc. London, A* **1940**, *174*, 220–234.

(11) Asmis, K. R. Electron-Molecule Collisions: A Novel Instrument for Measuring In- elastic Differential Cross Sections at 180° Angle and Applications. Ph.D. thesis, University of Freiburg, 1996.

(12) Lassettre, E. N.; Skerbele, A. Absolute generalized oscillator strengths for four electronic transitions in carbon monoxide. *J. Chem. Phys.* **1971**, *54*, 1597–1607.

(13) Moore, C. E. *Atomic Energy Levels as Derived from the Analyses of Optical Spectra: The spectra of chromium, manganese, iron, cobalt, nickel, copper, zinc, gallium, germanium, arsenic, selenium, bromine, krypton, rubidium, strontium, yttrium, zirconium, and niobium*; US Department of Commerce, National Bureau of Standards, 1952; Vol. 2.

(14) Wilden, D.; Comer, J. Rydberg states of C_2H_4 and C_2D_4: assignments using the technique of low-energy electron energy-loss spectroscopy. *J. Phys. B: Atom. Mol. Phys.* **1980**, *13*, 1009.

(15) Allan, M. Measurement of absolute differential cross section for the excitation of the lowest triplet state of ethene. *Chem. Phys. Lett.* **1994**, *225*, 156–160.

(16) Suto, M.; Wang, X.; Lee, L. Fluorescence from VUV excitation of formaldehyde. *J. Chem. Phys.* **1986**, *85*, 4228–4233.

(17) Palmer, M. H.; Walker, I. C.; Ballard, C. C.; Guest, M. F. The electronic states of furan studied by VUV absorption, near-threshold electron energy-loss spectroscopy and ab initio multi-reference configuration interaction calculations. *Chem. Phys.* **1995**, *192*, 111–125.

(18) Flicker, W. M.; Mosher, O. A.; Kuppermann, A. Electron impact investigation of electronic excitations in furan, thiophene, and pyrrole. *J. Chem. Phys.* **1976**, *64*, 1315–1321.

(19) Verhaart, G.; Brongersma, H. Triplet $\pi \rightarrow \pi^*$ and $\pi \rightarrow \pi^*$ transitions in glyoxal and

biacetyl by low-energy electron-impact spectroscopy. *Chem. Phys. Lett.* **1980**, *72*, 176–180.

(20) Manna, S.; Chaudhuri, R. K.; Chattopadhyay, S. Taming the excited states of butadiene, hexatriene, and octatetraene using state specific multireference perturbation theory with density functional theory orbitals. *J. Chem. Phys.* **2020**, *152*, 244105.

(21) Martin, W. C.; Zalubas, R. Energy levels of magnesium, Mg I through Mg XII. *J. Phys. Chem. Ref. Data* **1980**, *9*, 1–58.

(22) George, G.; Morris, G. The intensity of absorption of naphthalene from 30 000 cm^{-1} to 53 000 cm^{-1}. *J. Mol. Spectrosc.* **1968**, *26*, 67–71.

(23) Ari, T.; Güven, H.; Ecevit, N. Electron energy-loss spectroscopy in monosubstituted benzenes. *J. Electron Spectrosc. Relat. Phenom.* **1995**, *73*, 13–23.

(24) Walker, I. C.; Fluendy, M. A. Spectroscopy and dynamics of nitromethane (CH_3NO_2) and its anionic states. *Int. J. Mass Spectrom.* **2001**, *205*, 171–182.

(25) Walker, I. C.; Palmer, M. H.; Hopkirk, A. The electronic states of the azines. II. Pyridine, studied by VUV absorption, near-threshold electron energy loss spectroscopy and ab initio multi-reference configuration interaction calculations. *Chem. Phys.* **1990**, *141*, 365–378.

(26) Bolovinos, A.; Tsekeris, P.; Philis, J.; Pantos, E.; Andritsopoulos, G. Absolute vacuum ultraviolet absorption spectra of some gaseous azabenzenes. *J. Mol. Spectrosc.* **1984**, *103*, 240–256.

(27) Gray, H. B.; Sohn, Y.; Hendrickson, N. Electronic structure of metallocenes. *J. Am. Chem. Soc.* **1971**, *93*, 3603–3612.

(28) Swiderek, P.; Fraser, M.-J.; Michaud, M.; Sanche, L. Electron-energy-loss spectroscopy of the low-lying triplet states of styrene. *J. Chem. Phys.* **1994**, *100*, 70–77.

(29) Innes, K.; Ross, I.; Moomaw, W. R. Electronic states of azabenzenes and azanaphthalenes: A revised and extended critical review. *J. Mol. Spectrosc.* **1988**, *132*, 492–544.

(30) Innes, K. Approximate energy of the $^1A_u(\pi^\star n)$ electronic state of s-tetrazine. *J. Mol. Spectrosc.* **1988**, *129*, 140–144.

(31) Palmer, M. H.; McNab, H.; Reed, D.; Pollacchi, A.; Walker, I. C.; Guest, M. F.; Siggel, M. R. The molecular and electronic states of 1,2,4,5-tetrazine studied by VUV absorption, near-threshold electron energy-loss spectroscopy and ab initio multi-reference configuration interaction studies. *Chem. Phys.* **1997**, *214*, 191–211.

(32) Judge, R.; Drury-Lessard, C.; Moule, D. The far ultraviolet spectrum of thioformaldehyde. *Chem. Phys. Lett.* **1978**, *53*, 82–83.

(33) Chutjian, A.; Hall, R.; Trajmar, S. Electron-impact excitation of H_2O and D_2O at various scattering angles and impact energies in the energy-loss range 4.2–12 eV. *J. Chem. Phys.* **1975**, *63*, 892–898.

(34) Kuppermann, A.; Flicker, W. M.; Mosher, O. A. Electronic spectroscopy of polyatomic molecules by low-energy, variable-angle electron impact. *Chem. Rev.* **1979**, *79*, 77–90.

(35) Okuzawa, Y.; Fujii, M.; Ito, M. Direct observation of second excited ^{1,3}(n, π*) states of pyrazine by UV—IR double resonance dip spectroscopy. *Chem. Phys. Lett.* **1990**, *171*, 341–346.

(36) Nielsen, E. B.; Schellman, J. A. The absorption spectra of simple amides and peptides. *J. Phys. Chem.* **1967**, *71*, 2297–2304.

(37) Nagakura, S.; Kojima, M.; Maruyama, Y. Electronic spectra and electronic structures of nitrobenzene and nitromesitylene. *J. Mol. Spectrosc.* **1964**, *13*, 174–192.

(38) Meskers, S. C.; Polonski, T.; Dekkers, H. P. Polarized Absorption and Phosphorescence

Spectra and Magnetic Circular Dichroism of Dithioimides: Assignment of the Lower $^1n\pi^\star$ and $^3n\pi^\star$ States. *J. Phys. Chem.* **1995**, *99*, 1134–1142.

(39) Wheeler, R. A. Low-energy, doublet states of p-benzosemiquinone radical anion from SCF-CI and CASSCF calculations. *J. Phys. Chem.* **1993**, *97*, 1533–1537.

(40) Szczepanski, J.; Chapo, C.; Vala, M. Visible and infrared spectra of matrix-isolated perylene cations. *Chem. Phys. Lett.* **1993**, *205*, 434–439.

(41) Szczepanski, J.; Banisaukas, J.; Vala, M.; Hirata, S.; Bartlett, R. J.; Head-Gordon, M. Vibrational and electronic spectroscopy of the fluorene cation. *J. Phys. Chem. A* **2002**, *106*, 63–73.

(42) Pou-Amérigo, R.; Ortí, E.; Merchán, M.; Rubio, M.; Viruela, P. M. Electronic transitions in tetrathiafulvalene and its radical cation: a theoretical contribution. *J. Phys. Chem. A* **2002**, *106*, 631–640.

(43) Rosenstock, H.; Dannacher, J.; Liebman, J. The role of excited electronic states in ion fragmentation: C6H6+. *Radiat. Phys. Chem.* **1982**, *20*, 7–28.

(44) Starcke, J. H.; Wormit, M.; Dreuw, A. Nature of the lowest excited states of neutral polyenyl radicals and polyene radical cations. *J. Chem. Phys.* **2009**, *131*, 144311.

(45) Jones, T.; Maier, J. Study of the radical cation of all trans-1,3,5,7-octatetraene by its emission, $\tilde{A}^2Au \rightarrow \tilde{X}^2B_g$, and by photoelect. *J. Mass Spectrom. Ion Phys.* **1979**, *31*, 287–291.

(46) Kesper, K.; Münzel, N.; Pietzuch, W.; Specht, H.; Schweig, A. Matrix isolation radiation chemistry and photochemistry: electronic absorption spectra of o-xylylene and benzocyclobutene radical cations; localization of koopmans and non-koopmans bands in the photoelectron spectra of o-xylylene, styrene, toluene, o-xylene and benzocyclobutene. *J. Mol. Struct.* **1989**, *200*, 375–400.

(47) Ruščić, B.; Kovač, B.; Klasinc, L.; Güsten, H. Photoelectron Spectroscopy of Heterocycles. Fluorene Analogues. *Z. Naturforsch., A: Phys. Sci.* **1978**, *33*, 1006–1012.

(48) Lewerenz, M.; Nestmann, B.; Bruna, P. J.; Peyerimhoff, S. D. The electronic spectrum, photodecomposition and dissociative electron attachment of CF_2Cl_2: An ab initio configuration interaction study. *J. Mol. Struct.* **1985**, *123*, 329–342.

(49) Bravaya, K. B.; Kostko, O.; Dolgikh, S.; Landau, A.; Ahmed, M.; Krylov, A. I. Electronic structure and spectroscopy of nucleic acid bases: ionization energies, ionization-induced structural changes, and photoelectron spectra. *J. Phys. Chem. A* **2010**, *114*, 12305–12317.

(50) Bieri, G.; Åsbrink, L.; Von Niessen, W. 30.4-nm He (II) Photoelectron spectra of organic molecules: Part IV. Fluoro-compounds (C, H, F). *J. Electron Spectrosc. Relat. Phenom.* **1981**, *23*, 281–322.

(51) Hirata, S.; Head-Gordon, M.; Szczepanski, J.; Vala, M. Time-dependent density functional study of the electronic excited states of polycyclic aromatic hydrocarbon radical ions. *J. Phys. Chem. A* **2003**, *107*, 4940–4951.

(52) Maurice, D.; Head-Gordon, M. Configuration interaction with single substitutions for excited states of open-shell molecules. *Int. J. Quantum Chem.* **1995**, *56*, 361–370.

(53) Banisaukas, J.; Szczepanski, J.; Eyler, J.; Vala, M.; Hirata, S.; Head-Gordon, M.; Oomens, J.; Meijer, G.; Von Helden, G. Vibrational and electronic spectroscopy of acenaphthylene and its cation. *J. Phys. Chem. A* **2003**, *107*, 782–793.

(54) Rubio, M.; Ortí, E.; Pou-Amérigo, R.; Merchán, M. Electronic Spectra of $2,2'$-Bithiophene and $2,2' : 5',2''$-Terthiophene Radical Cations: A Theoretical Analysis. *J. Phys. Chem. A* **2001**, *105*, 9788–9794.

(55) Niederalt, C.; Grimme, S.; Peyerimhoff, S. Ab initio theoretical study of the electronic absorption spectra of polycyclic aromatic hydrocarbon radical cations of naphthalene, anthracene and phenanthrene. *Chem. Phys. Lett.* **1995**, *245*, 455–462.

(56) Mebel, A. M.; Chen, Y.-T.; Lin, S.-H. Ab initio molecular orbital study of excited electronic states of the vinyl radical. *Chem. Phys. Lett.* **1997**, *275*, 19–27.

(57) Shih, S.-K.; Peyerimhoff, S. D.; Buenker, R. J. Theoretical study of the vertical electronic spectrum of NO_2. *Chem. Phys. Lett.* **1977**, *46*, 201–207.

(58) Levchenko, S. V.; Krylov, A. I. Electronic structure of halogen-substituted methyl radicals: Excited states of CH_2Cl and CH_2F. *J. Chem. Phys.* **2001**, *115*, 7485–7494.

(59) Boschi, R.; Clar, E.; Schmidt, W. Photoelectron spectra of polynuclear aromatics. III. The effect of nonplanarity in sterically overcrowded aromatic hydrocarbons. *J. Chem. Phys.* **1974**, *60*, 4406–4418.

(60) Radziszewski, J. G.; Gil, M.; Gorski, A.; Spanget-Larsen, J.; Waluk, J.; Mróz, B. J. Electronic states of the phenoxyl radical. *J. Chem. Phys.* **2001**, *115*, 9733–9738.

(61) Radziszewski, J. G. Electronic absorption spectrum of phenyl radical. *Chem. Phys. Lett.* **1999**, *301*, 565–570.

(62) McDiarmid, R. Assignments in the ultraviolet spectra of MoF_6 and WF_6. *J. Chem. Phys.* **1974**, *61*, 3333–3339.

(63) Gray, H. B.; Beach, N. The electronic structures of octahedral metal complexes. I. Metal hexacarbonyls and hexacyanides. *J. Am. Chem. Soc.* **1963**, *85*, 2922–2927.

(64) Lever, A.; Ozin, G.; Hanlan, A.; Power, W.; Gray, H. B. Electronic absorption spectra of metal tetracarbonyls. *Inorg. Chem.* **1979**, *18*, 2088–2090.

(65) Johnson, D.; Sharpe, A. The preparation of cobalt (III) sulphate and its alums, and the magnetic, spectroscopic, and crystallographic properties of the $Co(H_2O)_6^{3+}$ ion. *J. Chem. Soc. A* **1966**, 798–801.

(66) Ford, P. C. The ligand field photosubstitution reactions of d6 hexacoordinate metal complexes. *Coord. Chem. Rev.* **1982**, *44*, 61–82.

(67) Holt, S. L.; Ballhausen, C. Low temperature absorption spectra of $KMnO_4$ in $KClO_4$. *Theor. Chim. Acta* **1967**, *7*, 313–320.

(68) Güdel, H.; Ballhausen, C. Low temperature absorption spectra of TcO_4^- and ReO_4^- in $KClO_4$. *Theor. Chim. Acta* **1972**, *25*, 331–337.

(69) Mullen, P.; Schwochau, K., et al. Vacuo ultraviolet spectra of permanganate, pertechnetate and perrhenate. *Chem. Phys. Lett.* **1969**, *3*, 49–51.

(70) Kirketerp, M.-B. S.; Nielsen, S. B. Absorption spectrum of isolated tris (2,2′-bipyridine) ruthenium (II) dications in vacuo. *Int. J. Mass Spectrom.* **2010**, *297*, 63–66.

(71) Rasmussen, S. C.; Ronco, S. E.; Mlsna, D. A.; Billadeau, M. A.; Pennington, W. T.; Kolis, J. W.; Petersen, J. D. Ground-and excited-state properties of ruthenium (II) complexes containing tridentate azine ligands, $Ru(tpy)(bpy)L^{2+}$, where L is a polymerizable acetylene. *Inorg. Chem.* **1995**, *34*, 821–829.

(72) Maestri, M.; Sandrini, D.; Balzani, V.; Maeder, U.; Von Zelewsky, A. Absorption spectra, electrochemical behavior, luminescence spectra, and excited-state lifetimes of mixed-ligand ortho-metalated rhodium (III) complexes. *Inorg. Chem.* **1987**, *26*, 1323–1327.

(73) Sandrini, D.; Maestri, M.; Balzani, V.; Maeder, U.; Von Zelewsky, A. Spectroscopic and electrochemical properties of new mixed-ligand orthometalated rhodium (III) complexes. *Inorg. Chem.* **1988**, *27*, 2640–2643.

(74) Frink, M. E.; Sprouse, S. D.; Goodwin, H. A.; Watts, R. J.; Ford, P. C. Synthesis and excited-state properties of rhodium (III) terpyridine complexes. *Inorg. Chem.* **1988**, *27*, 1283–1286.

(75) Sekino, H.; Kobayashi, H. A screened potential molecular-orbital calculation of the π-electron systems of metalloporphin, metallochlorin, and metallobacteriochlorin. *J. Chem. Phys.* **1987**, *86*, 5045–5052.

(76) Edwards, L.; Gouterman, M.; Rose, C. B. Synthesis and vapor spectrum of zinc tetrabenzporphine. *J. Am. Chem. Soc.* **1976**, *98*, 7638–7641.

(77) Van Cott, T. C.; Rose, J. L.; Misener, G. C.; Williamson, B. E.; Schrimpf, A. E.; Boyle, M. E.; Schatz, P. N. Magnetic circular dichroism and absorption spectrum of zinc phthalocyanine in an argon matrix between 14700 and 74000 cm^{-1}. *J. Phys. Chem.* **1989**, *93*, 2999–3011.

(78) Armstrong, A.; Smith, F.; Elder, E.; McGlynn, S. Electronic absorption spectrum of ferrocene. *J. Chem. Phys.* **1967**, *46*, 4321–4328.

(79) Sadlej, A. J. Medium-size polarized basis sets for high-level correlated calculations of molecular electric properties. *Collect. Czech. Chem. Commun.* **1988**, *53*, 1995–2016.

(80) Casida, M. E.; Jamorski, C.; Casida, K. C.; Salahub, D. R. Molecular excitation energies to high-lying bound states from time-dependent density-functional response theory: Characterization and correction of the time-dependent local density approximation ionization threshold. *J. Chem. Phys.* **1998**, *108*, 4439–4449.

(81) Weigend, F.; Ahlrichs, R. Balanced Basis Sets of Split Valence, Triple Zeta Valence and Quadruple Zeta Valence Quality for H to Rn: Design and Assessment of Accuracy. *Phys. Chem. Chem. Phys.* **2005**, *7*, 3297–3305.

(82) Leach, S.; Vervloet, M.; Després, A.; Bréheret, E.; Hare, J. P.; John Dennis, T.; Kroto, H. W.; Taylor, R.; Walton, D. R. Electronic spectra and transitions of the fullerene C60. *Chem. Phys.* **1992**, *160*, 451–466.

(83) Catalán, J. Towards the gas-phase UV-VIS absorption spectrum of C_{60}. *Chem. Phys. Lett.* **1994**, *223*, 159–161.

(84) Fukuda, R.; Nakatsuji, H. Formulation and implementation of direct algorithm for the symmetry-adapted cluster and symmetry-adapted cluster–configuration interaction method. *J. Chem. Phys.* **2008**, *128*, 094105.

(85) Fukuda, R.; Ehara, M. Electronic excitations of C_60 fullerene calculated using the ab initio cluster expansion method. *J. Chem. Phys.* **2012**, *137*, 134304.

(86) Bulliard, C.; Allan, M.; Leach, S. Electron energy-loss spectra of fullerene C_{60} in the gas phase. *Chem. Phys. Lett.* **1993**, *209*, 434–438.

(87) Abouaf, R.; Pommier, J.; Cvejanovic, S. Electron impact on free C_{60}. Excited states below 10 eV. *Chem. Phys. Lett.* **1993**, *213*, 503–508.

(88) Haufler, R. E.; Chai, Y.; Chibante, L. P. F.; Fraelich, M. R.; Weisman, R. B.; Curl, R. F.; Smalley, R. E. Cold molecular beam electronic spectrum of C_{60} and C_{70}. *J. Chem. Phys.* **1991**, *95*, 2197–2199.

(89) Menéndez-Proupin, E.; Delgado, A.; Montero-Alejo, A. L.; García de la Vega, J. The absorption spectrum of C_{60} in n-hexane solution revisited: Fitted experiment and TDDFT/PCM calculations. *Chem. Phys. Lett.* **2014**, *593*, 72–76.

(90) Loos, P.-F.; Boggio-Pasqua, M.; Scemama, A.; Caffarel, M.; Jacquemin, D. Reference Energies for Double Excitations. *J. Chem. Theory Comput.* **2019**, *15*, 1939–1956.

(91) Lyskov, I.; Kleinschmidt, M.; Marian, C. M. Redesign of the DFT/MRCI Hamiltonian. *J. Chem. Phys.* **2016**, *144*, 034104.

(92) Heil, A.; Marian, C. M. DFT/MRCI Hamiltonian for odd and even numbers of electrons. *J. Chem. Phys.* **2017**, *147*, 194104.

(93) Heil, A.; Kleinschmidt, M.; Marian, C. M. On the performance of DFT/MRCI Hamiltonians for electronic excitations in transition metal complexes: The role of the damping function. *J. Chem. Phys.* **2018**, *149*, 164106.

(94) Jovanović, V.; Lyskov, I.; Kleinschmidt, M.; Marian, C. M. On the performance of DFT/MRCI-R and MR-MP2 in spin-orbit coupling calculations on diatomics and polyatomic organic molecules. *Mol. Phys* **2016**, *115*, 109–137.

(95) Marian, C. M.; Gilka, N. Performance of the Density Functional Theory/Multireference Configuration Interaction Method on Electronic Excitation of Extended π-Systems. *J. Chem. Theory Comput.* **2008**, *4*, 1501–1515.

(96) Kleinschmidt, M.; Marian, C. M.; Waletzke, M.; Grimme, S. Parallel multireference configuration interaction calculations on mini-β-carotenes and β-carotene. *J. Chem. Phys.* **2009**, *130*, 044708.

Physical Chemistry Chemical Physics

PCCP

Electron affinities and lowest triplet and singlet state properties of para-oligophenylenes (n=3-5): Theory and experiment

Journal:	*Physical Chemistry Chemical Physics*
Manuscript ID	CP-ART-07-2023-003153
Article Type:	Paper
Date Submitted by the Author:	04-Jul-2023
Complete List of Authors:	Schulz, Timo; Heinrich-Heine-Universität Düsseldorf, Institute of Theoretical Chemistry Konieczny, Paul; Heinrich-Heine-Universität Düsseldorf, Institute of Physical Chemistry Dombrowski, Dennis; Heinrich-Heine-Universität Düsseldorf, Institute of Theoretical Chemistry Metz, Simon; Heinrich-Heine-Universität Düsseldorf, Institute of Theoretical Chemistry Marian, Christel; Heinrich-Heine-Universität Düsseldorf, Institute of Theoretical Chemsitry Weinkauf, Rainer; Heinrich-Heine-Universität Düsseldorf, Institute of Physical Chemistry

PCCP
Physical Chemistry Chemical Physics

Guidelines for Reviewers

Thank you very much for your agreeing to review this manuscript for *Physical Chemistry Chemical Physics (PCCP)*.

PCCP is an international journal for the publication of cutting-edge original work in physical chemistry, chemical physics and biophysical chemistry, spanning experiment, theory, computation and data science. To be suitable for publication in *PCCP,* articles must include significant innovation and/or insight into physical chemistry; this is the most important criterion that reviewers and the Editors will judge against when evaluating submissions. Further information on our scope can be found at rsc.li/pccp.

PCCP's Impact Factor is **3.945** (2021 Journal Citation Reports®)

The following manuscript has been submitted for consideration as a

PAPER

Full papers should contain original scientific work that has not been published previously. Full papers based on Communications are encouraged provided that they represent a substantial extension of the original material. There are no restrictions on the length of a paper. Authors should include a brief discussion in the Introduction that sets the context for the new work and gives their motivation for carrying out the study.

When preparing your report, please:

- Focus on the originality, importance, impact and reliability of the science. English language and grammatical errors do not need to be discussed in detail, except where it impedes scientific understanding.
- Use the journal scope and expectations to assess the manuscript's suitability for publication in *PCCP.*
- State clearly whether you think the article should be accepted or rejected and include details of how the science presented in the article corresponds to publication criteria.
- Inform the Editor if there is a conflict of interest, a significant part of the work you cannot review with confidence or if parts of the work have previously been published.

Best regards,

Professor Anouk Rijs
Editorial Board Chair
Vrije Universiteit Amsterdam, The Netherlands

Dr Michael A. Rowan
Executive Editor
Royal Society of Chemistry

Contact us

Please visit our reviewer hub for further details of our processes, policies and reviewer responsibilities as well as guidance on how to review, or click the links below.

What to do when you review

Reviewer responsibilities

Process & policies

Journal Name

ARTICLE TYPE

Cite this: DOI: 00.0000/xxxxxxxxxx

Electron affinities and lowest triplet and singlet state properties of *para*-oligophenylenes (n=3-5): Theory and experiment

Timo Schulz‡,[a] Paul Konieczny‡,[b] Dennis R. Dombrowski,[a] Simon Metz,[a] Christel M. Marian*[a]¶ and Rainer Weinkauf*[b]¶

Received Date
Accepted Date

DOI: 00.0000/xxxxxxxxxx

The molecules *para*-terphenyl (p3P), *para*-quaterphenyl (p4P) and *para*-quinquephenyl (p5P) are used as UV laser dyes and have therefore been extensively investigated. In this work, we apply photodetachment-photoelectron spectroscopy (PD-PES) to measure electron affinities and the energetics of the lowest excited electronic states of the neutral molecules, including especially the triplet states below S_1. The interpretation of the experimental data is based on the comparison to adiabatic electronic state energies and Dyson norms, calculated with combined density functional theory and multireference configuration interaction methods (DFT/MRCI), as well as Franck–Condon patterns. The comparison between calculated and experimental vibrational fine-structures reveals effects caused by resonant autodetachment and discloses structural peculiarities concerning the investigated electronic states, including the anion ground state. Moreover, the theoretical results rationalize the large optical S_0–S_1 cross sections.

1 Introduction

The chemical structures of the *para*-terphenyl (p3P), *para*-quaterphenyl (p4P) and *para*-quinquephenyl (p5P) molecules are shown in Fig. 1. Because of their high fluorescence quantum yields poly-*para*-phenylenes (ppPs) are mainly used as UV-laser dyes. For example, p3P was the gain medium in one of the first tunable UV dye lasers.[1–4] In the subsequent search for higher laser efficiencies, broader wavelengths tunabilities and new wavelength ranges it was found that also modified p3P chromophores[5] and longer ppPs can be used as UV laser dyes.[6]

Already in 1976, a fluorescence quantum yield of 0.93 was measured for p3P in solution, although its S_1 lifetime is rather short (1.2 ns).[3] Usually, short S_1 lifetimes are caused by rapid non-radiative intramolecular relaxation processes which lead to low fluorescence quantum yields. Thus the properties of p3P, namely "a short S_1 lifetime" and "a high fluorescence quantum yield" are exceptional and have been explained by Godard et al. by such a large $S_1 \rightarrow S_0$ optical emission cross section that the fluorescence rate alone causes the short S_1 lifetime.[3]

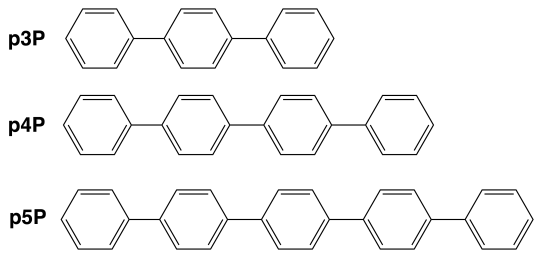

Fig. 1: Chemical structures of *para*-terphenyl (p3P), *para*-quaterphenyl (p4P) and *para*-quinquephenyl (p5P).

[a] *Institute of Theoretical and Computational Chemistry, Heinrich-Heine-University Düsseldorf, Universitätsstr. 1, 40225 Düsseldorf, Germany. Tel: +49 211 8113209; E-mail: Christel.Marian@hhu.de*

[b] *Institute of Physical Chemistry, Heinrich-Heine-University Düsseldorf, Universitätsstr. 1, 40225 Düsseldorf, Germany. Tel: +49 211 8111729; E-mail: Rainer.Weinkauf@hhu.de*

† Electronic Supplementary Information (ESI) available: xyz coordinates of all optimized structures, torsional angles of ground and excited state structures, electron density differences, energies and calculated spectra of conformers, displacement vectors of selected normal mode vibrations, additional computational details. See DOI: 00.0000/00000000.

‡ These authors contributed equally to this work.

¶ ORCID: 0000-0002-4702-6940 (RW), 0000-0001-7148-0900 (CMM)

In 1982, a resonant multi-photon ionization (REMPI) spectrum of the $S_0 \rightarrow S_1$ transition of cold p3P molecules in the gas phase was reported by Murakami et al.[7] In their spectrum, two long progressions of low-frequency vibrations (62 cm^{-1} and 89 cm^{-1}) are built upon the origin transition at 4.024 eV. These low-frequency modes have been assigned to the in-phase and the out-of-phase torsional twist modes around the C–C bonds between the phenyl rings. As explanation for the observed long twist mode progression, the authors[7] propose that in the equilibrium structure of the S_0 state the ring planes are twisted against each other along the C–C inter-ring bond, but lie in one plane in the S_1 state. Other experimental and theoretical publications dealing with the twisted ground state geometry of p3P have been reviewed in the theoretical paper of Baraldi and Ponterini.[8] Using semiempirical calculations, these authors found two nearly isoenergetic conformers for *para*- and *meta*-terphenyl: 1) a C_{2h} symmetric conformer with alternating signs of the inter-ring twist angles and 2) a helical conformer with D_2 symmetry. The barriers separating the two minima were predicted to be low enough to allow a thermal equilibration of the rotamers at room temperature in the gas phase. For the p3P ground state, the angles of the inter-ring twist were calculated to be 35°. Interestingly, in the REMPI S_0–S_1 gas phase spectrum of p3P, inspite of the high spectral resolution, no evidence for a second conformer can be found.[7] This means that either only one conformer is thermally populated or, more plausible, that the two conformers have identical $S_0 \rightarrow S_1$ transition energies.

Denicke et al.[9] worked with two-photon-two-colour femtosecond excitations of p3P into the S_1 and the S_2 states by using different orientations of the polarizations of the two beams. They claim that for the two possible S_0 ground state conformers the strengths of the transition moments for the $S_0 \rightarrow S_1$ and the $S_0 \rightarrow S_2$ excitations are exchanged between the two conformers.

A reinvestigation of the optical properties of p3P derivatives with and without a secondary ring bridge showed that the S_0–S_1 Stokes shifts are relatively large (∼60 nm) for the non-bridged compounds and are considerably smaller (40 nm) if the torsional angle between the phenyl rings is reduced in the S_0 state due to the presence of a ring bridge.[5] Interestingly, ring bridging with a methylene type linker did not appreciably alter the overall performance of the laser dyes whereas the incorporation of oxygen resulted in reduced photochemical stability. The large Stokes shift and the violation of the mirror-image-rule in p3P was later again subject of an experimental and theoretical investigation carried out by Heimel et al.[10] Employing a combination of Hartree–Fock theory and configuration interaction singles they calculated twist angles between 30 and 40 degrees for the ground state of p3P and agreed with previous findings that the S_1 state is planar. With Franck–Condon (FC) simulations the authors explained the shapes of the absorption and emission spectra. Only when the anharmonicities of the torsional potentials of the S_0 and the S_1 states were taken into account, Heimel et al. could reproduce the spectra and the experimentally observed breakdown of the mirror image rule. There are, however, two additional pieces of information buried in this publication: i) The S_1 state becomes planar because its inter-ring bonds are strengthened and adopt the character of double bonds. As a result, Heimel et al.[10] find four members of a sequence of an inter-ring stretch vibration (spaced by ∼1400 cm^{-1}) in their S_0–S_1 FC spectra. This progression of high-energetic vibrations mainly explains, why the emission spectrum of p3P is so broad (60 nm[5]). Combination modes involving the low-energetic torsions then only fill the remaining gaps between the peaks of the inter-ring stretch mode. ii) The S_1 state should have an inter-ring torsional potential which is flatter than the harmonic potential for small angular displacements. Indeed, by checking the data which stem from the well-resolved p3P S_0-S_1 gas phase excitation spectrum of Murakami et al.[7] we find, that the low-energetic twist vibration of 62 cm^{-1} (first quantum) does not show a normal anharmonicity in the S_1 state but has a small inverse anharmonicity (quantum number 7 observed at: 434 cm^{-1}, expected for a harmonic potential at 431 cm^{-1}). Investigations by[11] performed with time-dependent density functional theory (TDDFT) came finally to the conclusion that in the S_1 state of p3P the phenyl rings adapt a quinoid structure with almost full double bonds between the phenyl rings.

The role of non-radiative decay channels in S_1 is still an open question. In an experimental investigation which, besides p3P, also includes p4P, p5P and *para*-sexyphenyl (p6P),[12] the fluorescence quantum efficiencies were measured to be 0.84 (p3P), 0.81 (p4P); 0.89 (p5P) and 0.93 (p6P) and the corresponding lifetimes are 1.0 ns (p3P), 0.85 ns (p4P), 0.82 ns (p5P) and 0.78 ns (p6P). Both series of data follow the same line: the optical S_1-S_0 transition cross sections, being already high for p3P, still increase with the chain length and this cross-section-increase is also directly responsible for the increase in the fluorescence quantum efficiencies and the shortening of the S_1 lifetimes. To be consistent with the above-mentioned plausible explanation by Godard et al.,[3] intramolecular non-radiative relaxation processes should have very small rates in comparison to the optical rates. This is surprising, since one would expect that with the increase of the chain and π-conjugation lengths the probability for non-radiative processes should increase, because i) the energy gaps between the electronic states should decrease and ii) probably more than one triplet state should shift below the S_1 state. The effect ii) would evidently increase the number of possible radiation-less decay channels and the effect i) would increase the rates of these non-radiative channels, since for each additional channel the energy gaps between the involved electronic states become smaller (see "energy gap rule" by Englman and Jortner[13]). However, the data of Nijegorodov et al.[12] do not provide any evidence for the presence of competing non-radiative deactivation processes.

The T_1 triplet state energies for p3P (3.1 eV) and p4P (2.3 eV)

have been already measured by electron energy loss spectroscopy (EELS)[14], a method which competes with photodetachment-photoelectron spectroscopy (PD-PES), used in our investigation, because it also addresses triplet and singlet states of the neutral molecules on an equal footing. Strangely, no triplet states above T_1 have been found, although the energy range of the EELS spectra includes the S_1 states (p3P: 4.9 eV; p4P: 4,6 eV), the S_2 states and even higher singlet states.

Once the T_1 state position is known, another method to determine energies of higher excited triplet states would be the transient $T_1 \rightarrow T_n$ triplet–triplet absorption spectroscopy. With this method applied to p3P, the first absorption from T_1 was found at about 2.25 eV[15], which means that the upper triplet state lies about 5.35 eV above S_0 and therefore above the S_1 state. This finding does, however, not exclude that other triplet states lie below S_1. One has to consider that, for experimental reasons, the excited state absorption method is typically blind in the IR range. This means that the question, whether in ppPs the T_2 or even T_3 states lie below S_1 is still open.

The primary aim of the present work is to understand the large S_0–S_1 transition moment and why non-radiative deactivation processes are of minor importance in the ppPs. Our focus therefore lies on the energetics and electronic as well as geometric structures of the lowest triplet states and their possible role in intramolecular relaxation processes after photo excitation to the S_1 state. The most relevant question in this context is, however, how many triplet states do lie below the S_1 state. To answer this question, we apply PD-PES to intact parent radical anions. The fact that triplet states of the neutral sample molecule can be directly addressed by removal of an electron from an intact radical anion has been known for a long time.[16–19] We applied this method in former work to anthracene,[20] azulene,[21] N-methylacridone and N,N-dimethylquinacridone[22] as well as to some other molecules. With the same method, but using a magnetic bottle photoelectron spectrometer, the electron affinities (EA) of p3P and p4P were determined by Nakamura et al. (p3P: 0.39 $\pm$0.01 eV and p4P: 0.66 $\pm$0.02 eV) already in 2006.[23] In this former work, also theoretical EA values (B3LYP/6-31+G*) including zero-point vibrational energy (ZPVE) corrections were presented (p3P: 0.3 eV and p4P: 0.61 eV) which agree reasonably well with the experimental values. Besides electron affinities, we measure and assign the lowest electronic excited states including S_1. Finally, we compare calculated FC spectra with the shape of the corresponding measured spectra with the aim i) to detect effects of resonant anion excited states, ii) to gain new insights concerning the energetic, the geometric, but also the electronic structures of the investigated electronic states — especially the triplet states below S_1 — and iii) to eventually derive new information concerning the exceptional photo properties of the ppPs.

2 Methods

2.1 Anion photodetachment photoelectron spectroscopy (PD-PES): The experimental setup.

The sample molecules have been purchased from TCI. The apparatus used in this work for conducting photodetachment photoelectron spectroscopy (PD-PES) of molecular ppP radical anions has been described elsewhere.[21,22] In short, the PD-PES experiment consists of four vacuum chambers arranged in a sequence to stepwise reduce the vacuum pressure from the inlet chamber (chamber 1) to the photoelectron spectrometer (chamber 4). At the beginning of each measurement cycle (the experiment runs at 10 Hz repetition rate), a heated and pulsed stainless steel gas nozzle releases a short gas pulse of argon (20 bar back pressure) with a small percentage of thermally evaporated sample molecules. This pulsed co-expansion takes place through a small orifice (diameter 300 μm) into the first vacuum chamber (pressure in average better than 5×10^{-5} mbar). During expansion, radical anion formation by electron attachment to the sample molecules is performed directly in front of the nozzle orifice in the plume of the co-expansion. For energetic reasons, electron attachment is especially efficient for low-energetic electrons, which usually are difficult to produce in high numbers due to coulomb repulsion. In our apparatus, it seems that the mass-production of free electrons with low kinetic energy is achieved by shooting a time-synchronized pulse of high-energetic electrons (pulse width below 15 ns, energy 2 keV) into the centre of the dense gas plume, as close as possible to the nozzle orifice. These high-energy electrons then ionize Ar atoms and release secondary lower-energetic electrons. Some of these then can be captured by the ppP sample molecules forming mostly radical anions of intact parent molecules. During the ongoing expansion, the initially relatively hot radical anions (note that in minimum the binding energy of the surplus electron is present in form od vibrations) then quickly undergo many collisions with the dense Ar gas. By this the anions are energetically stabilized and their internal degrees of freedom are strongly cooled. The slow neutral atoms and molecules as well as all the negative sample anions and the positive Ar ions contained in the centre of the expansion pass after about 10 mm through a skimmer orifice into the second vacuum chamber. The latter is either used for vacuum pressure reduction between the chambers or the selection of these anions, which stem from the centre of the expansion and have undergone the maximum number of collisions with the argon carrier gas and therefore have minimum internal energy.

Despite that most of the sample radical anions are intact parent anions, mass selection is required before the photodetachment, because many aggregates between sample molecules and themself, sample molecules with residual water molecules and sample molecules with Ar atoms are formed. In chamber number two, for this reason, the ions enter a pulsed linear time-of-flight mass

spectrometer (ToF-MS) through chambers 3 and 4. After passing several ion focussing lenses and several deflection plates in chamber 3, the anion cloud crosses the PE spectrometer in chamber 4 and is detected at the rear side of chamber 4 on a micro-channel-plate (MCP) ion detector. The mass resolution is at this stage about 200. The ion flight path is parallel to the plane of the table on which the experiment is mounted. When crossing chamber 4, in the middle of the perpendicular μ-metal-shielded and therefore field-free PE spectrometer the anions interact with the pulsed detachment laser beam, which comes from above, perpendicular to the table plane. The electrons which are accidentally emitted perpendicular to the ion and the laser beams are detected on a MCP-detector. The energy of the electrons is then determined by a start-stop time-of-flight measurement. To achieve a high accuracy in the time measurement, the slightly focussed detachment laser has a pulse width below 1 ns. For this we used the fundamental and higher harmonics of a post-amplified Piccolo laser (Innolas, Germany, pulse width 800 ps).

In order to be able to hit as many anions as possible with the laser beam, after mass identification, the anions of interest are post-accelerated before chamber 4 and by this compressed in time and space[24]. Photoelectron spectra are recorded by measuring the time of flight (ToF) which the electrons take for the 60 cm long field-free drift tube form the detachment site to the electron MCP detector. The advantage of such a ToF-energy analyser is, that in the PE spectrum the full energy range corresponding to the photon energy is recorded for each measurement cycle. The disadvantages, however, of this method are i) the low transmission and ii) the fact that the smallest peak widths are only achieved for relatively low-energetic electrons (E$\leq$ 200 meV).

As indicated, the accuracy concerning the absolute energy E of an transition in a PD-PE spectrum as well as the spectrometer resolution ΔE depends on the absolute electron energy and hence also on the detachment wavelength used. To obtain a good energy resolution for most of the accessible electronic states of the neutral sample molecule, in this work, the overview anion PD-PE spectra are composed of sections of sub-spectra recorded with different detachment wavelengths. The disadvantage of this procedure is that the electronic state intensities in the sub-spectra are different due to Wigner´s threshold law[25] and therefore difficult to adjust to each other and therefore rather inaccurate. However, since we are especially interested in the energetics, such as electron affinities and triplet state energies, a comparison the intensities of the electronic states is of minor importance.

An additional aspect of using different detachment wavelengths is, that sometimes the influence of anion-excited states on the photodetachment can be avoided by choosing a different detachment wavelength. In the ideal case, a photo excitation of a radical anion would excite into the detachment continuum consisting of the neutral molecule and the leaving energetic electron. In this case the intensities of the vibronic transitions of the final electronic state of the neutral molecule are given by the FC factors between the anion ground state and the neutral electronic state to which the detachment process leads. Unfortunately anions can have anion-excited states even above the electron detachment threshold. These states, if resonantly photoexcited, can in a second step autoionize. Since in this case the resonant anion excited electronic state is directly involved, it can i) either disturb the anion-to-neutral FC factors[26–28], or ii) lead to a vibronically induced delayed autodetachment.[29] For this latter process the anion excited state — which lies above the photodetachment threshold — relaxes very fast by internal conversion (IC) to high-lying isoenergetic vibrational energy levels of the anion ground state, which then — with some time delay — can boil off a low-energetic electron. Both effects i) and ii) can only happen, if the wavelengths used for photodetachment are in resonance with an anion excited state. Since we use the harmonics of a Nd:YAG laser, we sometimes accidentally observe such effects, although in general they are undesired, if — as in this work — the main goal is the investigation of the excited states in neutral p3P, p4P and p5P. For p3P and p4P, photoabsorption spectra of the radical anions in solution show that in both anion species more or less strong photoabsorptions to anion excited states exist around 1064 nm and 532 nm.[30] Due to the lack of other lasers in our PD-PE laboratory, both photodetachment wavelengths could unfortunately only be avoided by using higher harmonics of the Nd:YAG laser (355 nm, 266 nm and/or 212.7 nm).

To avoid surface effects as much as possible, the inner spectrometer wall is heated to 340 K and the PE spectrometer is energy-calibrated from time to time with the two spin–orbit transitions of atomic iodide[31–33]. We found that the experimental accuracy concerning the absolute energy is $\pm$5 meV for electrons with energies below 300 meV, but the relative accuracy is for some transitions much better than this. The accuracy to determine the energy of the adiabatic origin of an electronic state may, however, be less than the experimental accuracy because the shape of the observed spectral structures might be broad and make an assignment of the exact origin transition of an electronic state difficult or even impossible. The latter remark holds especially for the positions of the S_0 ground states of the ppPs, for which the vibronic transitions are not or not well resolved (see Section 3.1).

2.2 Theoretical Methods and Computational Details

All geometry optimizations and frequency analyses were performed with the Gaussian 16 program[34] using the PBE0 density functional[35,36] and a valence triple-zeta basis set with polarization functions (TZVP)[37] for carbon and hydrogen. The geometries of the anionic ground states (D_0) were optimized at the level of unrestricted density functional theory (UDFT) while closed-shell Kohn–Sham (KS) DFT was employed for the neu-

tral ground states (S_0). The minima of the excited singlet states were determined with time-dependent density functional theory (TDDFT), those of the triplet states with TDDFT in the Tamm-Dancoff approximation (TDA). Electronic excitation energies and molecular wavefunctions at the optimized geometries were calculated with the DFT/MRCI method[38,39] employing the recently presented R2022 Hamiltonian[40] which is particularly well suited for extended π-systems. DFT/MRCI is a semi-empirical multireference configuration interaction ansatz based on KS orbitals and orbital energies of a closed-shell BH-LYP functional[41,42] determinant. For the construction of the two-electron integrals in the resolution-of-the-identity approximation, the auxiliary basis sets from the Turbomole library[43,44] were employed. Computational details concerning the DFT/MRCI parameter set, the selection thresholds for including configuration in the variational space and the number of roots determined in the Davidson diagonalization procedure for each molecule can be found in the ESI†. FC spectra were calculated via a fast Fourier transformation ansatz employing the VIBES program.[45,46]

Besides adiabatic energies and FC patterns of the excitation, photoionization cross sections are especially valuable for assigning closely spaced electronic states. To obtain an estimate for the photoionization probabilities, often Dyson orbitals ϕ_{IF}^{Dyson} and their respective squared norms σ_{IF} are used, disregarding the overlap between the outgoing electron and the ionization continuum states.[47–50] In the context of PES, Dyson orbitals are defined as the overlap between an initial N-electron state and a final N–1-electron state.

$$\phi_{IF}^{Dyson}(x_1) = \sqrt{N} \int \psi_F^{N-1}(x_2, x_3, \ldots, x_N) \psi_I^N(x_1, x_2, x_3, \ldots, x_N) \, dx_2, dx_3, \ldots, dx_N \quad (1)$$

Dyson orbitals can also be written as a linear combination of the molecular orbital set of the initial wave function $\{\phi_p\}$:

$$\phi_{IF}^{Dyson}(x_1) = \sum_p \gamma_p \phi_p(x_1) \quad (2)$$

where the expansion coefficients, also called Dyson amplitudes, are defined as:

$$\gamma_p = \left\langle \psi_F^{N-1} \middle| a_p \middle| \psi_I^N \right\rangle \quad (3)$$

Possible values range between 0 for states that cannot be described by a one-electron transition and 1 for two states that differ exactly the occupation of one spin orbital. Note, that a value of 1 is only possible if the electron is detached from a singly occupied molecular orbital of the anion. If the electron is removed from a doubly occupied shell, at most a Dyson amplitude of 0.5 can be expected. (For further explanations, see the ESI†.) The squared Dyson norm can then be described as the sum over the squared coefficients

$$\sigma_{IF} = ||\phi_{IF}^{Dyson}||^2 = \sum_p \gamma_p^2 \quad (4)$$

and is a measure for the probability of a photoionization (pole strength). In this work, DFT/MRCI wavefunctions of the anionic ground state and the ground and excited states of the respective neutral molecules have been used to determine the pole strengths.

3 Results and Discussion

In the following section, we present the experimental PD-PE overview spectra of p3P, p4P and p5P, explain their specialities and propose first assignments. Subsequently, we report on the results of our quantum chemical calculations before we compare them with the experimental data and discuss the resulting consequences.

3.1 Photodetachment photoelectron overview spectra

The overview PD-PE spectra of p3P, p4P and p5P (Fig. 2) show the transitions from the anion ground states to the S_0 and to the excited states of the neutral molecules. The estimated origin positions of the S_0 states are set to the zero position of the energy scale which is — as a consequence — the energy scale of the neutral molecules. It should be noted already at this point that for the S_0 states the determination of the origin energy is difficult and inaccurate due to the facts that there are i) large anion-to-S_0 geometry changes, almost planar in the anion ground state to twisted in the S_0 state and ii) the involved twist vibrations, which appear in long vibrational progressions in S_0, cannot be resolved (see below). In the following, this problem is first neglected in order to discuss the main features contained in Fig. 2 such as the energetic positions and state order. As a result of the definition of the energy axis, the anion ground states lie to the left of the zero point of the x-axis (S_0) and the electronically excited states of the neutral molecules to the right side. As expected, the EAs (difference between the anion and the neutral ground states) increase and the electronic excited state energies decrease with the increase of the number of phenyl rings. Note that the overview spectra are composed of sub-spectra recorded with different detachment wavelengths in order i) to show spectra with the best possible electron energy resolution or ii) to avoid for some detachment wavelengths strange vibrational FC effects as caused by accidentally populated anion excited states. Labels with the detachment wavelengths used are included in Fig. 2. The relative intensites of the subspectra have been adapted to each other according to graphical aspects. Relative intensities between two electronic states can be only interpreted if their spectral structures have been recorded with the same wavelength and the two states lie rather close in energy.

The assignments included in Fig. 2 are based on simple spectro-

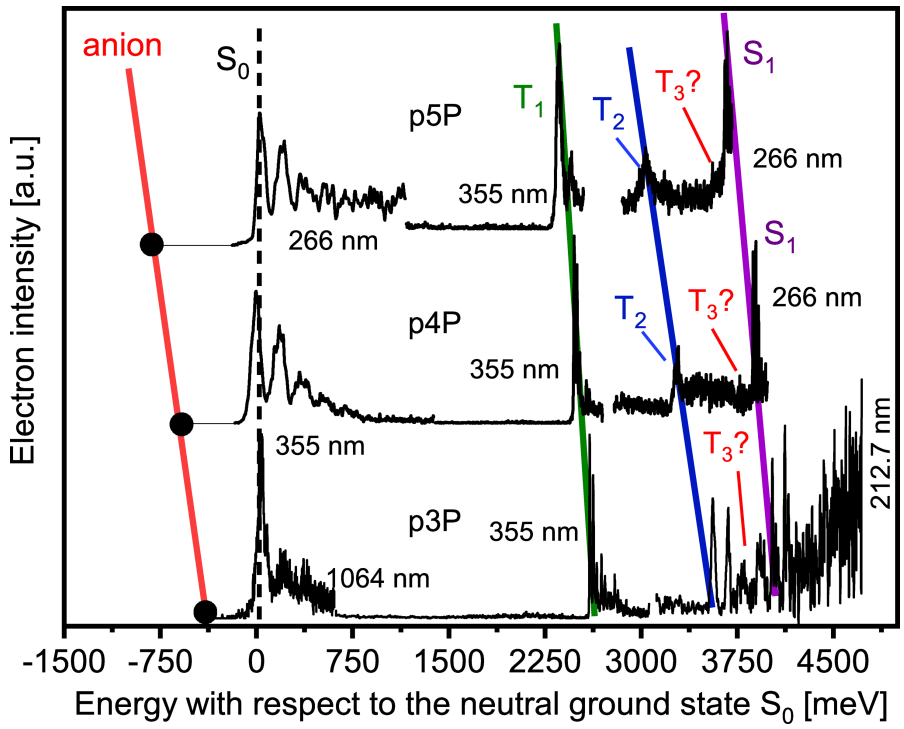

Fig. 2: PD-PE overview spectra of p3P, p4P and p5P including first assignments. The energy scale gives the energy with respect to the neutral S_0 ground state. Note that the EA increases with increasing number of phenyl rings whereas the neutral excited-state energies decrease. For p4P and p5P, the small structures in front of S_1 are tentatively assigned to the T_3 states. For further explanations see text.

scopic principles and literature data. The lowest-energetic transition from the radical anion to the neutral closed-shell molecule leads to the S_0 state of the neutral molecule. The assignment of the next spectral PE structures is also obvious: In a closed-shell molecule, the T_1 state is usually the first excited state above S_0 and does not appear in UV-VIS spectra. The assignment of the S_1 states can be performed on the basis of their energetics which agree with S_0–S_1 transition energies known from literature (see Table 1 below). Since the isolated transitions which are located between T_1 and S_1 have not been observed in the UV-VIS spectra[5], they are attributed to T_2. In addition, further peaks are assigned with some question mark to the T_3 state.

The EA values and the excited state energies of all three molecules are summarized in Table 1 and compared to experimental literature data. Table 1 shows that in all investigated ppPs definitively the T_2 states and — with some question mark — even the T_3 states lie below the respective S_1 states and that the S_1–T_2 energy gap is relatively small. In Fig. 2 one can see that the vibrational structures of the individual electronic states are rather different. For example, in p3P the first transition to S_0 is much broader (this sub-spectrum was recorded with 1064 nm, providing the best experimental resolution) than the peaks of the transitions to T_1, T_2 and S_1. If autodetachment effects were absent, these individual vibrational patterns should be correlated with structural changes between the molecular anion geometry and the geometries of the individual electronic states of the neutral molecules. Note that for the transitions from the anions to S_0 in p4P and p5p high-energetic photons (355 nm in the case of p4P and 266 nm in the case of p5P) have been used for photodetachment in order to avoid autodetachment effects. In section 3.3, expanded PD-PE spectra of most of the transitions to the individual electronic states of the neutral molecules are shown and compared to corresponding theoretical spectra.

3.2 Quantum chemical results

According to former investigations,[7,8,10,23] the changes of the torsional angles, which are allocated between the phenyl rings, play an important role for the interpretation of the electronic and vibronic spectra of the ppPs. Moreover, these twist angles seem to be correlated with C–C bond length alterations. Lukeš et al. postulated that ppPs exhibit a quinoid structure in the first excited singlet state and that the double-bond character of the C–C bond between the phenyl rings causes the planarity in S_1.[11] We here take these statements as a motivation for a more general investigation on the equilibrium geometry changes in the ground and excited electronic states of the neutral ppPs with regard to the

Table 1: Electron affinities and electronic state energies of p3P, p4P and p5P with respect to the neutral ground state S_0. Experimental data from this work and literature data. All values are given in meV. Note that the experimental energy error is about ±20 meV, as given by the accuracy with which the origin of the S_0 state can be determined

	p3P		p4P		p5P	
State	Lit.	This work	Lit.	This work	Lit.	This work
EA/S_0	390 [a]	379	660 [a]	620	-	840
S_1	4024 [b], 3962 [c], 4900d	4024	3731 [c], 4600 [d]	3872	3602 [c]	3653
S_2	6500 [d]	-	4029 [c], 6400 [d]	-	3967 [c]	-
T_1	2541 [c], 3100 [d], 2529 [e]	2598	2392 [c], 2300 [d]	2478	2318 [c]	2340
T_2	-	3558	-	3260	-	3038
T_3	-	3930 (?)	-	3771 (?)	-	3562 (?)

[a] 23 PD-PES [b] 7 REMPI, gas phase [c] 12 solution phase [d] 14 electron beam, gas phase [e] 51 crystal

anion ground state. In the following, the trends will be discussed in a qualitative manner.

As mentioned earlier, for the neutral *para*-phenylenes two or more stable rotamers exist which differ in the relative orientation of the phenyl rings, i.e., alternating or helical. Within the error bars of our experiment and our quantum chemical calculations we do not find energetic differences between the two (p3P) and multiple (p4P and p5P) possible conformers of the investigated ppPs, neither in the anions nor in the neutral electronic states. Whereas the equalities of the rotamer energies have been explicitly checked for all investigated states of p3P, for p4P and p5P they have been only tested for some states. Inter-conformer transitions have been also investigated. They have the same transition energies as intra-conformer transitions but have typically broader vibrational structures due to the larger geometry changes. To simplify the complex discussions, we only present the results for the conformers alternating in the sign of the torsion angles.

3.2.1 *para*-terphenyl (p3P)

Fig. 3 shows that D_0, S_1, S_2 and T_1 are nearly planar and that S_0 is strongly non-planar. The S_3 and T_2 states are predicted to have dihedral angles of ca. 20°. The minimum nuclear arrangement of the T_3 state could not be determined because the geometry optimization converges towards a conical intersection with the T_2 potential energy surface.

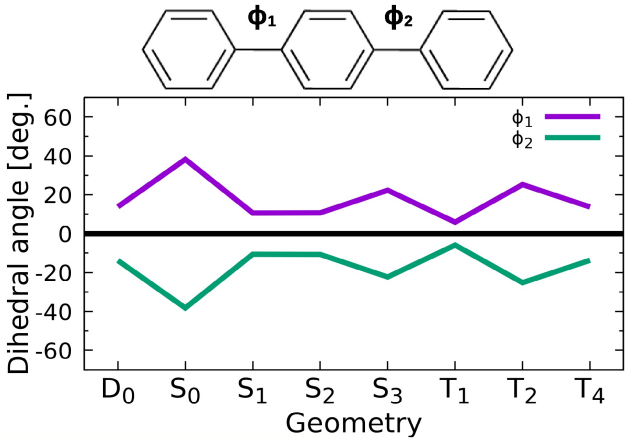

Fig. 3: Calculated torsional angles in the equilibrium geometries of selected anionic and neutral electronic states of p3P.

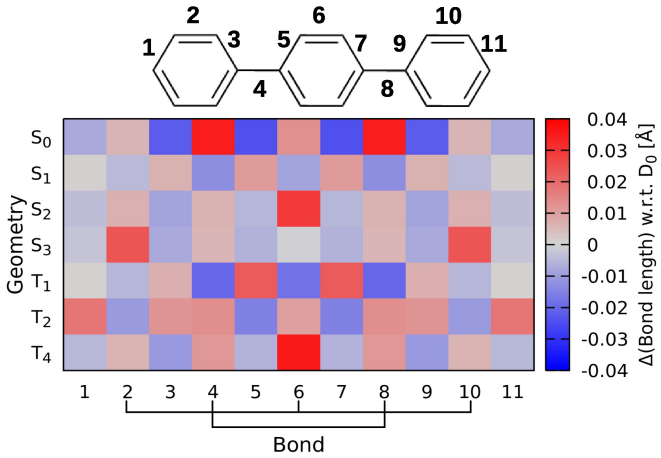

Fig. 4: Bond length differences between the respective neutral and D_0 anion state geometry of p3P. The colour bar at the right side gives the correlation between the colours and the bond length changes (in Å).

In Fig. 4, the calculated bond length changes with respect to the anion ground state D_0 are shown. These changes will be rationalized based on the leading configurations of the wavefunctions. To avoid confusion, we designate the molecular orbitals (MOs) according to their occupations in the ground state of the neutral molecule: The highest occupied molecular orbital (HOMO, H) is doubly occupied in both, S_0 and D_0, whereas the lowest unoccupied molecular orbital (LUMO, L) is empty in S_0 and singly occupied in D_0.

The leading term of the totally symmetric S_0 state is related to the D_0 state by the ejection of the LUMO electron. The LUMO has bonding character with regard to the inter-ring C–C bonds 4 and 8 (see Fig. 5b), where we have used the bond labelling introduced in Fig. 4. Also the C–C bond 6 in the central phenyl ring and, to a minor extent, the C–C bonds 2 and 10 in the terminal phenyl rings experience bonding interactions in LUMO. All other C–C bonds of p3P are intersected by nodal planes in the LUMO and therefore have antibonding character. The pattern of the bond length alterations, shown in Fig. 4, exactly follows the expected trends: If one electron is removed from the LUMO, the inter-ring C–C bonds 4 and 8 lose their double-bond character. Accordingly, the steric strain caused by the repulsion between the hydrogen atoms of two neighbouring phenyl rings prevails over the bonding forces and leads to an out-of-plane twist, as may be seen when comparing the torsional angles of the D_0 and the S_0 states in Fig. 3. Also the central bond 6 is strongly elongated in S_0 with respect to D_0 while the bonds carrying odd labels are shortened, but these bond length changes do not have a major impact on the dihedral angles.

If instead an electron is removed from the HOMO, the A_u-symmetric T_1 or S_1 states are reached, depending on the spin orientation of the outgoing electron. Although both states are well represented by the $(H)^1(L)^1$ configuration, the bonding patterns (Fig. 4) are not identical. We notice stronger bond length alterations in the triplet state, a phenomenon already observed for the $(H)^1(L)^1$ states of polyene chains[52]. Nodal planes intersect the even numbered bonds whereas high electron density is found between the carbon atoms connected by odd numbered bonds (see Fig. 5a). In the S_1 and T_1 states, therefore the inter-ring C–C bonds are strengthened and shortened whereas the neighbouring bonds are elongated. Even the bonds 2, 6 and 10 acquire partial double bond character, thus giving the three phenyl rings a quinoid structure.

The geometry changes of the higher-lying electronic states are not as easily deduced because they have multiconfigurational character. The wavefunction of the T_2 state exhibits A_g symmetry and is dominated by an almost equal mixture of $(H–1)^1(L)^1$ and $(H)^1(L+2)^1$ configurations. HOMO–1 and LUMO+2 have larger amplitudes on the terminal phenyl rings than on the central one (see Figs. 5c and 5f). Ejection of an electron from HOMO–1 and occupation of LUMO+2 both lead to a pronounced elongation of the terminal C–C bonds 1 and 11, other geometry changes are less obvious. Inter-ring twist angles intermediate between the D_0 and S_0 are found for the equilibrium geometry of this state. S_2 and T_4 transform according to the B_u irreducible representation with leading $(H)^1(L+1)^1$ and $(H–2)^1(L)^1$ terms. LUMO+1 and HOMO–2 do not involve the carbon atoms connecting the phenyl rings (see Figs. 5d and 5e). Therefore, the small twist angles (Fig. 3) are mainly caused by the removal of a HOMO electron in the first case and the remaining electron in the LUMO in the second case. The most pronounced bond length change involves the central C–C bond 6 which is markedly weakened with respect to the anion ground state (Fig. 4).

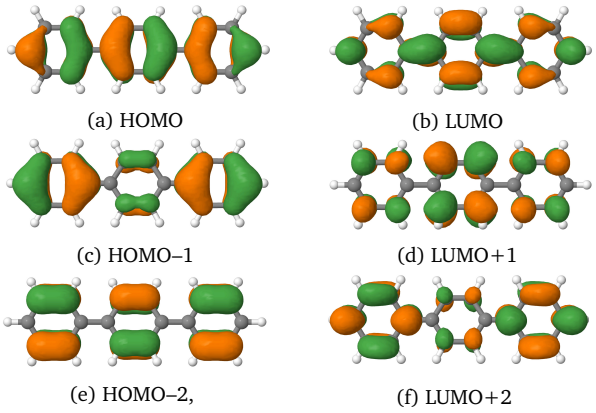

(a) HOMO (b) LUMO (c) HOMO–1 (d) LUMO+1 (e) HOMO–2, (f) LUMO+2

Fig. 5: Important MOs of p3P at the anion ground state geometry. Images of further MOs may be found in the ESI†.

3.2.2 *para*-quaterphenyl (p4P)

The structural differences between the electronic states of p4P show similar patterns as those of p3P (Figs. 6 and 7), save for a few distinct peculiarities concerning the central C–C bond and the related torsional angle Φ_2. In the anionic ground state, the torsional angles vary between 15° for Φ_2 and –20° for Φ_1 and Φ_3. The S_0 minimum geometry is again strongly non-planar and the inter-ring bonds are elongated with regard to the D_0 structure. The effect is more pronounced for the central bond 8 because the electron density in the LUMO (Fig. 8b), from which the electron is ejected, is higher than for the terminal inter-ring bonds 4 and 12. The S_1 and T_1 states of p4P adopt a quinoidal structure, again with stronger alterations for the central bond and the related twist angle due to the larger orbital amplitudes of the HOMO (Fig. 8a) in that spatial region.

T_2 and S_4 are interesting cases because here opposite tendencies are observed for the outer and inner phenyl rings and the related geometry parameters (Figs. 6 and 7) which can be traced back to the electron density distribution in the involved MOs. Like in p3P, T_2 and S_4 are multiconfigurational wavefunctions with the $(H–1)^1(L)^1$ and $(H)^1(L+1)^1$ configurations as leading terms. In-

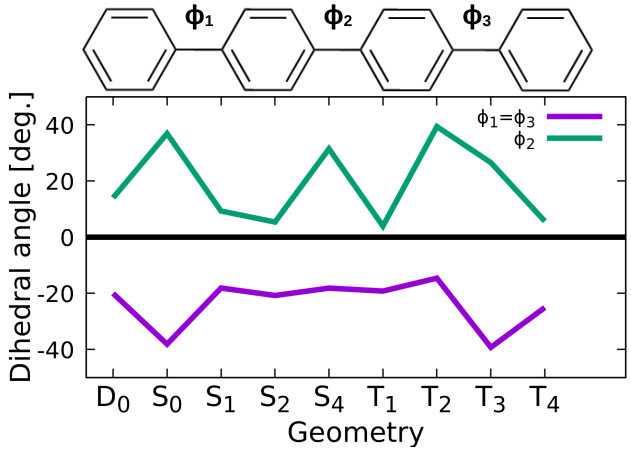

Fig. 6: Torsional angles in the different electronic states of p4P. Note the different behaviour of the outer angles Φ_1 and Φ_3 in comparison to Φ_2.

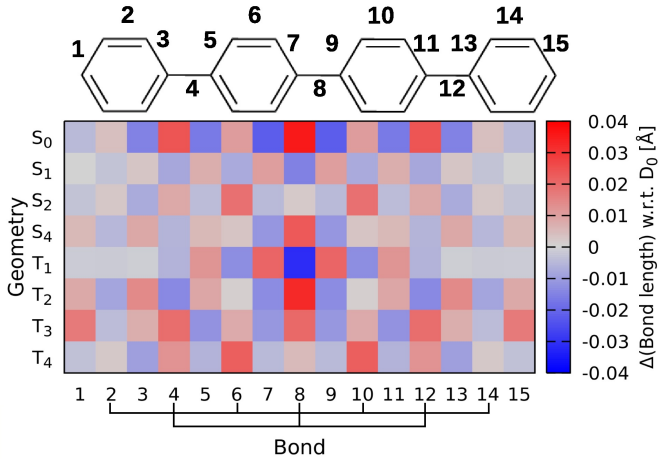

Fig. 7: Bond length differences between the neutral states of p4P with respect to the D_0 anion ground state geometry. For further explanations, see Fig. 4.

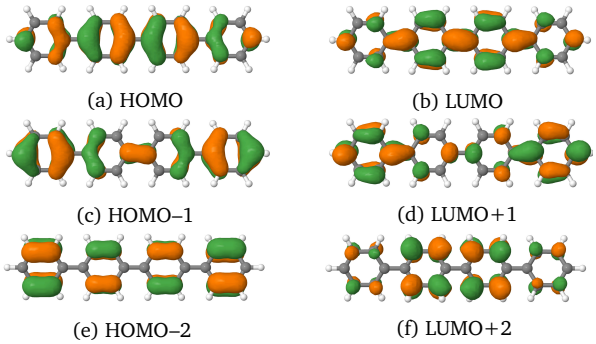

Fig. 8: Important MOs of p4P at the anion ground state geometry. Images of further MOs may be found in the ESI†.

spection of Fig. 8c reveals bonding character for 8 and antibonding character for 4 and 12 in HOMO–1. Annihilation of an electron in HOMO–1 therefore weakens the central inter-ring bond and strengthens the outer ones. The second configuration cannot be reached from D_0 by a single electron excitation, but requires the removal of an electron from HOMO accompanied by an excitation from LUMO to LUMO+1. While geometric effect caused by the lowering of the HOMO and LUMO populations nearly cancel, occupation of LUMO+1 (Fig. 8d) results in an elongation of the central C–C bond. While the electronic states of neutral p4P, discussed so far, are symmetric with respect to a rotation through 180° about the long C_2 axis (z axis), S_2 and T_4 are antisymmetric. To reach their leading $(H)^1(L+2)^1$ configuration from the D_0 state, again a two-electron process is necessary. Their secondary configuration, $(H–2)^1(L)^1$, is generated by PES through the ejection of an electron from HOMO–2. Neither HOMO–2 (Fig. 8e) nor LUMO+2 (Fig. 8f) exhibit notable amplitudes on the inter-ring C–C bonds. Ejection of an electron from HOMO–2 and occupation of LUMO+2 rather lead to a weakening of the bonds 6 and 10 (Fig. 7) without essentially changing the torsional angles with regard to the anion ground state (Fig. 6).

3.2.3 *para*-quinquephenyl (p5P)

Without repeating this kind of detailed discussion for p5P, we notice that for some electronic states the outer ($\Phi_1 = \Phi_4$) and the inner torsional angles ($\Phi_2 = \Phi_3$) differ considerably (Fig. 9). In the D_0 anion ground state, all twist angles are around 20° while the S_0 state of p5P is strongly twisted, with all torsional angles close to 40°). In S_1 and T_1 (configuration $(H)^1(L)^1$), the inner two twist angles are smaller than the outer ones, an effect which is even more pronounced in the T_1 state. The degree of torsion finds its direct correspondence in the inter-ring C–C bond distance (Fig. 10). The quinoidal structure appears to extend over the three innermost phenyl rings only. These trends are related to the observation that the electron densities in the HOMO (Fig. 11a) and LUMO (Fig. 11b) orbitals are mainly localized in this part of the molecule. In contrast, HOMO–1 (Fig. 11c) and LUMO+1 (Fig. 11d) have large amplitudes on the outermost phenyl rings and their neighbours and almost zero coefficients on the central phenyl ring. For that reason, the inner inter-ring bonds No. 8 and 12 are weakened whereas the outer inter-ring bonds (No. 4 and 16) are strengthened at the T_2 minimum where the $(H–1)^1(L)^1$ and $(H)^1(L+1)^1$ configurations have nearly equal weights. As a consequence, the outer twist angles are smaller than the inner ones, essentially reversed to the situation in the T_1 state. Also T_3 is not planar. It exhibits a nearly equal mixture of $(H–2)^1(L)^1$, $(H–1)^1(L+1)^1$ and $(H)^1(L+5)^1$ configurations (for orbitals see Fig. 11), Like in T_2, its inter-ring bonds 8 and 12 are elongated with respect to the D_0 structure, but the bond length alterations

in the central ring nearly level out.

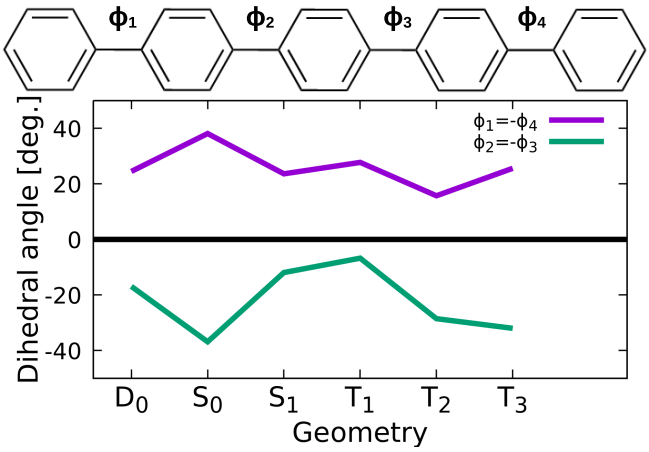

Fig. 9: Torsional angles in the different electronic states of p5P.

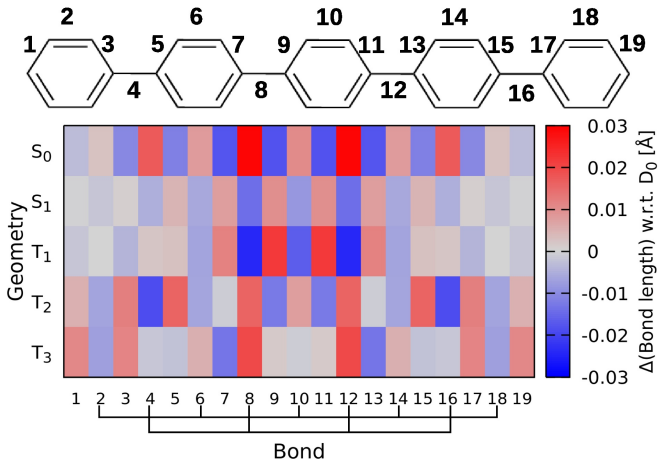

Fig. 10: Map of length differences between the C–C bonds in the lowest electronic states of p5P with respect to the C–C bonds in the anion D_0 state.

In conclusion of this section, with increasing chain length of the ppP, more and more local effects are observed where the inner and outer molecular sections behave differently in individual electronic states. The tendency that a nearly planar quinoidal structure in the S_1 state is restricted to the central parts of the molecule has been reported even for longer *para*-phenylene oligomers.[53] While trends for the first excited singlet state were discussed in detail by[11], we extended our investigation of the structural changes to several low-lying triplet states because anion PD-PE spectroscopy does not discriminate against spin-flip excitations. In the following, we use the theoretical information on the low-lying singlet and triplet states and their properties to assign and interpret the experimental spectra.

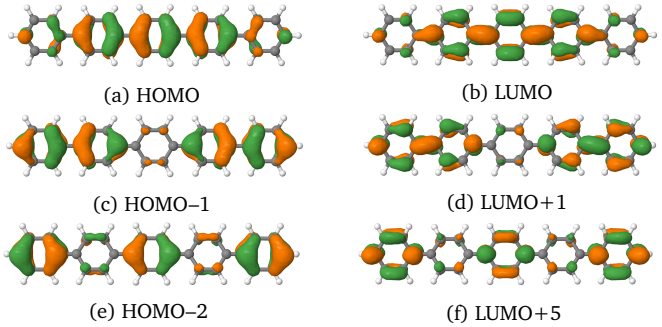

Fig. 11: Important MOs of p5P at the anion ground state geometry. Images of further MOs may be found in the ESI†.

3.3 Comparison of the experimental and computed spectra

In this chapter we present our theoretical results based on the DFT/MRCI method and compare them to the experimental data. Note that the energy scale of the experimental spectra in this section is given in meV and refers to the anion ground state, whereas the theoretical FC spectra (also in meV) refer to the origin of the respective electronic state. Please remember that the absolute error for the experimental electronic state energies with respect to the S_0 state is determined by the error with which the exact position of the transition to the S_0 origin can be determined. Due the broad unresolved structure of this transition the S_0 origin position may have only an accuracy of roughly 20 meV. Root mean square deviations of the DFT/MRCI method are typically in the 200 meV range for organic molecules with a closed-shell ground state when the R2022 Hamiltonian is employed.[40]

The overview tables contain i) the calculated leading electron configurations of the listed electronic states, ii) vertical excitation energies at the S_0 geometry, iii) adiabatic and zero-point-corrected excitation energies with respect to the neutral ground state S_0, iv) the experimental state energies as determined in this work, v) the computed optical oscillator strengths f with respect to S_0 and vi) the calculated probabilities (Dyson norms, see sec. 2.2) for photodetachment from the anion ground state (σ). Note that the latter do not take account of the overlap between the wavefunction of the outgoing electron and the ionization continuum which is reflected in Wigner's threshold laws[25] and therefore do not properly describe the intensities as observed in the experimental photodetachment spectra. Also autodetachment processes are not considered. Only in the special case that two electronic states are energetically not too far separated in an experimental spectrum, recorded with a single detachment wavelength, and that their intensities are very different, the corresponding Dyson intensities of the two states can be used to support or reject assignments.

3.3.1 *para*-terphenyl (p3P)

The agreement between the calculated and measured 0–0 energies is rather good (Table 2). This applies even to the electron affinity. With the exception of T_1 which matches the experimental value perfectly, the calculations appear to underestimate the experimental 0–0 energies by about 0.1 eV, whereas adiabatic DFT/MRCI energies which do not include ZPVE corrections are a bit too high. Note that the theoretical value of the T_3 energy, provided in Table 2, has been obtained for a C_s-symmetric saddlepoint structure with a small imaginary frequency (–13 cm^{-1}). Despite many attempts, a proper minimum could not be determined for the T_3 potential energy surface because it undergoes a conical intersection with the T_2 potential. According to the calculations, this saddlepoint lies energetically below the S_1 minimum if ZPVE corrections are taken into consideration. The strong vibronic coupling between two triplet states is held responsible for the irregular vibrational pattern observed between T_2 and S_1 in the overview spectrum. (See below for details.)

Interestingly, S_1 is not the lowest excited singlet state at the equilibrium geometry of the neutral ground state. With a value of ∼0.60 eV, its relaxation energy is much larger than for all other low-lying states, except for T_1 with which it shares the $(H)^1(L)^1$ configuration. This observation explains the large and irregular S_0–S_1 Stokes shifts determined in optical spectroscopy[5]. As noted above, the $S_0 \rightarrow S_1$ transition has a high oscillator strength (1.15 at the DFT/MRCI level in the FC region). In contrast, the oscillator strength of the $S_0 \rightarrow S_2$ excitation is close to 0 (1×10^{-4} at the DFT/MRCI level) although the transition is not electric dipole forbidden. The question arising in this context is whether one can find relatively simple graphical explanations for these peculiarities. Inspection of the MOs in Fig. 5 reveals that the HOMO is b_g symmetric while the LUMO exhibits b_u symmetry. The a_u symmetric $S_0 \rightarrow S_1$ transition dipole is therefore aligned with the long molecular C_2 axis. In contrast, the b_u symmetric $S_0 \rightarrow S_2$ transition dipole is oriented perpendicular to this axis. Moreover, S_2 is a multiconfigurational state. The anyhow much smaller dipole integrals of the leading terms carry opposite signs, which as a result partly cancel out.

The very different vibrational substructures of the individual transitions in the experimental p3P PD-PE spectrum shown in Fig. 2 indicate that some electronic states of the neutral molecule exhibit strong structural differences with respect to the anion ground state, an effect which is worth to be further investigated by calculations of FC patterns. Our geometry optimizations for p3P show that it is almost planar in the anion ground state (the twist angles between the phenyl planes are determined to be ±10°), strongly twisted in the neutral ground state S_0 (twist angles about ±40°) and planar in the S_1 state. For the S_0 and the S_1 states these finding agree well with the results of[11]. A quick look at the overview spectrum of p3P (see Fig. 2) confirms qualitatively these theoretical results: In contrast to the broad anion to S_0 transition, the transitions to excited electronic states, such as T_1 and S_1, contain intense origin transitions and relatively small intensities for the low-frequency vibrations. One can therefore expect them to have planar or almost planar structures.

For a more detailed analysis, individual expanded experimental spectra and the corresponding theoretical calculated FC transition spectra have been juxtaposed. Displacement vectors of the most important normal coordinates are visualized in the ESI†. Note that in the following figures the energy ranges chosen according to the widths of the measured spectral structures and do not have the same energy scales.

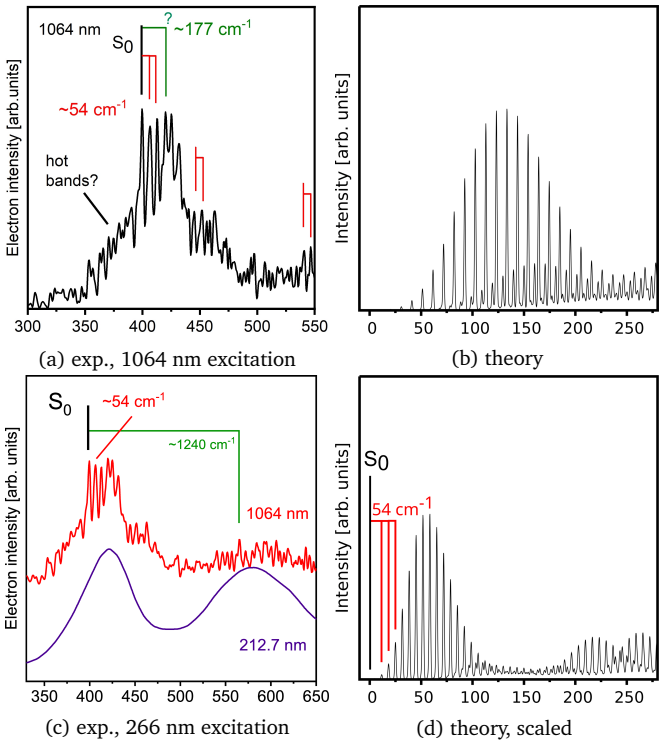

Fig. 12: p3P: Expanded experimental (in meV, with respect to the anion ground state) and calculated (in meV, with respect to the S_0 origin) spectra of the transition from the anion ground state to the S_0 state of the neutral p3P molecule. (a): experimental spectrum with detachment wavelength 1064 nm, (b) simulated FC spectrum (no adjustment) (c) PD-PE spectra recorded with 1064 and for comparison with 212.7 nm on an extended energy scale, (d) simulated FC-spectrum: The lowest torsional mode was adjusted to the experimental value. For further discussion, see text.

The experimental spectrum in Fig. 12a shows at the low-energetic side a smooth onset, then a steep rise at about 400 meV followed by some distinct peaks with spacings of about 54 cm^{-1} before the signal declines again. The width at half height of a

Table 2: Theoretical results for p3P: Coefficients (absolute values) of leading MO configurations, calculated vertical transition energies ($\Delta E_{\text{vert.}}$) at the S_0 geometry, calculated adiabatic transition energies ($\Delta E_{\text{adiab.}}$) and zero point corrected transition energies ΔE_{0--0} with respect to the S_0, experimental energies $\Delta E_{\text{exp.}}$ (this work only) and oscillator strengths f. In addition also calculated Dyson intensities σ for the photodetachment from the anion ground state D_0 are included. Energies are given in eV. Note, that for the experimental energy of S_0 the electron affinity (EA) is given. Experimentally not observed transitions are labelled as 'n.o.'

State		Configurations	$\Delta E_{\text{vert.}}$	$\Delta E_{\text{adiab.}}$	ΔE_{0--0}	$\Delta E_{\text{exp.}}$	f	σ
S_0	1^1A_g	0.97 GS			EA: 0.42	EA: 0.38	—	0.95
S_1	1^1A_u	0.95 $(H)^1(L)^1$	4.61	4.03	3.91	4.024	1.15	0.46
S_2	1^1B_u	0.67 $(H)^1(L+1)^1$	4.54	4.21	4.09	n.o.	0.00	0.17
		0.50 $(H-2)^1(L)^1$						
		0.28 $(H-4)^1(L)^1$						
S_3	1^1B_g	0.60 $(H-3)^1(L)^1$	4.63	4.50	4.34	n.o	0.00	0.18
		0.54 $(H)^1(L+3)^1$						
T_1	1^3A_u	0.91 $(H)^1(L)^1$	3.36	2.74	2.60	2.598	—	0.43
T_2	1^3A_g	0.65 $(H-1)^1(L)^1$	3.83	3.64	3.45	3.558	—	0.21
		0.60 $(H)^1(L+2)^1$						
T_3	2^3A_u	0.47 $(H-3)^1(L+3)^1$	4.17	4.04[a]	3.81[a]	3.93 (?)	—	0.09
		0.41 $(H-5)^1(L)^1$						
T_4	1^3B_u	0.69 $(H)^1(L+1)^1$	4.27	4.01	3.95	n.o.	—	0.16
		0.50 $(H-2)^1(L)^1$						
		0.24 $(H-4)^1(L)^1$						

[a] No minimum was found. In C_s symmetry, still a small imaginary frequency with –13 cm^{-1} is present at the saddlepoint.

fictive envelope of the complete S_0 structure would be about 50 meV. The important question now is where does the S_0 origin transition lie? Remember that the exact position of the S_0 origin affects the determination of the electron affinity and the derived energetic positions with respect to the neutral S_0 state. Since the S_0-S_1 origin transition energy of Murakami et al. has been determined by laser spectroscopy and is therefore very accurate (4.024 eV)[7] we can in return use this value and the position of the S_1 state, as measured in this work with respect to the anion ground state (4.403 eV), to identify the S_0 origin at about 380 meV above the anion ground state. With this procedure and considering our experimental long range error of 10-20 meV, the first peak of the steep rise could be tentatively attributed to the S_0 ground state origin. This would mean that the signals to the left are hot band transitions — presumably mostly due to excitations of the twist modes — which become especially intense for this transition to S_0 because of the present strong anion-to-S_0 geometry change and the resulting favourable FC factors. The hope was that this assignment might be confirmed by the corresponding FC calculations (see Fig. 12b). If one compares the experimental with the calculated FC spectrum, the peak spacings are roughly similar, however, the agreement of the peak intensities is rather poor: i) In the theoretical FC spectrum the width of the envelope over the vibrational fine structure is about 100 meV and therefore much broader than that of the experimental spectrum (50 meV) and ii) there are also no sudden intensity-changes in the calculated spectrum as observed in the experimental spectrum. Possible reasons for the deviations between experiment and theory could lie on the experimental or theoretical side. As mentioned in Sec. 1, resonant anion excited states could manipulate the anion-to neutral FC factors. The absorption spectrum of p3P anions published by Shida[30] shows only very small to vanishing absorption at 1064 nm, the wavelength used for photodetachment, which makes a strong influence on the vibronic intensities very improbable. This indicates that the theoretical treatment of the low-frequency torsional modes is inaccurate. To explain the deviation of the calculated FC spectra from the experiment, it should be noted that the harmonic oscillator model used to determine the FC spectra is not well suited for describing large-amplitude motions. Due to the large displacements in the torsional coordinates by about 30°, a long vibrational progression can be expected. Because the low-frequency torsion modes at 83 cm^{-1} (observed at 54 cm^{-1}) and 217 cm^{-1} (observed at 177 cm^{-1}), exhibit too high wavenumbers, the envelopes of the torsional potentials are too wide. If the frequency of the torsional mode is adjusted to the experimental value of 54 cm^{-1} in FC calculation (Fig. 12d), the vibrational structure is not only compressed because of the lower vibrational frequency, but also the FC factors change.

Since the equilibrium structures of the D_0 anionic ground state and the T_1 state of the neutral molecule both are quasi planar, the calculated FC spectrum are supposed to be more reliable. Indeed, Fig. 13 shows that the agreement between experiment (left side) and theory (right side) is quite good. The peak observed with a spacing of 225 cm^{-1} above the origin (see green line) can be identified with the calculated inter-ring vibration of 231 cm^{-1}. The next vibration identified in the experimental spectrum lies at 742

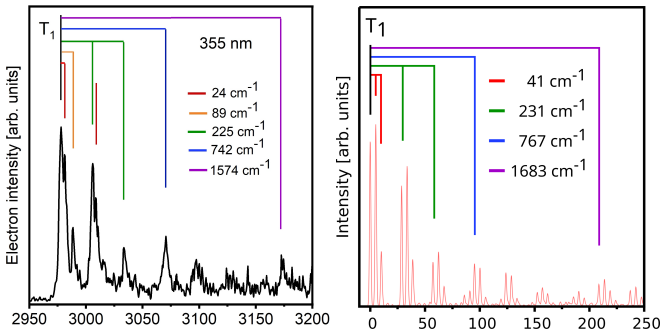

Fig. 13: Experimental (left side, in meV, with respect to the anion ground state) and calculated (right side, in meV, with respect to the S_0 origin) spectra of the transition to the T_1 state of p3P.

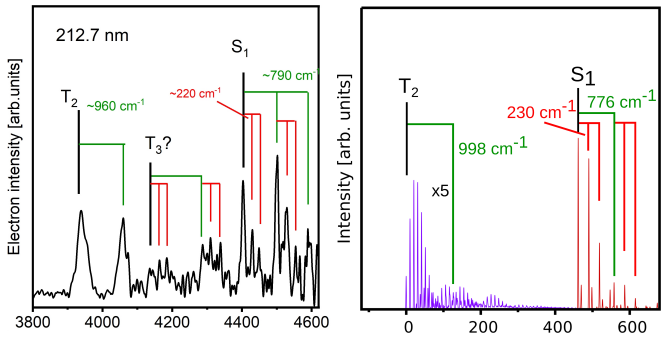

Fig. 14: Experimental (left side, recorded with one wavelength (212.7 nm)) and calculated (right side) spectra of the transitions to the T_2 and the S_1 states in p3P. Note that the T_3 state was omitted from the calculated spectrum because its proper minimum structure could not be determined.

cm^{-1} and corresponds nicely to the calculated collective phenyl-ring breathing mode with an energy of 767 cm^{-1}. The first two main peaks in the experimental spectrum have each two satellite peaks somewhat shifted to higher energies (red and orange lines), one directly in the shoulder of the first highest peak and another one at a distance of about 89 cm^{-1}. Because in the two three-fold structures the first peak and its neighbouring satellite peak are of similar height, so close in energy that they overlap, it is difficult to derive the underlying energetic spacing between the molecular vibronic states: The two peaks mainly overlap in the interval between them. By adding their signals, the appear to "attract" each other. Taking this effect into account, the spacing of the two corresponding vibronic levels should be considerably larger than the measured peak distance of 24 cm^{-1}. If one keeps this finding in mind and compares the three-dental structures (main peak with the two satellites) in the experimental spectrum with the corresponding three-peak structures in the theoretical spectrum, one recognizes a strong similarity and can, with high probability, assign the observed low-energetic satellites as quanta of the symmetric torsional mode with a calculated energy of 41 cm^{-1}. Since, in the experimental spectrum the position of the first overtone at 89 cm^{-1} might be not so much affected by the mentioned "peak attraction" effect, this would lead to a vibrational energy in one quantum of about 45 cm^{-1}). In conclusion, one can state that the spectrum of the transition to T_1 is very well reproduced by theory.

In Fig. 14 the expanded experimental PD-PES recorded with 212.7 nm and the corresponding calculated FC spectra of the spectral range covering the transition to T_2 up to the transition to S_1 is displayed. The experimental spectrum in Fig. 14 is a good example for the effect that the resolution of time-of-flight PES strongly depends on the electron excess energy: The closer the spectrum comes to the low-energy electron range (from left to right) the better the energy resolution becomes. The threshold law for photodetachment,[25] also called Wigner's threshold law, predicts an intensity loss for structures close to the detachment threshold. This holds especially true for the excitation to the S_1 state.

The experimental transition spectrum to T_2 essentially consists of two equally strong broad peaks with a spacing of 960 cm^{-1} (theoretical value 998 cm^{-1}) followed by two bunches of three-fold structures. The origin of the latter will be discussed below. We first concentrate of the two strong broad peaks in the transition spectrum to the T_2. They are both asymmetric and the second peak has clearly a second close side-peak. This indicates that also the first peak has a weak underlying satellite peak shifted slightly to the blue. At first glance, the calculated FC spectrum differs markedly from the experimental spectrum. It shows a comb-like peak structure with a small energy spacing of 83 cm^{-1} corresponding to a torsional mode. Note, however, that the resolution of the computed spectrum depends on the width of the Gaussisan damping function (here 5 cm^{-1} full width a half maximum) used in the Fourier transformation of the correlation function. The satellite peaks presumably arise from the excitation of a concertina-like stretching motion of the molecule along the C_2 symmetry axis with a frequency of 222 cm^{-1} in the computed spectrum. The comb of peaks starting 998 cm^{-1} above the 0–0 transition in the theoretical spectrum possibly corresponds to the second peak in the experimental spectrum, but has a much too low intensity in comparison to the spectrum on the left side. Obviously, the harmonic force calculations do not properly describe the properties of the T_2 state. This problem is closely connected with the failure to find the true minimum of the T_3 potential which undergoes a conical intersection with the T_2 potential. The non-adiabatic interactions between T_2 and T_3 distort the geometric structure in a way that only C_s symmetry is conserved and the rotation about the C_2 axis is no longer a symmetry operation.

The agreement between the experimental and the theoretical S_1 spectra is much better. The first three peaks in the experimen-

tal S_1 spectrum (spacing about 220 cm^{-1}) nicely correspond to the first three intense peaks in the theoretical spectrum (spacing 230 cm^{-1}). The repetition of this threefold structure shifted by 790 cm^{-1} (experimental value) is somewhat too weak in intensity in the theoretical spectrum (found at 776 cm^{-1} above the origin). It corresponds to an inter-ring C–C stretch vibration, which appears here as a result of the quinoidal reconstruction of the nuclear frame in the S_1 state. Interestingly, in the optical $S_0 \rightarrow S_1$ spectrum of Murakami et al.[7] the symmetric (62 cm^{-1}) and asymmetric (89 cm^{-1}) inter-ring torsion modes have been observed with long progressions. Both vibrations are not observed by us in the $D_0 \rightarrow S_1$ spectrum of Fig. 14) because the displacements in the torsional coordinates are very small and the excitation of these modes hence does not gain much intensity.

The two three-fold structures in-between T_2 and S_1 look so different in comparison to the spectral structures in T_2 and S_1 that they are tentatively attributed to the transitions to T_3. Interestingly, the small spacings of these close-lying sub-structures are similar to the distances of the peaks corresponding to the low-energy vibration in S_1, but their intensities are almost equal. An assignment of the three-fold structures to S_1 is excluded because of the experimentally determined energy for the S_1 origin by Murakami et al.[7]. Since the spacing between the two three-fold comb-like structures is similar to the spacing between the two strong peaks in T_2, one could argue that they correspond to T_2 and continue its peak sequence. This explanation is implausible since the peak structure in T_2 is too different for this. According to theory (see Table 2), T_3 is expected to lie below the S_1 origin and even the T_4 transition is close-by. The Dyson intensity for the photodetachment to T_3 is considerably weaker (0.09) than for the transition to T_2 (0.21), which is in qualitative agreement with the small intensity of the observed complex structure above T_2 (see Fig. 14). The PD-PE spectrum of the T_4 state (Dyson norm 0.16) is presumably buried beneath the S_1 bands because the two states are near degenerate according to the calculations. Unfortunately, the identity of these three-dental structures between T_2 and S_1 cannot be unambiguously clarified with the help of FC calculations, because T_3 undergoes a conical intersection with T_2 upon geometry optimization and the true minimum of its potential energy surface could not be located.

In conclusion, the comparison of the calculated to the experimental spectra of p3P shows excellent agreement for T_1 and S_1 and by this confirm the calculated geometric and electronic structures. The agreement between experiment and theory for the transitions to S_0 and T_2 is unfortunately only qualitative. The simulated FC spectrum for the transition to S_0 follows roughly the expectations insofar as it is a transition between planar and twisted structures, but the calculated progression is much too broad and long. As the simulated spectrum (see 12 (d)) with the adapted twist frequency shows, the differences between experiment and the FC-calculation seem to be due to the overestimation of the low-energetic frequencies in the calculation and presumably in addition due to anharmonicities in the torsional potentials of S_0, as proposed by[10], an effect neglected in the theoretical FC calculation by using harmonic potentials. The problems of the calculations to reproduce the experimentally observed peak intensities in the energy regime between the T_2 and S_1 origins are attributed to a conical intersection between the T_2 and T_3 potentials. The strong vibronic coupling in the neighbourhood of the intersection impedes a meaningful computation of spectral envelopes in a static approach and would require a quantum dynamical treatment which is, however, far beyond the scope of this work.

3.3.2 *para*-quaterphenyl (p4P)

The complete PD-PE overview spectrum of p4P in Fig. 2 is composed of three parts recorded with 266 nm and 355 nm. Astonishingly, in the energy range between T_1 and S_1 there is at first glance considerably less peak activity than in the spectrum of p3P. In the high-energetic range again the transitions to T_1 (neutral energy: 2478 $\pm$20 meV), T_2 (neutral energy: 3260 $\pm$20 meV) and S_1 (neutral energy: 3872 $\pm$20 meV) are observed. A small peak in front of S_1 might be the transition to T_3, an assignment which, however, needs further support by theory data. Interestingly, in contrast to the transition to S_0, the vibrational activities for the excited neutral states are weak in general. This holds especially true for the high-energetic vibrations.

In Table 3 the theoretical results are presented and compared to the experimental data. The calculated electron affinity is somewhat too high 703 meV (experimental: $\sim$620 meV), which is unexpected from a theoretical point of view, but has been observed for oligothiophenes[54] and other compounds[22] as well. The Dyson norm for the photodetachment of an electron from the singly occupied anion MO (LUMO in the nomenclature used here) has a value close to 1. The ratio of the Dyson intensities for the transitions to T_1 and to T_2 are about 2:1, in nice agreement with the spectrum recorded with 266 nm (not shown as a complete spectrum here). The transition to T_3 has a very low Dyson intensity of 0.12 (for comparison: the neighbouring transition to S_1 has a Dyson intensity of 0.44), which would qualitatively agree with the very small intensity of these peaks in the overview spectrum. the 0–0 transition energy of 3.55, determined in the DFT/MRCI calculations, supports the tentative assignment of T_3 closely below S_1.

In p4P, the singlet-coupled HOMO–LUMO excitation forms the first excited singlet state even in the FC region. The computed oscillator strength f of its optical $S_0 \rightarrow S_1$ transition is 1.67 and thus has considerably increased in comparison to p3P (f = 1.15). The nodal structure of the MOs involved in the $S_0 \rightarrow S_1$ transition is similar in both molecules (cp. Figs. 5 and 8). HOMO and LUMO both exhibit b symmetry with regard to the $C_2(z)$ symmetry axis. Hence, the transition moment for the $S_0 \rightarrow S_1$ transition lies, as in p3P, parallel to the long axis. The HOMO comprises seven nodal

Table 3: Theoretical results for p4P: Coefficients (absolute values) of leading MO configurations, calculated vertical transition energies ($\Delta E_{\text{vert.}}$) at the S_0 geometry, calculated adiabatic transition energies ($\Delta E_{\text{adiab.}}$) and zero point corrected transition energies $\Delta E_{N,0--0}$ with respect to the S_0, experimental energies $\Delta E_{\text{exp.}}$ (this work only) and oscillator strengths f for the excitation from S_0. In addition also calculated Dyson intensities σ for the photodetachment from the anion ground state D_0 are included. Energies are given in eV. Note, that the experimental energy of S_0 is the electron affinity (EA). Experimentally not observed transitions are labelled by 'n.o.'

State		Configurations	$\Delta E_{\text{vert.}}$	$\Delta E_{\text{adiab.}}$	$\Delta E_{N,0--0}$	$\Delta E_{\text{exp.}}$	f	σ
S_0	1^1A	0.96 $H^2(L)^0$		-	0.70	0.62	—	0.93
S_1	1^1B_1	0.94 $(H)^1(L)^1$	4.31	3.75	3.65	3.872	1.67	0.44
S_2	1^1B_2	0.66 $(H)^1(L+2)^1$	4.46	4.14	3.98	n.o.	0.00	0.15
		0.41 $(H-2)^1(L)^1$						
		0.35 $(H-4)^1(L)^1$						
S_3	1^1B_3	0.52 $(H)^1(L+3)^1$	4.49	[a]	[a]	n.o.	0.00	0.16
		0.42 $(H-3)^1(L)^1$						
		0.38 $(H-5)^1(L)^1$						
S_4	2^1A	0.66 $(H-1)^1(L)^1$	4.99	4.69	4.56	n.o.	0.00	0.23
		0.43 $(H)^1(L+1)^1$						
T_1	1^3B_1	0.89 $(H)^1(L)^1$	3.20	2.63	2.51	2.478	—	0.41
T_2	1^3A	0.64 $(H-1)^1(L)^1$	3.54	3.24	3.13	3.260	—	0.21
		0.60 $(H)^1(L+1)^1$						
T_3	2^3B_1	0.51 $(H-6)^1(L)^1$	3.94	3.86	3.55	3.771 (?)	—	0.12
		0.48 $(H-1)^1(L+1)^1$						
		0.44 $(H)^1(L+6)^1$						
T_4	1^3B_2	0.68 $(H)^1(L+2)^1$	4.19	3.94	3.79	n.o.	—	0.13
		0.40 $(H-2)^1(L)^1$						
		0.32 $(H-4)^1(L)^1$						

[a] No minimum was found in the calculations. At the converged structure still a small imaginary frequency is present.

planes perpendicular to this axis, the LUMO eight. This situation is similar to the wave function of a particle in a one-dimensional box, where subsequent wave functions only differ by one node and the selection rule is Δn is 1. As in p3P, the oscillator strengths for the transitions to the multiconfigurational S_2 and S_3 states are close to zero.

In the next figures, we compare the expanded experimental PD-PE spectra of some p4P transitions and compare them to the corresponding calculated FC spectra.

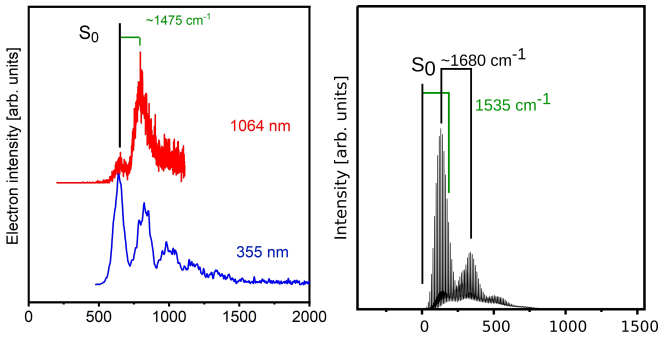

Fig. 15: p4P: Experimental (left side, detachment wavelengths 1064 nm and 355 nm) and calculated (right side) spectra of the transition to the S_0 state.

On the left side of Fig. 15, the PD-PE spectra of the transition to S_0, recorded with the wavelengths 1064 nm and 355 nm, are presented. The fact that the spectrum recorded with 266 nm and 212.7 nm (not shown here) look very similar in vibrational intensity to the spectrum recorded with 355 nm proves that the wavelength 1064 nm performs a resonant excitation of an anion-excited state which then decays via autodetachment. The p4P anion absorption spectrum of Shida in tetrahydrofuran[30] shows strong absorptions at 1220 nm and 1115 nm. The low-energy peak is presumably the origin transition of the excited state of the anion and the following peak is one of its vibronic states. The wavelength 1064 nm would be overlapping with the second peak at 1115 nm. In any case it is reasonable to assume that with 1064 nm a vibrational sub-structure of the anion-excited state, as detected by Shida, is resonantly excited at 1064 nm, with the consequence that it then preferentially autodetaches to a vibrationally excited state of the S_0 ground state. In order to prove and avoid this anion resonance we used the other detachment wavelengths such 355 nm (displayed in Fig. 15 (left side)). It shows a strong first peak followed by two or more peaks with spacings of about 1475 cm^{-1}. The spectrum recorded with 266 nm (considerably broader, and not shown) has very similar intensities and by this confirms that the PD-PES recorded with 355 nm is mainly the result of the direct anion-to-S_0 FC factors. The cor-

responding calculated FC spectrum is displayed in Fig. 15 (right side). It shows a dense peak structure with very small spacings of 88 cm^{-1} (inter-ring twist mode) which has a nearly Gaussian envelope. The width at half height of the envelope is about 100 meV and only slightly broader than the first peak in the experimental 355 spectrum. A second comb of low-energetic vibrations shifted by about 1535 cm^{-1} follows. These are combination bands with a high-energetic vibration (experiment: 1475 cm^{-1}, collective inter-ring stretch mode). The broader envelopes of the two structures in the FC spectrum in comparison to the experiment are–as in p3P–presumably also due to the overestimation of the force constant of the twist potential.

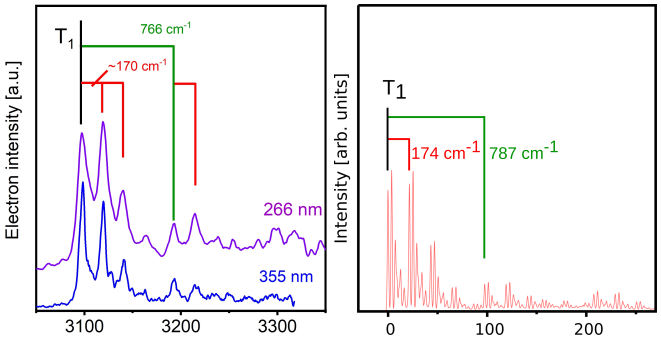

Fig. 16: Experimental spectra recorded with 355 nm and 266 nm (left side) and calculated (right side) FC spectra of the transition to the T_1 state in p4P. For discussion see text.

In Fig. 16 two experimental spectra and one calculated FC spectrum of the transition to T_1 are displayed. The two spectra agree well in the energetic positions and only slightly differ in intensities. This is an example showing that typically the spectra recorded with high excitation energies are not or not much influenced by anion-excited states. The observed mode with a frequency of 170 cm^{-1} can be assigned to a global stretching mode (calculated frequency: 174 cm^{-1}). The next observed mode with 766 cm^{-1} can be assigned to a collective breathing mode with a calculated frequency of 787 cm^{-1}. The most displaced mode, an antisymmetric torsional mode with a frequency of 30 cm^{-1}, which appears as a progression with three strong and two smaller peaks in the calculated spectrum, is not identified in the experimental spectrum. The reason is that in this energy range the energy resolution is not sufficient to resolve this vibration. If one, however, takes a close look on the first peak of T_1 one observes a small undulation in the rise of the peak and an asymmetry in the fall on the rear side (at 0.3 of the peak maximum) These two details could be indications for the presence of a substructure with spacings of 30 cm^{-1}. In general the agreement of the experimental and the calculated spectra is very good.

The expanded transition spectrum to T_2 is not shown here and has not been investigated by FC calculations because in its experimental spectrum no vibrational structure is observed.

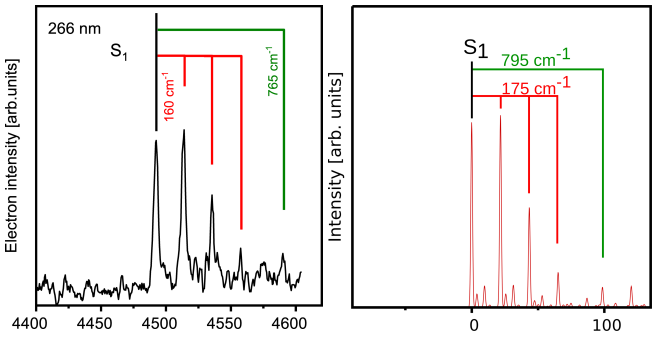

Fig. 17: p4P: Experimental (left side) and calculated (right side) spectra of the transition to the S_1 state.

In Fig. 17, the experimental and theoretical FC spectra of the transition to the S_1 state are juxtaposed. The first observed mode has an energy of 170 cm^{-1} in the experimental spectrum (left side) and can be identified with the calculated symmetric collective stretching mode along the molecular axis (calculated frequency: 175 cm^{-1}). The weakly observed mode with a frequency of 766 cm^{-1} presumably corresponds to the mode with the calculated frequency of 795 cm^{-1}, which is a collective ring breathing mode, at which especially the two inner phenyl rings participate. The intensity of the latter transition is presumably only so extremely small, because it is strongly affected by Wigner's threshold law.[25] The low-energetic torsion mode with a calculated energy of 78 cm^{-1} has a high displacement of 0.47 and appears in the calculated spectrum as a narrow progression of 4 peaks. This mode is not found and assigned in the experimental spectrum, presumably because of the low PE energy resolution in this energy range. Only by a close look at the first two strong peaks of the spectrum recorded with 355 nm, one finds small asymmetries at half height on their front side and at one third on their rear side. These shoulders may be caused by the presence of the four peaks of the 78 cm^{-1} vibration. Over all, for the transition to the S_1 the agreement between experiment and theory is considered very good.

In conclusion, the EA value, the oscillator strength and the energetic positions of the electronic states follow the classical expectations which are predicted for an increase in the π-conjugation length. The agreement of the calculated FC spectra with the experiment is rather good and the orbital and geometry calculations provide an understanding that in most of the electronic states bond length changes as well as twist angle changes occur, which can be, surprisingly, localized on the inner or the outer parts of the p4P molecule.

3.3.3 *para*-quinquephenyl (p5P)

As for p4P, the complete PD-PE overview spectrum of p5P (Fig. 2) is composed of three sub-spectra and the two energy scales are the same. Interestingly, except for the very broad transition to the S_0, the appearance of the spectrum of p5P is very similar to that of p4P. The right side of the spectrum is rather simple to explain. The transitions to T_1 (neutral energy: 2340 ±50 meV), T_2 (neutral energy: 3038 ±50 meV) and S_1 (neutral energy: 3653 ±50 meV) are observed. A very small additional structure in front of S_1 is found which could be tentatively assigned to T_3.

The ratio of the Dyson intensities of the transitions to T_3 and to S_1 are 0.13/0.44 = 0.29. This small value in tendency agrees with the small intensity of the structure in front of S_1, which was tentatively attributed to T_3. Note that the energetic position of this small structure is in agreement with the theoretical calculations as well.

The calculated value for the $S_0 \rightarrow S_1$ oscillator strength f is 2.17 and has again increased in comparison to p3P (f = 1.15) and p4P (f = 1.67). It seems that the oscillator strength increases by about 0.5 per added phenyl unit. The shapes of the MOs involved in the $S_0 \rightarrow S_1$ transition of p5P are still very similar to those in p3P (cp. Figs. 5 and 11). HOMO and LUMO both change sign upon rotation about the C_2 axis. With regard to the reflection at the σ_h mirror plane perpendicular to the long molecular axis, HOMO is antisymmetric and LUMO symmetric. As in the other two ppPs, the electric dipole transition moment for the optical $S_0 \rightarrow S_1$ transition lies parallel to the long axis. HOMO now has nine nodal planes perpendicular to the symmetry axis and LUMO ten (Δn = 1), as needed for an intense transition in the particle-in-the-box model.

In Fig. 18 (left) we present expanded experimental PD-PE spectra (detachment wavelengths 1064 nm (red), 532 nm (green) and 266 nm (violet)) of p5P. The vibrational peak patterns are very different, although the peak positions seem to be, within the experimental accuracy, the same in all three spectra. The reasons for the strong rise of the second peak in the PD-PE spectrum recorded with 1064 nm and the many intense peaks in the spectrum recorded with 532 nm are obviously— similar as in p4P — due to resonant photoabsorptions channels for the detachment wavelengths 1064 nm and 532 nm in the anionic species of p5P. Unfortunately no absorption spectrum exists for p5P anions, which could have directly proven the presence of two resonances. In the following, we tentatively take the first strong transition in the 266 nm spectrum as the S_0 origin (EA = 840 ±20 meV).

The calculated transition spectrum to S_0 (Fig. 18 right) shows very dense combs of peaks with a spacing which corresponds to a symmetric twist mode (calculated energy: 90 cm^{-1}). The envelopes of these twist mode peaks reproduce roughly the structures of the first three peaks in the experimental spectrum recorded with 266 nm. As in p3P and p4P also here the envelope in the theoretical spectrum is somewhat broader than the peak width in the 266 nm spectrum. The high-energetic spacing between the two comb of peaks in the experimental spectrum is about 1420 cm^{-1} which best agrees with a collective stretching mode (calculated energy: 1338 cm^{-1}).

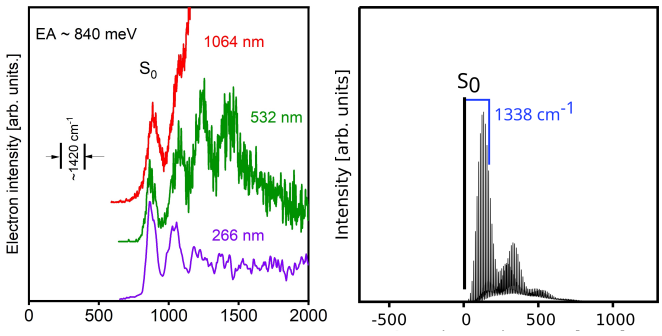

Fig. 18: p5P: Experimental spectra (left side) and the corresponding calculated spectrum (right side) of the transition to S_0 state. Three experimental spectra recorded with the wavelengths 1064 nm, 532 nm and 266 nm are shown. Note the different vibronic peak intensities in the three spectra. Presumably only the spectrum recorded with 266 nm contains intensities of the vibronic states, which are given by the anion-to-S_0 FC factors. For discussions see text

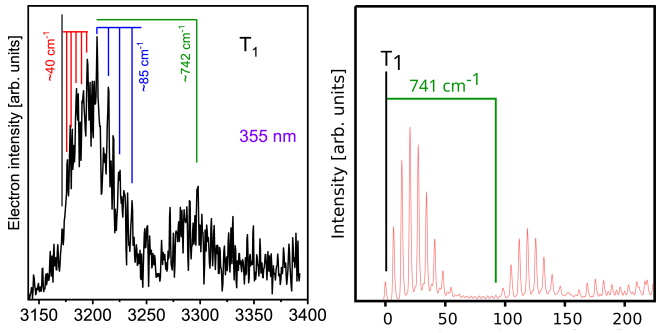

Fig. 19: Experimental spectrum (left side) and the calculated spectrum (right side) of the transition to the T_1 state in p5P. For explanations see text.

In Fig. 19, the experimental spectrum of the transition to T_1 of p5P, recorded with 355 nm (left side), and the calculated FC spectrum (right side) are displayed. Note that in the experimental spectrum the origin transition seems to be not the highest peak. Besides a comb of small peaks with a spacing of ∼40 cm^{-1} in the first part of the spectrum at the blue side some peaks with spacings of ∼85 cm^{-1} are observed. In addition, a vibration with an energy of about 742 cm^{-1} is present. A look at the FC simulation shows that a low-frequency mode of 55 cm^{-1} has the highest displacement and forms a comb of nine vibronic close-lying transitions. It should correspond to the observed peak spacing of about

Table 4: Theoretical results for p5P: Coefficients (absolute values) of leading MO configurations, calculated vertical transition energies ($\Delta E_{\text{vert.}}$) at the S_0 geometry, calculated adiabatic transition energies ($\Delta E_{\text{adiab.}}$) and zero point corrected transition energies $\Delta E_{N,0--0}$ with respect to the S_0, experimental energies $\Delta E_{\text{exp.}}$ (this work only) and oscillator strengths f for the excitation from S_0. In addition calculated Dyson intensities σ for the photodetachment from the anion ground state D_0 are included. Energies are given in eV

State		Configurations	$\Delta E_{\text{vert.}}$	$\Delta E_{\text{adiab.}}$	$\Delta E_{N,0--0}$	$\Delta E_{\text{exp.}}$	f	σ
S_0	1^1A_g	0.95 GS			0.88	0.84	—	0.93
S_1	1^1A_u	0.92 $(H)^1(L)^1$	4.13	3.59	3.49	3.65	2.17	0.44
T_1	1^3A_u	0.86 $(H)^1(L)^1$	3.10	2.56	2.40	2.34	—	0.39
T_2	1^3A_g	0.63 $(H\text{-}1)^1(L)^1$	3.33	3.02	2.94	3.04	—	0.20
		0.60 $(H)^1(L+1)^1$						
T_3	2^3A_u	0.51 $(H\text{-}2)^1(L)^1$	3.70	3.58	3.41	3.56 (?)	—	0.13
		0.50 $(H\text{-}1)^1(L+1)^1$						
		0.46 $(H)^1(L+5)^1$						

40 cm^{-1}, which is not fully resolved, at the rise of the hump. If one takes the envelope of the peaks in the calculated spectrum, it roughly fits the experimental features. The reason for the appearance of the measured peak spacings of 85 cm^{-1} appearing on the blue side of the hump in the experimental spectrum remains unclear. They could be either i) due to another torsional mode, for example the second torsional mode (calculated: 82 cm^{-1}) or ii) due to a quartic torsional potential when overcoming a certain threshold energy. The observed mode at about 742 cm^{-1} (measured between two well identified combination band peaks) is in an astonishing agreement with the calculated FC-active mode at 741 cm^{-1}. In conclusion, the calculated FC spectrum reasonably well agrees with the experimental spectrum. In comparison to the corresponding p3P and p4P spectra — the transition to T_1 is relatively broad in p5P, presumably due to the increase of vibrational degrees of freedom. A resonant excitation to an anion-excited state with 355 nm seems not to apply here since the spectrum recorded with 266 nm (not shown here) is also broad.

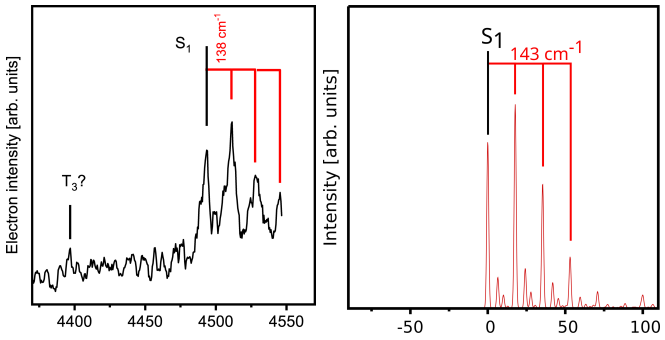

Fig. 20: Experimental spectrum (left side) and calculated spectrum (right side) of the transition to the S_1 state in p5P For assignments see text.

In the S_1 state, the geometry difference with respect to the D_0 structure are less pronounced than in the T_1 state. In the sharp PD-PE spectrum of S_1 (Fig. 20) four quanta of a progression of a vibration with an energy of about 138 cm^{-1} are observed. Since the S_1 state lies very close to the detachment energy of the laser wavelength 266 nm, the intensities of the latter peaks may be affected by Wigner's threshold law[25] and may be smaller than given by the FC factors. The observed mode with an energy of 138 cm^{-1} agrees well with with a global stretch mode calculated to have an energy of 143 cm^{-1}. Also the agreement between the intensities in the experimental and the calculated spectrum is very good.

The transition to T_2 is not shown here because — as for the T_2 in the spectrum of p4P — also in p5P no vibrational structure is observed.

4 Summary and conclusions

In this work, it was possible to record and assign PD-PE spectra of p3P, p4P and p5P. The experimental PD-PE spectra are partly vibrationally resolved and provide — in combination with calculated FC spectra — valuable information on the geometrical structures of the investigated ppPs in their lowest electronic states. No indications for spectral differences between the different possible rotamers have been found in the experimental spectra. For most of the electronic states the calculations are qualitatively confirmed by the experimental results, thus strengthening the credibility of the theoretical data. Dyson norms have been evaluated at the DFT/MRCI level of theory to estimate the individual photodetachment probabilities. For high kinetic energies of the photoelectron, the ratios of the Dyson norms compare well with measured photodetachment intensities. The agreement is less satisfactory for slow photoelectrons. Wigner's threshold law for photodetachment[25] predicts an intensity loss for structures close to the detachment threshold. To model this effect, the overlap between the wavefunction of the outgoing photoelectron and the ionization continuum would have to be taken into account, which is, however, beyond the scope of this work.

The calculations show that the character of the optical $S_0 \rightarrow S_1$ transition is the same in all molecules: The electric dipole transition moment is parallel to the long molecular axis. The calculated oscillator strengths increase almost linearly with increasing molecular length: p3P: $f = 1.15$, p4P: $f = 1.67$ and p5P: $f = 2.17$

somewhat smaller than the values calculated from experimental data (p3P: 2.060; p4P: 2.360; p5P: 2.600)[12]. Interestingly, a saturation of f with the molecular length is obviously not occurring in the investigated small ppPs as the oscillator strength increases by about 0.5 per added phenyl unit (experimentally derived increase per phenyl unit: 0.3[12]). The MOs involved in the $S_0 \rightarrow S_1$ transition, i.e., HOMO and LUMO, are similar in shape in all investigated ppPs (Figs. 5, 8, 11): The HOMO exhibits 2n–1 nodal planes perpendicular to the long molecular axis, n–1 of them cutting the inter-ring C–C bonds, where n is the number of phenyl rings in the molecule. The LUMO has exactly one additional nodal plane, thus shifting the pattern of double and single bonds by one unit along the C_2 symmetry axis. This pattern complies with the $\Delta n = \pm 1$ selection rule for electric dipole transitions in the particle-in-the-box model and explains the high oscillator strengths. This agrees well with the findings of Nijegorodov et al.[12], who reported that the fluorescence quantum yields increase and as a consequence the S_1 lifetimes decrease with the increasing number of phenyl rings in the ppPs. Our theoretical analysis supports this explanation that the S_1 lifetimes are exclusively determined by the high oscillator strengths of the $S_1 \rightarrow S_0$ transitions.

In all investigated ppP molecules, definitively two or even possibly three (as calculated and tentatively assigned) triplet states lie below S_1. Typically, in a molecule with such an electronic state energy scheme, one would expect high rates for intersystem crossing (ISC) transitions from the S_1 state to the triplet manifold. However, due to the absence of heteroatoms in the molecules, spin–orbit coupling (SOC) between the excited states is obviously so small that ISC cannot compete against the rapid radiative deactivation. The radiative lifetimes of the S_1 states are so short (below 2 ns)[3,12] that they seem to prevent efficiently all ISC processes.

In a former paper, we investigated the singlet–triplet splittings in azulene and found that the energy separation between two states of the same spatial MO configuration strongly depends on the overlap between the electron densities in the involved MOs.[21] The question is, whether this concept also applies for the ppPs investigated in this work. Since the oscillator strength is very high in the investigated ppPs — which is only possible if the orbital densities strongly overlap[21] — their S_1–T_1 energy gap should be large. In addition, it is expected that the S-T gap decreases with the length of the ppP since in longer molecular chains the two unpaired electrons are more and more efficiently able to avoid each other, thus weakening their interactions. Interestingly the experimentally observed T_1-to-S_1 splitting decreases very slowly in this molecular series (1.43 eV (p3P) over 1.39 eV (p4P) to 1.31 eV(p5P)) whereas the quantum chemical calculations predict much faster decreases of the 0–0 splittings (1.31 eV (p3P) over 1.14 eV (p4P) to 1.09 eV(p5P)). A similar trend results if the vertical S–T DFT/MRCI energy gaps at the respective ground state geometry (1.25 eV (p3P) over 1.11 eV (p4P) to 1.03 eV(p5P)) are compared. Hence, a strong impact of the molecular geometry on the S-T gap can be excluded. Rather, the fact that the S_1–T_1 energy gap is more and more underestimated as the chain length grows points towards a more general problem of the applied quantum chemical methods. If the S_0 energy is used as common reference, the adiabatic S_1 energies reproduce the experimental excitation energies quite well whereas the adiabatic T_1 energies lie too high. Application of ZPVE correction changes this picture. For all three compounds, it reduces the excitation energies of the T_1 and S_1 states. As a result, the energetic positions of the T_1 0–0 transitions match the experimental values almost perfectly whereas the 0–0 energies of the S_1 states appear to be underestimated by about 0.1-0.2 eV, i.e., well within the error bars of the DFT/MRCI method employing the R2022 Hamiltonian[40]. The number of samples (3 in this case) is, however, too small for a valid statistical analysis. Forthcoming investigations on other molecules with extended π-systems will have to show whether the observed deviation is systematic or coincidental.

In this work, we could show that the twist angles between the phenyl moieties and the bond lengths of the inter-ring C–C bonds are correlated. While the S_1 and T_1 states of the neutral molecule are practically planar in p3P, the quinoidal structure in the S_1 and T_1 states of p5P is essentially confined to the innermost three phenyl rings. The twist angles of the terminal rings are considerably larger than those of the central rings in the S_1 and T_1 states of this compound. We interpret these findings in terms of competing forces: While in general the H–H repulsion between neighbouring phenyl units stays the same, the effect of an electron in an orbital with strong bonding contributions in the inter-ring C–C bonds (here LUMO) washes out, because in a large-sized molecule the electron density is distributed over more atoms and bonds, thus less affecting individual bonds.

If one lists the EA values of the ppPs, still no saturation effect with regard to the number of phenyl rings (n) is found: EA(p3P) = 380 $\pm$20 meV (theor.: 417 meV), EA(p4P) = 620 $\pm$20 meV (theor.: 702 meV) and EA(p5P) = 840 $\pm$20 meV (theor. = 882 meV). The increase of the EA per phenyl ring is about 240 meV when going from n = 3 to n = 4 and about 220 meV when going from n = 4 to n = 5. There is obviously some decrease in the increment which has to be added to the EA if an additional phenyl ring is attached. This obviously means that the EA would still considerably increase for longer ppPs. Such a high EA for long ppPs would explain the experimental findings of Yuan et al.[55]. By AFM and STM methods, these authors observed twisted (benzoid) and planar (quinoid) ppP structures for long ppPs on surfaces. Interestingly, completely benzoid, completely quinoid but also mixed chains were found, where in one chain quinoid and benzoid sections exist. The observed dependence of the occurrence of the quinoid structure on the work function of the underlying surface suggested to the authors that the benzoid sections

of the ppP chains are charged. High EAs of longer ppP chains, as proposed by our work in combination with the observation of Yuan et al. that lower work functions favour quinoid structures, indicate that there might be a negative charge on the quinoid sections in ppP chains, in agreement with our finding that the anion is almost planar and the phenyl rings have partly a quinoid structure. The negative quinoid ppP section forms together with the surface a "surface-to-molecule" charge transfer (CT) state. Note that in such a case the charge separation has to occur only over a small distance. If the work function of the surface is not too high, this CT state is obviously energetically very close to the neutral ground state (neutral surface and neutral adsorbed molecule).

Conflicts of interest

There are no conflicts to declare.

Acknowledgements

The authors gratefully acknowledge financial support by the Deutsche Forschungsgemeinschaft (DFG, German Research Foundation) through MA 1051/19-1 and 396890929/GRK 2482.

References

1 K. Kato, *Japan J. Appl. Phys.*, 1972, **11**, 912–913.
2 G. A. Abakumov, V. V. Padeev, R. V. Khokhlov and A. P. Simonov, *Spectr. Lett.*, 1975, **8**, 651–667.
3 B. Godard and O. de Witte, *opt. Comm.*, 1976, **19**, 325–328.
4 H. Bücher and W. Chow, *Appl. Phys.*, 1977, **13**, 267–269.
5 D. J. Schneider, D. A. Landis, P. A. Fleitz, J. M. Kauffman and R. N. Steppel, *Laser Chem.*, 1991, **11**, 49–62.
6 C. J. Seliskar, D. A. Landis, J. M. Kauffman, R. N. Aziz, M. A. Steppel, C. J. Kelly, Y. Qin and A. Chiorghis, *Laser Chem.*, 1993, **13**, 9–28.
7 J. Murakami and M. Okuyama, K. Ito, *Bull. Chem. Soc. Jpn.*, 1982, **55**, 3422–3423.
8 I. Baraldi and G. Ponterini, *J. Mol. Struct. (Theochem)*, 1985, **122**, 287–298.
9 S. Denicke, K.-H. Gericke, A. Smolin, P. S. Shternin and O. S. Vasyutinskii, *J. Phys. Chem. A*, 2010, **114**, 9681–9692.
10 G. Heimel, M. Daghofer, J. Gierschner, E. J. W. List, A. C. Grimsdale, K. Müllen, D. Beljonne, J.-L. Brédas and E. Zojer, *J. Chem. Phys.*, 2005, **122**, 054501–1–11.
11 V. Lukeš, A. J. A. Aquino, H. Lischka and H.-F. Kauffmann, *J. Phys. Chem. B*, 2007, **111**, 7954–7962.
12 N. Nijegorodov, W. Downey and M. Danilov, *Spectrochem. Acta Part A*, 2000, **56**, 783–793.
13 R. Englman and J. Jortner, *Mol. Phys.*, 1970, **18**, 145–164.
14 N. A. Borisevich, S. M. Kazakov, É. Kolesnik, A. V. Kukhto, A. I. Mit'skovets, D. V. Murtazaliev and O. V. Khristoforov, *J. Appl. Spectr.*, 2001, **68**, 447–454.
15 X. Cai, M. Sakamoto, M. Hara, S. Tojo, K. Kawai, M. Endo, M. Fujitsuka and T. Majima, *J.Phys.Chem.A*, 2004, **108**, 9361–9364.
16 P. G. Wendthold, J. Hu, R. R. Squires and L. W. C., *J. Am. Chem. Soc.*, 1996, **118**, 475–476.
17 T. R. Taylor, R. T. Bise and D. M. Asmis, K. R. Neumark, *Chem Phys. Lett.*, 1999, **301**, 413–416.
18 R. Busani, M. Folkers and O. Cheshnovsky, *Phys, Rev. Lett.*, 1998, **81**, 3836–3839.
19 M. Kohno, S. Suzuki, H. Shiromaru and Y. Achiba, *J. Chem. Phys.*, 1999, **110**, 3781–3784.
20 J. Schiedt and R. Weinkauf, *Chem. Phys. Lett.*, 1997, **266**, 201–205.
21 S. Vosskötter, P. Konieczny, C. M. Marian and R. Weinkauf, *Phys. Chem. Chem. Phys.*, 2015, **17**, 23573–23581.
22 J. Meissner, B. Kosper, C. M. Marian and R. Weinkauf, *Phys. Chem. A*, 2021, **125**, 8777–8790.
23 T. Nakamura, N. Ando, Y. Matsumoto, S. Furuse, M. Mitsui and A. Nakajima, *Chem. Lett.*, 2006, **35**, 888–889.
24 G. R. Kinsel and M. V. Johnston, *Int. J. Mass Spectrom. Ion Processes*, 1989, **91**, 157–176.
25 E. P. Wigner, *Phys. Rev.*, 1948, 1002–1009.
26 J. Schiedt and R. Weinkauf, *J. Chem. Phys.*, 1999, 304–314.
27 C. R. Sagan, C. S. Anstöter, M. Thodika and S. Wilson, K. D. Matsika, *J. Phys. Chem. Lett.*, 2022, **13**, 10245–10252.
28 B. Jalehdoost, A. von Issendorff, *J. Chem. Phys.*, 2023, **158**, 194302–1–11.
29 L. G. Christophorou, J. G. Carter and A. A. Christodoulides, *Chem. Phys. Lett.*, 1969, **3**, 237–240.
30 T. Shida, *Phys. Science Data*, 1988, **34**, 1–308.
31 E. Luc-Koenig, C. Morillon and J. Vergès, *Phys. Scr*, 1975, **12**, 199.
32 D. Hanstorp and M. Gustafsson, *J. Phys B: At. Mol. Opt. Phys.*, 1992, **25**, 1773.
33 R. J. Peláez, C. Blondel, C. Delsart and C. Drag, *J. Phys B: At. Mol. Opt. Phys.*, 2009, **42**, 125001.
34 M. J. Frisch, G. W. Trucks, H. B. Schlegel, G. E. Scuseria, M. A. Robb, J. R. Cheeseman, G. Scalmani, V. Barone, G. A. Petersson, H. Nakatsuji, X. Li, M. Caricato, A. V. Marenich, J. Bloino, B. G. Janesko, R. Gomperts, B. Mennucci, H. P. Hratchian, J. V. Ortiz, A. F. Izmaylov, J. L. Sonnenberg, D. Williams-Young, F. Ding, F. Lipparini, F. Egidi, J. Goings, B. Peng, A. Petrone, T. Henderson, D. Ranasinghe, V. G. Zakrzewski, J. Gao, N. Rega, G. Zheng, W. Liang, M. Hada, M. Ehara, K. Toyota, R. Fukuda, J. Hasegawa, M. Ishida, T. Nakajima, Y. Honda, O. Kitao, H. Nakai, T. Vreven, K. Throssell, J. A. Montgomery, Jr., J. E. Peralta, F. Ogliaro, M. J. Bearpark, J. J. Heyd, E. N. Brothers, K. N. Kudin, V. N. Staroverov, T. A. Keith, R. Kobayashi, J. Normand, K. Raghavachari, A. P. Rendell, J. C. Burant, S. S. Iyengar, J. Tomasi, M. Cossi, J. M.

Millam, M. Klene, C. Adamo, R. Cammi, J. W. Ochterski, R. L. Martin, K. Morokuma, O. Farkas, J. B. Foresman and D. J. Fox, *Gaussian 16, Revision A.03*, 2016, Gaussian Inc. Wallingford CT.

35 J. P. Perdew, K. Burke and M. Ernzerhof, *Phys. Rev. Lett.*, 1996, **77**, 3865–3868.

36 C. Adamo and V. Barone, *J. Chem. Phys.*, 1999, **110**, 6158–6170.

37 A. Schäfer, H. Horn and R. Ahlrichs, *J. Chem. Phys.*, 1992, **97**, 2571–2577.

38 S. Grimme and M. Waletzke, *J. Chem. Phys.*, 1999, **111**, 5645–5655.

39 C. M. Marian, A. Heil and M. Kleinschmidt, *WIREs Comp. Mol. Sci.*, 2019, **9**, e1394.

40 D. Dombrowski, T. Schulz, M. Kleinschmidt and C. M. Marian, *J. Phys. Chem. A*, 2023, **1127**, 2011–2025.

41 C. Lee, W. Yang and R. G. Parr, *Phys. Rev. B*, 1988, **37**, 785–789.

42 A. D. Becke, *J. Chem. Phys.*, 1993, **98**, 1372–1377.

43 *TURBOMOLE V7.5.1 2021, a development of University of Karlsruhe and Forschungszentrum Karlsruhe GmbH, 1989-2007, TURBOMOLE GmbH, since 2007; available from* `http://www.turbomole.com`.

44 F. Weigend, M. Häser, H. Patzelt and R. Ahlrichs, *Chem. Phys. Lett.*, 1998, **294**, 143–152.

45 M. Etinski, J. Tatchen and C. M. Marian, *J. Chem. Phys.*, 2011, **134**, 154105.

46 M. Etinski, J. Tatchen and C. M. Marian, *Phys. Chem. Chem. Phys.*, 2014, **16**, 4740–4751.

47 M. Spanner, S. Patchkovskii, C. Zhou, S. Matsika, M. Kotur and T. C. Weinacht, *Phys. Rev. A*, 2012, **86**, 053406.

48 W. Arbelo-González, R. Crespo-Otero and M. Barbatti, *J. Chem. Theory Comput.*, 2016, **12**, 5037–5049.

49 M. L. Vidal, A. I. Krylov and S. Coriani, *Phys. Chem. Chem. Phys.*, 2020, **22**, 2693–2703.

50 B. N. C. Tenorio, A. Ponzi, S. Coriani and P. Decleva, *Molecules*, 2022, **27**, 1203.

51 E. Morikawa and M. Kotani, *Z. Naturforsch.*, 1980, **35a**, 823–827.

52 C. M. Marian and N. Gilka, *J. Chem. Theory Comput.*, 2008, **4**, 1501–1515.

53 E. Artacho, M. Rohlfing, M. Côté, P. D. Haynes, R. J. Needs and C. Molteni, *Phys. Rev. Lett.*, 2004, **93**, 116401.

54 R. Weinkauf, L. Lehr, E. W. Schlag, S. Salzmann and C. M. Marian, *Phys. Chem. Chem. Phys.*, 2008, **10**, 393–404.

55 B. Yuan, C. Li, Y. Zhao, O. Gröning, X. Zhou, P. Zhang, D. Guan, Y. Li, H. Zheng, C. Liu, Y. Mai, P. Liu, W. Ji, J. Jia and S. Wang, *J. Am. Chem. Soc.*, 2020, **142**, 10034–10041.

Unable to Convert Image

The dimensions of this image (in pixels) are too large to be converted. For this image to convert, the total number of pixels (height x width) must be less than 40,000,000 (40 megapixels).

Electronic Supplementary Material (ESI) for PCCP:

Electron affinities and lowest triplet and singlet state properties of *para*-oligophenylenes (n=3-5): Theory and experiment

Timo Schulz‡,[a] Paul Konieczny‡,[a] Dennis R. Dombrowski,[b] Simon Metz,[a]
Christel M. Marian*[a]¶ and Rainer Weinkauf*[b]¶

Contents

S1 Further Computational Details

- If not noted otherwise, all geometries were optimized on the PBE0/TZVP level of theory.
- The Tamm-Dancoff approximation was used in the optimization of excited triplet state geometries.
- For all DFT/MRCI calculations the one-particle basis was generated with BHLYP/TZVP and the R2022 Hamiltonian with the standard parameter set was used. For p3P and p-quinquephenyl 6 roots in the totally symmetric and 5 in every other irreducible representation were solved. For p4P 11 roots in the totally symmetric and 10 in every other roots were solved.
- For the first run, a selection threshold of 0.8 E_H was used to truncate the CI-expansion.
- For the second run, the selection threshold was increased to 1.0 E_H.
- The VIBES calculations were done in internal coordinates, 65536 grid points and a time interval of 3000 fs. The temperature was set to 10 K. The damping funciton was set to 100 cm^{-1}.
- For the VIBES calculations with less damping 1048576 grid points and a time interval of 10000 fs were used. The damping function was reduced to 5 cm^{-1}.

S2 p3P

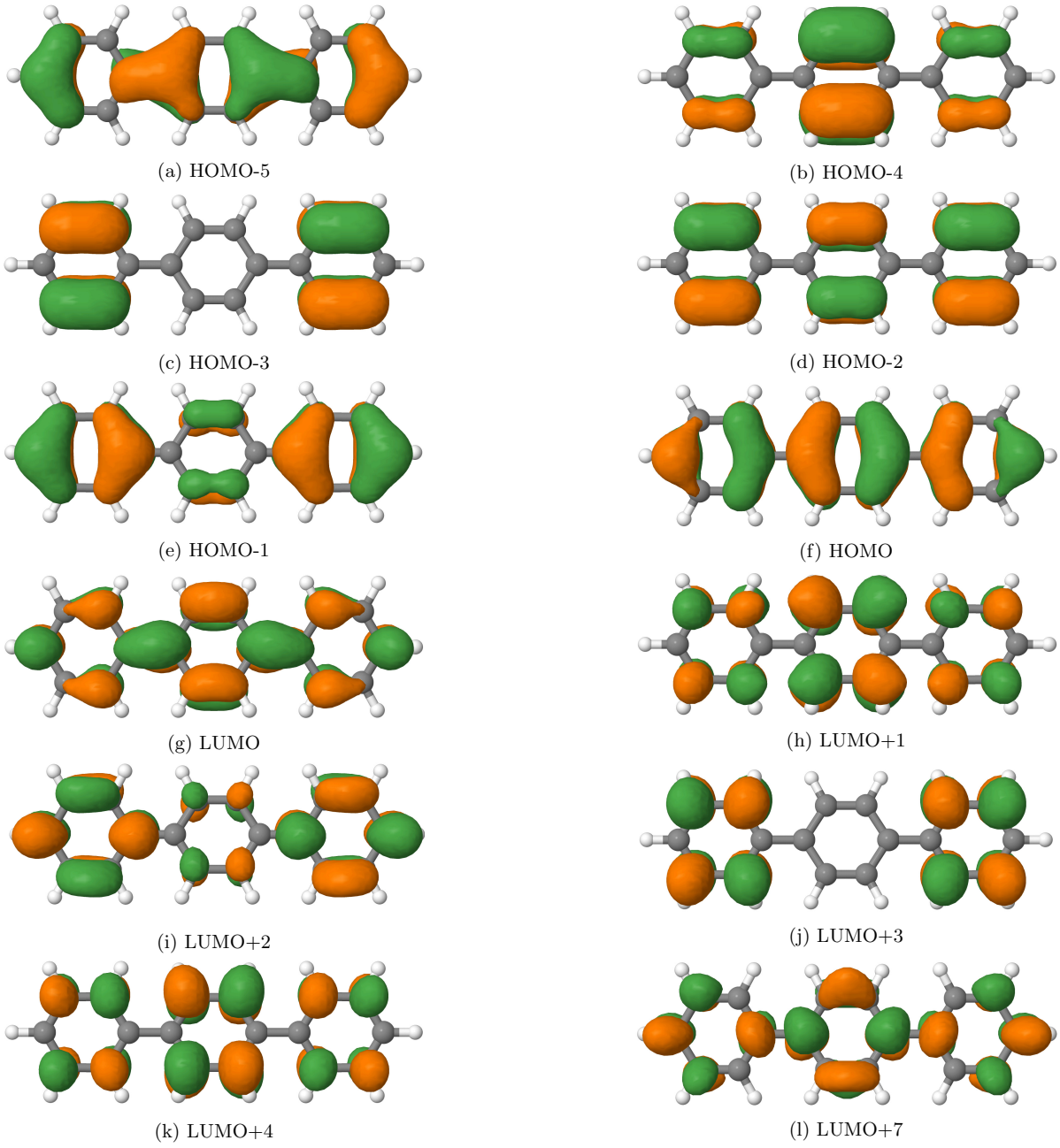

(a) HOMO-5 (b) HOMO-4

(c) HOMO-3 (d) HOMO-2

(e) HOMO-1 (f) HOMO

(g) LUMO (h) LUMO+1

(i) LUMO+2 (j) LUMO+3

(k) LUMO+4 (l) LUMO+7

Figure S1: Important molecular orbitals at the anion ground state geometry of p3P.

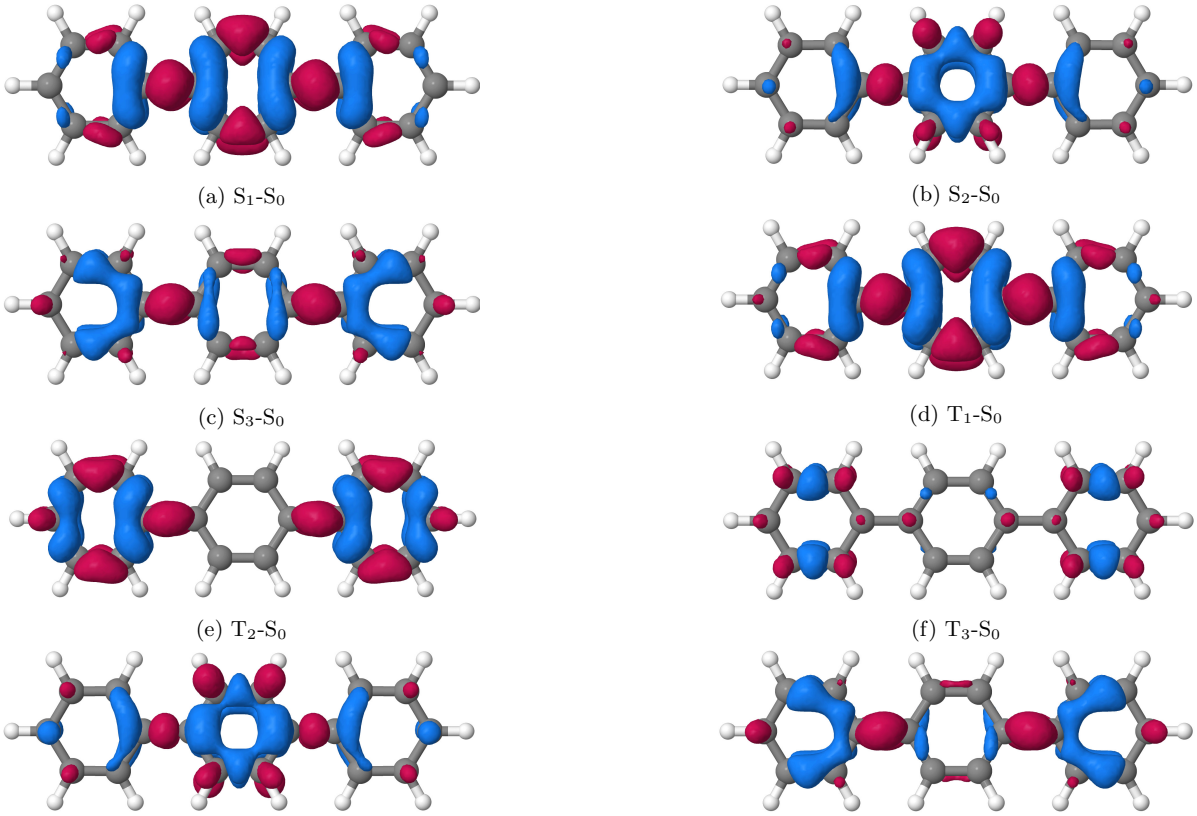

(a) S_1-S_0 (b) S_2-S_0 (c) S_3-S_0 (d) T_1-S_0 (e) T_2-S_0 (f) T_3-S_0 (g) T_4-S_0 (h) T_5-S_0

Figure S2: Difference densities (± 0.001) between the excited states and the neutral ground state at the anion ground state geometry of p3P. Blue coloured areas indicate a loss of electron density in the excited state, red coloured areas a gain.

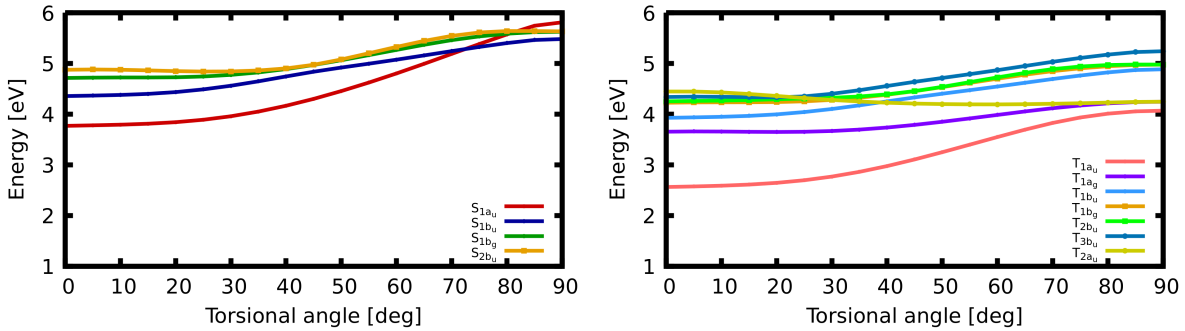

Figure S3: TDDFT scan of the symmetric torsion of singlet and triplet states of p3P. The D_0 geometry was used for the unrelaxed scan from 0° to 90°.

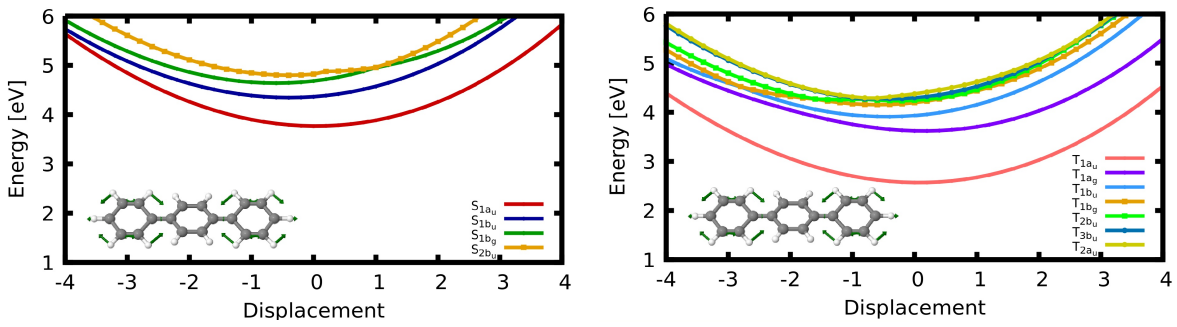

Figure S4: TDDFT scan of singlet and triplet states along the symmetric C–C normal mode of p3P. The D_0 geometry was used for the unrelaxed scan.

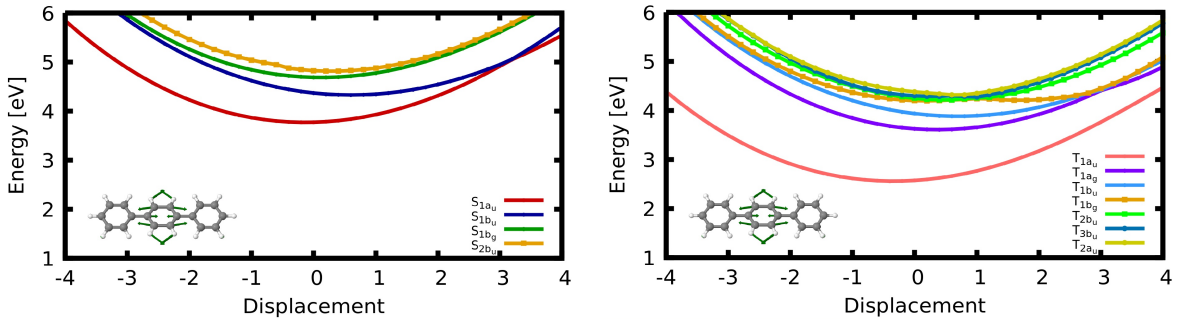

Figure S5: TDDFT scan of singlet and triplet states along the symmetric C–C normal mode of p3P. The D_0 geometry was used for the unrelaxed scan.

Table S1: Comparison of adiabatic energies of alternating and helical conformers of p3P. All values in eV

State	Conformer	TDDFT ΔE_{adiab} w.r.t. S_0	DFT/MRCI ΔE_{adiab} w.r.t. S_0
S_0	alternating		
S_0	helical	0.001	0.004
S_1	alternating	3.940	4.027
S_1	helical	3.943	4.028

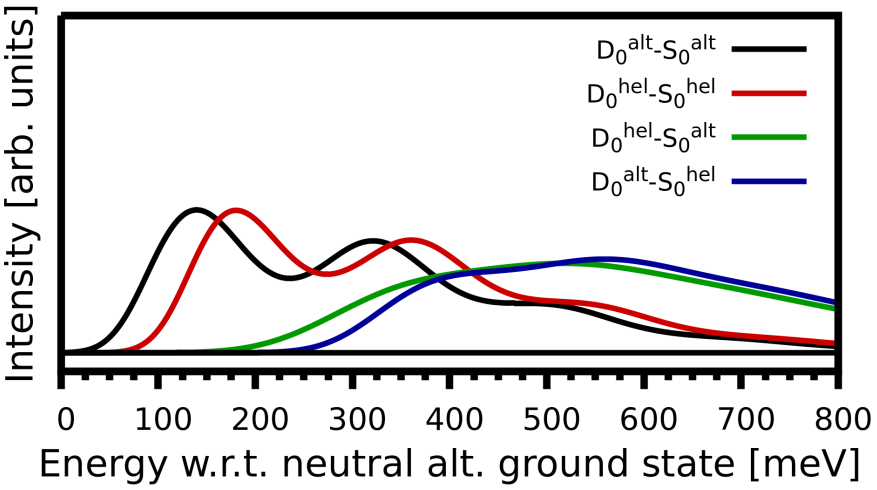

Figure S6: Comparison of spectra calculated between alternating and helical conformers of the D_0 and S_0 states of p3P. The origin of the spectra was shifted to be the 0–0 transition between the alternating conformers of D_0 and S_0.

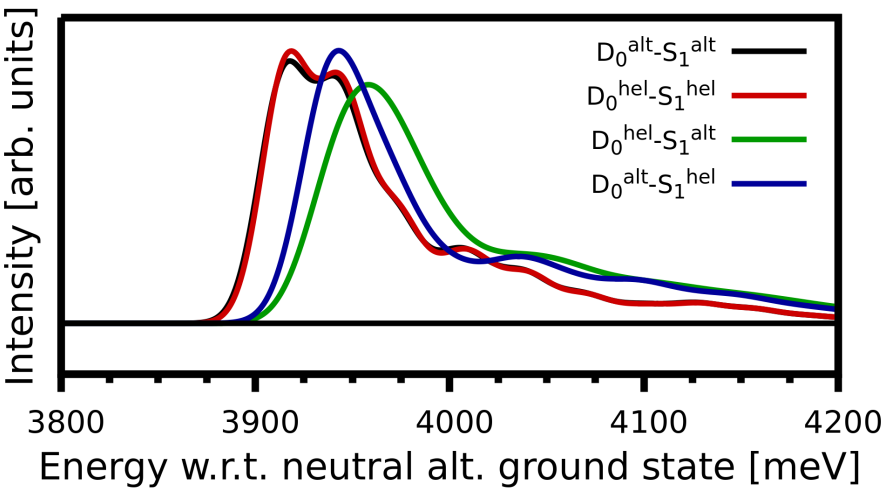

Figure S7: Comparison of spectra calculated between alternating and helical conformers of the D_0 and S_1 states of p3P. The origin of the spectra was shifted to be the 0–0 transition between the alternating conformers of D_0 and S_0.

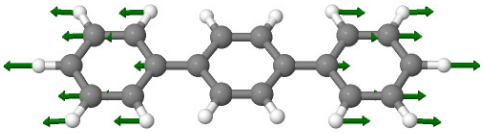

(a) Mode 8 with a frequency of 231 cm^{-1}.

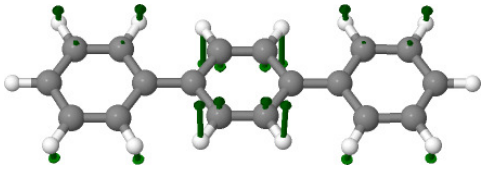

(b) Mode 3 with a frequency of 41 cm^{-1}.

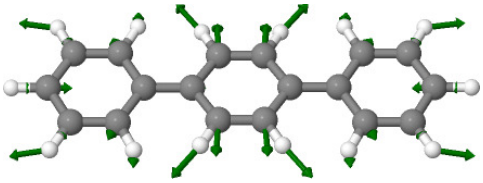

(c) Mode 30 with a frequency of 767 cm^{-1}.

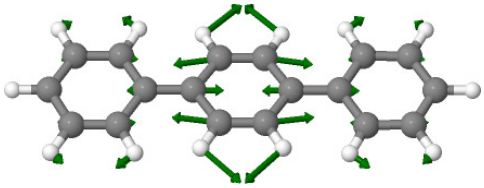

(d) Mode 76 with a frequency of 1683 cm^{-1}.

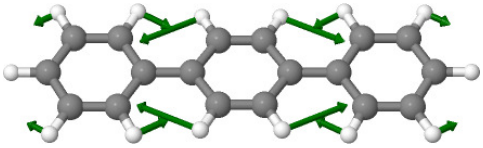

(e) Mode 57 with a frequency of 1263 cm^{-1}.

Figure S9: Displacement vectors of selected vibrational modes in the T_1 state of p3P.

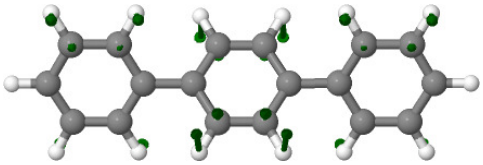

(a) Mode 4 with a frequency of 83 cm^{-1}.

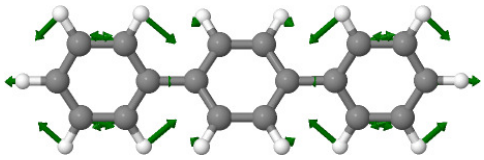

(b) Mode 74 with a frequency of 1671 cm^{-1}.

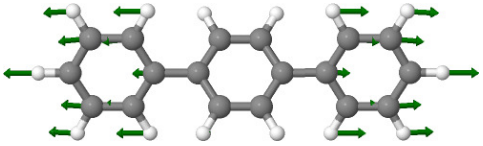

(c) Mode 7 with a frequency of 217 cm^{-1}.

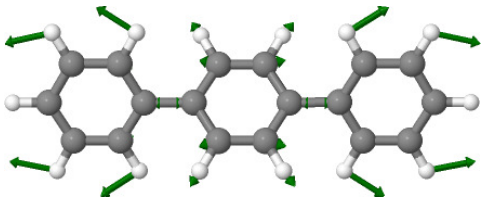

(d) Mode 60 with a frequency of 1331 cm^{-1}.

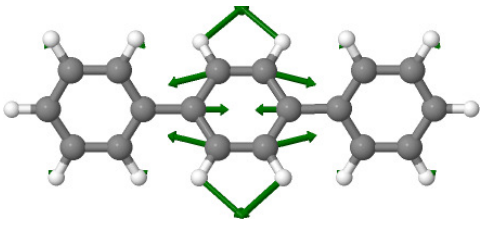

(e) Mode 76 with a frequency of 1680 cm^{-1}.

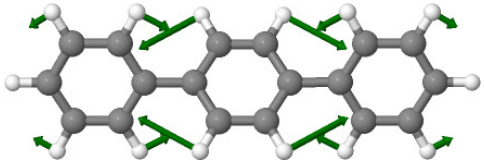

(f) Mode 56 with a frequency of 1217 cm^{-1}.

Figure S8: Displacement vectors of selected vibrational modes in the S_0 state of p3P.

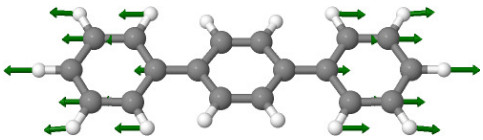

(a) Mode 8 with a frequency of 230 cm^{-1}.

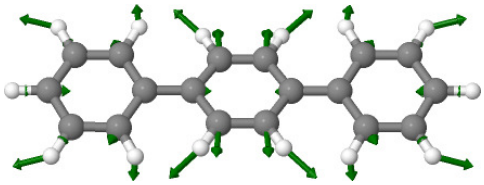

(b) Mode 30 with a frequency of 776 cm^{-1}.

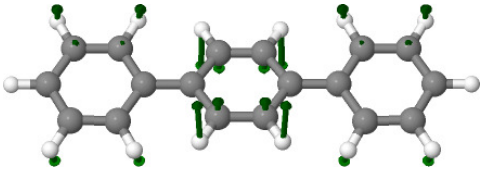

(c) Mode 3 with a frequency of 66 cm^{-1}.

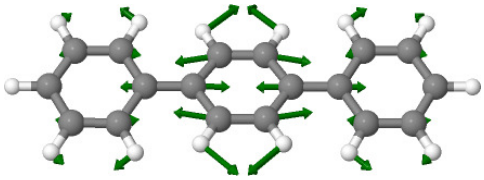

(d) Mode 76 with a frequency of 1711 cm^{-1}.

Figure S10: Displacement vectors of selected vibrational modes in the S_1 state of p3P.

S3 p4P

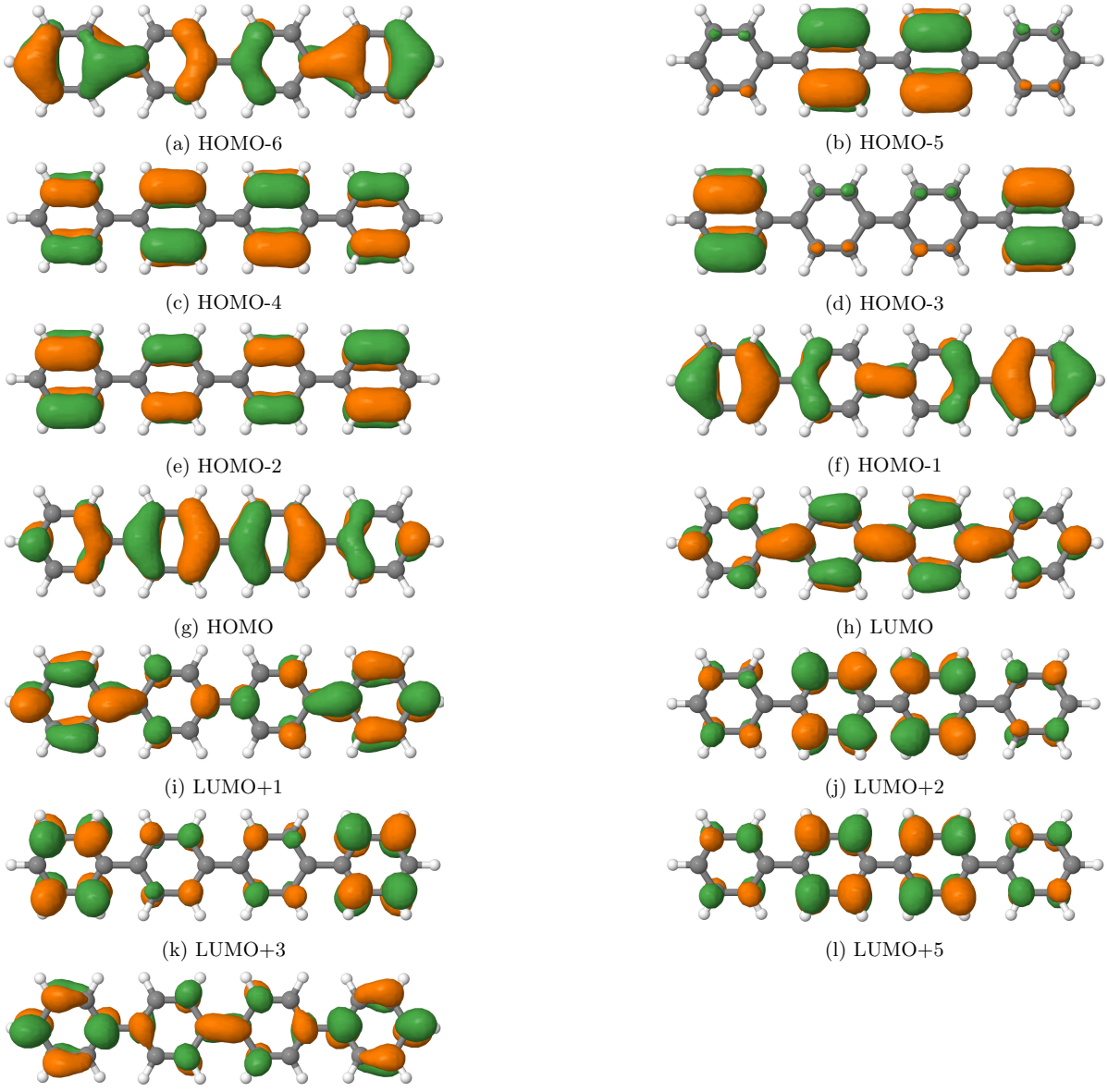

(a) HOMO-6 (b) HOMO-5

(c) HOMO-4 (d) HOMO-3

(e) HOMO-2 (f) HOMO-1

(g) HOMO (h) LUMO

(i) LUMO+1 (j) LUMO+2

(k) LUMO+3 (l) LUMO+5

(m) LUMO+6

Figure S11: Important molecular orbitals at the anion ground state geometry of p4P.

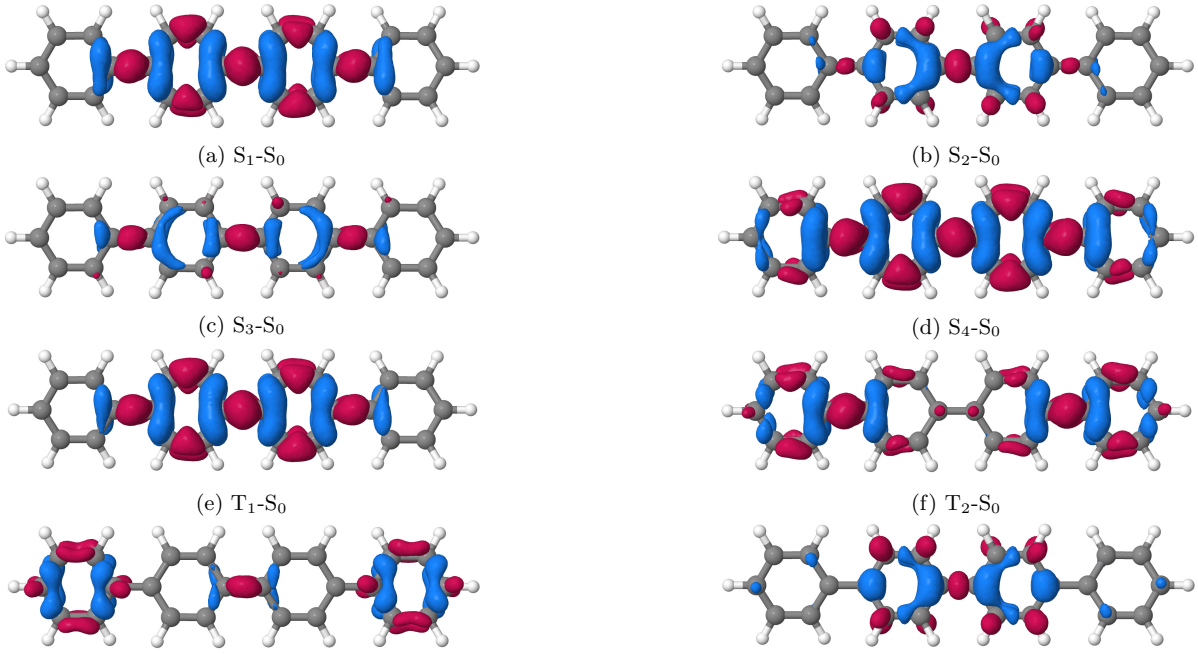

(a) S_1-S_0 (b) S_2-S_0 (c) S_3-S_0 (d) S_4-S_0 (e) T_1-S_0 (f) T_2-S_0 (g) T_3-S_0 (h) T_4-S_0

Figure S12: Difference densities (± 0.001) between the excited states and the neutral ground state at the anion ground state geometry of p4P. For colour codes see Fig. S2.

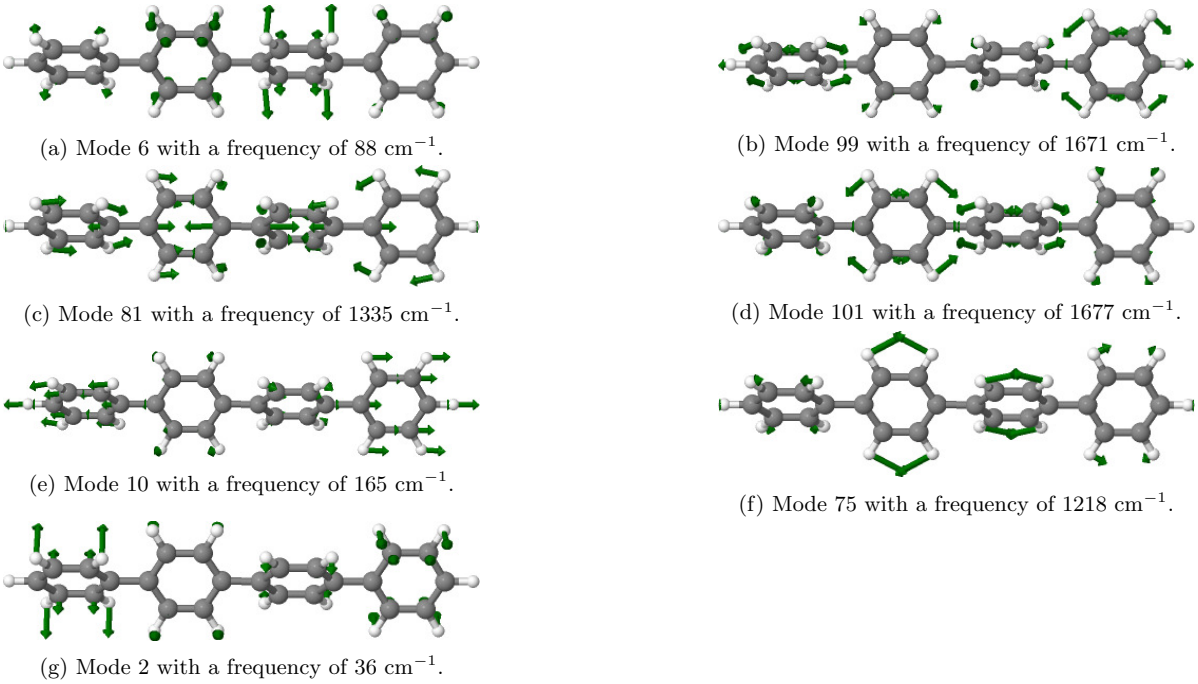

(a) Mode 6 with a frequency of 88 cm^{-1}. (b) Mode 99 with a frequency of 1671 cm^{-1}. (c) Mode 81 with a frequency of 1335 cm^{-1}. (d) Mode 101 with a frequency of 1677 cm^{-1}. (e) Mode 10 with a frequency of 165 cm^{-1}. (f) Mode 75 with a frequency of 1218 cm^{-1}. (g) Mode 2 with a frequency of 36 cm^{-1}.

Figure S13: Displacement vectors of selected vibrational modes in the S_0 state of p4P.

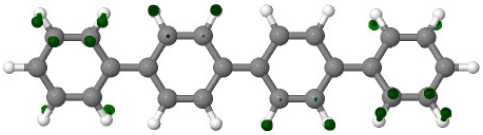

(a) Mode 2 with a frequency of 30 cm^{-1}.

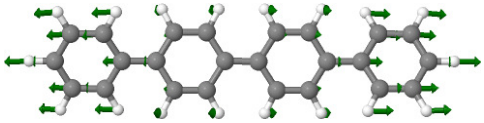

(b) Mode 10 with a frequency of 174 cm^{-1}.

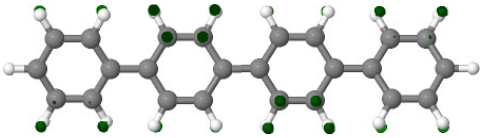

(c) Mode 6 with a frequency of 73 cm^{-1}.

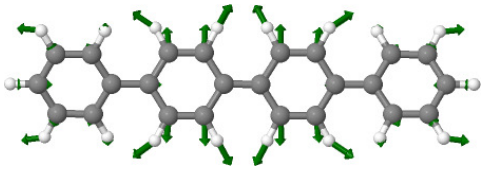

(d) Mode 42 with a frequency of 787 cm^{-1}.

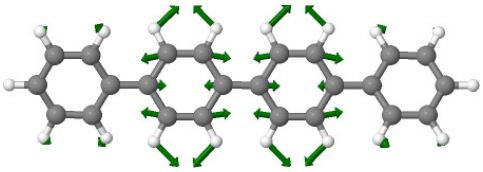

(e) Mode 102 with a frequency of 1675 cm^{-1}.

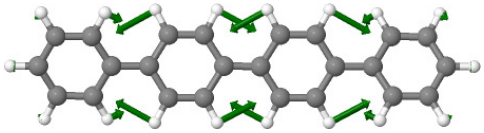

(f) Mode 75 with a frequency of 1256 cm^{-1}.

Figure S14: Displacement vectors of selected vibrational modes in the T_1 state of p4P.

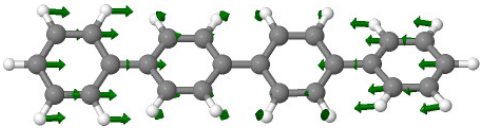

(a) Mode 10 with a frequency of 175 cm^{-1}.

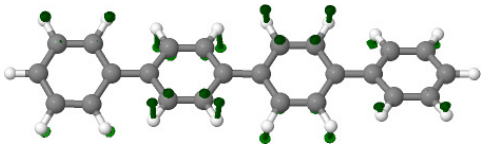

(b) Mode 6 with a frequency of 78 cm^{-1}.

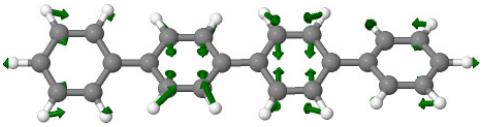

(c) Mode 42 with a frequency of 795 cm^{-1}.

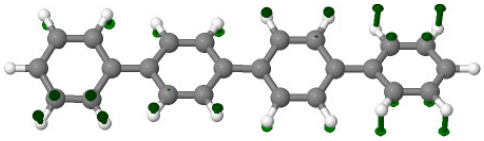

(d) Mode 2 with a frequency of 32 cm^{-1}.

Figure S15: Displacement vectors of selected vibrational modes in the S_1 state of p4P.

S4 p5P

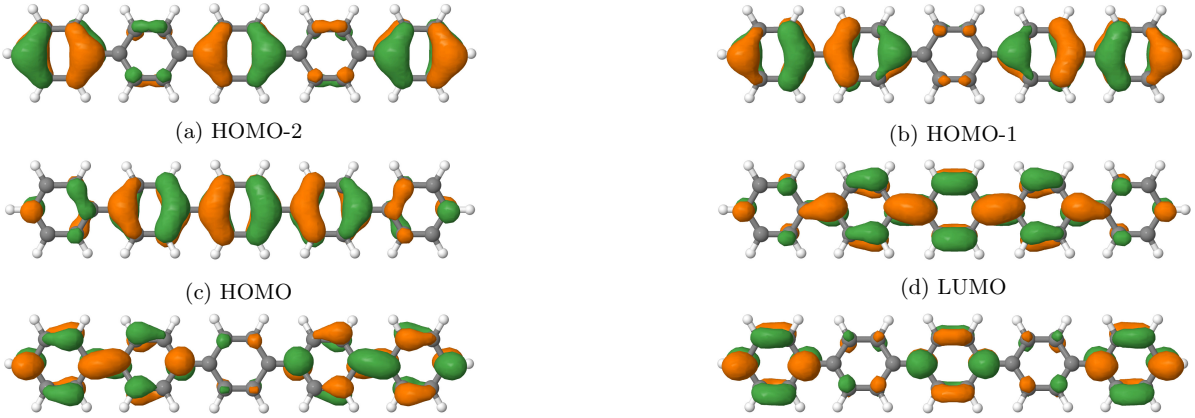

(a) HOMO-2 (b) HOMO-1

(c) HOMO (d) LUMO

(e) LUMO+1 (f) LUMO+5

Figure S16: Important molecular orbitals at the anion ground state geometry of p5P.

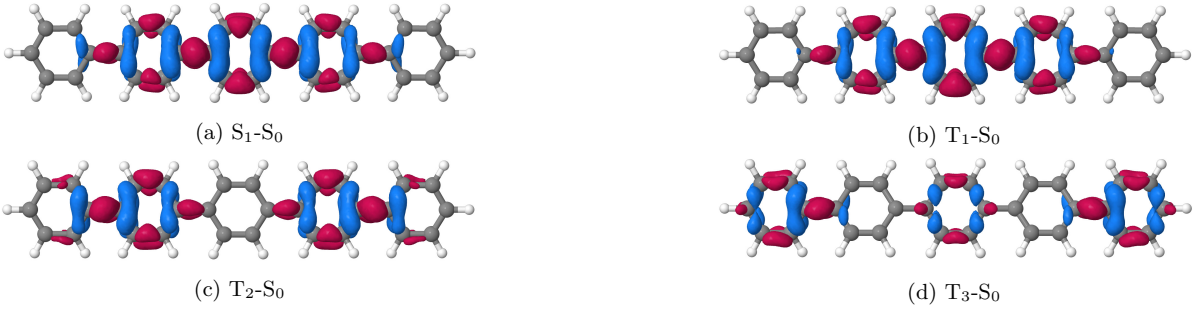

(a) S_1-S_0 (b) T_1-S_0

(c) T_2-S_0 (d) T_3-S_0

Figure S17: Difference densities (± 0.001) between the excited states and the neutral ground state at the anion ground state geometry of p5P. For colour codes see Fig. S2.

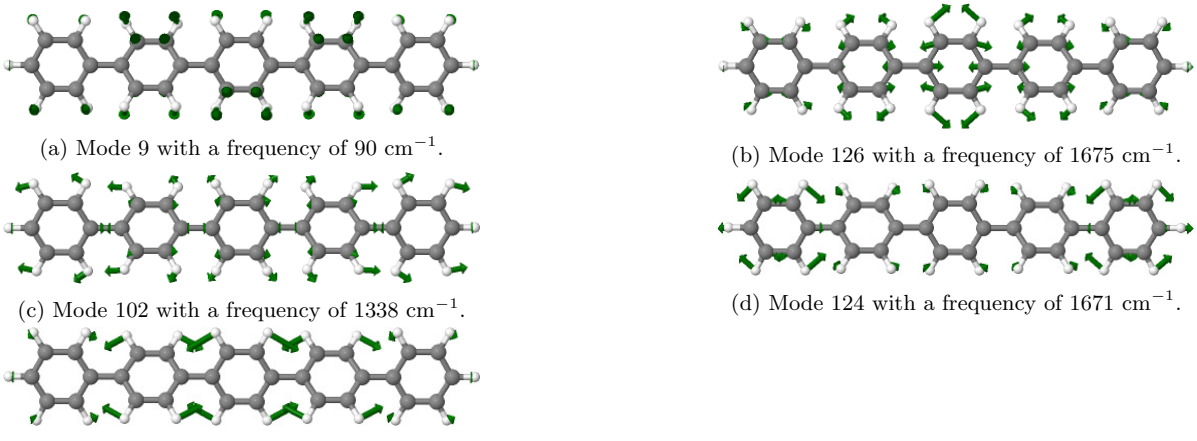

(a) Mode 9 with a frequency of 90 cm^{-1}. (b) Mode 126 with a frequency of 1675 cm^{-1}.

(c) Mode 102 with a frequency of 1338 cm^{-1}. (d) Mode 124 with a frequency of 1671 cm^{-1}.

(e) Mode 94 with a frequency of 1218 cm^{-1}.

Figure S18: Displacement vectors of selected vibrational modes in the S_0 state of p5P.

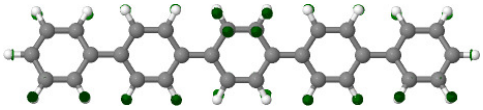

(a) Mode 5 with a frequency of 55 cm^{-1}.

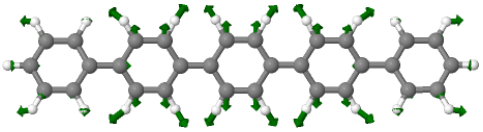

(b) Mode 55 with a frequency of 791 cm^{-1}.

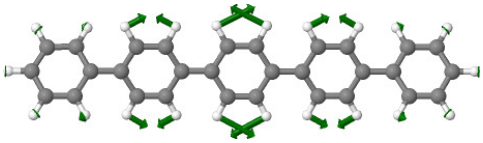

(c) Mode 94 with a frequency of 1249 cm^{-1}.

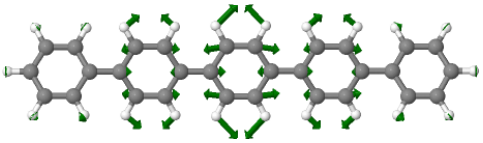

(d) Mode 128 with a frequency of 1654 cm^{-1}.

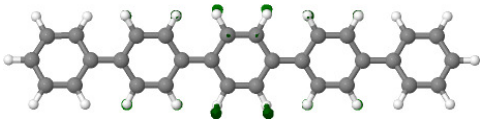

(e) Mode 49 with a frequency of 741 cm^{-1}.

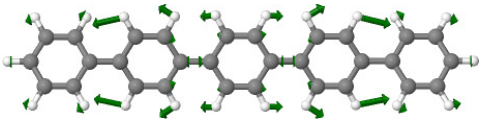

(f) Mode 108 with a frequency of 1390 cm^{-1}.

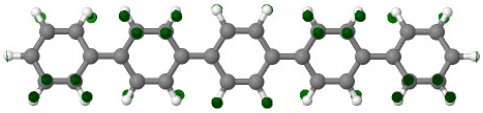

(g) Mode 8 with a frequency of 82 cm^{-1}.

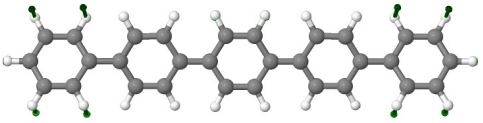

(h) Mode 59 with a frequency of 842 cm^{-1}.

Figure S19: Displacement vectors of selected vibrational modes in the T_1 state of p5P.

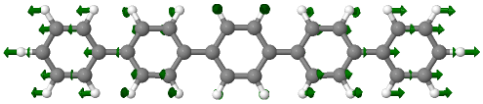

(a) Mode 12 with a frequency of 143 cm^{-1}.

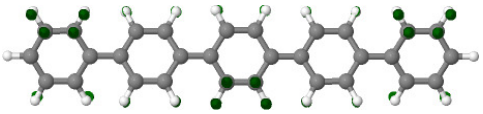

(b) Mode 5 with a frequency of 52 cm^{-1}.

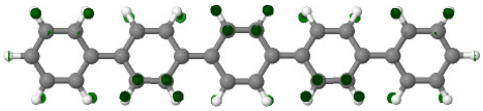

(c) Mode 8 with a frequency of 82 cm^{-1}.

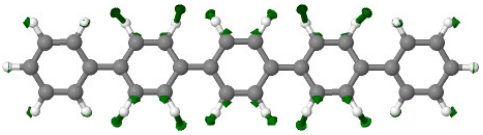

(d) Mode 55 with a frequency of 807 cm^{-1}.

Figure S20: Displacement vectors of selected vibrational modes in the S_1 state of p5P.

S5 Dihedral Angles

Table S2: Dihedral angles of the alternating conformer of p3P

State	Φ_1	Φ_2
D_0	13.8	-13.8
S_0	38.2	-38.2
S_1	10.6	-10.6
S_2	10.7	-10.7
S_3	22.3	-22.3
T_1	5.9	-5.9
T_2	25.2	-25.2
T_3	37.9	-39.5
T_4	13.7	-13.7

Table S3: Dihedral angles of the alternating conformer of p4P

State	Φ_1	Φ_2	Φ_3
D_0	-20.0	14.0	-20.0
S_0	-38.1	36.9	-38.1
S_1	-18.1	9.3	-18.1
S_2	-20.8	5.4	-20.8
S_3			
S_4	-18.2	31.5	-18.2
T_1	-19.2	4.0	-19.2
T_2	-14.6	39.4	-14.6
T_3	-39.3	26.6	-39.3
T_4	-25.1	5.7	-25.1

Table S4: Dihedral angles of the alternating conformer of p5P

State	Φ_1	Φ_2	Φ_3	Φ_4
D_0	24.5	-16.9	16.9	-24.5
S_0	38.1	-36.9	36.9	-38.1
S_1	23.6	-11.9	11.9	-23.6
T_1	27.8	-6.8	6.8	-27.8
T_2	15.7	-28.6	28.6	-15.7
T_3	25.6	-32.0	32.0	-25.6

S6 Geometries

The cartesian coordinates of all investigated geometries are given below in Å.

S6.1 p3P

D_0 alternating

C	0.0000000	0.0000000	1.4515980
C	0.0000000	0.0000000	2.8913400
C	1.1727840	-0.2503910	3.6498240
C	1.1686500	-0.2501910	5.0298780
C	0.0000000	0.0000000	5.7513340
C	-1.1686500	0.2501910	5.0298780
C	-1.1727840	0.2503910	3.6498240
H	2.1112030	-0.4183150	3.1343470
H	2.0986970	-0.4397840	5.5594460
H	0.0000000	0.0000000	6.8356100
H	-2.0986970	0.4397840	5.5594460
H	-2.1112030	0.4183150	3.1343470
C	1.0764720	-0.5210750	0.6852610
C	1.0764720	-0.5210750	-0.6852610
C	0.0000000	0.0000000	-1.4515980
C	-1.0764720	0.5210750	-0.6852610
C	-1.0764720	0.5210750	0.6852610
H	1.9181440	-0.9797430	1.1934970
H	1.9181440	-0.9797430	-1.1934970
C	0.0000000	0.0000000	-2.8913400
H	-1.9181440	0.9797430	-1.1934970
H	-1.9181440	0.9797430	1.1934970
C	1.1727840	-0.2503910	-3.6498240
C	1.1686500	-0.2501910	-5.0298780
C	0.0000000	0.0000000	-5.7513340
C	-1.1686500	0.2501910	-5.0298780
C	-1.1727840	0.2503910	-3.6498240
H	2.1112030	-0.4183150	-3.1343470
H	2.0986970	-0.4397840	-5.5594460
H	0.0000000	0.0000000	-6.8356100
H	-2.0986970	0.4397840	-5.5594460
H	-2.1112030	0.4183150	-3.1343470

D_0 helical

H	2.1070350	0.4417650	3.1404395
H	-2.1070350	-0.4417650	3.1404395
H	2.1021320	0.4223150	5.5625305
H	-2.1021320	-0.4223150	5.5625305
H	0.0000000	0.0000000	6.8397325
H	2.1544730	-0.0136170	1.1906505
H	-2.1544730	0.0136170	1.1906505
H	2.1545730	0.0066040	-1.1902965
H	-2.1545730	-0.0066040	-1.1902965
H	2.1078900	-0.4380260	-3.1407495
H	-2.1078900	0.4380260	-3.1407495
H	2.1028450	-0.4187530	-5.5625435
H	-2.1028450	0.4187530	-5.5625435
H	0.0000000	0.0000000	-6.8398785
C	0.0000000	0.0000000	1.4533775
C	0.0000000	0.0000000	2.8936955
C	1.1761710	0.2311910	3.6535065
C	-1.1761710	-0.2311910	3.6535065
C	1.1720830	0.2311770	5.0335245
C	-1.1720830	-0.2311770	5.0335245
C	0.0000000	0.0000000	5.7554735
C	1.1948600	0.0031320	0.6853375
C	-1.1948600	-0.0031320	0.6853375
C	1.1948540	-0.0066050	-0.6851365
C	-1.1948540	0.0066050	-0.6851365
C	0.0000000	0.0000000	-1.4533175
C	0.0000000	0.0000000	-2.8935945
C	1.1765160	-0.2292750	-3.6536005
C	-1.1765160	0.2292750	-3.6536005
C	1.1723980	-0.2293710	-5.0335945
C	-1.1723980	0.2293710	-5.0335945
C	0.0000000	0.0000000	-5.7556245

S_0 alternating

C	0.0000000	0.0000000	1.4121040
C	0.0000000	0.0000000	2.8863880
C	-0.7537970	0.9320700	3.6020900
C	-0.7537990	0.9324770	4.9880100
C	0.0000000	0.0000000	5.6873190
C	0.7537990	-0.9324770	4.9880100
C	0.7537970	-0.9320700	3.6020900
H	-1.3658400	1.6472640	3.0637250
H	-1.3529390	1.6594040	5.5251730
H	0.0000000	0.0000000	6.7713970
H	1.3529390	-1.6594040	5.5251730
H	1.3658400	-1.6472640	3.0637250
C	-0.0158960	1.1952240	0.6916710
C	-0.0158960	1.1952240	-0.6916710
C	0.0000000	0.0000000	-1.4121040
C	0.0158960	-1.1952240	-0.6916710
C	0.0158960	-1.1952240	0.6916710
H	0.0069320	2.1390480	1.2251490
H	0.0069320	2.1390480	-1.2251490
C	0.0000000	0.0000000	-2.8863880
H	-0.0069320	-2.1390480	-1.2251490
H	-0.0069320	-2.1390480	1.2251490
C	-0.7537970	0.9320700	-3.6020900
C	-0.7537990	0.9324770	-4.9880100
C	0.0000000	0.0000000	-5.6873190
C	0.7537990	-0.9324770	-4.9880100
C	0.7537970	-0.9320700	-3.6020900
H	-1.3658400	1.6472640	-3.0637250
H	-1.3529390	1.6594040	-5.5251730
H	0.0000000	0.0000000	-6.7713970
H	1.3529390	-1.6594040	-5.5251730
H	1.3658400	-1.6472640	-3.0637250

S_0 helical

C	0.0000000	0.0000000	1.4119740
C	0.0000000	0.0000000	2.8863810
C	-0.9367550	-0.7479900	3.6021010
C	-0.9370390	-0.7480560	4.9880360
C	0.0000000	0.0000000	5.6874030
C	0.9370390	0.7480560	4.9880360
C	0.9367550	0.7479900	3.6021010
H	-1.6558230	-1.3555930	3.0638790
H	-1.6676330	-1.3427960	5.5251170
H	0.0000000	0.0000000	6.7714790
H	1.6676330	1.3427960	5.5251170
H	1.6558230	1.3555930	3.0638790
C	-1.1952800	-0.0005660	0.6916710
C	-1.1952890	0.0003690	-0.6917050
C	0.0000000	0.0000000	-1.4119900
C	1.1952890	-0.0003690	-0.6917050
C	1.1952800	0.0005660	0.6916710
H	-2.1391170	0.0152870	1.2254150
H	-2.1390920	-0.0155730	-1.2255020
C	0.0000000	0.0000000	-2.8864180
H	2.1390920	0.0155730	-1.2255020
H	2.1391170	-0.0152870	1.2254150
C	-0.9365300	0.7483110	-3.6020860
C	-0.9368140	0.7483630	-4.9880250
C	0.0000000	0.0000000	-5.6873590
C	0.9368140	-0.7483630	-4.9880250
C	0.9365300	-0.7483110	-3.6020860
H	-1.6553690	1.3561060	-3.0637780
H	-1.6672410	1.3432780	-5.5251400
H	0.0000000	0.0000000	-6.7714360
H	1.6672410	-1.3432780	-5.5251400
H	1.6553690	-1.3561060	-3.0637780

S_1 alternating

C	0.0000000	0.0000000	1.4406780
C	0.0000000	0.0000000	2.8673640
C	1.1796710	-0.2779700	3.6175790
C	1.1728310	-0.2722080	4.9927890
C	0.0000000	0.0000000	5.7008310
C	-1.1728310	0.2722080	4.9927890
C	-1.1796710	0.2779700	3.6175790
H	2.1123680	-0.4668680	3.1022050
H	2.0916740	-0.4771820	5.5313350
H	0.0000000	0.0000000	6.7845140
H	-2.0916740	0.4771820	5.5313350
H	-2.1123680	0.4668680	3.1022050
C	1.1090350	-0.4911470	0.6807740
C	1.1090350	-0.4911470	-0.6807740
C	0.0000000	0.0000000	-1.4406780
C	-1.1090350	0.4911470	-0.6807740
C	-1.1090350	0.4911470	0.6807740
H	1.9614420	-0.9152420	1.1951350
H	1.9614420	-0.9152420	-1.1951350
C	0.0000000	0.0000000	-2.8673640
H	-1.9614420	0.9152420	-1.1951350
H	-1.9614420	0.9152420	1.1951350
C	1.1796710	-0.2779700	-3.6175790
C	1.1728310	-0.2722080	-4.9927890
C	0.0000000	0.0000000	-5.7008310
C	-1.1728310	0.2722080	-4.9927890
C	-1.1796710	0.2779700	-3.6175790
H	2.1123680	-0.4668680	-3.1022050
H	2.0916740	-0.4771820	-5.5313350
H	0.0000000	0.0000000	-6.7845140
H	-2.0916740	0.4771820	-5.5313350
H	-2.1123680	0.4668680	-3.1022050

S_1 helical

C	0.0000000	0.0000000	1.4417709
C	0.0000000	0.0000000	2.8688569
C	-0.4075240	1.1410420	3.6199649
C	-0.4083040	1.1323630	4.9951649
C	0.0000000	0.0000000	5.7034729
C	0.4083040	-1.1323630	4.9951649
C	0.4075240	-1.1410420	3.6199649
H	-0.7524320	2.0287130	3.1062109
H	-0.7341790	2.0157780	5.5334039
H	0.0000000	0.0000000	6.7871499
H	0.7341790	-2.0157780	5.5334039
H	0.7524320	-2.0287130	3.1062109
C	-0.2307930	1.1900100	0.6807699
C	-0.2175420	1.1924970	-0.6807781
C	0.0000000	0.0000000	-1.4417571
C	0.2175420	-1.1924970	-0.6807781
C	0.2307930	-1.1900100	0.6807699
H	-0.3950280	2.1286090	1.1932059
H	-0.4057320	2.1265970	-1.1931961
C	0.0000000	0.0000000	-2.8688711
H	0.4057320	-2.1265970	-1.1931961
H	0.3950280	-2.1286090	1.1932059
C	-0.0352950	1.2111070	-3.6199571
C	-0.0313920	1.2033140	-4.9951661
C	0.0000000	0.0000000	-5.7034721
C	0.0313920	-1.2033140	-4.9951661
C	0.0352950	-1.2111070	-3.6199571
H	-0.0368450	2.1634430	-3.1062281
H	-0.0489970	2.1447570	-5.5333951
H	0.0000000	0.0000000	-6.7871501
H	0.0489970	-2.1447570	-5.5333951
H	0.0368450	-2.1634430	-3.1062281

S_2 alternating

C	0.0000000	0.0000000	1.4298380
C	0.0000000	0.0000000	2.8758580
C	1.1758870	-0.2722900	3.6049720
C	1.1745950	-0.2662450	4.9915980
C	0.0000000	0.0000000	5.6893960
C	-1.1745950	0.2662450	4.9915980
C	-1.1758870	0.2722900	3.6049720
H	2.1043100	-0.4566550	3.0826810
H	2.0922030	-0.4702210	5.5309340
H	0.0000000	0.0000000	6.7735970
H	-2.0922030	0.4702210	5.5309340
H	-2.1043100	0.4566550	3.0826810
C	1.1093120	-0.4879550	0.6996950
C	1.1093120	-0.4879550	-0.6996950
C	0.0000000	0.0000000	-1.4298380
C	-1.1093120	0.4879550	-0.6996950
C	-1.1093120	0.4879550	0.6996950
H	1.9560800	-0.9150670	1.2166650
H	1.9560800	-0.9150670	-1.2166650
C	0.0000000	0.0000000	-2.8758580
H	-1.9560800	0.9150670	-1.2166650
H	-1.9560800	0.9150670	1.2166650
C	1.1758870	-0.2722900	-3.6049720
C	1.1745950	-0.2662450	-4.9915980
C	0.0000000	0.0000000	-5.6893960
C	-1.1745950	0.2662450	-4.9915980
C	-1.1758870	0.2722900	-3.6049720
H	2.1043100	-0.4566550	-3.0826810
H	2.0922030	-0.4702210	-5.5309340
H	0.0000000	0.0000000	-6.7735970
H	-2.0922030	0.4702210	-5.5309340
H	-2.1043100	0.4566550	-3.0826810

S_3 alternating

C	0.0000000	0.0000000	1.4276480
C	0.0000000	0.0000000	2.8730540
C	-0.6677290	1.0064990	3.6023030
C	-0.6659820	1.0037520	5.0062800
C	0.0000000	0.0000000	5.7061950
C	0.6659820	-1.0037520	5.0062800
C	0.6677290	-1.0064990	3.6023030
H	-1.2332750	1.7657850	3.0778600
H	-1.1968870	1.7812170	5.5425550
H	0.0000000	0.0000000	6.7899230
H	1.1968870	-1.7812170	5.5425550
H	1.2332750	-1.7657850	3.0778600
C	-0.2355380	1.1799530	0.6848550
C	-0.2355380	1.1799530	-0.6848550
C	0.0000000	0.0000000	-1.4276480
C	0.2355380	-1.1799530	-0.6848550
C	0.2355380	-1.1799530	0.6848550
H	-0.3702130	2.1185900	1.2087240
H	-0.3702130	2.1185900	-1.2087240
C	0.0000000	0.0000000	-2.8730540
H	0.3702130	-2.1185900	-1.2087240
H	0.3702130	-2.1185900	1.2087240
C	-0.6677290	1.0064990	-3.6023030
C	-0.6659820	1.0037520	-5.0062800
C	0.0000000	0.0000000	-5.7061950
C	0.6659820	-1.0037520	-5.0062800
C	0.6677290	-1.0064990	-3.6023030
H	-1.2332750	1.7657850	-3.0778600
H	-1.1968870	1.7812170	-5.5425550
H	0.0000000	0.0000000	-6.7899230
H	1.1968870	-1.7812170	-5.5425550
H	1.2332750	-1.7657850	-3.0778600

T_1 alternating

C	0.0000000	0.0000000	1.4494320
C	0.0000000	0.0000000	2.8687540
C	1.1692760	-0.3120750	3.6225990
C	1.1628820	-0.3078810	4.9970620
C	0.0000000	0.0000000	5.7064320
C	-1.1628820	0.3078810	4.9970620
C	-1.1692760	0.3120750	3.6225990
H	2.0944460	-0.5414380	3.1116330
H	2.0747760	-0.5444540	5.5342710
H	0.0000000	0.0000000	6.7897370
H	-2.0747760	0.5444540	5.5342710
H	-2.0944460	0.5414380	3.1116330
C	1.1387790	-0.4335820	0.6761620
C	1.1387790	-0.4335820	-0.6761620
C	0.0000000	0.0000000	-1.4494320
C	-1.1387790	0.4335820	-0.6761620
C	-1.1387790	0.4335820	0.6761620
H	2.0206140	-0.7973920	1.1861440
H	2.0206140	-0.7973920	-1.1861440
C	0.0000000	0.0000000	-2.8687540
H	-2.0206140	0.7973920	-1.1861440
H	-2.0206140	0.7973920	1.1861440
C	1.1692760	-0.3120750	-3.6225990
C	1.1628820	-0.3078810	-4.9970620
C	0.0000000	0.0000000	-5.7064320
C	-1.1628820	0.3078810	-4.9970620
C	-1.1692760	0.3120750	-3.6225990
H	2.0944460	-0.5414380	-3.1116330
H	2.0747760	-0.5444540	-5.5342710
H	0.0000000	0.0000000	-6.7897370
H	-2.0747760	0.5444540	-5.5342710
H	-2.0944460	0.5414380	-3.1116330

T_2 alternating

C	0.0000000	0.0000000	1.4256650
C	0.0000000	0.0000000	2.8784670
C	1.2079600	-0.1822670	3.6231860
C	1.2051790	-0.1779630	4.9924250
C	0.0000000	0.0000000	5.7094920
C	-1.2051790	0.1779630	4.9924250
C	-1.2079600	0.1822670	3.6231860
H	2.1457330	-0.2875730	3.0914290
H	2.1366410	-0.3014780	5.5333300
H	0.0000000	0.0000000	6.7920920
H	-2.1366410	0.3014780	5.5333300
H	-2.1457330	0.2875730	3.0914290
C	0.9948760	-0.6657250	0.6901830
C	0.9948760	-0.6657250	-0.6901830
C	0.0000000	0.0000000	-1.4256650
C	-0.9948760	0.6657250	-0.6901830
C	-0.9948760	0.6657250	0.6901830
H	1.7619330	-1.2258020	1.2117800
H	1.7619330	-1.2258020	-1.2117800
C	0.0000000	0.0000000	-2.8784670
H	-1.7619330	1.2258020	-1.2117800
H	-1.7619330	1.2258020	1.2117800
C	1.2079600	-0.1822670	-3.6231860
C	1.2051790	-0.1779630	-4.9924250
C	0.0000000	0.0000000	-5.7094920
C	-1.2051790	0.1779630	-4.9924250
C	-1.2079600	0.1822670	-3.6231860
H	2.1457330	-0.2875730	-3.0914290
H	2.1366410	-0.3014780	-5.5333300
H	0.0000000	0.0000000	-6.7920920
H	-2.1366410	0.3014780	-5.5333300
H	-2.1457330	0.2875730	-3.0914290

T_3 alternating

C	0.0021057	0.0185111	1.4155400
C	-0.0102033	0.0169831	2.8882730
C	-0.7807543	0.9117981	3.5985520
C	-0.7827943	0.9067751	5.0200110
C	0.0017277	-0.0273869	5.7177140
C	0.7711357	-0.9295029	5.0231750
C	0.7783727	-0.9194249	3.6036220
H	-1.4146733	1.6139531	3.0692340
H	-1.3946643	1.6193081	5.5590980
H	-0.0016473	-0.0317079	6.8017670
H	1.3859457	-1.6483669	5.5522480
H	1.4192587	-1.6040479	3.0620560
C	-0.0325473	1.2211781	0.6908190
C	-0.0325473	1.2211781	-0.6908190
C	0.0021057	0.0185111	-1.4155400
C	0.0423837	-1.1840999	-0.6909160
C	0.0423837	-1.1840999	0.6909160
H	-0.0238373	2.1629651	1.2279040
H	-0.0238373	2.1629651	-1.2279040
C	-0.0102033	0.0169831	-2.8882730
H	0.0401907	-2.1269349	-1.2263740
H	0.0401907	-2.1269349	1.2263740
C	-0.7807543	0.9117981	-3.5985520
C	-0.7827943	0.9067751	-5.0200110
C	0.0017277	-0.0273869	-5.7177140
C	0.7711357	-0.9295029	-5.0231750
C	0.7783727	-0.9194249	-3.6036220
H	-1.4146733	1.6139531	-3.0692340
H	-1.3946643	1.6193081	-5.5590980
H	-0.0016473	-0.0317079	-6.8017670
H	1.3859457	-1.6483669	-5.5522480
H	1.4192587	-1.6040479	-3.0620560

T_4 alternating

C	0.0000000	0.0000000	1.4200670
C	0.0000000	0.0000000	2.8712290
C	1.1802580	-0.2496350	3.5969920
C	1.1801950	-0.2418260	4.9831180
C	0.0000000	0.0000000	5.6782240
C	-1.1801950	0.2418260	4.9831180
C	-1.1802580	0.2496350	3.5969920
H	2.1097900	-0.4144050	3.0700520
H	2.1012760	-0.4261680	5.5234330
H	0.0000000	0.0000000	6.7626980
H	-2.1012760	0.4261680	5.5234330
H	-2.1097900	0.4144050	3.0700520
C	1.0985050	-0.5282030	0.7028950
C	1.0985050	-0.5282030	-0.7028950
C	0.0000000	0.0000000	-1.4200670
C	-1.0985050	0.5282030	-0.7028950
C	-1.0985050	0.5282030	0.7028950
H	1.9178570	-0.9968680	1.2270040
H	1.9178570	-0.9968680	-1.2270040
C	0.0000000	0.0000000	-2.8712290
H	-1.9178570	0.9968680	-1.2270040
H	-1.9178570	0.9968680	1.2270040
C	1.1802580	-0.2496350	-3.5969920
C	1.1801950	-0.2418260	-4.9831180
C	0.0000000	0.0000000	-5.6782240
C	-1.1801950	0.2418260	-4.9831180
C	-1.1802580	0.2496350	-3.5969920
H	2.1097900	-0.4144050	-3.0700520
H	2.1012760	-0.4261680	-5.5234330
H	0.0000000	0.0000000	-6.7626980
H	-2.1012760	0.4261680	-5.5234330
H	-2.1097900	0.4144050	-3.0700520

S6.2 p4P

D_0 alternating

C	0.7806110	0.9082350	5.8062540
C	0.0000000	-0.0000000	5.0592930
C	-0.7806110	-0.9082350	5.8062540
C	-0.7770680	-0.9084050	7.1883870
C	0.0000000	-0.0000000	7.9034120
C	0.7770680	0.9084050	7.1883870
C	0.0000000	-0.0000000	3.6091760
C	-0.4206990	-1.1173320	2.8541870
C	-0.4189390	-1.1200580	1.4814770
C	0.0000000	-0.0000000	0.7187820
C	0.4189390	1.1200580	1.4814770
C	0.4206990	1.1173320	2.8541870
C	0.0000000	-0.0000000	-0.7187820
C	-0.6778190	-0.9851910	-1.4814770
C	-0.6745760	-0.9850710	-2.8541870
C	0.0000000	-0.0000000	-3.6091760
C	0.6745760	0.9850710	-2.8541870
C	0.6778190	0.9851910	-1.4814770
C	0.0000000	-0.0000000	-5.0592930
C	0.2969660	1.1601960	-5.8062540
C	0.2991360	1.1573900	-7.1883870
C	0.0000000	-0.0000000	-7.9034120
C	-0.2991360	-1.1573900	-7.1883870
C	-0.2969660	-1.1601960	-5.8062540
H	1.4249810	1.6057570	5.2837790
H	1.4009910	1.6213220	7.7197070
H	0.0000000	-0.0000000	8.9877030
H	-1.4009910	-1.6213220	7.7197070
H	-1.4249810	-1.6057570	5.2837790
H	-0.7127600	-2.0271880	3.3685410
H	-0.7096120	-2.0314240	0.9712230
H	0.7096120	2.0314240	0.9712230
H	0.7127600	2.0271880	3.3685410
H	1.2581170	1.7456730	-0.9712230
H	1.2528420	1.7458250	-3.3685410
H	-1.2528420	-1.7458250	-3.3685410
H	-1.2581170	-1.7456730	-0.9712230
H	-0.4993250	-2.0879890	-5.2837790
H	-0.5258290	-2.0772490	-7.7197070
H	0.0000000	-0.0000000	-8.9877030
H	0.5258290	2.0772490	-7.7197070
H	0.4993250	2.0879890	-5.2837790

S_0 alternating

C	0.8795760	0.8144520	5.7510770
C	0.0000000	0.0000000	5.0353420
C	-0.8795760	-0.8144520	5.7510770
C	-0.8796100	-0.8148620	7.1369860
C	0.0000000	0.0000000	7.8363060
C	0.8796100	0.8148620	7.1369860
C	0.0000000	0.0000000	3.5611650
C	-0.1883300	-1.1803710	2.8405490
C	-0.1880870	-1.1804740	1.4573630
C	0.0000000	0.0000000	0.7363860
C	0.1880870	1.1804740	1.4573630
C	0.1883300	1.1803710	2.8405490
C	0.0000000	0.0000000	-0.7363860
C	-0.8596390	-0.8306120	-1.4573630
C	-0.8594150	-0.8307530	-2.8405490
C	0.0000000	0.0000000	-3.5611650
C	0.8594150	0.8307530	-2.8405490
C	0.8596390	0.8306120	-1.4573630
C	0.0000000	0.0000000	-5.0353420
C	0.1634190	1.1875520	-5.7510770
C	0.1637350	1.1878150	-7.1369860
C	0.0000000	0.0000000	-7.8363060
C	-0.1637350	-1.1878150	-7.1369860
C	-0.1634190	-1.1875520	-5.7510770
H	1.5879400	1.4344680	5.2128190
H	1.5767510	1.4484170	7.6741390
H	0.0000000	0.0000000	8.9203800
H	-1.5767510	-1.4484170	7.6741390
H	-1.5879400	-1.4344680	5.2128190
H	-0.3018830	-2.1176590	3.3739400
H	-0.3007970	-2.1181450	0.9244990
H	0.3007970	2.1181450	0.9244990
H	0.3018830	2.1176590	3.3739400
H	1.5634900	1.4603130	-0.9244990
H	1.5624700	1.4609250	-3.3739400
H	-1.5624700	-1.4609250	-3.3739400
H	-1.5634900	-1.4603130	-0.9244990
H	-0.2656050	-2.1233710	-5.2128190
H	-0.2834490	-2.1221950	-7.6741390
H	0.0000000	0.0000000	-8.9203800
H	0.2834490	2.1221950	-7.6741390
H	0.2656050	2.1233710	-5.2128190

S_1 alternating

C	0.7924300	0.9082380	5.7668040
C	-0.0000000	0.0000000	5.0272370
C	-0.7924300	-0.9082380	5.7668040
C	-0.7918470	-0.9030350	7.1458170
C	-0.0000000	0.0000000	7.8516470
C	0.7918470	0.9030350	7.1458170
C	-0.0000000	0.0000000	3.5855390
C	-0.4703320	-1.1099330	2.8356370
C	-0.4702680	-1.1143980	1.4706740
C	-0.0000000	0.0000000	0.7110070
C	0.4702680	1.1143980	1.4706740
C	0.4703320	1.1099330	2.8356370
C	-0.0000000	0.0000000	-0.7110070
C	-0.6443440	-1.0236490	-1.4706740
C	-0.6406470	-1.0211440	-2.8356370
C	-0.0000000	0.0000000	-3.5855390
C	0.6406470	1.0211440	-2.8356370
C	0.6443440	1.0236490	-1.4706740
C	-0.0000000	0.0000000	-5.0272370
C	0.2908590	1.1697190	-5.7668040
C	0.2869270	1.1662610	-7.1458170
C	-0.0000000	0.0000000	-7.8516470
C	-0.2869270	-1.1662610	-7.1458170
C	-0.2908590	-1.1697190	-5.7668040
H	1.4428280	1.5999130	5.2460210
H	1.4211410	1.6045190	7.6826410
H	-0.0000000	0.0000000	8.9354360
H	-1.4211410	-1.6045190	7.6826410
H	-1.4428280	-1.5999130	5.2460210
H	-0.7996870	-2.0013870	3.3548360
H	-0.8009330	-2.0091520	0.9595870
H	0.8009330	2.0091520	0.9595870
H	0.7996870	2.0013870	3.3548360
H	1.1885530	1.8070770	-0.9595870
H	1.1829000	1.8016090	-3.3548350
H	-1.1829000	-1.8016090	-3.3548350
H	-1.1885530	-1.8070770	-0.9595870
H	-0.4854990	-2.0989910	-5.2460220
H	-0.5016940	-2.0838490	-7.6826410
H	-0.0000000	0.0000000	-8.9354360
H	0.5016940	2.0838490	-7.6826410
H	0.4854990	2.0989910	-5.2460220

S_2 alternating

C	0.3461190	-1.1512730	5.7516580
C	0.0000000	-0.0000000	5.0266860
C	-0.3461190	1.1512730	5.7516580
C	-0.3403400	1.1518780	7.1359980
C	0.0000000	-0.0000000	7.8353260
C	0.3403400	-1.1518780	7.1359980
C	0.0000000	-0.0000000	3.5684430
C	-0.7351640	0.9573620	2.8430910
C	-0.7388320	0.9571740	1.4515590
C	0.0000000	-0.0000000	0.7196920
C	0.7388320	-0.9571740	1.4515590
C	0.7351640	-0.9573620	2.8430910
C	0.0000000	-0.0000000	-0.7196910
C	-0.6457730	1.0222680	-1.4515590
C	-0.6472080	1.0188880	-2.8430910
C	0.0000000	-0.0000000	-3.5684430
C	0.6472080	-1.0188880	-2.8430910
C	0.6457730	-1.0222680	-1.4515590
C	0.0000000	-0.0000000	-5.0266860
C	0.9627720	-0.7199280	-5.7516580
C	0.9653230	-0.7147080	-7.1359980
C	0.0000000	-0.0000000	-7.8353260
C	-0.9653230	0.7147080	-7.1359980
C	-0.9627720	0.7199280	-5.7516580
H	0.5867850	-2.0649050	5.2229150
H	0.6001660	-2.0566240	7.6737430
H	0.0000000	-0.0000000	8.9194340
H	-0.6001660	2.0566240	7.6737430
H	-0.5867850	2.0649050	5.2229150
H	-1.3482030	1.6777390	3.3680010
H	-1.3475790	1.6853030	0.9362870
H	1.3475790	-1.6853030	0.9362870
H	1.3482030	-1.6777390	3.3680010
H	1.1209990	-1.8437950	-0.9362870
H	1.1136790	-1.8417870	-3.3680010
H	-1.1136790	1.8417870	-3.3680010
H	-1.1209990	1.8437950	-0.9362870
H	-1.7384760	1.2593050	-5.2229150
H	-1.7261080	1.2690360	-7.6737430
H	0.0000000	-0.0000000	-8.9194340
H	1.7261080	-1.2690360	-7.6737430
H	1.7384760	-1.2593050	-5.2229150

S_4 alternating

C	0.6069690	1.0493430	5.7647140
C	0.0000000	0.0000000	5.0256130
C	-0.6069690	-1.0493430	5.7647140
C	-0.6096780	-1.0410090	7.1415530
C	0.0000000	0.0000000	7.8481720
C	0.6096780	1.0410090	7.1415530
C	0.0000000	0.0000000	3.5813070
C	-0.2486290	-1.1807970	2.8372420
C	-0.2455620	-1.1762170	1.4617650
C	0.0000000	0.0000000	0.7304210
C	0.2455620	1.1762170	1.4617650
C	0.2486290	1.1807970	2.8372420
C	0.0000000	0.0000000	-0.7304230
C	-0.8236710	-0.8748450	-1.4617660
C	-0.8256690	-0.8799830	-2.8372430
C	0.0000000	0.0000000	-3.5813070
C	0.8256690	0.8799830	-2.8372430
C	0.8236710	0.8748450	-1.4617660
C	0.0000000	0.0000000	-5.0256130
C	0.5126670	1.0985010	-5.7647130
C	0.5042830	1.0959510	-7.1415520
C	0.0000000	0.0000000	-7.8481710
C	-0.5042830	-1.0959510	-7.1415520
C	-0.5126670	-1.0985010	-5.7647130
H	1.1128070	1.8506130	5.2401730
H	1.0943710	1.8471110	7.6810790
H	0.0000000	0.0000000	8.9317400
H	-1.0943710	-1.8471110	7.6810790
H	-1.1128070	-1.8506130	5.2401730
H	-0.3983910	-2.1191130	3.3569720
H	-0.3988110	-2.1087600	0.9305020
H	0.3988110	2.1087600	0.9305020
H	0.3983910	2.1191130	3.3569720
H	1.5004340	1.5344770	-0.9305030
H	1.5091610	1.5400600	-3.3569760
H	-1.5091610	-1.5400600	-3.3569760
H	-1.5004340	-1.5344770	-0.9305030
H	-0.8798760	-1.9720350	-5.2401700
H	-0.8875610	-1.9549170	-7.6810780
H	0.0000000	0.0000000	-8.9317390
H	0.8875610	1.9549170	-7.6810780
H	0.8798760	1.9720350	-5.2401700

T_1 alternating

C	-1.1475270	0.3606200	5.7673450
C	0.0000000	0.0000000	5.0310780
C	1.1475270	-0.3606200	5.7673450
C	1.1437460	-0.3623540	7.1477840
C	0.0000000	0.0000000	7.8525030
C	-1.1437460	0.3623540	7.1477840
C	0.0000000	0.0000000	3.5871180
C	1.2080340	0.0374120	2.8335880
C	1.2142750	0.0418590	1.4742370
C	0.0000000	0.0000000	0.7029880
C	-1.2142750	-0.0418590	1.4742370
C	-1.2080340	-0.0374120	2.8335880
C	0.0000000	0.0000000	-0.7029880
C	1.2142740	-0.0418930	-1.4742370
C	1.2080330	-0.0374440	-2.8335880
C	0.0000000	0.0000000	-3.5871180
C	-1.2080330	0.0374440	-2.8335880
C	-1.2142740	0.0418930	-1.4742370
C	0.0000000	0.0000000	-5.0310780
C	-1.1475380	-0.3605870	-5.7673450
C	-1.1437560	-0.3623220	-7.1477830
C	0.0000000	0.0000000	-7.8525030
C	1.1437560	0.3623220	-7.1477830
C	1.1475380	0.3605870	-5.7673450
H	-2.0424930	0.6760220	5.2456790
H	-2.0392180	0.6566910	7.6839800
H	0.0000000	0.0000000	8.9361860
H	2.0392180	-0.6566910	7.6839800
H	2.0424930	-0.6760220	5.2456790
H	2.1551830	0.1056840	3.3544890
H	2.1676000	0.1049530	0.9674000
H	-2.1676000	-0.1049530	0.9674000
H	-2.1551830	-0.1056840	3.3544890
H	-2.1675970	0.1050130	-0.9674000
H	-2.1551800	0.1057410	-3.3544890
H	2.1551800	-0.1057410	-3.3544890
H	2.1675970	-0.1050130	-0.9674000
H	2.0425130	0.6759640	-5.2456790
H	2.0392360	0.6566350	-7.6839800
H	0.0000000	0.0000000	-8.9361860
H	-2.0392360	-0.6566350	-7.6839800
H	-2.0425130	-0.6759640	-5.2456790

T_2 alternating

C	-1.2083900	-0.1024650	5.7729604
C	0.0000000	0.0000000	5.0241274
C	1.2083900	0.1024650	5.7729604
C	1.2031180	0.0978450	7.1462874
C	0.0000000	0.0000000	7.8572974
C	-1.2031180	-0.0978450	7.1462874
C	0.0000000	0.0000000	3.5881054
C	1.1376900	0.4018770	2.8373254
C	1.1307610	0.4049010	1.4637674
C	0.0000000	0.0000000	0.7348894
C	-1.1307610	-0.4049010	1.4637674
C	-1.1376900	-0.4018770	2.8373254
C	0.0000000	0.0000000	-0.7348886
C	1.1307450	-0.4049440	-1.4637676
C	1.1376750	-0.4019200	-2.8373256
C	0.0000000	0.0000000	-3.5881056
C	-1.1376750	0.4019200	-2.8373256
C	-1.1307450	0.4049440	-1.4637676
C	0.0000000	0.0000000	-5.0241276
C	-1.2083860	0.1025130	-5.7729606
C	-1.2031140	0.0978940	-7.1462876
C	0.0000000	0.0000000	-7.8572976
C	1.2031140	-0.0978940	-7.1462876
C	1.2083860	-0.1025130	-5.7729606
H	-2.1570730	-0.1506710	5.2544144
H	-2.1421820	-0.1635250	7.6845834
H	0.0000000	0.0000000	8.9404374
H	2.1421820	0.1635250	7.6845834
H	2.1570730	0.1506710	5.2544144
H	2.0222250	0.7558520	3.3508194
H	2.0071390	0.7540900	0.9287204
H	-2.0071390	-0.7540900	0.9287204
H	-2.0222250	-0.7558520	3.3508194
H	-2.0071100	0.7541670	-0.9287206
H	-2.0221960	0.7559290	-3.3508186
H	2.0221960	-0.7559290	-3.3508186
H	2.0071100	-0.7541670	-0.9287206
H	2.1570670	-0.1507570	-5.2544146
H	2.1421750	-0.1636120	-7.6845836
H	0.0000000	0.0000000	-8.9404376
H	-2.1421750	0.1636120	-7.6845836
H	-2.1570670	0.1507570	-5.2544146

T_3 alternating

C	-1.0953480	0.5299630	5.7659680
C	0.0000000	0.0000000	5.0371010
C	1.0953480	-0.5299630	5.7659680
C	1.0952280	-0.5295040	7.1437290
C	0.0000000	0.0000000	7.8561680
C	-1.0952280	0.5295040	7.1437290
C	0.0000000	0.0000000	3.5677430
C	1.1652740	0.2788230	2.8431650
C	1.1683600	0.2757770	1.4627240
C	0.0000000	0.0000000	0.7287830
C	-1.1683600	-0.2757770	1.4627240
C	-1.1652740	-0.2788230	2.8431650
C	0.0000000	0.0000000	-0.7287850
C	1.1683330	-0.2758970	-1.4627270
C	1.1652500	-0.2789310	-2.8431670
C	0.0000000	0.0000000	-3.5677470
C	-1.1652500	0.2789310	-2.8431670
C	-1.1683330	0.2758970	-1.4627270
C	0.0000000	0.0000000	-5.0370990
C	-1.0953320	-0.5300080	-5.7659660
C	-1.0952110	-0.5295490	-7.1437250
C	0.0000000	0.0000000	-7.8561670
C	1.0952110	0.5295490	-7.1437250
C	1.0953320	0.5300080	-5.7659660
H	-1.9287200	0.9622280	5.2239030
H	-1.9373050	0.9467440	7.6840460
H	0.0000000	0.0000000	8.9390520
H	1.9373050	-0.9467440	7.6840460
H	1.9287200	-0.9622280	5.2239030
H	2.0749780	0.5310880	3.3769110
H	2.0813350	0.5314300	0.9380110
H	-2.0813350	-0.5314300	0.9380110
H	-2.0749780	-0.5310880	3.3769110
H	-2.0812820	0.5316420	-0.9380140
H	-2.0749290	0.5312780	-3.3769170
H	2.0749290	-0.5312780	-3.3769170
H	2.0812820	-0.5316420	-0.9380140
H	1.9286830	0.9623050	-5.2238960
H	1.9372700	0.9468230	-7.6840450
H	0.0000000	0.0000000	-8.9390510
H	-1.9372700	-0.9468230	-7.6840450
H	-1.9286830	-0.9623050	-5.2238960

T_4 alternating

C	-1.1113640	0.4570660	5.7413175
C	0.0000000	0.0000000	5.0200115
C	1.1113640	-0.4570660	5.7413175
C	1.1080770	-0.4632920	7.1255045
C	0.0000000	0.0000000	7.8237785
C	-1.1080770	0.4632920	7.1255045
C	0.0000000	0.0000000	3.5575885
C	1.2093940	0.0581720	2.8417365
C	1.2112120	0.0600810	1.4470695
C	0.0000000	0.0000000	0.7211375
C	-1.2112120	-0.0600810	1.4470695
C	-1.2093940	-0.0581720	2.8417365
C	0.0000000	0.0000000	-0.7211165
C	1.2112110	-0.0600080	-1.4470595
C	1.2093880	-0.0581350	-2.8417165
C	0.0000000	0.0000000	-3.5575845
C	-1.2093880	0.0581350	-2.8417165
C	-1.2112110	0.0600080	-1.4470595
C	0.0000000	0.0000000	-5.0200205
C	-1.1115470	-0.4565830	-5.7413295
C	-1.1082790	-0.4627830	-7.1255195
C	0.0000000	0.0000000	-7.8237915
C	1.1082790	0.4627830	-7.1255195
C	1.1115470	0.4565830	-5.7413295
H	-1.9709550	0.8438560	5.2080245
H	-1.9732670	0.8335720	7.6636515
H	0.0000000	0.0000000	8.9079515
H	1.9732670	-0.8335720	7.6636515
H	1.9709550	-0.8438560	5.2080245
H	2.1466240	0.1542520	3.3732055
H	2.1538280	0.1469940	0.9284955
H	-2.1538280	-0.1469940	0.9284955
H	-2.1466240	-0.1542520	3.3732055
H	-2.1538370	0.1468250	-0.9284895
H	-2.1466330	0.1541730	-3.3731645
H	2.1466330	-0.1541730	-3.3731645
H	2.1538370	-0.1468250	-0.9284895
H	1.9713170	0.8430010	-5.2080585
H	1.9736490	0.8326460	-7.6636615
H	0.0000000	0.0000000	-8.9079645
H	-1.9736490	-0.8326460	-7.6636615
H	-1.9713170	-0.8430010	-5.2080585

S6.3 p5P

D_0 alternating

C	-1.1738910	0.2351780	7.9603890
C	0.0000000	-0.0000000	7.2214840
C	1.1738910	-0.2351780	7.9603890
C	1.1734760	-0.2314770	9.3437310
C	0.0000000	-0.0000000	10.0545230
C	-1.1734760	0.2314770	9.3437310
C	0.0000000	-0.0000000	5.7644800
C	1.1617870	0.2718210	5.0179380
C	1.1627960	0.2756740	3.6427440
C	0.0000000	-0.0000000	2.8867880
C	-1.1627960	-0.2756740	3.6427440
C	-1.1617870	-0.2718210	5.0179380
C	0.0000000	-0.0000000	1.4433890
C	1.1923890	-0.0749440	0.6863580
C	1.1923890	-0.0749440	-0.6863580
C	0.0000000	-0.0000000	-1.4433890
C	-1.1923890	0.0749440	-0.6863580
C	-1.1923890	0.0749440	0.6863580
H	2.1419820	-0.1817010	1.1992170
H	2.1419820	-0.1817010	-1.1992170
C	0.0000000	-0.0000000	-2.8867880
H	-2.1419820	0.1817010	-1.1992170
H	-2.1419820	0.1817010	1.1992170
H	2.0791510	0.5421570	3.1287330
H	2.0780420	0.5344980	5.5368180
H	-2.0780420	-0.5344980	5.5368180
H	-2.0791510	-0.5421570	3.1287330
H	2.0952640	-0.4541850	7.4330060
H	2.0994810	-0.4252470	9.8764660
H	0.0000000	-0.0000000	11.1388150
H	-2.0994810	0.4252470	9.8764660
H	-2.0952640	0.4541850	7.4330060
C	1.1627960	0.2756740	-3.6427440
C	1.1617870	0.2718210	-5.0179380
C	0.0000000	-0.0000000	-5.7644800
C	-1.1617870	-0.2718210	-5.0179380
C	-1.1627960	-0.2756740	-3.6427440
H	2.0791510	0.5421570	-3.1287330
H	2.0780420	0.5344980	-5.5368180
C	0.0000000	-0.0000000	-7.2214840
H	-2.0780420	-0.5344980	-5.5368180
H	-2.0791510	-0.5421570	-3.1287330
C	1.1738910	-0.2351780	-7.9603890
C	1.1734760	-0.2314770	-9.3437310
C	0.0000000	-0.0000000	-10.0545230
C	-1.1734760	0.2314770	-9.3437310
C	-1.1738910	0.2351780	-7.9603890
H	2.0952640	-0.4541850	-7.4330060
H	2.0994810	-0.4252470	-9.8764660
H	0.0000000	-0.0000000	-11.1388150
H	-2.0994810	0.4252470	-9.8764660
H	-2.0952640	0.4541850	-7.4330060

S_0 alternating

C	-1.1588400	0.3067680	7.8999070
C	-0.0000000	0.0000000	7.1841980
C	1.1588400	-0.3067680	7.8999070
C	1.1591950	-0.3065990	9.2858160
C	-0.0000000	0.0000000	9.9851180
C	-1.1591950	0.3065990	9.2858160
C	-0.0000000	0.0000000	5.7100280
C	1.0977740	0.4729520	4.9894260
C	1.0977510	0.4732030	3.6062600
C	-0.0000000	0.0000000	2.8852930
C	-1.0977510	-0.4732030	3.6062600
C	-1.0977740	-0.4729520	4.9894260
C	-0.0000000	0.0000000	1.4126330
C	1.1620570	-0.2801980	0.6915110
C	1.1620570	-0.2801980	-0.6915110
C	-0.0000000	0.0000000	-1.4126330
C	-1.1620570	0.2801980	-0.6915110
C	-1.1620570	0.2801980	0.6915110
H	2.0709620	-0.5367340	1.2243720
H	2.0709620	-0.5367340	-1.2243720
C	-0.0000000	0.0000000	-2.8852930
H	-2.0709620	0.5367340	-1.2243720
H	-2.0709620	0.5367340	1.2243720
H	1.9500370	0.8800660	3.0733900
H	1.9501860	0.8788440	5.5228640
H	-1.9501860	-0.8788440	5.5228640
H	-1.9500370	-0.8800660	3.0733900
H	2.0617720	-0.5730350	7.3616370
H	2.0675410	-0.5561730	9.8229800
H	-0.0000000	0.0000000	11.0691910
H	-2.0675410	0.5561730	9.8229800
H	-2.0617720	0.5730350	7.3616370
C	1.0977510	0.4732030	-3.6062600
C	1.0977740	0.4729520	-4.9894260
C	-0.0000000	0.0000000	-5.7100280
C	-1.0977740	-0.4729520	-4.9894260
C	-1.0977510	-0.4732030	-3.6062600
H	1.9500370	0.8800660	-3.0733900
H	1.9501860	0.8788440	-5.5228640
C	-0.0000000	0.0000000	-7.1841980
H	-1.9501860	-0.8788440	-5.5228640
H	-1.9500370	-0.8800660	-3.0733900
C	1.1588400	-0.3067680	-7.8999070
C	1.1591950	-0.3065990	-9.2858160
C	-0.0000000	0.0000000	-9.9851180
C	-1.1591950	0.3065990	-9.2858160
C	-1.1588400	0.3067680	-7.8999070
H	2.0617720	-0.5730350	-7.3616370
H	2.0675410	-0.5561730	-9.8229800
H	-0.0000000	0.0000000	-11.0691910
H	-2.0675410	0.5561730	-9.8229800
H	-2.0617720	0.5730350	-7.3616370

S_1 alternating

C	-1.1768970	0.2462770	7.9169150
C	0.0000000	0.0000000	7.1851960
C	1.1768970	-0.2462770	7.9169150
C	1.1741040	-0.2477160	9.2983320
C	0.0000000	0.0000000	10.0021110
C	-1.1741040	0.2477160	9.2983320
C	0.0000000	0.0000000	5.7333170
C	1.1754900	0.2459740	4.9910220
C	1.1792330	0.2479450	3.6219230
C	0.0000000	0.0000000	2.8675890
C	-1.1792330	-0.2479450	3.6219230
C	-1.1754900	-0.2459740	4.9910220
C	0.0000000	0.0000000	1.4385610
C	1.2067710	-0.0011280	0.6820820
C	1.2067710	-0.0011280	-0.6820820
C	0.0000000	0.0000000	-1.4385610
C	-1.2067710	0.0011280	-0.6820820
C	-1.2067710	0.0011280	0.6820820
H	2.1587990	-0.0437660	1.1953300
H	2.1587990	-0.0437660	-1.1953300
C	0.0000000	0.0000000	-2.8675890
H	-2.1587990	0.0437660	-1.1953300
H	-2.1587990	0.0437660	1.1953300
H	2.1022290	0.4888040	3.1103420
H	2.0941350	0.4843460	5.5137580
H	-2.0941350	-0.4843460	5.5137580
H	-2.1022290	-0.4888040	3.1103420
H	2.0960160	-0.4748330	7.3908610
H	2.0939040	-0.4532140	9.8349030
H	0.0000000	0.0000000	11.0859860
H	-2.0939040	0.4532140	9.8349030
H	-2.0960160	0.4748330	7.3908610
C	1.1792330	0.2479450	-3.6219230
C	1.1754900	0.2459740	-4.9910220
C	0.0000000	0.0000000	-5.7333170
C	-1.1754900	-0.2459740	-4.9910220
C	-1.1792330	-0.2479450	-3.6219230
H	2.1022290	0.4888040	-3.1103420
H	2.0941350	0.4843460	-5.5137580
C	0.0000000	0.0000000	-7.1851960
H	-2.0941350	-0.4843460	-5.5137580
H	-2.1022290	-0.4888040	-3.1103420
C	1.1768970	-0.2462770	-7.9169150
C	1.1741040	-0.2477160	-9.2983320
C	0.0000000	0.0000000	-10.0021110
C	-1.1741040	0.2477160	-9.2983320
C	-1.1768970	0.2462770	-7.9169150
H	2.0960160	-0.4748330	-7.3908610
H	2.0939040	-0.4532140	-9.8349030
H	0.0000000	0.0000000	-11.0859860
H	-2.0939040	0.4532140	-9.8349030
H	-2.0960160	0.4748330	-7.3908610

T_1 alternating

C	-1.1564420	0.3213850	7.9172570
C	0.0000000	-0.0000000	7.1917800
C	1.1564420	-0.3213850	7.9172570
C	1.1549520	-0.3224310	9.3006770
C	0.0000000	-0.0000000	10.0025160
C	-1.1549520	0.3224310	9.3006770
C	0.0000000	-0.0000000	5.7328100
C	1.1734770	0.2541330	4.9933550
C	1.1787340	0.2569760	3.6249780
C	0.0000000	-0.0000000	2.8654380
C	-1.1787340	-0.2569760	3.6249780
C	-1.1734770	-0.2541330	4.9933550
C	0.0000000	-0.0000000	1.4464490
C	1.2076560	0.1172700	0.6779530
C	1.2076560	0.1172700	-0.6779530
C	0.0000000	-0.0000000	-1.4464490
C	-1.2076560	-0.1172700	-0.6779530
C	-1.2076560	-0.1172700	0.6779530
H	2.1597300	0.1813150	1.1878480
H	2.1597300	0.1813150	-1.1878480
C	0.0000000	-0.0000000	-2.8654380
H	-2.1597300	-0.1813150	-1.1878480
H	-2.1597300	-0.1813150	1.1878480
H	2.1042470	0.4941640	3.1176130
H	2.0904710	0.4924360	5.5197940
H	-2.0904710	-0.4924360	5.5197940
H	-2.1042470	-0.4941640	3.1176130
H	2.0579730	-0.6055570	7.3872450
H	2.0597710	-0.5858830	9.8371920
H	0.0000000	-0.0000000	11.0864050
H	-2.0597710	0.5858830	9.8371920
H	-2.0579730	0.6055570	7.3872450
C	1.1787340	0.2569760	-3.6249780
C	1.1734770	0.2541330	-4.9933550
C	0.0000000	-0.0000000	-5.7328100
C	-1.1734770	-0.2541330	-4.9933550
C	-1.1787340	-0.2569760	-3.6249780
H	2.1042470	0.4941640	-3.1176130
H	2.0904710	0.4924360	-5.5197940
C	0.0000000	-0.0000000	-7.1917800
H	-2.0904710	-0.4924360	-5.5197940
H	-2.1042470	-0.4941640	-3.1176130
C	1.1564420	-0.3213850	-7.9172570
C	1.1549520	-0.3224310	-9.3006770
C	0.0000000	-0.0000000	-10.0025160
C	-1.1549520	0.3224310	-9.3006770
C	-1.1564420	0.3213850	-7.9172570
H	2.0579730	-0.6055570	-7.3872450
H	2.0597710	-0.5858830	-9.8371920
H	0.0000000	-0.0000000	-11.0864050
H	-2.0597710	0.5858830	-9.8371920
H	-2.0579730	0.6055570	-7.3872450

T_2 alternating

C	-1.2054540	0.0807890	7.9221800
C	0.0000000	0.0000000	7.1782810
C	1.2054540	-0.0807890	7.9221800
C	1.2005160	-0.0841430	9.2986560
C	0.0000000	0.0000000	10.0067470
C	-1.2005160	0.0841430	9.2986560
C	0.0000000	0.0000000	5.7402940
C	1.1819550	0.2490220	4.9874500
C	1.1780430	0.2499260	3.6187720
C	0.0000000	0.0000000	2.8795670
C	-1.1780430	-0.2499260	3.6187720
C	-1.1819550	-0.2490220	4.9874500
C	0.0000000	0.0000000	1.4203910
C	1.1466610	-0.3414270	0.6900980
C	1.1466610	-0.3414270	-0.6900980
C	0.0000000	0.0000000	-1.4203910
C	-1.1466610	0.3414270	-0.6900980
C	-1.1466610	0.3414270	0.6900980
H	2.0425820	-0.6505790	1.2159990
H	2.0425820	-0.6505790	-1.2159990
C	0.0000000	0.0000000	-2.8795670
H	-2.0425820	0.6505790	-1.2159990
H	-2.0425820	0.6505790	1.2159990
H	2.0937440	0.4894150	3.0905530
H	2.1027930	0.4909830	5.5024880
H	-2.1027930	-0.4909830	5.5024880
H	-2.0937440	-0.4894150	3.0905530
H	2.1505030	-0.1761050	7.4030890
H	2.1394140	-0.1601730	9.8359320
H	0.0000000	0.0000000	11.0901380
H	-2.1394140	0.1601730	9.8359320
H	-2.1505030	0.1761050	7.4030890
C	1.1780430	0.2499260	-3.6187720
C	1.1819550	0.2490220	-4.9874500
C	0.0000000	0.0000000	-5.7402940
C	-1.1819550	-0.2490220	-4.9874500
C	-1.1780430	-0.2499260	-3.6187720
H	2.0937440	0.4894150	-3.0905530
H	2.1027930	0.4909830	-5.5024880
C	0.0000000	0.0000000	-7.1782810
H	-2.1027930	-0.4909830	-5.5024880
H	-2.0937440	-0.4894150	-3.0905530
C	1.2054540	-0.0807890	-7.9221800
C	1.2005160	-0.0841430	-9.2986560
C	0.0000000	0.0000000	-10.0067470
C	-1.2005160	0.0841430	-9.2986560
C	-1.2054540	0.0807890	-7.9221800
H	2.1505030	-0.1761050	-7.4030890
H	2.1394140	-0.1601730	-9.8359320
H	0.0000000	0.0000000	-11.0901380
H	-2.1394140	0.1601730	-9.8359320
H	-2.1505030	0.1761050	-7.4030890

T_3 alternating

C	-1.1980150	0.1818510	7.9200220
C	-0.0000000	0.0000000	7.1832130
C	1.1980150	-0.1818510	7.9200220
C	1.1948860	-0.1844870	9.2960330
C	-0.0000000	0.0000000	10.0059680
C	-1.1948860	0.1844870	9.2960330
C	-0.0000000	0.0000000	5.7281180
C	1.1456550	0.3499150	4.9938280
C	1.1437140	0.3516200	3.6135670
C	-0.0000000	0.0000000	2.8852790
C	-1.1437140	-0.3516200	3.6135670
C	-1.1456550	-0.3499150	4.9938280
C	-0.0000000	0.0000000	1.4222340
C	1.1684910	-0.3116910	0.6858880
C	1.1684910	-0.3116910	-0.6858880
C	-0.0000000	0.0000000	-1.4222340
C	-1.1684910	0.3116910	-0.6858880
C	-1.1684910	0.3116910	0.6858880
H	2.0688830	-0.5959830	1.2182340
H	2.0688830	-0.5959830	-1.2182340
C	-0.0000000	0.0000000	-2.8852790
H	-2.0688830	0.5959830	-1.2182340
H	-2.0688830	0.5959830	1.2182340
H	2.0365920	0.6660570	3.0850540
H	2.0406940	0.6656180	5.5166140
H	-2.0406940	-0.6656180	5.5166140
H	-2.0365920	-0.6660570	3.0850540
H	2.1262060	-0.3582770	7.3899790
H	2.1227720	-0.3406770	9.8348260
H	-0.0000000	0.0000000	11.0891430
H	-2.1227720	0.3406770	9.8348260
H	-2.1262060	0.3582770	7.3899790
C	1.1437140	0.3516200	-3.6135670
C	1.1456550	0.3499150	-4.9938280
C	-0.0000000	0.0000000	-5.7281180
C	-1.1456550	-0.3499150	-4.9938280
C	-1.1437140	-0.3516200	-3.6135670
H	2.0365920	0.6660570	-3.0850540
H	2.0406940	0.6656180	-5.5166140
C	-0.0000000	0.0000000	-7.1832130
H	-2.0406940	-0.6656180	-5.5166140
H	-2.0365920	-0.6660570	-3.0850540
C	1.1980150	-0.1818510	-7.9200220
C	1.1948860	-0.1844870	-9.2960330
C	-0.0000000	0.0000000	-10.0059680
C	-1.1948860	0.1844870	-9.2960330
C	-1.1980150	0.1818510	-7.9200220
H	2.1262060	-0.3582770	-7.3899790
H	2.1227720	-0.3406770	-9.8348260
H	-0.0000000	0.0000000	-11.0891430
H	-2.1227720	0.3406770	-9.8348260
H	-2.1262060	0.3582770	-7.3899790